Università degli Studi di Napoli "Federico II"

Scuola Politecnica e delle Scienze di Base

Area Didattica Scienze Matematiche Fisiche Naturali

Dipartimento di Fisica

Tesi di Laurea Magistrale in Fisica

Spin-CP properties of the new Higgs-like particle in $H \rightarrow ZZ^{(*)} \rightarrow 4\ell$ decay channel with the ATLAS detector at LHC

Relatori:
Prof. Giovanni Chiefari
Dott.ssa Elvira Rossi

Candidato:
Nello Bruscino
Matricola: N94/118

Anno Accademico 2012/2013

Contents

Introduction

The search for the Higgs boson is one of the main goals of the physics program of the ATLAS and CMS experiments at the LHC. The Higgs mechanism and the Higgs boson have been introduced to explain how the particles acquire mass. The Standard Model predict with an high precision its production and decay mode, its couplings and also its spin-parity (spin-CP) but not its mass. On the 4th of July 2012 both ATLAS and CMS announced the discovery of a new particle with a mass around 125 GeV compatible with the theoretical and experimental limits for a Standard Model Higgs boson. A signal with a significance $> 5\sigma$ has been clearly seen in the study of the $H \to \gamma\gamma$ and $H \to ZZ^{(*)} \to 4\ell$ decay channels with an integrated luminosity of $4.6\,\mathrm{fb}^{-1}$ at $\sqrt{s} = 7\,\mathrm{TeV}$ and $20.7\,\mathrm{fb}^{-1}$ at $\sqrt{s} = 8\,\mathrm{TeV}$.

A large number of measurements like mass, width, spin-parity, cross-section, couplings, branching ratios of the new particle became fundamental to reveal its nature and to answer the question if it is or not the Higgs boson predicted by the Standard Model. The main subject of my analysis has been the study of the spin-parity properties of the new boson in the $H \to ZZ^{(*)} \to 4\ell$ decay channel. The four leptons channel is called "Golden channel" because of its clear signature and its characteristics furnish also a powerful tool in the measurement of all the Higgs parameters, in particular the spin-parity. This thesis work has been devoted to the development of a procedure to distinguish between different spin-parity hypotheses using the kinematic distribution such as the production and decay angles. A multivariate approach based on the Matrix Element likelihood (MELA) has been applied to estimate the exclusion significance of one spin-parity model respect to an other.

Using useful kinematic observables a discriminant has been build to test pair-wise two spin hypotheses. This approach could be used in a more general analysis to measure the HZZ vertex couplings but at the moment the low statistic doesn't give a precise estimations.

This thesis is divided in 5 chapters:

- **Chapter 1**: the first chapter present the theoretical background that leads to the introduction of the Higgs mechanism and of the Higgs boson. Its production mechanism and also its decay channel in proton-proton collisions are illustrated. The discovery of the new particle and the actual theoretical and experimental limits on the Higgs boson mass are also reported.

- **Chapter 2**: the chapter 2 give a short overview of the LHC and the ATLAS apparatus with particular attention on their characteristics useful for this analysis.

- **Chapter 3**: in chapter 3 the main subjects are how the physical objects (electrons, muon and jets) are identified and reconstructed in ATLAS. A slight accent has been put on the reconstruction of the leptons and the performance of the Muon Spectrometer and calorimeters.

- **Chapter 4**: in the chapter 4 my analysis is described in details. The Golden channel and the measurement of its characteristics are presented. This Chapter provides an extensive illustration of the MELA analysis and explains in details the developments I worked on.

- **Chapter 5**: Finally the results of this study and in particular of the Hypothesis Test are presented in chapter 5.

Last chapter gives the final comments and conclusions.

Chapter 1

Theory introduction: Standard Model Higgs boson

This Chapter gives a brief outline of the Standard Model Theory. The Standard Model of particle physics is a gauge theory describing the fundamental components of matter and their interactions, and features our current understanding of the world at the level of elementary particles. The Standard Model was formulated in the 1970s [1, 2, 3, 4], and since then has been tested to an unprecedented level of precision. This Chapter also provides a short description of the electroweak symmetry breaking mechanism, the current state of constraints given by direct and indirect searches and the discovery of the Higgs boson. Finally we give a description of the main mechanisms of production and decay.

1.1 The Standard Model

According to the Standard Model there are three kinds of elementary particles: leptons, quarks and the force mediators, referred to as gauge bosons. The leptons and the quarks are called fermions (spin-1/2 particles) obeying to Fermi-Dirac statistics. The force mediators are integer spin particles and thus obey to Bose-Einstein statistics. They are called bosons. An antiparticle corresponds to each of the elementary particles.

There are three generations of leptons. Every generation is composed by the charged lepton and its neutrino. The charged leptons differ only in their masses, which are increased in every generation with respect to the previous one. In Table 1.1 the lepton generations are presented along with their mass and charge. The second and third generation of charged leptons, the muon (μ) and the tau (τ), are unstable and decay to other particles.

Generation	lepton/quark	charge $[Q/e]$	mass [MeV]
First	e	-1	0.511
	ν_e	0	$< 0.225 \times 10^{-3}$
Second	μ	-1	105.7
	ν_μ	0	< 0.19
Third	τ	-1	1777
	ν_τ	0	< 18.2
First	u	$+\frac{2}{3}$	$< 2.3 \times 10^{-3}$
	d	$-\frac{1}{3}$	$< 4.8 \times 10^{-3}$
Second	c	$+\frac{2}{3}$	1.28
	s	$-\frac{1}{3}$	95×10^{-3}
Third	t	$+\frac{2}{3}$	173.5
	b	$-\frac{1}{3}$	4.18

Table 1.1: The six leptons and six quark flavors form three generations of leptons and qualks. The quoted masses are the cited averages or limits set according to [5].

There are six “flavors” of quarks, each with fractional charge, forming three generations of increasing mass: “up” and “down”, “charm” and “strange”, “top” and “bottom”, denoted by the first letter of their names. Every quark comes in three colors: “red”, “blue”, “green”. Their mass values or mass limits are shown in Table 1.1.

The force mediators of the fundamental interactions in nature (the gravitational, the electromagnetic, the weak and the strong) are the gauge bosons. In Table 1.2 the gauge bosons are presented along with their mass, charge and the interaction type they correspond to.

The gravitational interaction appears between all types of particles and is by far the weakest (about 10^{38} times weaker than the electromagnetic force). Therefore it has negligible impact on microscopic particle interactions. The graviton (G), a purely theoretical spin-2 boson, is considered to be the gauge boson.

The electromagnetic force is carried by spin-1 photons and acts between electrically charged particles. The weak interaction, responsible for nuclear β-decays, and absorption and emission of neutrinos, is approximately 1000 times weaker than the electromagnetic force. It has three gauge bosons: $W^{\pm}$ and Z, which are massive with spin 1.

At last, the strong interaction is roughly 100 times stronger than the electromagnetic force. Its gauge bosons acting between quarks are the eight massless, spin-1 gluons (g).

Effort has been made in the last century in order to describe the four

boson	charge $[Q/e]$	mass [GeV]	interaction
G	0	$< 7 \times 10^{-41}$ [6]	gravitational
γ	0	0	electromagnetic
$W^{\pm}$	± 1	80.4	weak
Z	0	91.2	weak
g	0	0	strong

Table 1.2: There are six bosons for the four fundamental forces. The quoted masses are the cited averages or limits set according to [5].

fundamental interactions as different manifestations of a single field. This is partially achieved by the Standard Model. The Standard Model is a renormalizable quantum field theory describing the electromagnetic, weak and strong interactions based on a combination of local gauge symmetry groups $\mathrm{SU}(3)_C \otimes \mathrm{SU}(2)_L \otimes \mathrm{U}(1)_Y$, where:

- $\mathrm{SU}(3)_C$ refers to a colour local symmetry, with a corresponding gauge invariance and the associated 8 gauge bosons without mass – gluons, that hold quarks together through the strong force[1];

- $\mathrm{SU}(2)_L \otimes \mathrm{U}(1)_Y$, instead, refers to the weak isospin symmetry group, which unify electromagnetic and weak interactions (denoted Electroweak Theory[2]). The Electroweak Theory (EW) was developed by Sheldon Lee Glashow, Abdus Salam, and Steven Weinberg [1, 2, 3] in the 1960s and is mediated by three weak massive gauge boson (W^+, W^-, Z) and one massless boson, the photon (γ).

The SM explains three of the four fundamental forces in a single theory.

[1]The strong interactions of colored quarks and gluons, developed by David Politzer, Frank Wilczek and David Gross, are described by the gauge field theory called Quantum Chromodynamics (QCD).

[2]The electroweak theory is not an unification theory, because two coupling constants don't come from one unified coupling constant. Exactly, the $\mathrm{U}(1)_Y \otimes \mathrm{SU}(2)_L$ group is the product between two different gauge groups, whose relation between coupling constants is not predicted by the theory. G could be called unification group only if:

$$G \supset \mathrm{SU}(2)_L \otimes \mathrm{U}(1)_Y .$$

In this instance we can predict the relation between the coupling constants. The Standard Model is not a unification theory too: it is the product between three gauge groups. Some theories, named GUT (Grand Unification Theory), seek to unify these three groups:

$$G \supset \mathrm{SU}(3)_C \otimes \mathrm{SU}(2)_L \otimes \mathrm{U}(1)_Y .$$

The SM Lagrangian can be parted in two: the QCD lagrangian, which describes the strong interations, and the electroweak (EW) lagrangian, which describes electromagnetic and weak interactions:

$$\mathcal{L}_{SM} = \mathcal{L}_{QCD} + \mathcal{L}_{EW} \tag{1.1}$$

The strong interactions are completely symmetric under $SU(3)_C$ transformations: it is an exact symmetry. In the electroweak interactions, conversely, the vector bosons aren't massless (according to many experimets): we could say that the symmetry is "broken". So, it's necessary to introduce a mechanism of "spontaneous $SU(2)_L \otimes U(1)_Y$ symmetry breaking" to give a mass to vector bosons. The Higgs mechanism [4] is a mechanism of spontaneous symmetry breaking and, as will be described in the following Sections, it predicts a scalar particle, the Higgs boson, whose mass is free parameter in the SM theory.

1.1.1 Quantum Field Theory

Quantum Field Theory (QFT) is a theory that extends quantum mechanics from single localised particles to fields that exist everywhere. It describes the behavior of particles and their interactions. In classic quantum mechanics, a system is described by its state represented by the wave function ψ, whereas, in the quantum field theories, each particle is described as excitation of the local field $\phi(x)$. From the classical mechanics, the properties and the interactions of the field $\phi(x)$ are determined by the Lagrangian density $\mathcal{L}$, using the field and its space-time derivatives

$$\mathcal{L}(x) = \mathcal{L}(\phi, \partial_\mu \phi) \tag{1.2}$$

The evolution of a system occurs along a path for which the action (S) is stationary

$$\delta S = \delta \int \mathcal{L}(\phi, \partial_\mu \phi)\, d^4x = 0 \tag{1.3}$$

which leads to the Euler-Lagrange equation that describes the motion of the field

$$\partial_\mu \left[\frac{\partial \mathcal{L}}{\partial(\partial_\mu \phi)} \right] - \frac{\partial \mathcal{L}}{\partial \phi} = 0 \tag{1.4}$$

A gauge symmetry is any continuous transformation of the field that does not affect δS and consequently, does not change the equations of motion. These transformations form the gauge symmetry groups of the system.

Based on the Euler-Lagrange equation, a transformation

$$\phi \to \phi + \epsilon\, \Delta\phi \tag{1.5}$$

where ϵ is an infinitesimal parameter, can be a symmetry of the system if the Lagrangian density is invariant under this transformation up to a four-divergence

$$\mathcal{L} \to \mathcal{L} + \epsilon\, \partial_\mu J^\mu \tag{1.6}$$

According to Noether's Theorem, every symmetry yields a conservation law and, every conservation law represents a symmetry. Given this theorem, the current $j_\mu(x) = \dfrac{\partial \mathcal{L}}{\partial(\partial_\mu \phi)} \Delta\phi - J^\mu$ is conserved, meaning $\partial_\mu j^\mu = 0$.

1.1.2 Quantum Electrodynamics

Quantum electrodynamics (QED) is the first relativistic quantum field theory that have been developed. It is an abelian gauge theory describing a fermion field ψ and its electromagnetic field. The field's Lagrangian is required to satisfy the "local gauge invariance" principle, and therefore be invariant under the local gauge transformation,

$$\psi \to U\psi = e^{\mathrm{i}\alpha(x)}\psi \tag{1.7}$$

where $\alpha(x)$ is an arbitrary parameter depending on the space and time coordinates. The family of such phase transformations forms a unitary abelian group known as the U(1) group.

The Dirac Lagrangian density for a spin-1/2 field of mass m satisfying the local gauge invariance an be written as:

$$\mathcal{L} = [\mathrm{i}\bar{\psi}\gamma^\mu \partial_\mu \psi - m\bar{\psi}\psi] + e\bar{\psi}\gamma^\mu A_\mu \psi \tag{1.8}$$

where $\bar{\psi} = \psi^\dagger \psi^0$ and γ^μ are the 4×4 Dirac matrices satisfying the anticommutation relation $\{\gamma^\mu, \gamma^\nu\} = \gamma^\mu\gamma^\nu + \gamma^\nu\gamma^\mu = 2g^{\mu\nu}$, with $g^{\mu\nu}$ being the metric tensor; e is later identified as the elementary charge and A_μ is a new field, called "gauge field" transforming under the law $A_\mu \to A_\mu + \dfrac{1}{e}\partial_\mu \alpha$.

The covariant derivative D_μ needs to be introduced $D_\mu = \partial_\mu - \mathrm{i}eA_\mu$ transforming as $D_\mu\psi \to e^{\mathrm{i}\alpha(x)} D_\mu \psi$. This Lagrangian describes the interaction between electrons, ψ, and the electromagnetic field, A_μ and it includes also solutions for an anti-particle, the positron. In order to satisfy the gauge principle, the gauge field is required to be massless and the full Lagrangian density is

$$\mathcal{L} = -\frac{1}{4} F^{\mu\nu} F_{\mu\nu} + \bar{\psi}(\mathrm{i}\gamma^\mu D_\mu - m)\psi \tag{1.9}$$

where $F^{\mu\nu}$ is the electromagnetic field strength tensor, defined as $F^{\mu\nu} = \partial_\mu A_\nu - \partial_\nu A_\mu$.

1.1.3 Quantum Chromodynamics

The Quantum Chromodynamics (QCD) is a non-abelian theory with 8 generators each of them introducing a mediator, so it explain the behavior of the quarks and the force carriers, the gluons. The structure of QCD is extracted from local gauge invariance, replacing the U(1) group used for the QED with the group of phase transformations on the quark color fields, SU(3). The free Lagrangian density is

$$\mathcal{L} = \sum_j \bar{q}_j(\mathrm{i}\gamma^\mu \partial_\mu - m_j)q_j \tag{1.10}$$

where $q_j = (q_r, q_b, q_g)^T_j$, with $j = 1, ..., 6$ is the color triplet (corresponding to the six quark flavors). The equations will be given for one quark flavor hereafter but summation is implied.

Requiring the Lagrangian density to be invariant under

$$q(x) \to Uq(x) = e^{-\mathrm{i}g\alpha_a(x)T_a}q(x) \tag{1.11}$$

where U is an arbitrary 3×3 unitary matrix, g is the strong coupling constant, α_a are arbitrary parameters, and $T_a = \dfrac{\lambda_a}{2}$ with $a = 1, ..., 8$, the generators of the SU(3) group where λ_a the Gell-Mann matrices, a set of linearly independent traceless 3×3 matrices.

In order to satisfy SU(3) local gauge invariance, the final QCD Lagrangian density is

$$\mathcal{L} = -\frac{1}{4}G^\alpha_{\mu\nu}G^{\mu\nu}_\alpha + \bar{q}(\mathrm{i}\gamma_\mu D^\mu - m)q \tag{1.12}$$

where $G^\alpha_{\mu\nu}$ the gluon field tensor

$$G^{\mu\nu}_\alpha = \partial_\mu G^\nu_a - \partial_\nu G^\mu_a - gf^{abc}G^\mu_b G^\nu_c \tag{1.13}$$

and where f^{abc} are the structure constants of SU(3).

Due to the non-Abelian character of the theory, resulting to the last term in Equation 1.13, the Lagrangian contains terms corresponding to self-interaction between the gauge boson fields. The self-interactions form three and four gluon vertices.

1.2 Electroweak Theory

The weak interaction is caused by the emission or absorption of W and Z bosons and it describe the decay of muons. Weak charged current data and electromagnetic processes are invariant under weak isospin SU(2) and weak hyper-charge U(1) transformations. This is described by the unified theory of electromagnetic and weak interactions.

As QED and QCD, also the Electroweak Theory is based on the same principle of gauge invariance. It treats the weak and electromagnetic interactions as different manifestations of the same force. Its gauge symmetry group is $\mathrm{SU}(2)_L \otimes \mathrm{U}(1)_Y$. $\mathrm{SU}(2)_L$ refers to the weak isospin (I): the subscript L reminds that it involves only left-handed fields. $\mathrm{U}(1)_Y$ refers to the weak hypercharge (Y) and involves both states of chirality, left (L) and right(R). The weak hypercharge is connected to the charge and the weak isospin by $Q = I_3 + \frac{Y}{2}$, where I_3 is the third component of the weak isospin. For the left-handed doublets and right-handed singlets, the U(1) transformation corresponds to multiplication by a phase factor $e^{\mathrm{i}\alpha^a(x)\frac{Y}{2}}$. The left-handed doublets transform as

$$\psi_L \to e^{\mathrm{i}\beta^a(x)\frac{\tau^a}{2}}\psi_L \tag{1.14}$$

where $a = 1, 2, 3$ and τ^a the Pauli matrices and $\frac{\tau^a}{2}$ the generators of the SU(2) group.

By applying the gauge principle four gauge fields are introduced. Three gauge field (isotriplet), W^i_μ, are associated to $\mathrm{SU}(2)_L$ and couple only to the left-handed components, while one gauge field (singlet), B_μ, is associated to $\mathrm{U}(1)_Y$ and couples to both chiralities of the fermion fields. The interaction terms between the fermions and the gauge fields is

$$\mathcal{L}_{\mathrm{int}} = -\psi_L\gamma^\mu\left(g\frac{\tau_a}{2}W^a_\mu + g'\frac{Y}{2}B_\mu\right)\psi_L - \bar{\psi}_R\gamma^\mu\left(g'\frac{Y}{2}B_\mu\right)\psi_R \tag{1.15}$$

where $W^a_{\mu\nu}$ and $B_{\mu\nu}$ the fields tensors

$$W^i_{\mu\nu} = \partial_\mu W^i_\nu - \partial_\nu W^i_\mu - g\epsilon^{ijk}W^j_\mu W^k_\nu \tag{1.16}$$

$$B_{\mu\nu} = \partial_\mu B_\nu - \partial_\nu B_\mu \tag{1.17}$$

where ϵ^{ijk} the structure constants of SU(2).
The coupling of the W^a_μ is visible only to the left-handed components. In order to conserve the gauge invariance, no fermion mass terms are in the Lagrangian density. Therefore, fermion masses will be generated by gauge invariant Yukawa interactions with the Higgs field.

Finally, the full electroweak Lagrangian will be

$$\mathcal{L}_{\mathrm{EW}} = \mathcal{L}_{\mathrm{f,g}} + \mathcal{L}_H + \mathcal{L}_{\mathrm{Yukawa}} \tag{1.18}$$

where $\mathcal{L}_{\mathrm{f,g}}$, $\mathcal{L}_H$, $\mathcal{L}_{\mathrm{Yukawa}}$ are the fermionic and gauge, Higgs and Yukawa terms, respectively.

1.3 The Higgs mechanism: simmetry breaking

So far, no quadratic terms of the gauge fields were present in the Lagrangian densities mentioned in the previous Sections. The gauge bosons are considered to be massless. The vector bosons of the weak interaction are experimentally known to be massive, with $m_{W^{\pm}} = 80.4\,\text{GeV}$ and $m_{Z^0} = 91.2\,\text{GeV}$ [5], accordingly. However, adding a mass component leads to violation of the gauge invariance. The same stands for the fermion masses.
In a proposed solution, called the Higgs mechanism, the universe is filled with a Higgs field [3]. By interacting with this field, the gauge bosons and fermions acquire masses. States with a Higgs field are not orthogonal to the ground state (or vacuum state) which means that the SU(2) and U(1) quantum numbers of the vacuum are non-zero. This mechanism was introduced to solve this issue: the symmetry is still valid for the Lagrangian but not for the vacuum state of the system. Such symmetry is called a spontaneously broken symmetry.
To achieve this, an additional $\text{SU}(2)_L$ isospin doublet of complex scalar fields with $Y = 1$

$$\phi = \begin{pmatrix} \phi^+ \\ \phi^0 \end{pmatrix} \tag{1.19}$$

is introduced with the corresponding contribution in the Lagrangian

$$\mathcal{L}_H = (D_\mu \phi)^\dagger (D^\mu \phi) - V(\phi) \tag{1.20}$$

where the potential term

$$V(\phi) = \mu^2 \phi^\dagger \phi + \lambda (\phi^\dagger \phi)^2 = \mu^2 \phi^2 + \lambda \phi^4 \tag{1.21}$$

To determine the ground state, ϕ_0, the potential is minimized. For $\mu^2 > 0$, $\phi_0 = 0$. However, for $\mu^2 < 0$ the shape of the potential is shown in Figure 1.1 and $\phi_0^2 = -\frac{\mu^2}{2\lambda} \equiv \frac{u^2}{2}$. In the context of $\mu^2 < 0$, the potential has a non-trivial minimum. A non-vanishing vacuum expected value [4] for ϕ^2 in the physical vacuum state has been obtained. The reference ground state for the local gauge transformation is chosen to be

$$\phi = \frac{1}{\sqrt{2}} \begin{pmatrix} 0 \\ u \end{pmatrix} \tag{1.22}$$

[3] According to the Higgs mechanism, the Higgs field is a doublet in SU(2) space, has a non-zero U(1) hypercharge and is a SU(3) colour singlet

[4] The absolute value of the field at the minimal of the potential is known as the vacuum expected value.

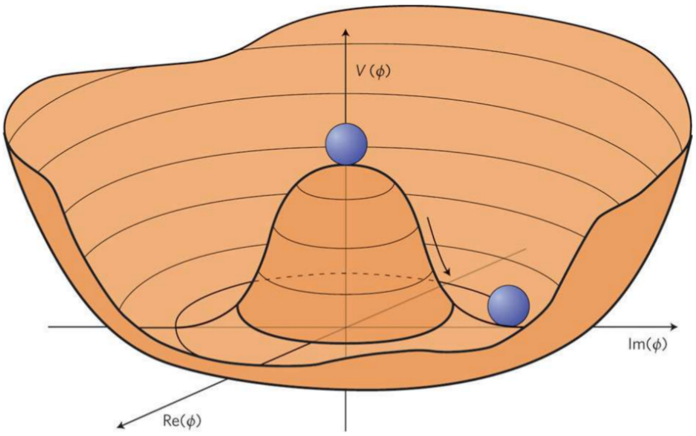

Figure 1.1: The shape of the Higgs potential $V(\phi) = \mu^2\phi^2 + \lambda\phi^4$.

which breaks the $\mathrm{SU}(2)_L$ symmetry while the Lagrangian remains invariant under $\mathrm{SU}(2)_L \otimes \mathrm{U}(1)_Y$ transformations (spontaneous symmetry breaking). Expanding about this minimum the scalar doublet ϕ is redefined

$$\phi(x) = e^{\frac{i\xi_a(x)\tau^a}{2u}} \begin{pmatrix} 0 \\ \frac{u+H(x)}{\sqrt{2}} \end{pmatrix} \tag{1.23}$$

where $\xi_a(x)$ $(a = 1, 2, 3)$ are new real fields and $H(x)$ is the real scalar Higgs field. The Lagrangian is locally SU(2) invariant and by using the freedom of gauge transformations, the $\xi_a(x)$ disappear from the Lagrangian

$$\phi(x) = \frac{1}{\sqrt{2}} \begin{pmatrix} 0 \\ u + H(x) \end{pmatrix} \tag{1.24}$$

Remembering that $D^\mu = \partial^\mu + \mathrm{i}gW_a^\mu\frac{\tau^a}{2} + \mathrm{i}g'\frac{1}{2}B^\mu$, where g is the SU(2) and g' the U(1) coupling constants, the kinetic part of the Lagrangian $\mathcal{L}_H$ component becomes

$$(D_\mu\psi)^\dagger(D^\mu\psi) \to \frac{1}{2}\partial^\mu H\partial_\mu H + \frac{1}{8}g^2(u+H)^2|W^1_\mu + W^2_\mu|^2 + \frac{1}{8}(u+H)^2|g'W^3_\mu - gB_\mu|^2 \tag{1.25}$$

The charged physical fields $W^\pm$ are then defined as $W^\pm_\mu = \frac{1}{\sqrt{2}}(W^1_\mu \mp \mathrm{i}W^2_\mu)$, while the neutral physical fields of the photon and the Z boson are defined, to be orthogonal to each other, as

$$Z_\mu = \frac{g'W^3_\mu - gB_\mu}{\sqrt{g'^2 + g^2}} \tag{1.26}$$

$$A_\mu = \frac{g'W^3_\mu + gB_\mu}{\sqrt{g'^2 + g^2}} \tag{1.27}$$

By introducing the "weak mixing angle" θ_w

$$\cos\theta_\mathrm{w} = \frac{g'}{\sqrt{g'^2+g^2}},\ \sin\theta_\mathrm{w} = \frac{g}{\sqrt{g'^2+g^2}} \tag{1.28}$$

neutral fileds become

$$Z_\mu = -B_\mu \sin\theta_\mathrm{w} + W^3_\mu \cos\theta_\mathrm{w} \tag{1.29}$$

$$A_\mu = B_\mu \cos\theta_\mathrm{w} + W^3_\mu \sin\theta_\mathrm{w} \tag{1.30}$$

The masses of the gauge bosons are extracted from the mass terms in Equation 1.25: $M_W = \frac{gu}{2}$ and $M_Z = \frac{\sqrt{g'^2+g^2}u}{2}$, while the photon remains massless. One can also write:

$$\frac{M_W}{M_Z} = \cos\theta_\mathrm{w} \tag{1.31}$$

which links together the masses of the weak bosons through the electroweak mixing angle.

As said in the previuos Section, also the fermion masses are generated by the spontaneous breaking of the $\mathrm{SU}(2)_L \otimes \mathrm{U}(1)_Y$ gauge symmetry through the Yukawa interactions between the Higgs and the fermion fields. For a single generation

$$\mathcal{L}_\mathrm{Yukawa} = -Y_\ell \bar{L}_L \phi \ell_R - Y_d \bar{Q}_L \phi d_R - Y_u \bar{Q}_L \tilde{\phi} u_R + \mathrm{h.c.} \tag{1.32}$$

where $L_L = (\nu_L, \ell_L)^T$ and $Q_L = (u_L, d_L)^T$ are the left-handed lepton and quark doublets, $\tilde{\phi} = -\mathrm{i}\tau_a \phi^*$ is the charge conjugate of the Higgs douplet, ℓ is the charged lepton, and Y_ℓ, Y_d, Y_u are the matrices of Yukawa coupling constants between the fermions and the Higgs boson.
How the vacuum expectation value of ϕ gives mass to fermions will be described in the next Section.
We implicitly suppose that there is only one ϕ doublet, but there is no reason except simplicity. Two or more doublets could exist: this is translated into the existence of multiple neutral and charged Higgs bosons. A particularly important model, the Two Higgs Doublet Model (2HDM), assumes the existence of two separate scalar complex doublets: $\phi_1 = \begin{pmatrix} \phi_1^+ \\ \phi_1^0 \end{pmatrix}$ and $\phi_2 = \begin{pmatrix} \phi_2^+ \\ \phi_2^0 \end{pmatrix}$ with vacuum expectation values $\langle\phi_1\rangle = \begin{pmatrix} 0 \\ v_1 \end{pmatrix}$ and $\langle\phi_2\rangle = \begin{pmatrix} 0 \\ v_2 \end{pmatrix}$.

The Standard Model gives a very good and convincing description of the fundamental structure of the observable matter. It requires only 19 independent and arbitrary parameters.

- 6 quarks masses, 3 lepton masses,
- 3 gauge couplings (e, θ_{w} and α_s),
- 3 Cabibbo mixing angles and the CP violating Kobayashi-Maskawa complex phase,
- the QCD vacuum angle,
- the Higgs boson mass and the vacuum expectation value v.

Experiments have measured with unprecedented precision quantities that confirm accurate predictions of the SM. A typical example is the high order corrections of the electron gyromagnetic ratio.
Open questions like the absence of right handed neutrino sector, the particles mass hierarchy, the matter anti-matter asymmetry could be partially solve with theory beyond the SM. The most popular of these theory is the Supersymmetry theory (SUSY) [7]. It relates fermions and bosons by introducing operators that turns fermionic states into bosonic states and vice versa. This extension predicts the existence of new particles supersymmetric partners of the SM (higgsinos, squarks, sleptons, goldstinos, neutralinos, charginos, and gluinos).

1.4 The Higgs boson

The Higgs mechanism gives mass to fermions also. The introduction of mass terms, as mentioned in Section 1.1.2, break $\mathrm{SU}(2)_L$ symmetry: through a spontaneous symmetry breaking, fermion masses will be generated dynamically by gauge invariant Yukawa interactions with the Higgs field (Equation 1.32). Replacing with Higgs vacuum state 1.24, the terms from $\mathcal{L}_{\mathrm{Yukawa}}$ involving the vacuum expectation value will become fermion mass terms of the form:

$$\mathcal{L}_{\text{fermion mass}} = -(\bar{d'}_L M_d d'_R + \bar{u'}_L M_u u'_R) + \text{h.c.} \tag{1.33}$$

where $M_{u,d} = (\sqrt{2}u)Y_{u,d}$. Lepton terms are neglected in short, u' and d' are quark weak eigenstates (SU(2) doublet $Q_L = \begin{pmatrix} u'_L \\ d'_L \end{pmatrix}$ and two singlets u'_R, d'_R). These Yukawa coupling matrices may be diagonalized by unitary transformations $U_{L,R}$ and $D_{L,R}$ from the weak eigenstates u' and d' to the mass eigenstates u and d:

$$\begin{aligned}\begin{pmatrix} u' \\ c' \\ t' \end{pmatrix}_{L.R} &= U_{L,R}\begin{pmatrix} u \\ c \\ t \end{pmatrix} \\ \begin{pmatrix} d' \\ s' \\ b' \end{pmatrix}_{L.R} &= D_{L,R}\begin{pmatrix} d \\ s \\ b \end{pmatrix}\end{aligned} \tag{1.34}$$

such that

$$\begin{aligned}U_R^{-1} M_u U_L &= \begin{pmatrix} m_u & 0 & 0 \\ 0 & m_c & 0 \\ 0 & 0 & m_t \end{pmatrix} \\ D_R^{-1} M_d D_L &= \begin{pmatrix} m_d & 0 & 0 \\ 0 & m_s & 0 \\ 0 & 0 & m_b \end{pmatrix}\end{aligned} \tag{1.35}$$

The fact that the weak eigenstates are not exactly the same as the mass eigenstates leads to electroweak symmetry breaking, the rich structure of the CKM matrix (U_{CKM}) and flavor changing interactions. The analogous structure exists also for the neutrino sector. Generally, CKM matrix can be written as

$$\begin{pmatrix} V_{ud} & V_{us} & V_{ub} \\ V_{cd} & V_{cs} & V_{cb} \\ V_{td} & V_{ts} & V_{tb} \end{pmatrix} \tag{1.36}$$

where diagonal elements lead to flavor changing interactions. The definition of CKM matrix up to a phase not eliminable leads to the CP violation.

After the interaction with Higgs field, the fermion masses are given:

$$m_f = \frac{\eta}{\sqrt{2}} g^f \tag{1.37}$$

Here the coupling constant between fermions and the Higgs is proportional to the mass of fermions. For this reason fermion couplings are very different from each other (from $m_\nu < 1\,\text{eV}$ up to $m_t = 174\,\text{GeV}$). From the free Lagrangian of Higgs boson

$$\mathcal{L} = \frac{1}{2}(\partial_\mu H)(\partial^\mu H) - \lambda u^2 H^2 - \lambda u H^3 \frac{\lambda}{4} H^4 \tag{1.38}$$

we obtain autointeraction terms (cubic and quadratic) and mass term $m_H^2 = 2\lambda u^2$. While the vacuum expectation value is defined by the Fermi constant

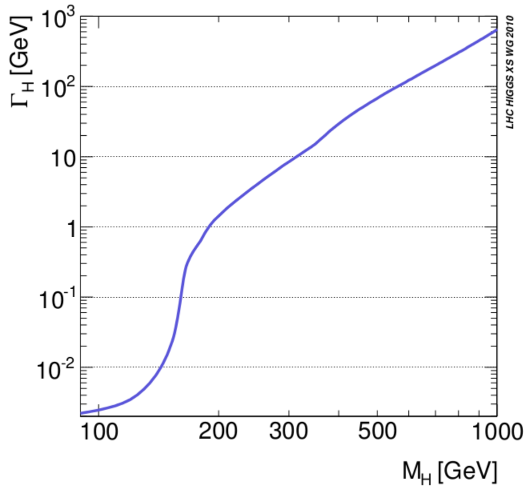

Figure 1.2: The Higgs total width is presented as a function of its mass. For low masses the Higgs is a narrow resonance while for high masses, the mass and the width are of the same order of magnitude.

G_F as $u = (\sqrt{2G_F})^{\frac{1}{2}} \approx 246\,\mathrm{GeV}$, on the contrary the constant λ is unknown. So, the value of Higgs boson mass is free parameter in the SM theory, but interesting theoretical and expeimental constraints can be derived.

The partial decay width of the Higgs boson (Figure 1.2) to fermion anti-fermion is:

$$\Gamma(H \to f\bar{f}) = \frac{c_f}{4\sqrt{2}\pi} G m_H m_f^2 \beta^3 \tag{1.39}$$

where $\beta = \sqrt{1 - \frac{4m_f^2}{m_H^2}}$. Otherwise the decay width to boson vectors is:

$$\Gamma(H \to VV) = k\frac{G_F m_H^3}{8\sqrt{2}\pi}\beta(1 - 4x + 12x^2) \tag{1.40}$$

where $\beta = \sqrt{1 - \frac{4m_V^2}{m_H^2}} ex = \frac{m_V^2}{m_H^2}$. In low mass region the decay width is very strict than the experimental resolution in LHC. Increasing the mass other processes become accessible and the rapid width variation is noticed. At higher mass, $\mathcal{O}(1\,\mathrm{TeV})$, the width value is equal to mass value: hence to discriminate Higgs from background become more difficult.

1.4.1 Theoretical constraints on the Higgs mass

All the parameters of the SM including the coupling constants, gauge boson and fermion masses, and quark mixing angles, have been determined experimentally, except for the Higgs boson mass. It is a free parameter of the

Standard Model but interesting theoretical constraints can be derived from assumptions on the energy range in which the SM is valid before perturbation theory breaks down and new phenomena emerge. These constraints are based on perturbative unitarity in scattering amplitudes, triviality, vacuum stability and fine-tuning.

Perturbative unitarity

Fermi's theory of weak interactions predicted cross sections at very high energies (comparable with Fermi Scale) that violated unitarity: for this reason this theory was replaced. In this theory, the cross section of the process $\nu_\mu e \to \nu_e \mu$ at high energy is $\sigma \simeq G_\mu^{-1/2} s$ (in opposition to a limited trend s^{-1}): for energy up to $\sqrt{s} \simeq G_\mu^{-1/2} \simeq 300\,\text{GeV}$ unitarity will be violated. The introduction of the massive boson vector W solved this problem, but create another one in $\nu\bar{\nu} \to W^+W^-$, solved introducing neutral Z boson. An analogous problem was presented in the WW elastic scattering. Its cross section in the SM is calculated with a number of Feynman diagrams shown in Figure 1.3. If only the left three diagrams are used (leading order processes involving γ and Z exchange diagrams and W-W self-interaction diagrams) to calculate the WW scattering cross section, the amplitude for the scattering of longitudinal W and Z increases with the energy, which finally violates the unitarity at some stage. However if the contribution from the Higgs intermediate state is introduced, in channels s and t and shown in the right two diagrams in Figure 1.3, the unitarity is restored. Thus the total amplitude at high energy scale is a constant value proportional to $\lambda = \frac{m_H^2}{2u^2}$. If λ is high the divergence continues and the unitarity isn't restored [8]. Expanding the cross section in partial waves through the optical theorem:

$$\sigma = \frac{1}{s}\text{Im}[A(\theta = 0)] = \frac{16\pi}{s}\sum_{l=0}^{\infty}(2l+1)|a_l|^2 \tag{1.41}$$

the unitarity condition is

$$|\text{Re}(a_i)| < \frac{1}{2} \tag{1.42}$$

As the constant amplitude means $l = 0$ and assuming that Higgs boson mass is greater than invariant mass of the process ($m_H \gg s$)

$$a_0 \xrightarrow{M_H^2 \gg s} -\frac{s}{32\pi v^2} \Rightarrow \sqrt{s} \lesssim 1.2\,\text{TeV} \tag{1.43}$$

If Higgs boson was heavy or even if didn't exist, the unitarity will be restored introducing "new physics" or using non-perturbation theories.

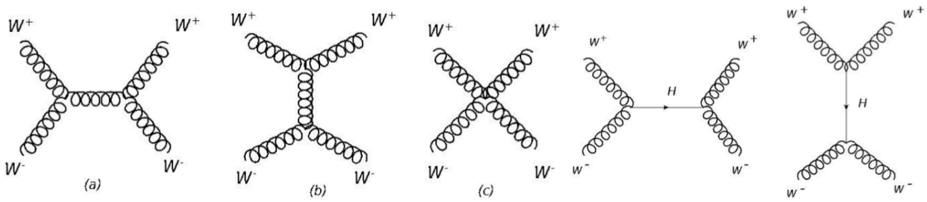

Figure 1.3: Feynman diagrams for WW elastic scattering. The left three plots are nominal WW interacton and the right two plots are the Higgs mediated contribution.

Triviality and vacuum stability

Taking into account one-loop radiative corrections to the Higgs boson quartic coupling λ with contributions of the Higgs boson itself only, leads to a logarithmic dependence of λ on the squared energy scale, Q^2.

$$\lambda(Q^2) = \lambda(v^2)\left[1 - \frac{3}{4\pi^2}\lambda(v^2)\log\left(\frac{Q^2}{v^2}\right)\right]^{-1} \tag{1.44}$$

At very small energies ($Q^2 \ll v^2$) the quartic coupling vanishes making the theory trivial, non interacting. On the other hand, for very large energies it can become infinite. The energy cut off Λ_c can be established,

$$\Lambda_c = \nu \exp\left(\frac{2\pi^2}{3\lambda\nu^2}\right) = \nu \exp\left(\frac{4\pi^2\nu^2}{3m_H^2}\right) \tag{1.45}$$

below which the self-coupling λ remains finite and the theory remains

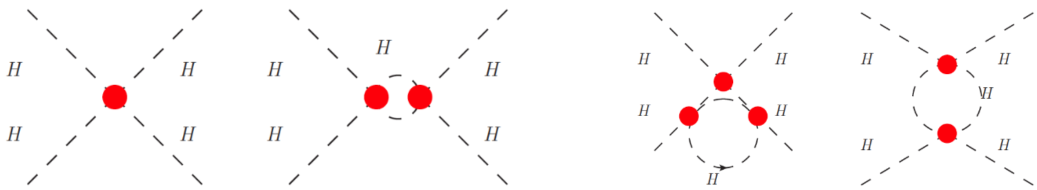

Figure 1.4: Feynman diagrams for the self-interaction contribution at one-loop to the tree level

perturbative. A non-perturbative regime is established if m_H is greater. To set $\Lambda_c < 1$ can be translated into an upper bound in the SM. To add terms from gauge bosons and fermions to the running of λ can be translated into a lower bound. In detail, only loop involving massive vector bosons and the quark top are relevant, because Higgs coupling is proportional to the mass of interacting particle. Taking account of these contributions in Figure 1.4 λ becames

$$\lambda(Q^2) = \lambda(v^2) + \frac{1}{16\pi^2}\{-12\frac{m_{\text{top}}^4}{\nu^4} + \frac{3}{16}[2g^4 + (g^2 + (g')^2)^2]\}\ln\frac{Q^2}{\nu^2} \quad (1.46)$$

Furthermore, top quark loops tend to drive the Higgs quartic coupling λ to negative values, for which the vacuum is no more stable since it has no minimum. To avoid this instability, the Higgs boson mass must exceed a minimum value for a given top mass.

$$m_H > \frac{\nu^2}{8\pi^2}\{-12\frac{m_{\text{top}}^4}{\nu^4} + \frac{3}{16}[2g^4 + (g^2 + (g')^2)^2]\}\ln\frac{Q^2}{\nu^2} \quad (1.47)$$

Definitively, in Figure 1.5 the bounds are shown both for the triviality and vacuum stability as a function of the energy cut-off Λ_c [9]. Bounds of uncertainties are refered to $\alpha_s = 0.118$ and the mass of quark top $m_{\text{top}} = 175\,\text{GeV}$. If the cut-off scale is 1 TeV, the range of values for Higgs mass is

$$\Lambda_c \approx 1\,\text{TeV} \Rightarrow 50\,\text{GeV} \leq m_H \leq 800\,\text{GeV} \quad (1.48)$$

instead, if the cut-off scale is on the order of the Planck mass, M_P, the range becomes closer

$$\Lambda_c \approx M_P \Rightarrow 130\,\text{GeV} \leq m_H \leq 180\,\text{GeV} \quad (1.49)$$

If the Higgs boson mass was out of ranges, processes of "new physics" will be possible at unexplored energy scales.

1.4.2 Experimental constraints on the Higgs mass and the discovery

With the discovery of the Higgs boson on 4 July 2012 a great step is made in the comprehension of the nature.

Various experiments over the last decades have aimed for either direct or indirect searches of the Higgs boson. The results of direct Higgs searches from experiment at LEP, Tevatron and LHC will be introduced in this Section. Electroweak measurements, which reach a very high precision also help constrain the Higgs mass; they will be discussed in this Section. Finally we will present a brief description about the discovery.

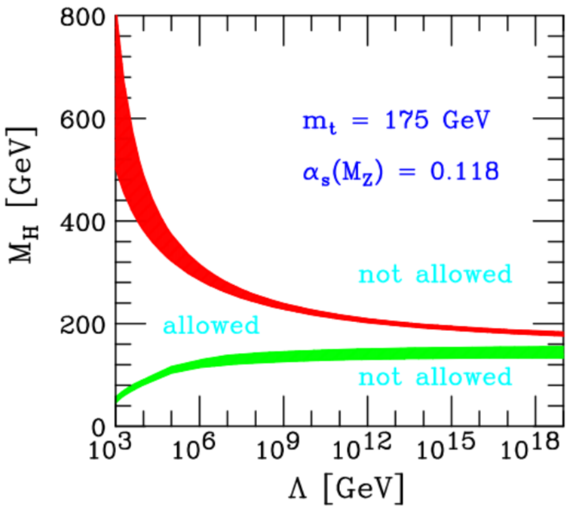

Figure 1.5: The allowed M_H range as set by the triviality (upper) bound and the vacuum stability (lower) bound as a function of the cut-off scale Λ_c. The bands correspond to the theoretical uncertainties.

Direct searches

The Large Electron-Positron Collider (LEP) built at CERN, started operation in 1989 and the four experiments (ALEPH, DELPHI, L3 and OPAL) took data at a center-of-mass energy $\sqrt{s}$ = 89-93 GeV in the first phase (LEP I) and $\sqrt{s}$ = 161-209 GeV in the second phase (LEP II). At LEP the Standard Model Higgs boson was expected to be produced mainly in association with a Z boson through the Higgs strahlung process, $e^+e^- \to HZ$. The searches were concentrated on four final state topologies:

- four-jet final state: $H \to b\bar{b}$ and $Z \to q\bar{q}$
- missing energy final state: $H \to b\bar{b}$ and $Z \to \nu\bar{\nu}$
- leptonic final state: $H \to b\bar{b}$ and $Z \to e^+e^-$ or $Z \to \mu^+\mu^-$
- tau lepton production: $H \to \tau^+\tau^-$ and $Z \to q\bar{q}$, or $H \to b\bar{b}$ and $Z \to \tau^+\tau^-$

The final result of LEP combining LEP1 and LEP2 is that, there is no SM Higgs of $m_H < 114.4$ GeV at the 95% confidence level while the expected limit is $m_H < 115.3$ GeV, as shown in Figure 1.6. The difference of the two limits comes from an excess of observed events near 116 GeV, with a significance of 1.7σ, which is not sufficient to declare an observation [10].

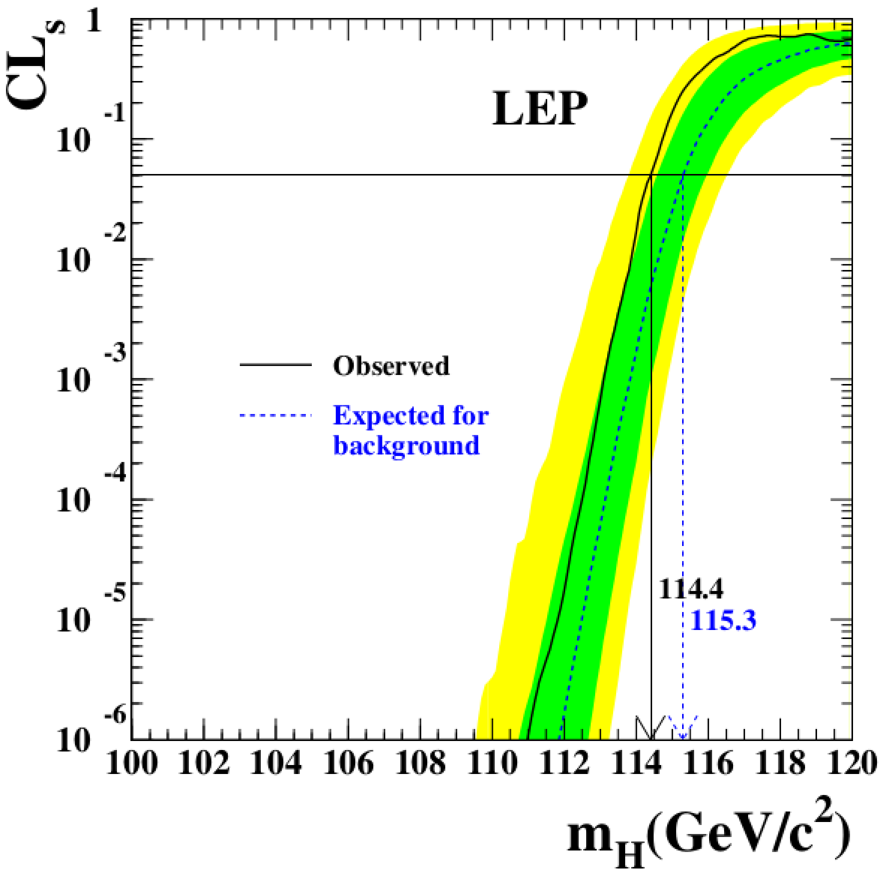

Figure 1.6: The ratio $\mathrm{CL}_s = \mathrm{CL}_{s+b}/\mathrm{CL}_b$ for the signal plus background hypothesis is presented for the combination of the LEP experiments. The dashed line represents the median background expectation and the solid line, the observation. The bands correspond to the 68% and 95% probability bands.

The Tevatron experiment, CDF and D0 at Fermilab analyses $p\bar{p}$ collisions at the c.m. energy of 1.96 TeV started taking data in 1985 up to 2011. They search for the Higgs boson in the mass range of 100–200 GeV. The most important Higgs productions mechanisms in Tevatron were:

- gluon fusion: $gg \to H$
- associated production with a vector boson: $q\bar{q} \to WH$ or $q\bar{q} \to ZH$
- vector boson fusion: $q\bar{q} \to q\bar{q}H$, where the quarks radiate weak gauge bosons which fuse to produce H.

The most sensitive channels are $H \to b\bar{b}$, $H \to WW^{(*)} \to \ell\nu\ell\nu$ and $H \to ZZ^{(*)} \to 4\ell$ for low Higgs masses ($m_H < 125\,\text{GeV}$) and $H \to WW^{(*)} \to \ell\nu\ell\nu$ for higher masses. In Figure 1.7 the combination results presented in June 2012 are shown using $10.0\,\text{fb}^{-1}$ [11]. The mass ranges $100 < m_H < 103\,\text{GeV}$ and $147 < m_H < 180\,\text{GeV}$ have been excluded at 95% CL. An excess of data events with respect to the background estimation has been observed in the mass range $115 < m_H < 140\,\text{GeV}$. At $m_H = 120\,\text{GeV}$, the p-value for a background fluctuation to produce this excess has been $\sim 1.5 \times 10^{-3}$, corresponding to a local significance of 3.0σ. The global significance for such an excess anywhere in the full mass range is approximately 2.5σ.

The results of the experiments at LHC (ATLAS and CMS) reduce the allowed range of mass. In Figures 1.8 the results are shown using $5\,\text{fb}^{-1}$ recorded in 2010 and 2011. For results from CMS all channel except with associated production with vector bosons are included. For results from ATLAS, instead, only $b\bar{b}$ channel isn't comprised. Usind data recorded at LHC in CMS, we can exclude at 95% CL the mass region:

$$127\,\text{GeV} < m_H < 600\,\text{GeV}$$

meanwhile, in ATLAS:

$$110\,\text{GeV} < m_H < 117.5\,\text{GeV}$$

$$118.5\,\text{GeV} < m_H < 122.5\,\text{GeV}$$

$$129\,\text{GeV} < m_H < 539\,\text{GeV}$$

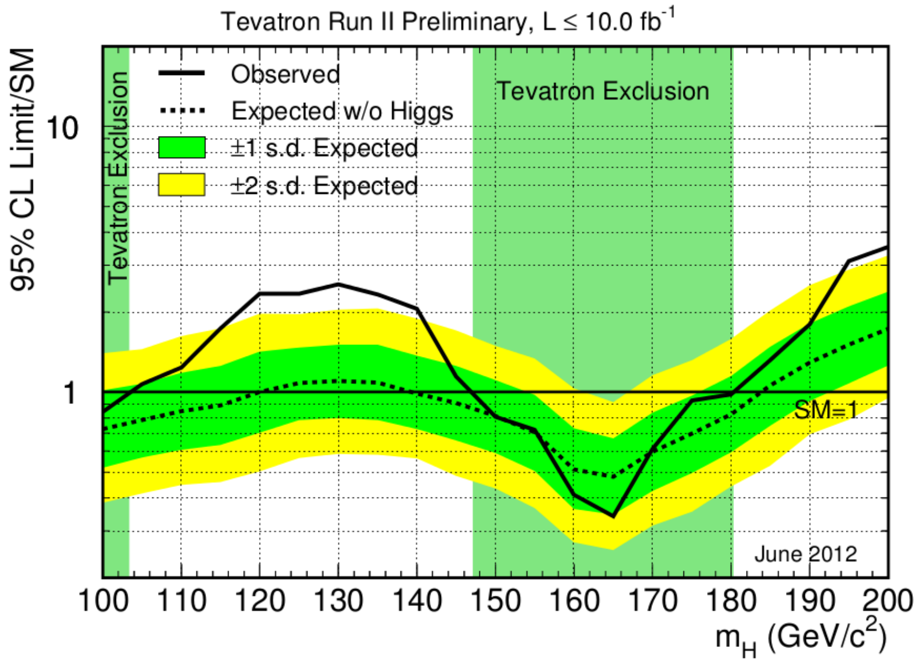

Figure 1.7: Observed and expected 95% CL upper limits on the ratio of the Standard Model cross section as a function of the Higgs boson mass for the combined Tevatron analyses. The bands correspond to the 68% and 95% probability bands.

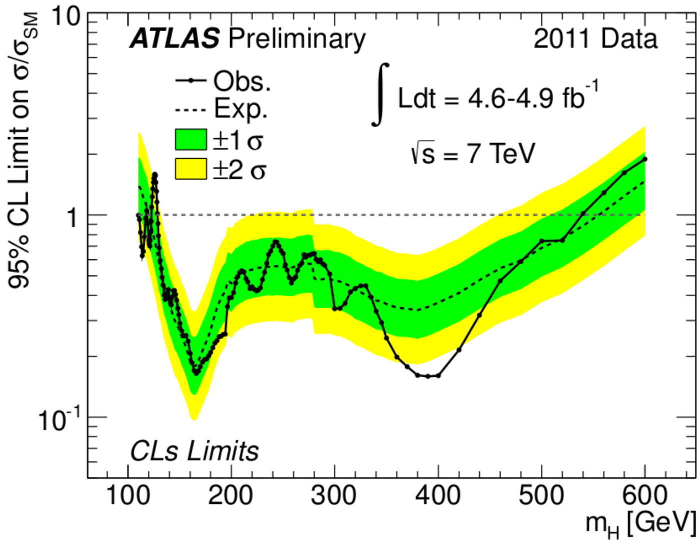

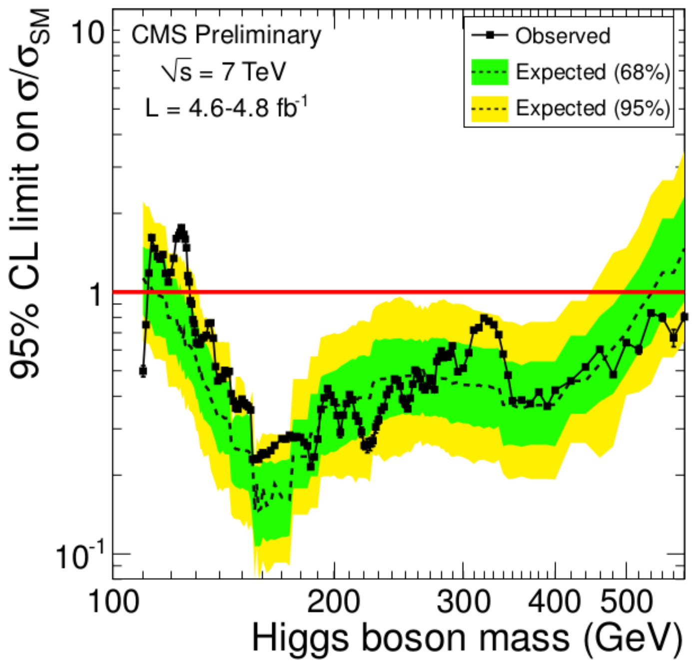

Figure 1.8: Observed and expected 95% CL upper limits on the ratio of the Standard Model cross section as a function of the Higgs boson mass for the combined ATLAS analyses (on top) and for the combined CMS analyses (on low). The bands correspond to the 68% and 95% probability bands.

Indirect searches

Precision measurements of the electroweak observables are used to put indirect limits on the Higgs mass, because the existence of the Higgs boson would contribute to the radiative correction in the electroweak sector, which can be measured with high precision. The Standard Model predictions are calculated by GFITTER based on a χ^2 minimization technique using the most recent experimental measurements as well as the latest theoretical predictions of electroweak observables and leaving free other parameters such as the m_Z and m_H.

The latest result of GFitter with combination of LEP, Tevatron, SLC, and BaBar was published in September 2011, which uses the experiment data up to July 2011 [5]. The fit yields the Higgs boson mass of

$$m_H = 95^{+30}_{-24}\,\text{GeV}$$

and the upper limit is $m_H < 166\,\text{GeV}$ at 95% confidence level.
In Figure 1.9 the $\Delta\chi^2 = \chi^2 - \chi^2_{\text{min}}$ is presented as a function of the m_H for the standard fit not including direct Higgs searches. In Figure 1.10, the complete fit results are shown including results from Higgs direct searches in LEP, Tevatron and LHC. When including results from direct Higgs search results, the fit yields

$$m_H = 125^{+8}_{-10}\,\text{GeV}$$

and the limit is $m_H < 154\,\text{GeV}$.

In Figure 1.11, the compatibility between the complete fit results and the electroweak measurements is presented, where good agreement is observed.

Discovery of a new Higgs-like particle

According to the Standard Model, the Higgs boson is a neutral particle with spin zero. Its mass is a free parameter in the Standard Model: it has to be measured experimentally.

The great work at the Large Hadron Collider, in both the ATLAS and CMS experiments led to the discovery of a new particle compatible with the Higgs boson [**?**] on 4 July 2012. The discovery is based on datasets of 4.6-4.8 fb^{-1} and 5.1 fb^{-1} taken by ATLAS and CMS at $\sqrt{s} = 7\,\text{TeV}$ in 2011 and of 5.8-5.9 fb^{-1} and 5.3 fb^{-1} at $\sqrt{s} = 8\,\text{TeV}$ in 2012, respectively.

The new boson is been observed in decay channels $\gamma\gamma$, ZZ and WW. The mass of the new Higgs-like boson was estimated to be about 125-126 GeV.

[5] After that, GFitter still regularly updated their results, but with integration of result from LHC, therefore those results will not be quoted here.

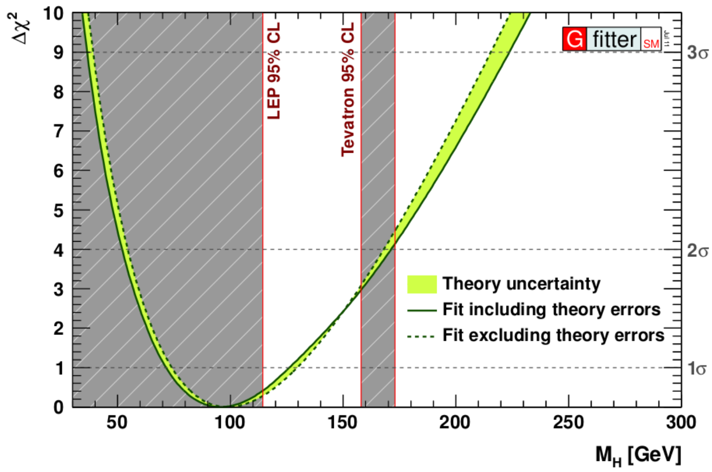

Figure 1.9: $\Delta\chi^2$ as a function of m_H for the standard fit, not including direct Higgs searches. The solid line gives the results when including theoretical errors while the dashed line gives the results ignoring the theoretical errors. The vertical bands correspond to excluded regions.

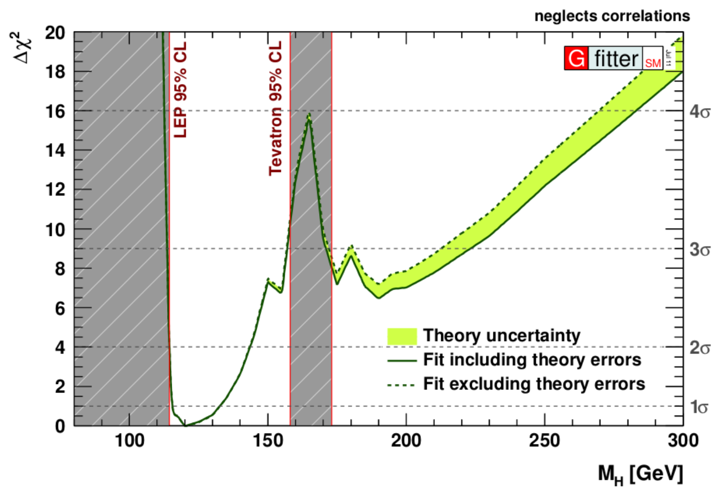

Figure 1.10: $\Delta\chi^2$ as a function of m_H for the complete fit including results from LEP, Tevatron and LHC. The solid line gives the results when including theoretical errors while the dashed line gives the results ignoring the theoretical errors. The vertical bands correspond to excluded regions.

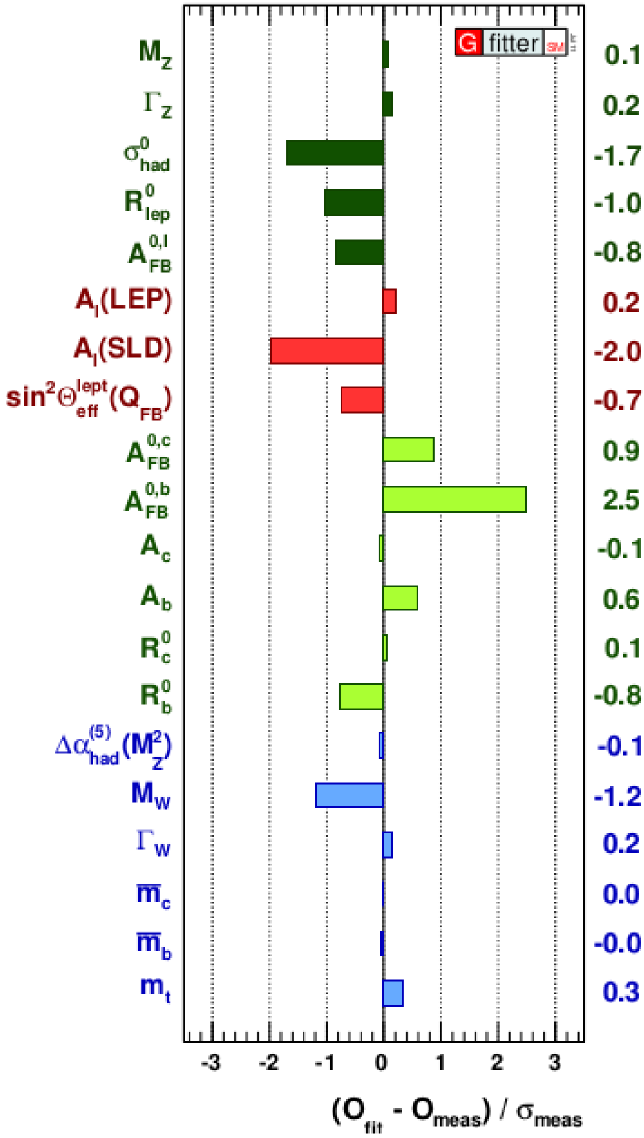

Figure 1.11: Pull values of the results of the complete fit, including direct Higgs searches, to the direct electroweak measurements are presented.

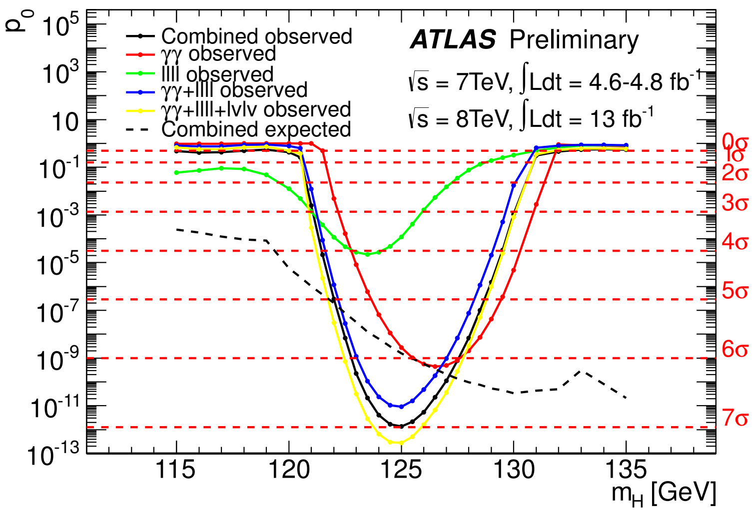

Figure 1.12: The local probability p-value for a background-only experiment to be more signal-like than the observation as a function of m_H for various progressive cases of combinations: $H \to \gamma\gamma$ (red line); $H \to ZZ^{(*)} \to 4\ell$ (green line); combination of $H \to \gamma\gamma$ and $H \to ZZ^{(*)} \to 4\ell$ (blue line); combination of $H \to \gamma\gamma$, $H \to ZZ^{(*)} \to 4\ell$ and $H \to WW^{(*)} \to \ell\nu\ell\nu$ (magenta line) and the combination of all channels, including $H \to bb$ and $H \to \tau\tau$ (black line). The dashed black curve shows the median expected local p-value under the hypothesis of a Standard Model Higgs boson production signal at that mass for the combination of all channels. The horizontal dashed lines indicate the $p$values corresponding to significances of 0σ to 7σ.

The decay channels combination has shown a discrepancy between the data and the background-only hypothesis greater than 5σ, thus allowing to claim for a discovery. It will be described in more detail in the Chapter 4.

Using $\gamma\gamma$ and ZZ decay channels, the Higgs mass is measured by ATLAS and CMS to $m_H = 126.0 \pm 0.4(\text{stat}) \pm 0.4(\text{sys})\text{GeV}$ and $m_H = 125.3 \pm 0.4(\text{stat}) \pm 0.5(\text{sys})\text{GeV}$, respectively.

Figure 1.12 shows the p-value for various progressive cases of combinations. In order to prove that the new particle is the Standard Model Higgs boson, further measurements are still needed.

1.5 Standard Model Higgs boson production

The Higgs boson discovery is one of the main goal of the LHC experiment. The LHC has joined this search in 2010, after the search at Tevatron. The

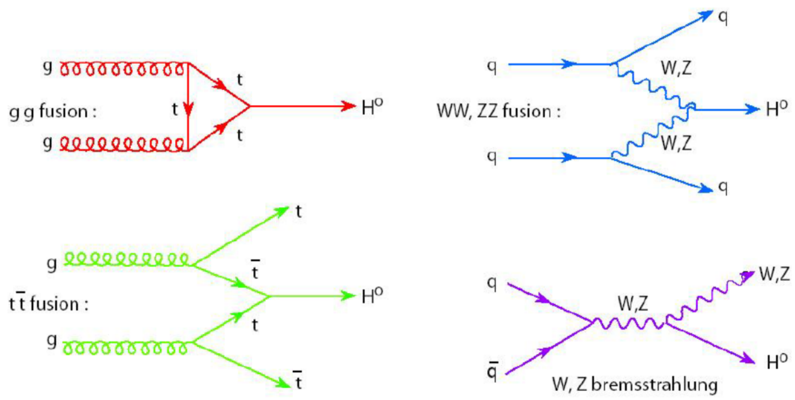

Figure 1.13: Leading Order Feynman diagram for main SM Higgs boson production at LHC loop.

most important production and decay mechanism will be briefly described.

1.5.1 Production mechanisms

As it can be seen on Figure 1.13, the SM Higgs boson can be produced through four main mechanisms, in the LHC. Due to the large gluon luminosities expected in the high energy beams of proton-proton collisions, the fusion of gluons through a loop of heavy quarks is the dominant production process. It is followed by the vector boson fusion (VBF) process, in which a Higgs boson particle is produced through the emission of virtual bosons from incoming partons. The production in association with a W or a Z boson becomes relevant in the region of a low Higgs boson mass hypothesis. This production is quite suppressed in pp colliders[6]. The typically high transverse momentum (p_{T}) leptonic signatures of the decay of the weak bosons can be used to trigger and discriminate from huge multi-jet background and simultaneously profit out of the large decay branching ratio (BR) of the Higgs bosons going into a pair of heavy flavour quarks. Finally, the production of a Higgs boson together with a top quark pair can be also used, in the case of a very low mass Higgs boson.

Figure 1.14 summarises the cross-section predictions as function of Higgs mass m_H at $\sqrt{s} = 7\,\mathrm{TeV}$ and $\sqrt{s} = 8\,\mathrm{TeV}$.

[6]As opposite to the Tevatron's $p\bar{p}$ collider in which the presence of valence quarks and anti quarks enhances the Higgs boson production in association with vector bosons.

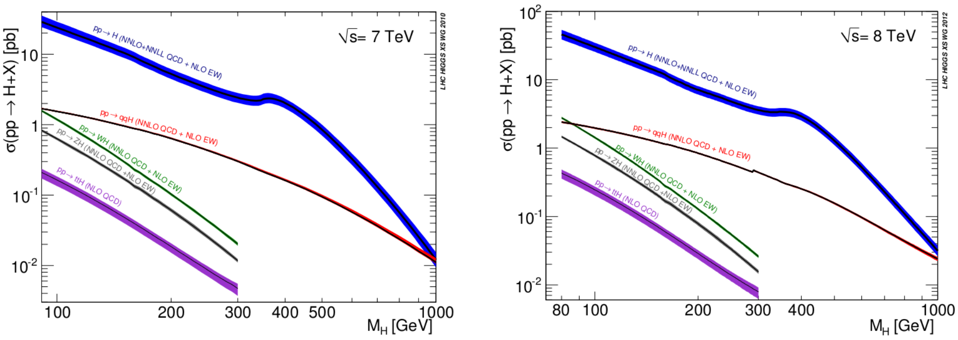

(a) (b)

Figure 1.14: The Higgs production cross sections are presented for $\sqrt{s} = 7\,\text{TeV}$ and $\sqrt{s} = 8\,\text{TeV}$ at the LHC as a function of the Higgs mass values.

1.5.2 Higgs decays

Once the Higgs mass is fixed, the Higgs decay and the branching ratio are uniquely determined. The branching ratios are known at NNLO [12, 13], including QCD and electroweak corrections: they are presented in Figure 1.15 as a function of the Higgs mass.
The decay mode could be devided into two groups: the decays to fermions and the decays to bosons.

$H \to q\bar{q}$

In the low mass region, $m_H \leq 130\,\text{GeV}$, concerning the Higgs decays to fermions, the dominant mode is $H \to b\bar{b}$. Due to the large QCD background, it is not possible to extract the signal in the ggF mode. Another important channel in the low mass region is the decay $qqH \to \tau^+\tau^-$: the taus subsequently decay in the semi-leptonic mode, leptonic mode, or into pairs of hadrons. This process results to two relatively forward jets.

$H \to ZZ/WW$

Higgs can also decay into pairs of vector bosons. The $H \to ZZ^{(*)}/\gamma^{(*)} \to 4\ell$, where $\ell = \mu, e$, is also known as the "golden" channel due to the clean final state signature, the capability to fully reconstruct the Higgs mass and the coverage of a large mass range, from 120 GeV to 600 GeV. It will be described in more details in Chapter 4. A decrease in sensitivity is noticed when the channel to two W bosons opens, for $m_H \approx 2M_W$.

In the mass range $2M_W < m_H < 2M_Z$ the $H \to WW^{(*)}$ decay is

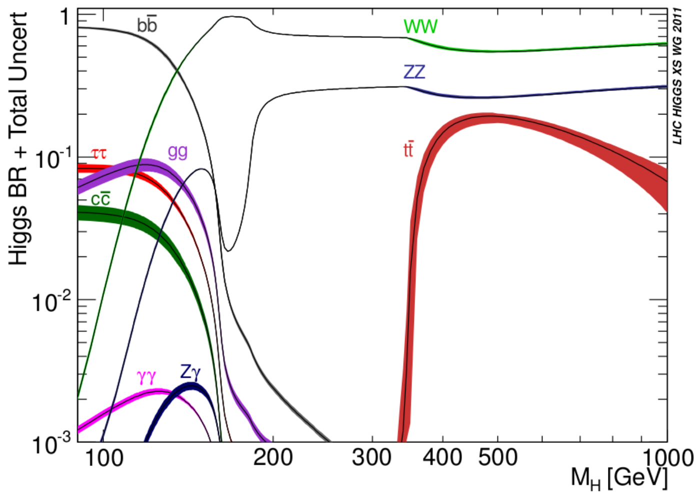

Figure 1.15: The decay branching ratios and their uncertainties of the Standard Model Higgs boson as a function of its mass.

dominant. This decay with the largest branching ratio complements the $H \to ZZ^{(*)}/\gamma^{(*)} \to 4\ell$ searches. The final states are $\ell\nu\ell\nu$ and $\ell\nu q\bar{q}$. Due to the presence of high missing energy (high p_{T} neutrinos), only the transverse mass of the Higgs boson can be reconstructed.

$H \to \gamma\gamma/gg$

Massless photons and gluons do not couple directly to the Higgs boson but through loops by involving massive charged and/or colored particles. The $H \to gg$ cannot be observed in a hadron collider due to the huge QCD background while the $H \to \gamma Z(\to e^+e^-/\mu^+\mu^-)$ channel is a particular search channel because it needs separation from the huge $Z+$jets background.

The $H \to \gamma\gamma$ plays a very important role in Higgs boson searches. It is a promising channel for the mass range up to $m_H \approx 140\,\mathrm{GeV}$ (from the LEP exclusion limit) in spite of its low branching ratio. It forms a narrow invariant mass peak, having a distinctive signature due to the two high energetic photons.

As previously said, Higgs is a very narrow resonance with $\Gamma(H) \leq 10\,\mathrm{MeV}$ for low masses. The behavior of the decay width of the Higgs boson as a function of its mass is shown in Figure 1.2. For higher masses, the width rapidly increases up to $\sim 1\,\mathrm{MeV}$ at the ZZ threshold. For even larger masses, the width is of the same order of magnitude as the Higgs mass.

Chapter 2

The ATLAS experiment at the Large Hadron Collider

The European Organization for Nuclear Research (CERN) is one of the world's largest and presently the most renowned centre for scientific research. Its main activity is to find out what the Universe is made of and how it works, in the field of the fundamental physics. At CERN, the most complex and up to date scientific instruments are used to study the basic constituents of matter. The CERN Laboratory sits in between the Franco-Swiss border, close to Geneva. After the II World War, it was founded in 1954 to create an European scientific centre of excellence. It was one of Europe's first joint ventures and now has 20 Member States. The instruments used at CERN are particle accelerators and detectors: accelerators produce collisions of particles (protons, ions) at very high energy, while detectors detect and record what is produced from these collisions.

This Chapter introduces the Large Hadron Collider accelerator (LHC) and provides a short description of the ATLAS experiment including the detector components and working. More details about structure and functions of each ATLAS subsystem are described in the Technical Design Report (TDR) [14].

2.1 The Large Hadron Collider

The Large Hadron Collider (LHC) at CERN is a circular machine dedicated to accelerating and colliding protons. Designed to provide proton-proton collisions with a center-of-mass energy of 14 TeV, and an instantaneous luminosity of $10^{34}\,\mathrm{cm^{-2}s^{-1}}$, the LHC is the highest energy collider ever built. In addition to the proton-proton collisions, the LHC is also designed to provide lead ion collisions at a center-of-mass energy of 2.76 TeV per nucleon, and an

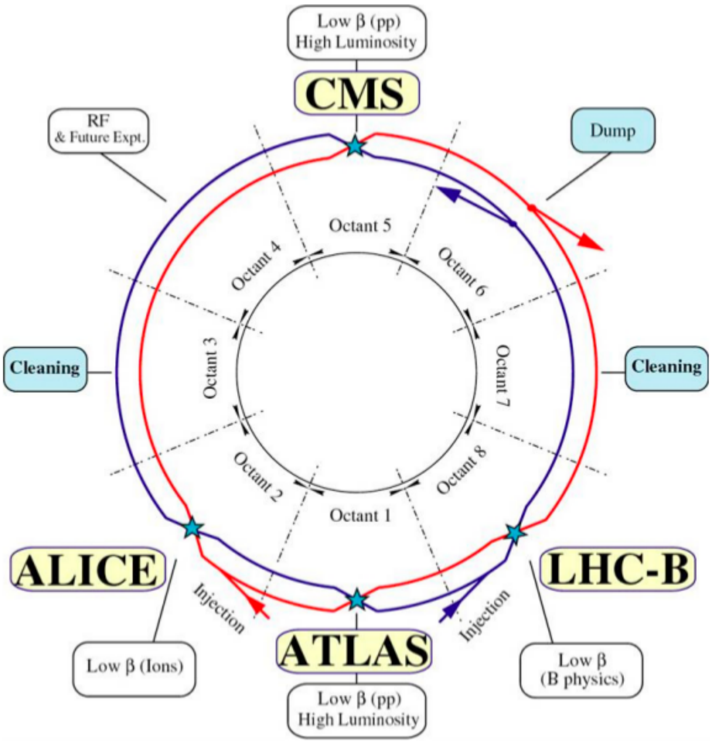

Figure 2.1: The layout of the LHC.The stars show the four collision points [16].

instantaneous luminosity of $10^{27}\,\mathrm{cm}^{-2}\mathrm{s}^{-1}$.

As can be seen in Figure 2.1, the rotating proton beams of the LHC collide in four interaction points, where four particle detector have been build in order to analyze the products of the high-energy collisions. The data recorded with the ATLAS ("**A** **T**oroidal **L**HC **A**pparatu**S**") detector [15] are used in this thesis. Other three detectors, CMS, ALICE and LHCb, are briefly described in Section 2.2. In addition, there are smaller experiments, such as TOTEM and LHCf, installed at some distance from the interaction points to study the production of particles in the forward region (along the beam direction).

2.1.1 Machine design

Housed in the tunnel built between 1984 and 1989 for the LEP ("**L**arge **E**lectron–**P**ositron Collider"), the LHC is a 27 km long superconducting-hadron collider. The LEP tunnel had been designed with an internal diameter of 3.7 m to take into account the possibility of housing, at a later stage,

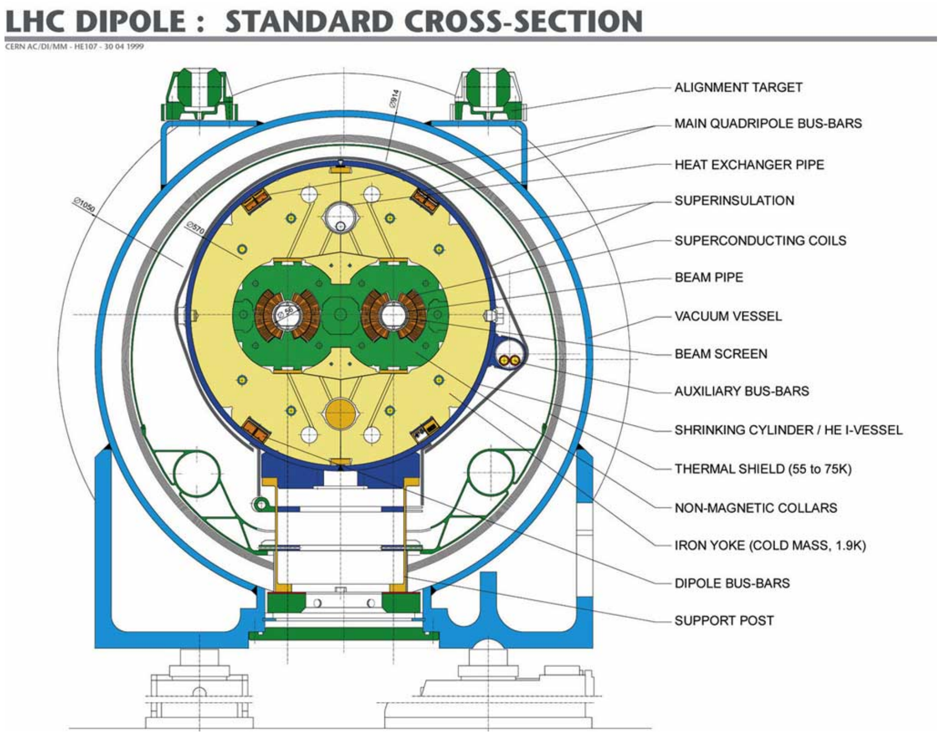

Figure 2.2: An example of an LHC dipole magnet with the twin bore design [18].

a hadron machine with superconducting magnets supported by cryogenic equipment [17]. The tunnel is located between 45 m and 170 m below the ground surface, between Geneva airport and the Jura mountains.

The LHC magnets are made with niobium-titaniun (NbTi) cables and have to reach superconductivity (9.2 K) and to remain superconductive despite the high currents (11.850 A) and large magnetic fields (8.33 T). For this reason they are cooled to less than 2 K with superfluid helium. The large magnetic fields are required to bend the 7 TeV proton beams around the LHC ring: moreover, the dipole magnets used to bend the beam, quadrupole and higher order magnets are used for correcting the beam and shrinking it into the small area where collisions are produced. Due to the limited space in the tunnel, only a single cryogenic structure fits. Therefore, a twin-bore design is used, with both proton rings in the same cryostat. Nevertheless oppositely oriented magnetic fields are required to allow the coexistence of two counter circulating proton beams along the same circumference: the twin-bore structure results in a very complicated design, as the two rings are close enough to influence each other's magnetic field. One of the LHC twin-bore dipole magnets can be seen in Figure 2.2.

This advanced collider is designed to accelerate protons to an energy

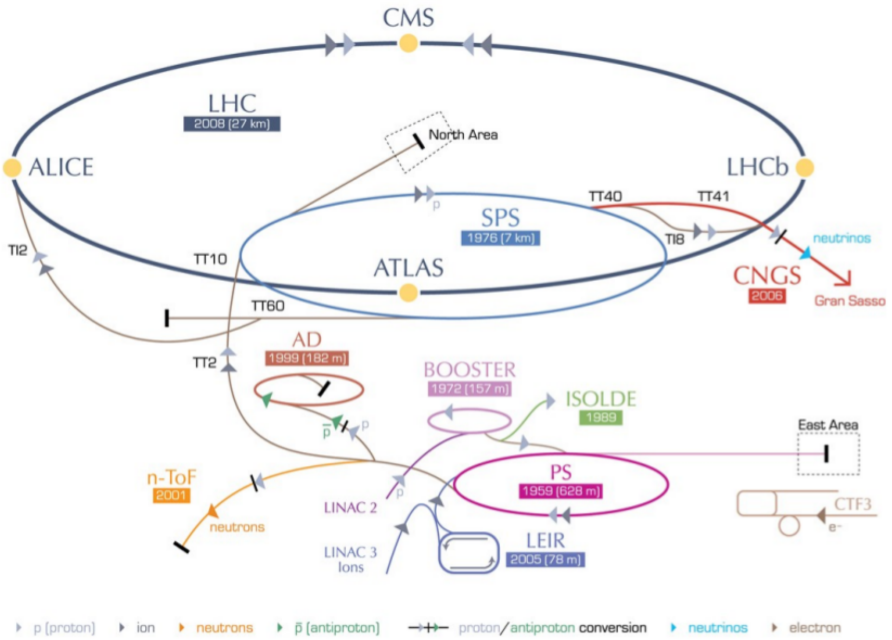

Figure 2.3: The layout of the LHC and the CERN accelerator complex acting as the injector chain for the LHC (© CERN 2008).

of 7 TeV, starting from an initial energy of 450 GeV. The existing CERN accelerators system are used to accelerate protons up to 450 GeV, and inject them into the LHC ring later on. As illustrated in Figure 2.3, 50 MeV protons are initially produced in the LINAC 2 linear accelerator. These protons are accelerated to 1.4 GeV by the Proton Synchrotron Booster (PSB), and consequently reach 25 GeV in the Proton Synchrotron (PS). The Super Proton Synchrotron (SPS) is then used to reach 450 GeV, and inject the protons into the LHC. Eight radio frequency (RF) cavities per beam provide acceleration within the LHC. The frequency of this superconducting system is 400 MHz, which accelerates the beam by 485 keV at each turn. The 400 MHz cavities create 35640 RF *buckets* of 2.5 ns length, and each tenth bucket can be filled with a proton *bunch*.

Each beam is injected into the LHC in a series of bunches of 1.15×10^{11} protons. The limit to higher bunch intensities is set by the need to minimize beam-beam interaction of each proton when the bunches collide with each other, which can result in orbit instabilities and radiation losses (tune shifts [1]) Tune shifts can produce the heating and subsequent loss of superconductivity (*quenching*) of the magnets. Each beam is designed to have 2808 circulating

[1]The tune is the number of transverse oscillations of the beam in one full LHC turn.

proton bunches. The bunches are arranged in *trains* of 72 bunches, with 25 ns spacing within the train, and 12 empty bunches between two trains.

Collisions between circulating beams occur at every *bunch crossing*, resulting in a peak collision rate of 40 MHz. The beams are squeezed to a transverse size of $\sim 17\,\mu\mathrm{m}$ at the IP to maximize the proton-proton collision rate. Near the interaction point (IP), the two beams are brought together in a single beam pipe, for approximately 140 m in each direction. In order to avoid unwanted collisions in the shared beam pipe, the beams are kept on parallel orbits. When the parallel beams are ready for colliding at the interaction point, the separation can be removed.

2.1.2 Luminosity

The rate at which collisions occur depends on the instantaneous luminosity $\mathcal{L}$ and the collision cross section σ, related by:

$$\frac{dN}{dt} = \mathcal{L} \cdot \sigma \tag{2.1}$$

The total cross section for proton-proton collisions at the LHC has been measured to be $98.3 \pm 0.2(\mathrm{stat}) \pm 2.8(\mathrm{syst})$ mb at a centre of mass energy of 7 TeV [19], and $101.7 \pm 2.9(\mathrm{syst})$ mb at 8 TeV [20]: thus at the LHC design luminosity of $1 \times 10^{34}\,\mathrm{cm}^{-2}\mathrm{s}^{-1}$ collisions occur at a rate of approximately 100 MHz.

The rate at which a particular physics process occurs depends on the cross section for the process in question. Since many of the physics processes under study at the LHC are very rare and have small cross sections, it is important to maximise the luminosity as much as possible. The instantaneous luminosity is given by:

$$\mathcal{L} = \frac{N_b^2 n_b f_{\mathrm{rev}} F \gamma_{\mathrm{r}}}{4\pi \epsilon_n \beta^*} \tag{2.2}$$

where:

- N_b is the number of particles per bunch,
- n_b is the number of bunches per beam,
- f_{rev} is the revolution frequency,
- F is a geometric function to account for the crossing angle between the beams (since they are generally not collided head on),
- γ_{r} is the relativistic Lorentz factor $(1 - v^2/c^2)^{-1/2}$

- ϵ_n is the beam emittance, a measure of how uniform the momentum of particles in the beam is or how small the beam can be 'squeezed',
- β^* is a measure of how narrow the beam is at the interaction point, or how 'squeezed' it is,

The geometrical cross section of the beam at the interaction point is proportional to $\epsilon_n \cdot \beta^*$. The instantaneous luminosity can be maximised by increasing the number of particles per bunch, decreasing the bunch spacing (or equivalently increasing the number of bunches per beam) or decreasing the size of the bunch at the interaction point by decreasing $\epsilon_n \cdot \beta^*$.

A measure of how many collisions have occurred is the integrated luminosity:

$$L = \int \mathcal{L}\, dt \tag{2.3}$$

The number of events occurring for a given process with cross section σ_{process} in a data sample corresponding to an integrated luminosity L is given by:

$$N_{\text{process}} = L \cdot \sigma_{\text{process}} \tag{2.4}$$

2.1.3 The LHC operation in 2011 and 2012

The LHC began operation in November 2009 with collisions at a centre of mass energy of 900 GeV, with the centre of mass energy rising to 2.36 TeV by the end of the year. In 2010 the centre of mass energy was successfully increased to 7 TeV. Over 2010 and 2011 the LHC continued to run at $\sqrt{s} = 7$ TeV, with the instantaneous luminosity steadily increasing. In 2010 the LHC delivered 48.1 pb^{-1} of integrated luminosity 5.43 pb^{-1} in 2011 to ATLAS. In 2012 the centre of mass energy was increased to 8 TeV, and the instantaneous luminosity further increased by decreasing $\epsilon_n \cdot \beta^*$ and increasing the number of particles per bunch slightly, leading to a total integrated luminosity delivered to ATLAS in 2012 of 22.8 fb^{-1}. Figure 2.4 shows the instantaneous luminosity as measured by ATLAS as a function of time between 2010 and 2012. Figure 2.5 shows the cumulative integrated luminosity delivered to ATLAS in 2011 and 2012. In Table 2.1 details of the LHC operational parameters, together with the nominal design values, in 2011 and 2012 are given.

2.2 The experiments of the LHC

There are six main experiments of the LHC. They are:

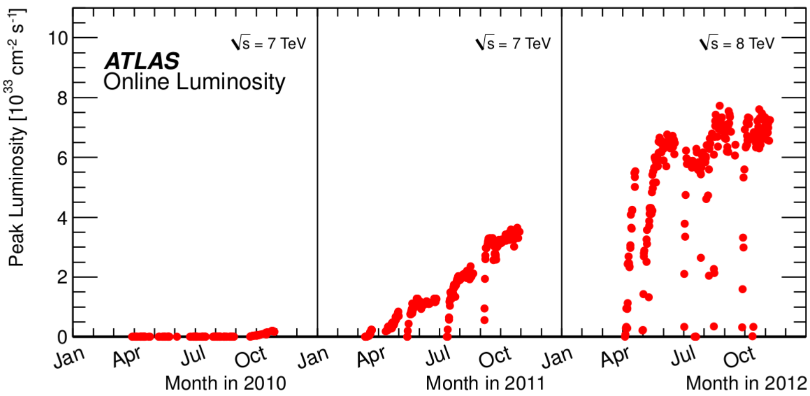

Figure 2.4: Peak instantaneous luminosity delivered by the LHC per run as a function of time from 2010 to 2012. Figure from [21]

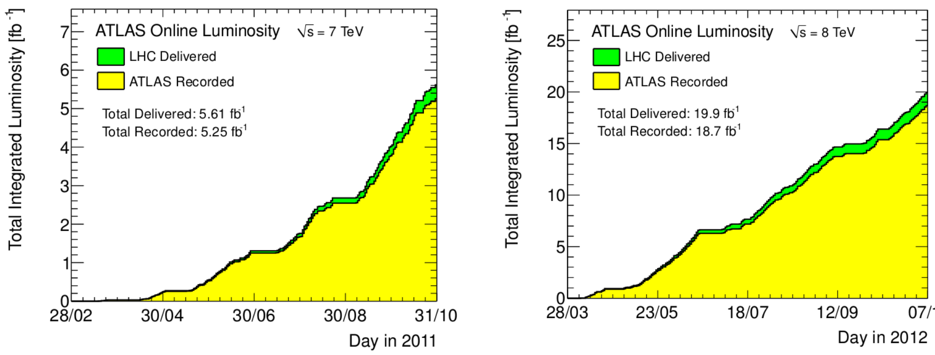

(a) (b)

Figure 2.5: Cumulative integrated luminosity as a function of time in (a) 2011 and (b) 2012. The totals for the two years are separate. Figures from [21].

Parameter	Nominal	2011 Operation	2012 Operation
Proton Energy	7 TeV	3.5 TeV	4 TeV
N_b	1.15×10^{11}	1.5×10^{11}	1.6×10^{11}
n_b	2808	1380	1380
Bunch spacing[ns]	25	50	50
β^*[m]	0.55	1.0	0.6
$\epsilon_n[\mu m]$	3.75	$1.9 - 2.3$	$1.7 - 3.0$
Peak $\mathcal{L}[\text{cm}^{-2}\text{s}^{-1}]$	1.0×10^{34}	3.6×10^{33}	7.7×10^{33}

Table 2.1: LHC operational parameters. A comparison is made of the nominal design parameters, and those used in 2011 operation and in 2012 operation.

- **A Toroidal LHC ApparatuS (ATLAS)**
  ATLAS [15] is a multi-purpose detector, it will be described in detail in the following section.

- **CMS**
  The **C**ompact **M**uon **S**olenoid [22] is also a general purpose detector: it's optimised to measure high energy particles covering a great part of the solid angle. The huge solenoid superconducting magnet produces a magnetic field of almost 4 T, a series of densely arranged muon chambers and its colossal crystal calorimeter allow unprecedented momentum and energy measurements achieving high detection efficiencies. The CMS experiment shares a similar physics program with ATLAS, where more luminosity are required.

- **ALICE**
  It is **A L**arge **I**on **C**ollider **E**xperiment [23] wose purpose is to explore the primordial state of matter, before the hadrons composition. High energy densities are needed to form the so-called quark-gluon plasma: they are achieved by colliding lead ions at centre-of-mass energies up to 1.15 PeV. The ALICE apparatus is designed to cope with the large amount of informations produced in collisions between nuclei.

- **LHCb**
  The **LHC** "**b**eauty" experiment [24] was built to probe rare decays in B mesons and CP-violating processes. It's set up to explore what happened after the Big Bang that allowed matter to survive and build the Universe we inhabit today. It is a single arm forward spectrometer which surrounds the collision point along the very forward pseudorapidity region approaching as close as possible the IP. Opposed to CMS and ATLAS, the LHCb physics' program requires clean events (low pile-up) while large amounts of luminosity are not necessarily needed.

- **Totem** and **LHCf**
  The **Tot**al **E**lastic and diffractive cross-section **M**easurement experiment [25] and the **LHC f**orward experiments [26] explore the phenomena that can be study by detecting the particles that are scattered very close to the beam pipes. This includes total pp cross-sections, proton structure measurements, and the usage of these forward particles to recreate the showers produced by cosmic rays in the atmosphere.

2.3 The ATLAS detector

Built to study both proton-proton and ion-ion interactions, ATLAS (**A** **T**oroidal **L**HC **A**pparatu**S**) is one of two general purpose particle physics detectors at the LHC. The high centre of mass energy and high luminosity of LHC proton-proton collisions allows the study of physics at the TeV scale. ATLAS has been designed to permit a wide range of measurements. The main are:

- searching for and measuring the properties of the Higgs Boson;
- searches for supersymmetry;
- high precision tests of QCD, flavour physics and electroweak interactions;
- measurements of the properties of the top quark;
- searches for new vector bosons and searches for extra-dimensions.

The extremely high luminosity gives high possibility of discovery but also a difficult scenario. At the designed luminosity 10^9 inelastic collisions occur per second resulting in multiple scattering. In Figure 2.6 the mean number of interaction per crossing is shown, up to 35 multiple interactions per bunch have been observed during 2012 data taking period. The detector has been designed to cope with these high 'pile-up' conditions, as well as be capable of operating in the high radiation environment arising from the high luminosity. The detector must permit distinguish processes of interest from the background: many of the physics processes of interest often occur at very small rates with respect to extremely high QCD background rates.

To meet these challenges, ATLAS was designed to have:

- full azimuthal coverage to allow for missing transverse energy measurement, and large acceptance in pseudo-rapidity;
- high granularity to cope with high particle fluxes and overlapping events;
- precision tracking to provide high charged particle momentum resolution and reconstruction efficiency, and to allow observation of secondary vertices to identify b-hadrons and τ-leptons;
- precise electromagnetic calorimetry for electron and photon identification;
- full-coverage hadronic calorimetry for accurate jet and missing transverse energy measurements;

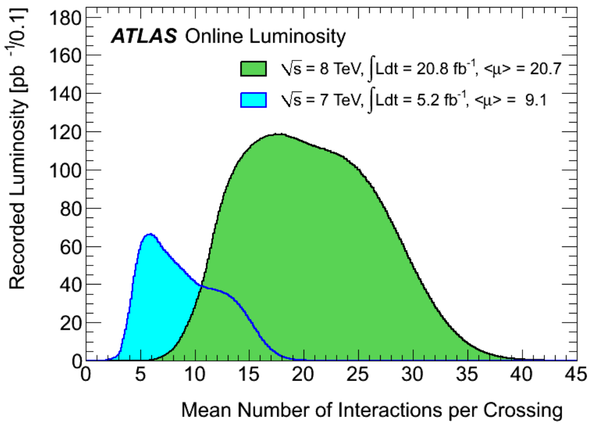

Figure 2.6: The luminosity-weighted distribution of the mean number of interactions per crossing for the 2011 and 2012 data. The mean number of interactions per crossing corresponds the mean of the Poisson distribution on the number of interactions per crossing calculated for each bunch [21].

Detector Component	Design Resolution	η coverage	
		Measurement	Level 1 Trigger
Tracking	$\sigma_{p_\mathrm{T}}/p_\mathrm{T} = 0.05\% p_\mathrm{T} \oplus 1\%$	± 2.5	None
EM Calorimetry	$\sigma_E/E = 10\%/\sqrt{E} \oplus 0.7\%$	± 3.2	± 2.5
Hadronic Calorimetry			
Barrel and End-Cap	$\sigma_E/E = 50\%/\sqrt{E} \oplus 3\%$	± 3.2	± 3.2
Forward	$\sigma_E/E = 100\%/\sqrt{E} \oplus 10\%$	$3.1 < \lvert\eta\rvert < 4.9$	$3.1 < \lvert\eta\rvert < 4.9$
Muon Spectrometer	$\sigma_{p_\mathrm{T}}/p_\mathrm{T} = 10\%$ at $p_\mathrm{T} = 1\,\mathrm{TeV}$	± 2.7	± 2.4

Table 2.2: Performance goals of the ATLAS detector. Units of p_T and E are GeV.

- high muon identification efficiency, momentum resolution and charge determination over a wide range of momentum;
- efficient triggering on low transverse-momentum objects.

In Table 2.2 the main performance goals are given.

Figure 2.7 shows a scheme of the ATLAS detector. The detector consists of an inner tracking detector, which is surrounded by electromagnetic calorimeters, hadronic calorimeters and finally a muon spectrometer. The inner detector is immersed in a solenoidal field of 2 T to allow for momentum measurement. The muon spectrometer is also immersed in a magnetic field, provided by an air-core toroid system which generates strong bending power over a large volume with a minimum of material: therefore this toroidal system minimizes multiple-scattering effects. A three-level trigger system is

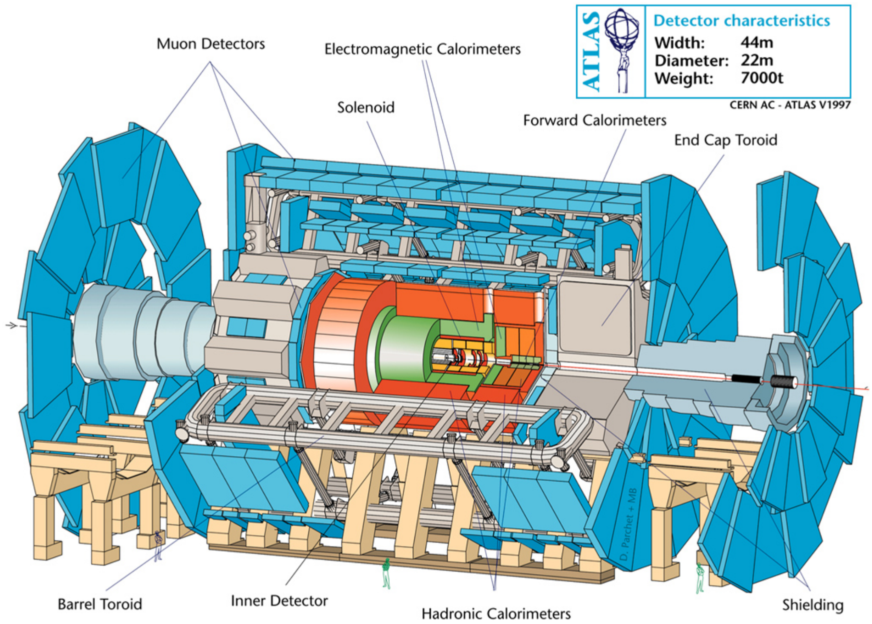

Figure 2.7: Cut-away view of the ATLAS detector [27]. The various detector sub-systems are labelled.

used to select events to read out (more detalis in Section 3.1). The various sub-systems are described in detail in the following sections.

2.3.1 Coordinate system

The ATLAS coordinate system is a right-handed Cartesian system with the origin located at the nominal interaction point (Figure 2.8). The z-axis lies along the beam line: the positive direction points towards the Geneva airport (known as the A-side), and the negative direction towards the Jura mountain (known as the C-side). Furthermore the x-y plane is transverse to the beam line, with positive x pointing into the center of the LHC ring and positive y pointing upward.

Moreover a cylindrical coordinate system is also employed. In the cylindrical coordinate system θ denotes the polar angle, r and ϕ denote the radius and the azimuthal angle in the x-y plane. The two angles, θ and ϕ, are measured respectively from the positive z-axis and from the positive x-axis. The θ angle is often transformed in the pseudo-rapidity,

$$\eta = -\ln\tan\left(\frac{\theta}{2}\right)$$

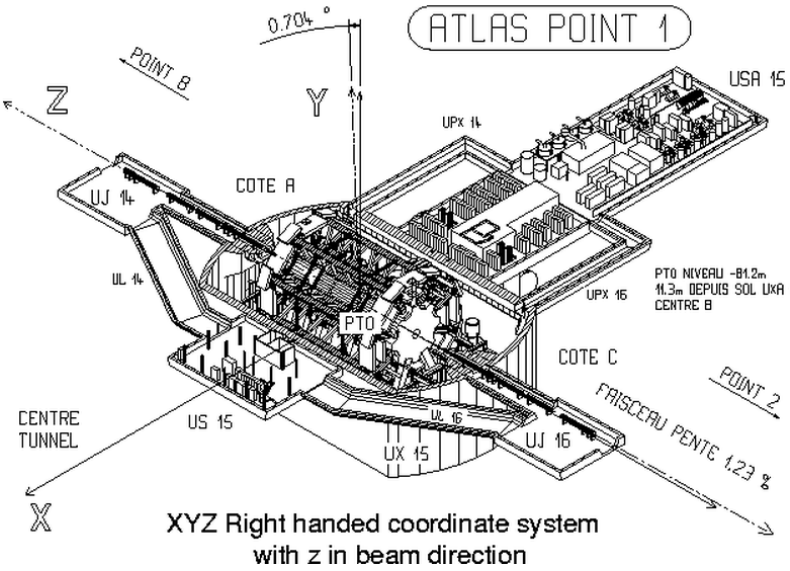

Figure 2.8: The coordinate system in the ATLAS detector. The general tilt of the LEP/LHC tunnel causes the y-axis to be slightly different from vertical.

which approaches the rapidity

$$y = \frac{1}{2} \ln \frac{E + p_z}{E - p_z}$$

in the limit where $E \gg m$. The pseudo-rapidity is 0 in the transverse plane and infinity along the z axis, with $\eta = 1$ at 45 degrees from the axis. The difference in rapidity between two particles is invariant under boosts along the z axis, and as a result the rapidity and the pseudo-rapidity are natural variables for describing angles in a system where the initial z-momentum is unknown. The angular distance between objects in the ϕ/η plane is a commonly used quantity, defined as

$$\Delta R = \sqrt{\Delta\eta^2 + \Delta\phi^2}$$

The energy and momentum of outgoing particles, E and p, are often projected onto the transverse plane. This is because momentum conservation can easily be implemented in the transverse plane, where the initial momentum is known to be zero, but not in the z direction, where the initial momentum is not known. The transverse momentum is then defined as $p_{\mathrm{T}} = \sqrt{p_x^2 + p_y^2}$, and transverse energy as $E_{\mathrm{T}} = E \sin\theta$.

Charged particles in a solenoidal magnetic field follow a helical trajectory, or track, which can be computed at each point in space using 5 parameters:

r, z, ϕ, θ, q/p. The variables r, z, ϕ and θ are the cylindrical coordinates described earlier, while the variables q and p are respectively the charge of the track and its momentum, and q/p represent the bending of the track. Other used variables focuses on the track parameters closest to the interaction point. They are: d_0, defined as the transverse impact parameter representing the transverse distance to the beam axis at the closest approach point; z_0, the longitudinal impact parameter at the closest approach point.

2.3.2 Magnetic field

The ATLAS detector uses four superconducting magnets to provide the magnetic field for bending charged tracks [2]. The inner detector magnetic field is provided by a solenoid producing a 2 T field in the z-direction. The muon spectrometer magnetic field is provided by three air-core toroid magnets producing fields between 0.5 T and 4 T in the ϕ direction. As a result of the z and ϕ fields, tracks bend in the ϕ direction in the inner detector, and in the η direction in the muon spectrometer.

Both the solenoid and toroid magnets are made of Al stabilized NbTi cables cooled to 4.5 K. To reduce the material thickness and the resulting energy losses of tracks, the solenoid has a thickness of only ~ 0.66 radiation lengths (10 cm), and it is housed in the same cryostat as the electromagnetic calorimeter. For the same reasons, the toroid is built following an air-core design, whereby most muons can traverse the magnetic field without having to cross any of the superconducting coils. The size of the toroid is chosen to provide a large bending volume for muons, resulting in a better lever arm for the muon spectrometer tracking.

Figure 2.9 shows the layout of the magnet system. The small and partially obscured green cylinder in the center of the drawing in Figure 2.9 is the solenoid magnet. The three air-core toroids are also visible: the large barrel one and the two small end-cap ones.

As a results of the complex leyout of the ATLAS magnet system, the B-field strenght affecting each particle has a strong dependence on the particle path. In particular, it is useful to consider the integrated magnetic field affecting a particle on a given trajectory, or $\int B \cdot dl$, which is also called the bending power. The *sagitta* of a particle track, defined as its distance from a straight path, is proportional to the bending power along its path and inversely proportional to the track momentum in the plane perpendicular to the B field. Therefore, a large bending power is necessary to leads to non-zero

[2] The momentum component of a charged track that is perpendicular to a uniform magnetic field can be estimated by measuring its bending radius R in a magnetic field B: $p[\mathrm{GeV}] = 0.3B[\mathrm{T}]R[\mathrm{m}]$.

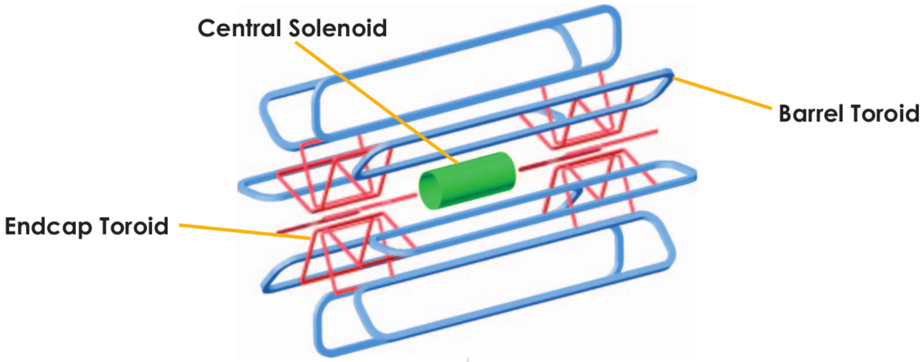

Figure 2.9: Layout of the ATLAS magnet system.

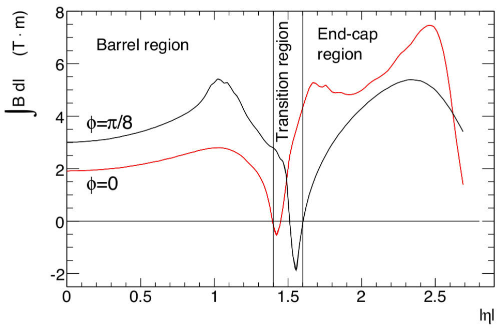

Figure 2.10: Bending power in the ATLAS toroid magnets [15].

sagittas for very high momentum tracks. Figure 2.10 shows the bending power of the ATLAS toroid system as a function of $|\eta|$, in two different ϕ directions. At $\phi = 0$ the barrel field is weaker than the end-cap field, while the converse is true at $\phi = \pi/8$, due to the position of the toroid coils. It can also be seen that the transition region between the barrel and end-cap is particularly complex, resulting in negative bending power for some (η, ϕ) directions.

2.3.3 Inner detector

The ATLAS inner detector (ID) is designed to reconstruct the paths of charged particles as they traverse a 2 T solenoidal magnetic field. Individual particle tracks are reconstructed using high-resolution position measurements known as hits, and multiple tracks are used in order to reconstruct vertices. The ID is built as a cylinder around the interaction point, with a radius of 1.1 m radius and a length of 7 m. Track hits are measured using three technologies: an innermost Pixel detector composed of silicon pixels, an intermediate silicon

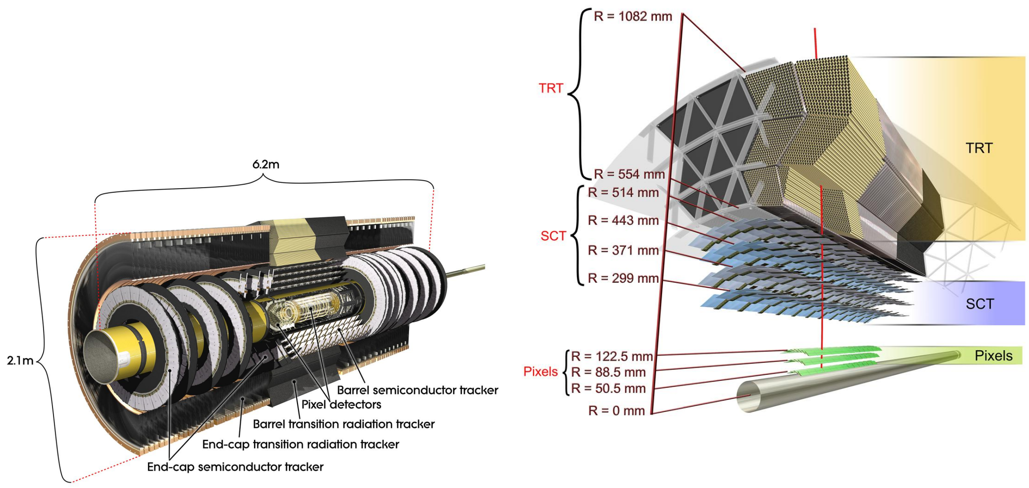

(a) (b)

Figure 2.11: (a) Layout of the ATLAS Inner detector. (b) A 3D zoomed view of the ATLAS Inner detector, consisting of three subdetectors: the Pixel Detector, the SemiConductor Tracker and the Transition Radiation Tracker.

strip detector (SCT), and an outermost transition radiation tracker built from small drift tubes (TRT). Figure 2.11a shows a three-dimensional rendering of the ID layout, while Figure 2.11b includes a more detailed layout.

The primary goal of the inner detector is to provide accurate and efficient tracking for charged particles with $p_{\mathrm{T}} > 0.5\,\mathrm{GeV}$ within $|\eta| < 2.5$, with a transverse momentum resolution of 1% (5%) for track p_{T} of 0.5 GeV (100 GeV), as specified in Table 2.2. In addition to single track measurements, multiple tracks can be combined to enable the reconstruction of primary vertices from *pp* collisions and secondary vertices from the decays of long-lived particles. Several challenges are added to these requirements, such as the high occupancy and high radiation environment, and the low material budget required to prevent multiple scattering and energy losses before the calorimeters. At design luminosity, each bunch crossing is expected to generate ~ 40 primary vertices and ~ 1000 charged particles with $p_{\mathrm{T}} > 0.5 GeV$.

The ID design is therefore driven by several constraints, and results in a combination of different technologies. A brief overview of the ID detectors is provided below.

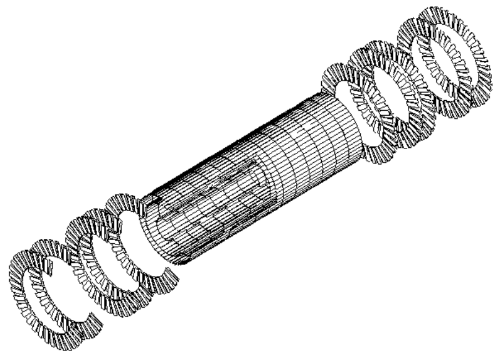

Figure 2.12: Layout of the ATLAS Pixel detector.

Silicon Pixel Tracker

The pixel detector (Figure 2.12) is the detector component closest to the beam. It is formed of layers of silicon semiconducting pixels, and is designed to have a very high granularity for resolving primary and secondary interaction vertices. There are three barrel layers closed by an endcap consisting of three disks at each end. The closest layer to the beam pipe, termed the b-layer (due to its important role in detecting secondary vertices for b physics), is positioned at a radius of 50.5 mm. Due to the high radiation dose that it will receive at this position, it will need to be replaced after three years of operation at design luminosity.

The detector layers are formed of silicon sensor modules, each consisting of $46,080$ active pixels with nominal dimensions of $50 \times 400\,\mu\mathrm{m}^2$. In total there are approximately 80.4 million pixels (consequently, readout channels).

Particles with $|\eta| < 2.5$ will traverse three layers of the detector; in most case producing three space-points. The Pixel detector allows for a resolution of $\sigma_\phi = 10\,\mu\mathrm{m}$ in the bending direction (ϕ), and $\sigma_{z,R} = 115\,\mu\mathrm{m}$ in the z (barrel) or R (end-cap) direction.

Semiconductor Tracker (SCT)

The SCT is a silicon strip detector, consisting of four barrel layers and two end-caps consisting of nine disks each. The barrel layers consist of 2112 separate modules. Each endcap consists of 988 modules, arranged in such a way that a particle must pass through four layers of the detector.

SCT modules are made from two layers of single sided p-in-n silicon chips biased at 150 V (this voltage will increase as the detector become radiation damaged). Charged particles passing through the depletion region at the centre of the junction produce electron hole pairs, which are swept apart by the bias voltage. The electrons are then collected on the top of the chip, producing a signal which can be read out.

Each side of the module consists of 768 strips of length 6.4 cm, with a pitch of 80 µm for barrel modules, and an average pitch of 80 µm for endcap modules. The strips on one layer of the module run parallel to the beam axis on the barrel, and along the R direction on the endcap. The other layer is placed at a stereo angle of 40 mrad to form a two-sided module. In total there are approximately 6.3×10^6 readout channels.

The stereo angle gives the ability to determine where along the strip the hit occurred, giving resolution in $z(R)$ in the barrels (endcaps). The spatial resolution of the detector is $\sigma_\phi = 17\,\mu\text{m}$ in the bending direction (ϕ), and $\sigma_{z,R} = 580\,\mu\text{m}$ in the z (barrel) or R (end-cap) direction.

Transition Radiation Tracker (TRT)

The Transition Radiation Tracker is a straw drift tube tracker, with additional particle identification capabilities from transition radiation. It consists of modules formed from bundles of 4 mm diameter straws, filled with a gas mixture consisting of 70% Xe, 27% CO_2 and 3% O_2. A tungsten wire runs down the centre of the tube to collect charge. In the barrel the straws run parallel with the beam axis and are electrically divided into two halves at $|\eta| = 0$ and read out at either end (this subdivision leads to an inefficiency along a length of approximately 2 cm at the centre of the TRT). In the endcaps the straws run radially. In total there are $351,000$ readout channels.

All charged tracks with $p_{\mathrm{T}} > 0.5\,\text{GeV}$ and $|\eta| < 2.0$ will traverse at least 36 straws, except in the barrel to endcap transition region ($0.8 < |\eta| < 1.0$) where only 22 straws will be traversed. In the bending direction (ϕ) the spatial resolution is $\sigma_\phi = 130\,\mu\text{m}$. Despite the low resolution compared to the silicon trackers, and the lack of a measurement in the z direction, the hits in the TRT contribute significantly to the pattern recognition and momentum resolution due to the large number of measurements and longer measured track length.

The barrel straws are embedded in a matrix of polypropylene fibres, and the endcap disk layers are sandwiched between polypropylene foils. When charged particles cross the boundary between the straw and the fibre they emit transition radiation photons. These photons are then absorbed by the Xenon gas mixture, and produce much larger signals than minimum-ionising charged particles. The energy of the transition radiation photons depends heavily on particle type, and is approximately 200 keV for a 20 GeV electron and 1 keV for a 20 GeV pion. This difference can be exploited for particle identification, by counting the number of hits over a higher energy threshold. Electrons with $p_{\mathrm{T}} > 2\,\mathrm{GeV}$ typically produce 7-10 high threshold hits, whereas pions and other charged particles will produce far fewer.

2.3.4 Calorimetry

The ATLAS calorimeter systems sit outside the inner detector and its magnetic field. The purpose of the calorimeter is to measure the energy and position of particles. A particle entering the calorimeter produces a 'shower' of secondary particles; the energy of this shower is then measured. ATLAS uses sampling calorimeters, in which different materials sandwiched together in layers are used to initiate the shower development (absorption) and to measure the energy of its constituents. This allows for a more compact design and hence better shower containment. Position measurement is obtained by segmenting the calorimeter in the z and ϕ directions.

Different absorbers are required depending on whether the particle interacts via the electromagnetic or the strong force, and the properties of the showers that develop are different. The ATLAS calorimeters are divided into two distinct subsystems, the electromagnetic calorimeter and the hadronic calorimeter.
An electromagnetic shower consists of electrons, positrons and photons, and is normally fully contained in the calorimeter; thus it can be fully detected. Hadronic showers involve many more particle types, including neutrons, muons, and neutrinos which escape detection, and tend to be longer and wider, often spilling out of the calorimeter. The full energy of the shower is thus not fully detected, and so a calibration of the energy response is required. It is important for the calorimeter to provide good containment of electromagnetic and hadronic showers, not only for the purposes of energy measurement, but also to allow a good missing transverse energy requirement, and to prevent punch-through into the muon system.

A cutaway view showing the location of the various calorimeter elements is shown in Figure 2.13. The calorimeters cover the range $|\eta| < 4.9$. Over the η range of the inner-detector, the electromagnetic calorimeter gives fine granularity to allow precise measurement of electrons and photons. The hadronic calorimeter is more coarsely segmented, but is sufficient to meet the requirements of jet and missing transverse energy measurement.

Electromagnetic Calorimeters

The electromagnetic (EM) calorimeter (also referred to as the LAr) uses liquid argon as the active detector material, and lead as an absorber. Charged

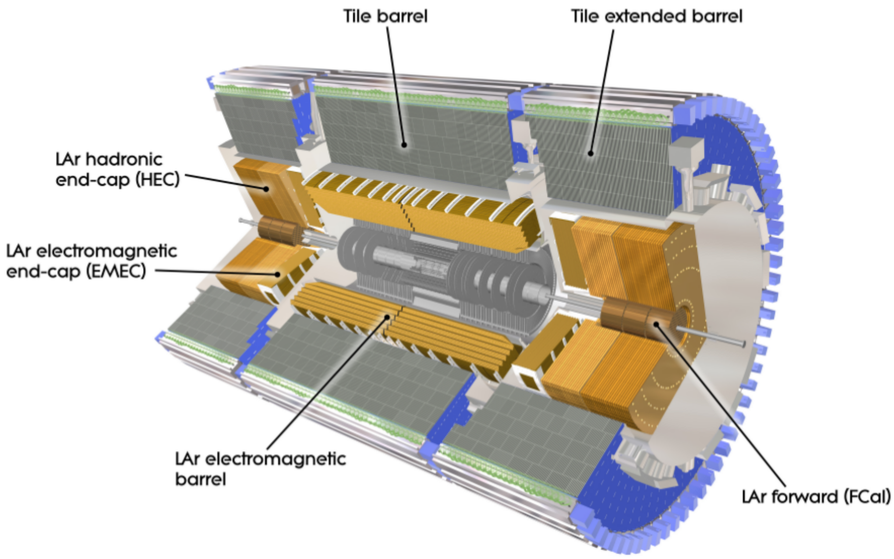

Figure 2.13: Cut-away view of the ATLAS calorimeter system.

particles in the shower ionise the liquid argon, where the electrons drift to copper electrodes in the presence of an electric field.

The LAr consists of two half barrels extending to $|\eta| < 1.475$ (with a 4 mm gap at $z = 0$), and two coaxial wheels on each side (named the EMEC), the first covering $1.375 < |\eta| < 2.5$ and the second covering $2.5 < |\eta| < 3.2$. Additional material needed to instrument and cool the detector creates a 'crack' region at $1.375 < |\eta| < 1.52$, where the energy resolution is significantly degraded.

The barrel calorimeter has an accordion structure in order to avoid azimuthal cracks and to provide full ϕ symmetry, as shown in Figure 2.14. The accordion structure is made of the lead absorber, with the liquid argon filling the 2.1 mm gaps between the absorbers. The barrel of the LAr calorimeter is divided into three layers, with different cell granularity. The first layer is divided into cells of $\Delta\eta \times \Delta\phi = 0.0031 \times 0.098$. The fine granularity in η of this layer is used to determine the pseudo-rapidity of the particle, and for measurements of the shower shape, an important input to particle identification. The second layer has cell size $\Delta\eta \times \Delta\phi = 0.025 \times 0.0245$ and contains the largest energy fraction of the shower, measuring approximately 16 radiation lengths. The third layer, with cell size $\Delta\eta \times \Delta\phi = 0.05 \times 0.0245$, collects the tail of the shower. The first wheel of the LAr calorimeter is also segmented into three layers with the same granularity as the barrel. The second wheel has a coarser granularity that varies as a function of pseudora-

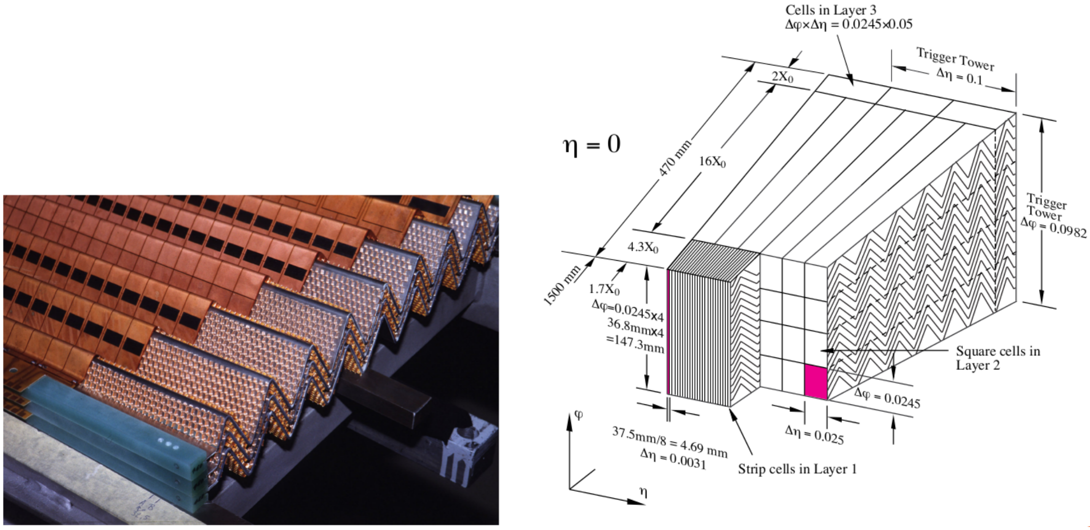

(a) (b)

Figure 2.14: A photo (a) and a Diagram (b) of ATLAS liquid argon calorimeter, showing the accordion structure and the different granularity in the different layers, ©1993 CERN.

pidity. A liquid argon pre-sampler exists for $|\eta| < 1.8$ to correct for energy lost by incident particles traversing material before the calorimeters, and to aid with discriminating between $\pi^0 \rightarrow \gamma\gamma$ decays and prompt photons.

The energy in the EM calorimeter is calculated by measuring ADC signals in each cell and summed by layers after calibration, as shown:

$$E_{\text{tot}} = w_{\text{glob}}(w_{\text{ps}}E_{\text{ps}} + E_{\text{front}} + E_{\text{mid}} + E_{\text{back}}) \tag{2.5}$$

The presampler weight w_{ps} is used to optimise the energy resolution. The corresponding energy resolution is generally expressed as:

$$\frac{\sigma_E}{E} = \frac{a}{E} \oplus \frac{b}{\sqrt{E}} \oplus c \tag{2.6}$$

in which a, b and c represent the noise term, the sampling term and the constant term, respectively. The symbol $\oplus$ is interpreted as the quadratic sum. The expected resolution is $\sigma_E/E = 10\%/\sqrt{E} \oplus 0.7\%$ (see Table 2.2).

Hadronic Calorimeter

The hadronic calorimeter consists of a plastic scintillator tile calorimeter (referred to as the tile calorimeter) covering $|\eta| < 1.7$ and a liquid argon endcap calorimeter (referred to as the HEC) covering $1.5 < |\eta| < 3.2$ (Figure 2.13).

The tile calorimeter consists of a barrel covering $|\eta| < 0.8$ and two extended barrels covering $0.8 < |\eta| < 1.7$, and is located immediately behind the EM calorimeter. The active material consists of 3 mm thick layers of the plastic scintillator placed perpendicular to the beam direction, sandwiched between steel absorbers. The scintillators are connected at each end to readout photomultiplier tubes by wavelength-shifting fibres. The fibres are grouped together to form readout cells, giving projective towers in η. There are three layers of cells, with a granularity of $\Delta\eta \times \Delta\phi = 0.1 \times 0.1$ in the first two layers, and $\Delta\eta \times \Delta\phi = 0.2 \times 0.1$ in the third.

The HEC consists of two wheels per endcap, HEC1 and HEC2, located directly behind the EMEC and sharing the same cryostat. Each wheel has two layers of cells. The HEC covers $1.5 < |\eta| < 3.2$ and so overlaps with the tile calorimeter on one side and the FCAL on the other, thus avoiding cracks in the transition regions.

The energy resolution is generally expressed as:

$$\frac{\sigma_E}{E} = \sqrt{\frac{c_{\text{int}}^2 + c_{\text{camp}}^2}{E}} \oplus a \tag{2.7}$$

in which a is a constant term that describes the non-gaussian fluctations of electromagnetic showers, c_{int} represents gaussian fluctation of the initial energy and c_{camp} refers statistical and sampling fluctations. The resolution of the tile calorimeter for hadrons is $\sigma_E/E = 50\%/\sqrt{E} \oplus 3\%$ (see Table 2.2).

Forward Calorimeter

The forward calorimeter (*FCal*) covers $3.1 < |\eta| < 4.9$. To reduce the neutron flux, the FCAL begins 1.2 m away from the EM calorimeter front face. Due to the high particle fluxes and energies in the forward region, the calorimeter must contain relatively long showers in the small volume allowed by design constraints, and thus must be very dense. The FCAL is divided into three compartments. The first, FCAL1, is designed for electromagnetic measurements, and uses copper as an passive material with liquid argon as a active material. The second two compartments, FCAL2 and FCAL3, are designed for hadronic measurements, and use tungsten as a passive material, chosen for its high density to provide containment and minimize the lateral spread of hadronic showers. An additional copper alloy shielding plate is placed behind FCAL3 to reduce background to the muon endcap system.

The resolution of the forward calorimeter is $\sigma_E/E = 100\%/\sqrt{E} \oplus 10\%$ (see Table 2.2).

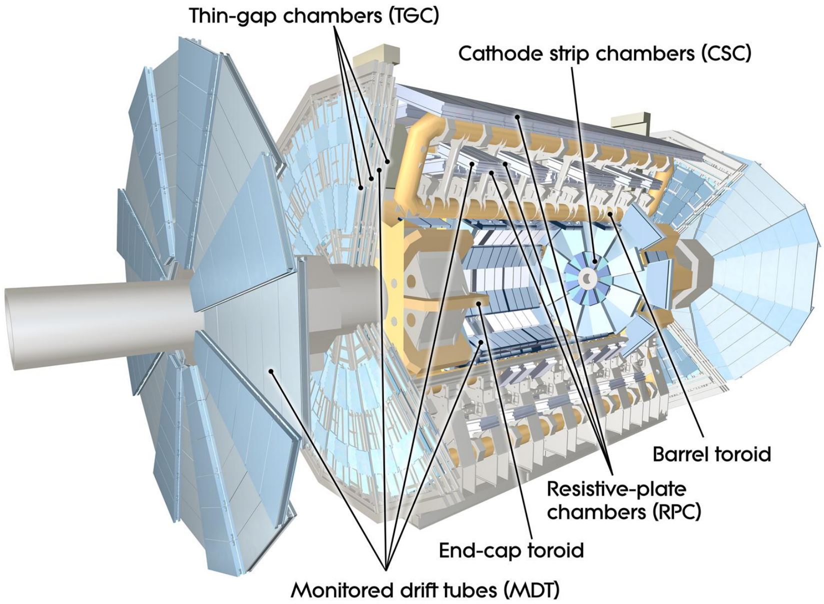

Figure 2.15: A schematic of the ATLAS muon spectrometer.

2.3.5 Muon spectrometer

The ATLAS muon spectrometer (MS) [**?**] uses four different detector technologies to provide accurate direction and momentum measurements for muons with momenta from $\sim 6\,\mathrm{GeV}$ up to a few TeV. It also provides efficient triggering for muons in the same momentum range. The MS is located outside of the calorimeter system and occupies a large fraction of the ATLAS cavern. It relies on the bending power of the barrel and end-cap toroid magnets to bend the muon trajectories over a large distance, and requires a very good hit resolution in order to measure the curved tracks. Figure 2.15 shows the overall layout of the muon spectrometer and the toroid magnets.

The benchmark goal of the MS is a 10% momentum resolution for 1 TeV muon tracks (see Table 2.2). In order to reach this goal, accurate hit resolution and B-field modeling are required, as well as modeling of the material crossed by the muon track. Given the bending power of the toroid magnets, the sagitta of a 1 TeV muon track is $\sim 500\,\mu\mathrm{m}$, so the hit resolution required for a 10% measurement is approximately $50\,\mu\mathrm{m}$. The hit resolution is determined by the intrinsic resolution of each detector element, and by the alignment, which is the knowledge of the position of that detector element within ATLAS.

Since the four subsystems of the MS are combined together when reconstructing muon tracks, the B-field monitoring and the alignment monitoring are shared between them. The magnetic field is monitored by almost two

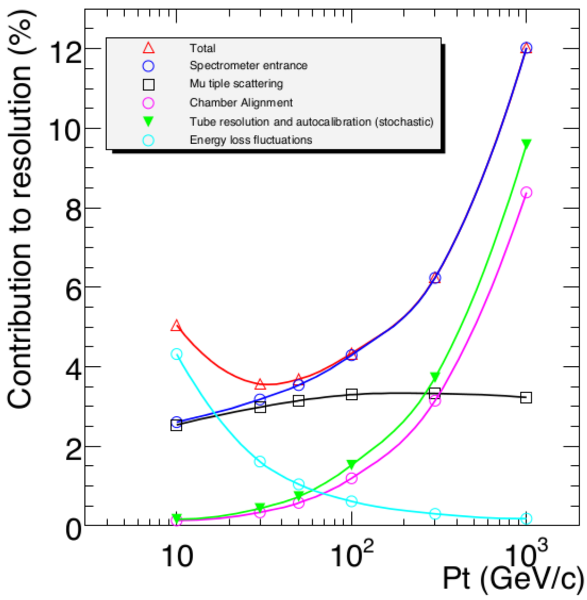

Figure 2.16: Primary contributions to muon stand-alone tracking resolution as described by the ATLAS Monte Carlo simulation [29].

thousand Hall probes throughout the MS, which are used to correct B-field modeling software. The alignment is monitored by more than ten thousand optical sensors, which are able to detect position changes at the 20 µm level. The expected momentum resolution of the MS is shown in Figure 2.16. At low energies, the resolution is dominated by energy loss in material before the MS, while multiple scattering dominates at medium energies, and alignment and intrinsic detector resolution at high energies.

The four detector technologies used in the MS define four systems. Muon trigger signals are provided by two of them: the Resistive Plate Chambers (RPC) in the barrel region and the Thin Gap Chambers (TGC) in the end-cap region. Both the RPC and TGC are fast tracking detectors with time resolution much smaller than the 25 ns bunch spacing. The high precision measurements in the bending direction is provided by the Monitored Drift Tubes (MDT) over most of the detector acceptance, and by the Strip Chambers (CSC) the forward region, where the particle flux is too high for MDT chambers.

The layout of the MS is shown in Figure 2.17. In the upper drawing, the layout of the barrel region can be seen in the transverse plane, showing the sixteen sectors in ϕ (based on the eight-fold symmetry toroid), and the three layers of MDT and RPC chambers. The lower drawing shows additionally the three layers of MDT and TGC chambers in the end-cap, and the position of the CSC chambers in the forward region. While the barrel toroid encloses the first two layers of MDT and RPC, in the end-cap region the toroid lies between the first and second MDT layers, and before the three TGC layers. An additional (not labeled) TGC layer lies to the right of the innermost MDT end-cap layer. It provides a ϕ-coordinate measurement used in tracking, but it does not participate in the trigger decision. A brief overview of the muon spectrometer systems is provided below, while more details can be found in references [15, 28].

Monitored Drift Tubes

MDT chambers are composed of six or eight layers of drift tubes. Each tube has a 3 cm diameter and a 50 μm thick anode wire at the center. The wire is held at 3080 V while the tube is held at ground, generating a radial electric field. The tubes are filled with a gas mixture of 93% argon, 7% CO_2, and 1 part per million H_2O, held at pressure of 3 bars. The mixture is chosen for its ageing properties, preventing the accumulation of deposits on the anode wires, as well as for its gain of $\sim 2 \times 10^4$. When a muon passes through an MDT tube it ionizes the gas, initiating an avalanche of electrons which drift to the central wire, causing a voltage drop. With this gas mixture, the maximum drift time of electrons in the tubes is approximately 700 ns. When MDT hits are read out, the time of arrival is also recorded, as it can be related to the distance of the muon track from the wire. Using this method, each hit has a resolution of approximately 80 μm on the hit radius, even though the full tube radius is 1.5 cm. The ϕ coordinate (along the tube) is not measured by MDTs, and it is extracted from the RPC and TCC hits.

Cathode Strip Chambers

The CSC chambers cover the forward region of the end-cap inner layer ($2.0 < |\eta| < 2.7$), and they are placed behind the hadronic end-cap calorimeter (see Figure 2.17). They are multi-wire proportional chambers. A plane of anode wires is placed between two planes of cathode strips, separated by a 2.5 mm gas gap from both. When a muon ionizes the gas, electrons drift towards the wires, inducing charges on the cathode strips which are read out. One set of strips is oriented parallel to the wires, and one perpendicular, resulting in a two-dimensional measurement. The hit resolution, obtained by interpolating the charge measured in neighboring strips, is 60 μm in η and 5 mm in ϕ.

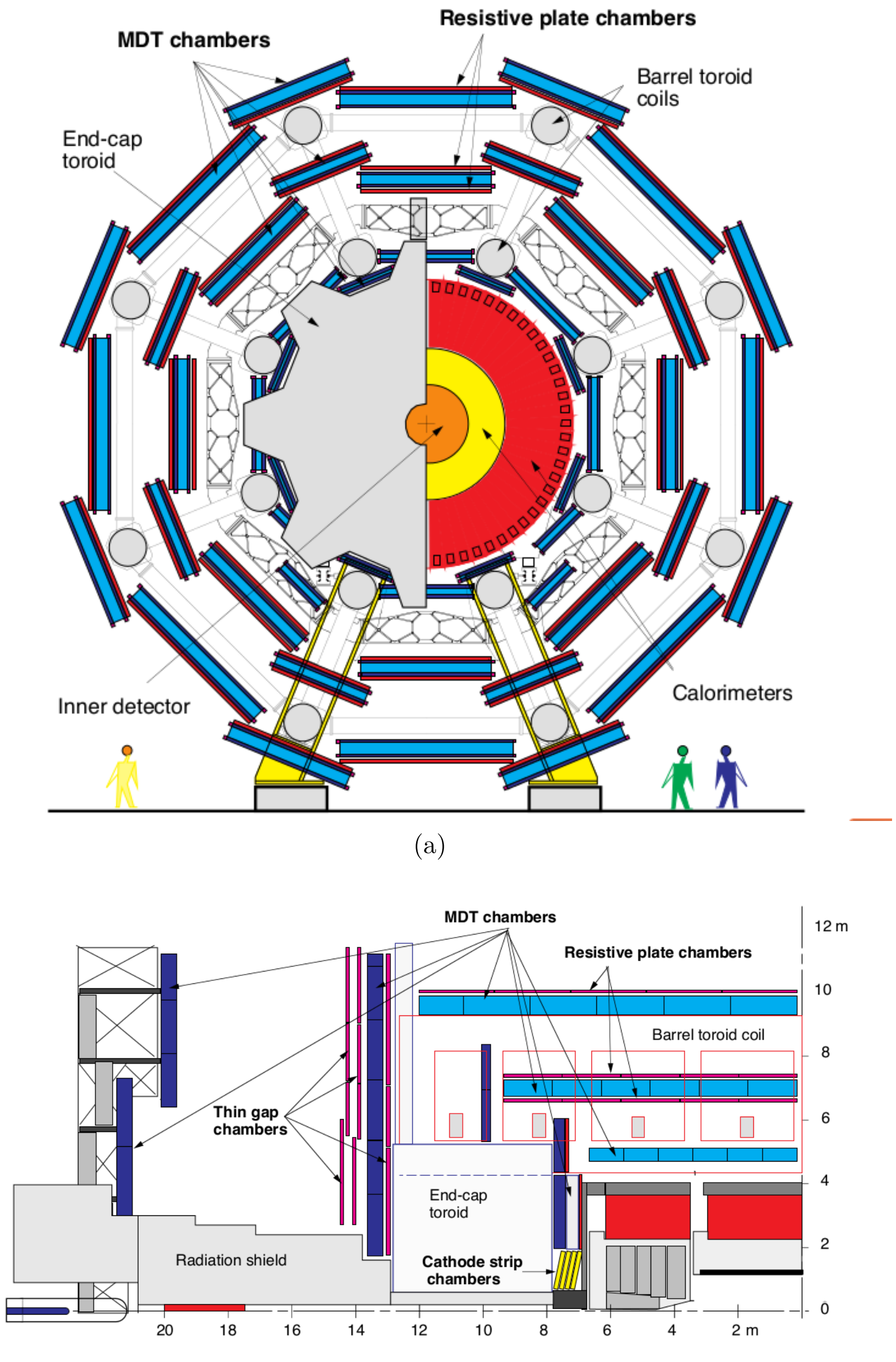

(a)

(b)

Figure 2.17: The layout of the muon spectrometer in the x-y plane (top) and in the y-z plane (bottom) [28]. The lower drawing only shows a quarter of the y-z plane, with the interaction point located in the lower right corner.

Resistive Plate Chambers

The RPC chambers provide trigger signals and ϕ-coordinate measurements in the barrel region, and they are placed adjacently to the second and third MDT layers (see Figure 2.17). Due to spatial constraints from support structures and services, the RPC chambers only cover approximately 80% of the barrel region. The RPC chambers are based on two resistive plates, separated by a 2 mm gas gap with a $\sim 4.8\,\mathrm{kV/mm}$ electric field. When a muon ionizes the gas, it creates a charged avalanche. Electrons from the avalanche then drift towards the anode plate, inducing charges on the read out strips that are mounted outside the resistive plates. The strips on the upper and lower plates are oriented in perpendicular directions, providing a two-dimensional measurement.

Thin Gap Chambers

The TGC chambers provide the triggering and ϕ-coordinate measurements in the end-cap region, and they are placed around the second layer of MDT end-cap chambers. Additional chambers not used for triggering are located on the first layer MDT end-cap chambers. TGC chambers are used in the end-cap due to their higher rate capabilities, their higher granularity, and their radiation resistance. The TGC chambers are multi-wire proportional chambers, like the CSCs, but they have a smaller anode-cathode separation ($\sim 1.5\,\mathrm{mm}$), resulting in an improved time resolution. Both the anode wires and the strips are read out, providing a measurement of η and ϕ. The wire-to-wire distance is very small, 1.8 mm, and wires can be read out as smaller or larger groups, depending on the resolution required in each η region. Each TGC chamber contains two or three gas gaps held together with a honeycomb structure, called doublet and triplet chambers respectively, as seen in Figure 2.18.

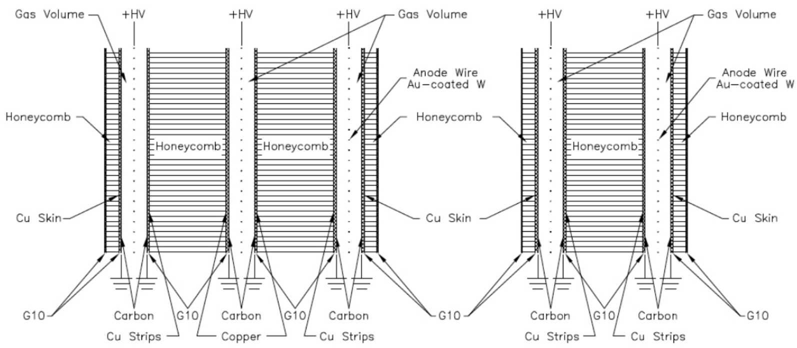

Figure 2.18: The structure of the TGC triplet (left) and doublet (right) chambers.

Chapter 3

Physics object reconstruction and computing model in ATLAS

In the search of the Higgs boson, we must trigger on and then collect the data events containing the Higgs boson signal. In order to form a total description of the event we must be able to reconstruct all of the objects present in each event. A precise understanding of all event objects and all components of the detector is required for the Higgs boson search in the $ZZ^{(*)}$ decay mode.
The same algorithms are used for real data and for simulated data (Monte Carlo): discrepancies can be adjusted through the respective calibrations.

The software algorithms used for reconstructing ID tracks, primary vertices, electrons, muons, jets, b-tagged jets, and missing transverse energy and also the computing model are described in the following sections.

3.1 Trigger and Data acquisition

The ATLAS trigger and data acquisition (TDAQ) system [?] identify interesting events, read them out and record them. The trigger system (Figure 3.1) analyzes events at three consecutive levels of increasing complexity: the first level (L1) is implemented using custom-made electronics, the second and third level (L2 and Event Filter or EF) are implemented using computers and networking equipment and form the High Level Trigger (HLT). Figure 3.2 shows the event rate and the processing tile before and after each trigger selection.
The L1 trigger searches for signatures from large p_{T} electrons, photons,

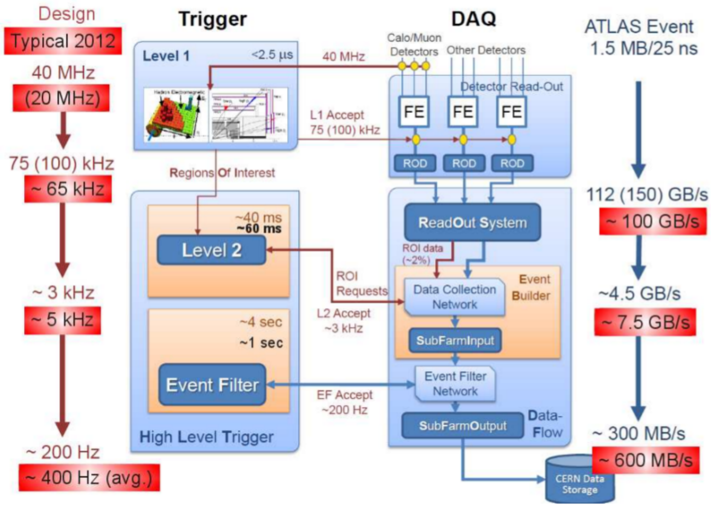

Figure 3.1: An overview of the ATLAS trigger and DAQ system. The design and 2012 typical trigger rates at each level are shown on the left, and the design and 2012 typical output bandwidths are shown on the right.

muons, jets, τ leptons decaying into isolated hadrons. It is also designed to select events with high $E_{\mathrm{T}}^{\mathrm{miss}}$ and high total transverse energy ($\sum E_{\mathrm{T}}$). The informations coming from the ID tracking system are not used at this trigger level because it will lead to a rise of the time response. The L1 trigger consists of three main components: L1Calo (a Calorimeter Trigger) and L1Muon (a Muon Trigger), to process the input data from the calorimeters and the muon detector, and a Central Trigger Processor (CTP), which combines the results of the two trigger subsystems.
With an input rate of $\sim 100\,\mathrm{kHz}$ (provided by the L1) the L2 perform decisions within 40 ms. The EF analyzes the L2-triggered events at a 3.5 kHz rate and provides an output rate of $\sim 400\,\mathrm{Hz}$. The high input and output rates of the HLT are achieved by analyzing multiple events in parallel. The L2 decision is much faster than the EF one because it only uses the event information located in the Region-of-Interest (or RoI, the specific region where the L1 trigger originated). The EF, instead, analyzes the entire event.
Both systems are software-based, and have access to the full-granularity and full-precision calorimeter and muon data, and also to the ID tracking data.

The Data Acquisition (DAQ) system monitors the movement of the data from the detector to the storage disks. When the L1 trigger accepts an event, the DAQ moves the full event data from the detector electronics into the detector-specific Read-Out Drivers (ROD): the data are encoded in a common format and transfered to the common Read-Out System (ROS). If the L2

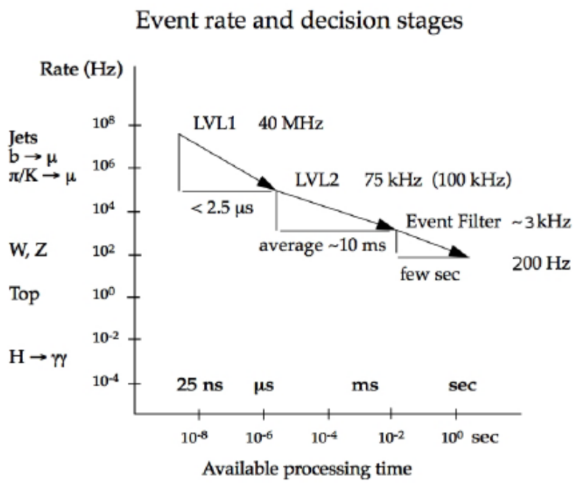

Figure 3.2: Events rate before and after trigger selection.

trigger passes, the event data from different detector regions is merged into a single structure, and provided to the EF. If the EF trigger passes, the event is recorded to disk.

The Higgs boson decay channel presented in this thesis involves the leptonic decays of the weak bosons. The goal from the trigger is to keep "low" p_T muon and electron (the order of 20 GeV for single lepton triggers and 12 GeV in the case of di-lepton triggers).

3.1.1 The Calorimeter Trigger

The L1Calo is a digital system, designed to process about 7200 analogue trigger signals of low granularity, $\Delta\eta \times \Delta\phi = 0.1 \times 0.1$, from the entire ATLAS calorimetry, within a fixed latency of $\sim 1\,\mu$s. The energy deposits in the calorimeters is described by an analogue trigger signals. The L1Calo uses this information to identify various physics objects with high E_T and to compute global and scalar energy sums. Some programmable energy thresholds discriminate the results of these investigations, and the obtained multiplicities are passed to the CTP.

3.1.2 The Muon Trigger

The L1Muon identifies candidates with p_T above six programmable thresholds and assigns them to the correct bunch-crossing, using the tracking measurements performed by the RPCs (in the barrel region) and the TGCs (end-cap) systems of the Muon Spectrometer. For an efficient reconstruc-

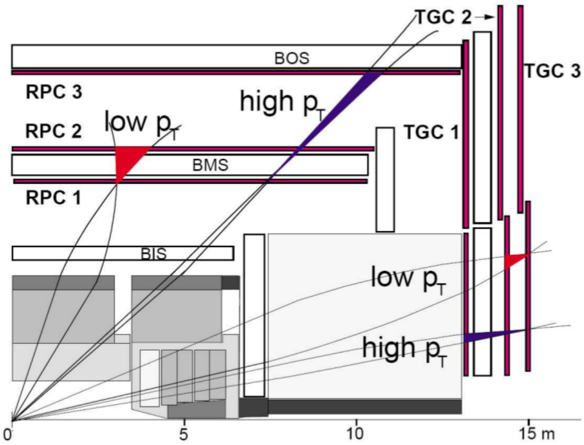

Figure 3.3: The ATLAS Muon Trigger Chambers and examples of muon tracks generating triggers.

tion of the p_{T} over a wide range, the logic of the L1Muon divides the six programmable thresholds into two groups: the first three thresholds are associated with a low p_{T} trigger, and cover the approximative E_{T} range of 6-9 GeV, whereas the last three thresholds are associated with a high p_{T} trigger, and cover the E_{T} range $\sim$ 9-35 GeV.

The L1Muon trigger algorithm is based on coincidence of hits in the different muon trigger chambers. One of the stations is used as a pivot plane, then the algorithm searches for time-correlated hits in the other two stations (named as confirm planes). The identification of a coincidence is developed within a geometrical road, of which centre is defined by the line of conjunction of the interaction point with the hit in the pivot plane: this line is the path of a muon with infinite momentum, originated from the interaction point (see Figure 3.3). Howover no muon will traverse the detector without being deflected by the toroidal magnetic field. The width of the geometrical road is related to the chosen p_{T} threshold: the higher the p_{T} threshold, the closer the road. For an efficient reconstruction, the algorithm uses all six p_{T} thresholds in the same time. The algorithm is performed simultaneously in both projections (η-ϕ in the barrel, R-ϕ in the end-cap), in order to reduce significantly the rate of accidental triggers due to low-energy particles, *i.e.* thermalised slow neutrons leaking from the hadronic calorimeter.

The results obtained are combined into one set of threshold multiplicities for each bunch-crossing, and sent to the CTP.

3.1.3 The Central Trigger Processor

The CTP combines the information from the L1Calo and the L1Muon to make the Level-1 trigger decision, within a latency of $\sim$ 100 ns. The CTP implements a trigger menu of up to 256 programmable trigger items: a logical combination of 1 to 256 trigger conditions. For example, a trigger item could be the combination of many trigger conditions: a muon candidate with $E_{\mathrm{T}} > 15\,\mathrm{GeV}$ and an e/γ candidate with $E_{\mathrm{T}} > 10\,\mathrm{GeV}$. The overall L1 trigger decision is then obtained by logically OR'ing all the items of the trigger menu.

In addition to forming the trigger decision, the CTP receives timing signals from the LHC machine, *e.g.* the 40.08 MHz bunch-crossing clock, and provides them to all the ATLAS sub-detectors.

3.2 Physics object reconstruction

The first step in particle reconstruction involves reconstructing tracks in the inner detector and the muon spectrometer, identifying clusters of energy deposits in the calorimeter systems and identifying interaction vertices. These are then combined to reconstruct particles such as electrons, muons, photons, jets and tau leptons, as well as to measure properties of the event such as missing transverse energy. Triggering on electrons and muons is a crucial component of the measurements described in this thesis and is also described in more detail.

Figure 3.4 shows schematically how different types of particle interact with the different detector components:

- muons leave a track in the inner detector, typically deposit little energy in the calorimeters and then leave a track in the Muon Spectrometer;

- photons leave no track in the inner detector, and will typically deposit all of their energy in the EM calorimeter, leaving an electromagnetic shower;

- electrons also typically deposit all of their energy in the EM calorimeter, but will also leave a track in the inner detector;

- charged hadrons such as protons leave a track in the inner detector, deposit minimal amounts of energy in the EM calorimeter, and then deposit most of their energy in the hadronic calorimeter, leaving a long wide shower;

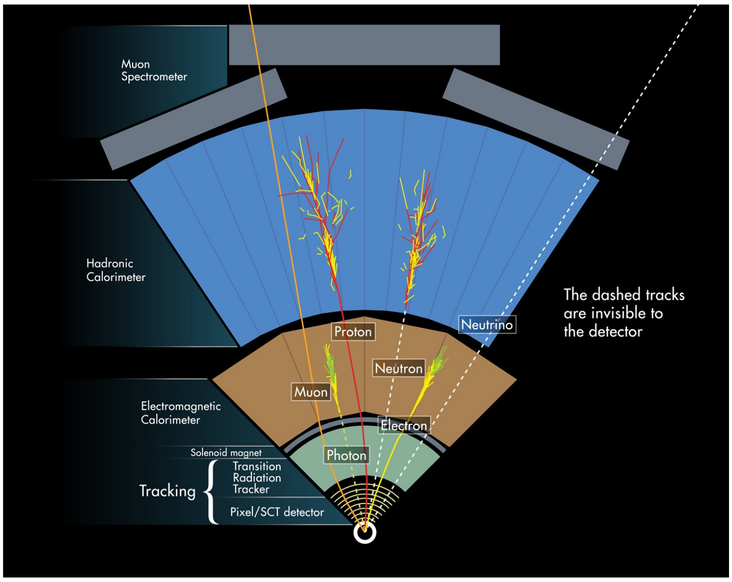

Figure 3.4: Schematic view of the progression of different types of particle through the ATLAS detector. Figure from [18].

- neutral hadrons such as neutrons behave in a similar manner to charged hadrons, but do not leave a track in the inner detector;
- neutrinos completely escape the detector leaving no trace in any of the detectors systems.

3.2.1 Tracking

Particles traversing the inner detector travel in an approximately helical path under the influence of the magnetic field, leaving hits in the various detector components that they traverse. It is necessary to reconstruct particle tracks from these hits to identify and measure particles, in a process known as tracking. At the collision energies and levels of pileup at the LHC, there will typically be hundreds of hits in the Inner Detector. The tracking algorithm must be able to correctly associate hits with tracks, as well as reconstruct the track parameters, taking account of multiple scatterings, ionisation energy loss and, especially for electrons, radiation energy loss from bremsstrahlung. A detailed description of the ATLAS tracking is given in [30].

As said in Section 2.3.1, a particle's trajectory can be described by five parameters, x_i. In ATLAS, the parameters are chosen to be:

$$\mathbf{x_i} = (l_1, l_2, \phi, \theta, q/p) \tag{3.1}$$

where l_1, l_2 are two co-ordinates in the frame of the detector surface in which a measurement is made, and the other three parameters describe the momentum of the track in the global frame.

Inside-Out Tracking

The main tracking algorithm is known as 'inside-out' tracking: it begins in the inner detector layers and works outwards. The first step is the formation of space-points from the measurements in the silicon detectors. While a space-point corresponds simply to a hit in the Pixel detector, in the SCT space-points are required to have hits in both sides of the module in order to give a measurement in z (due to the stereo-angle). Track seeds are then formed from combinations of space-points in the three Pixel detector layers and the first layer of the SCT.

These seeds are used to build roads through the rest of the detector elements. A Kalman fitter [31] is used to follow the trajectory, successively adding hits to the track taking into account linear distortions to the track from multiple scattering and from ionisation energy loss. Energy loss through bremsstrahlung is, highly non-gaussian: so it is not modelled well in this approach. Roughly 10% of seeds will lead to track candidates.

The next step is ambiguity resolution. Many of the track candidates found in the track finding will share hits, or will be as a result of fakes. At this stage the track is refitted with a global χ^2 fit [32], using a refined reconstruction geometry with more detailed material description. A score is assigned to each track, based upon the fit quality $\chi^2/\mathrm{N_{dof}}$, the number of hits on the track, the presence of overlapping hits on a layer, with penalties for 'holes' (missing hits). Ambiguities are resolved by choosing the track with the greater score; tracks with a score below a certain threshold are rejected.

The track is then extended into the TRT and these extended tracks are refitted once again, by using the full information of all three detectors. The quality of the extended track is compared to the quality of the silicon only track; the track extension is kept only if it improves the quality of the fit.

Outside-In Tracking

The inside-out tracking procedure fails to find tracks from photon conversions or decays of long lived particles, as these particles will not produce hits in the inner layers of the detector and so will not produce seeds. A complementary tracking procedure called 'outside-in' tracking attempts to solve these problems by starting from the TRT and working inwards. It begins by searching for track segments in the TRT using hits not already associated with a silicon track extension. These track segments are fitted using a Kalman filter to take into account the drift-time measurements. They are then extended back into the SCT and Pixel detectors, where hits not already associated to tracks are associated to them.

3.2.2 Vertex Finding

Location of interaction vertices is important in order to know which particles are associated with the primary interaction vertex, and to construct parameters such as the longitudinal and transverse impact parameters, which can be used to distinguish leptons from conversions or from secondary decays in jets. In the ATLAS reconstruction process vertex-finding performs after reconstruction of inner detector tracks, as described in Section 3.2.1. The vertex-finding algorithm must associate tracks with vertices, and obtain a best fit for the vertex positions.

The default ATLAS approach to vertex finding is called ‘finding-through-fitting’ [33]. Tracks are preselected by consistency with the interaction region, and a single seed vertex is formed from all of the preselected tracks. This is fitted using an ‘Adaptive Vertex Finding’ [34] algorithm, which uses a Kalman filter to minimise the least squares distances of the tracks from the vertex position. After a preliminary fit, tracks are assigned a weight depending on their compatibility with the vertex. The process is iterated until convergence. Following the fit, tracks identified as outliers are used to create a second vertex seed. A simultaneous fit is then carried out using the two vertices, and again outlier tracks are used to create a new primary vertex. The procedure is iterated until none of the remaining outliers fits with any vertex give a χ^2 probability of more than 1%.

3.2.3 Electron Reconstruction and Identification

Electron Reconstruction

The electrons are reconstructed by combining tracking and calorimeter information. In the inner detector, tracks are reconstructed according to the description of Section 3.2.1. Then a cluster based algorithm are performed to reconstruct the electrons. Using a sliding window clustering method, energy deposits in the electromagnetic calorimeter are used to form energy clusters. The cells of the calorimeter are shown in Figure 2.14. In this algorithm the η-ϕ space is divided into a grid of $N_\phi \times N_\eta$ elements ($\Delta\phi\eta = 0.025 \times 0.025$). In the EM calorimeter, 256 bins in ϕ and 200 bins in η from -2.5 to 2.5 are defined. In each bin, energies of all cells across the longitudinal layers are summed

Particle type	Barrel	End-cap
Electron	$N_\phi \times N_\eta = 3 \times 7$	$N_\phi \times N_\eta = 5 \times 5$
Photon-converted	$N_\phi \times N_\eta = 3 \times 5$	$N_\phi \times N_\eta = 5 \times 5$
Photon-unconverted	$N_\phi \times N_\eta = 3 \times 5$	$N_\phi \times N_\eta = 5 \times 5$

Table 3.1: Various cluster sizes for different particle types and calorimeter regions.

as the tower energy. Then a fixed size window (nominal $N_\phi \times N_\eta = 5 \times 5$) is used to define a pre-cluster. The seed found in the pre-cluster is used to reconstruct the final EM clusters. All of the cells within a given η-ϕ range to the seed are filled into the final cluster. The size of the clusters for different egamma candidates is shown in Table 3.1. After reconstructing the clusters, the shower shapes are calculated. Only one track matched cluster is stored as an electron. The energy in each cluster is corrected by taking into account the leakage outside the window and also the losses in the crack scintillators. Then the tracks are refitted by considering bremsstrahlung. Thus, in each electron object, two sets of 4-vectors are filled: usually the track 4-vectors are used to define the direction and the information in cluster 4-vectors is used to provide energy measurement.

Electron Identification

The electron candidates reconstructed as described in the previous section will contain a high contamination from jets faking electrons, non-isolated electrons from decays in jets, and electrons from photon conversions. In order to identify prompt electrons, a cut-based identification is used. Cuts are made on variables relating to the shape of the electromagnetic shower, the quality of the inner detector track and the track-calorimeter matching. The cuts were optimised using a multivariate analysis program (TMVA): three reference sets of cuts are used, denoted Loose++, Medium++ and Tight++, designed to give progressively greater background rejection, against the signal efficiency. The expected jet rejections (from simulation) of the three points are 500, 5000 and 50000 respectively [35]. In 2012, the identification selections were re-optimised with respect to the 2011 selections to prevent drops in efficiency of up to 20% in events with high pileup.

Loose++ Requirements In both 2011 and 2012 the Loose++ selection makes cuts on shower-shape variables in the first and second layers of the EM calorimeter, leakage into the hadronic calorimeter, track quality in the silicon detectors, and loose track cluster matching. The selecting variables are:

- **Shower Shapes**: cuts are made on the some shower-shape variables which distinguish between electromagnetic showers originating from electrons or photons and hadronic showers originating from particles in jets.

- **Silicon Hits**: at least 7 hits in the silicon detectors, of which at least one must be in the pixel detector. This ensures good track quality and rejects backgrounds from conversions or decays such as $\pi^0 \to e^+e^-$.

- **Track-Cluster matching**: a loose matching in η is applied, requiring $\Delta\eta < 0.015$; this ensures that the track and the cluster originate from the same physical particle and rejects backgrounds from combinatoric fakes.

Medium++ Requirements All Loose++ cuts are required to be passed, and in addition:

- **Shower Shapes**: the shower-shape cuts made in Loose++ are made tighter.

- **Track-Cluster matching**: a tighter matching in η is applied, requiring $\Delta\eta < 0.005$.

- **Impact Parameter**: require that the electron's track has a transverse impact parameter $|d_0| < 5\,\text{mm}$; this rejects backgrounds from electrons originating from decays of hadrons in jets.

- **Silicon Hits**: stricter requirements are made on hits in the silicon detectors. It is required that there is at least one hit in the b-layer for $|\eta| < 2.01$ ($|\eta| < 2.37$ in 2012).

- **Fraction in third calorimeter layer** f_3: for 2012 a cut on the fraction of the shower energy deposited in the third layer of the EM calorimeter was added to compensate for the loosening of the cuts in the first layer of the calorimeter.

- **TRT High Threshold Hits**: A loose requirement is made on the fraction of high-threshold (HT) hits from transition radiation photons in the TRT detector.

Tight++ Requirements All Medium++ cuts are required to be passed, and in addition:

- **Shower Shapes**: cuts on shower-shape variables are made at equal or tighter values to those for Medium++.
- **Track-Cluster matching**: a cluster matching in ϕ is added, requiring $\Delta\phi < 0.02$, and cuts are made on the ratio of the cluster energy to the track momentum, E/p.
- **Impact Parameter**: the transverse impact parameter cut is tightened to $|d_0| < 1\,\mathrm{mm}$.
- **Silicon Hits**: stricter requirements are made on hits in the silicon detectors, requiring that there is at least one hit in the b-layer for all η, and, in 2012, at least 2 hits in the Pixel detector for all η.
- **Conversion Rejection**: candidates matched to reconstructed photon conversions are rejected. hits from transition radiation photons in the TRT detector.

In the forward region identification must rely on calorimeter shower-shape variables alone, since there is no tracking from the inner detector. A good discrimination between electrons and hadrons may be made due to the fine transverse and longitudinal segmentation of the calorimeter, but it is not possible to distinguish electrons and photons in the forward region.

Electron Identification Efficiencies

In Figure 3.5 the electron identification efficiency in 2011 and 2012 is shown, as a function of the number of reconstructed primary vertices in the event. Using the 2011 identification requirements, the efficiency can drop by over 5% in events with 18 reconstructed primary vertices with respect to the efficiency in events with a single primary vertex. Figure 3.6, instead, shows the Loose++ identification efficiency as a function of E_{T}, using the 2011 requirements. The efficiency measured in data differs from the efficiency measured in Monte Carlo simulation at the level of a few percent: this is mainly attributed to mis-modelling of the shower-shape variables in the Monte Carlo. Thus scale-factors, parameterised as a function of η and E_{T}, are applied to the Monte Carlo to correct the reconstruction efficiency to that observed in data.

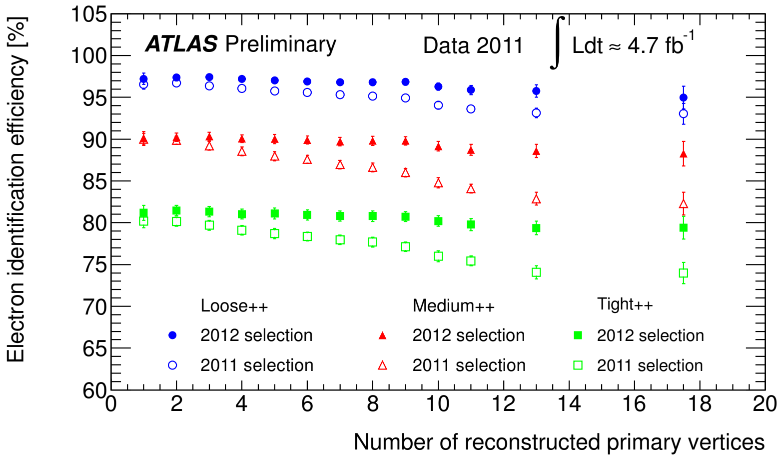

Figure 3.5: Electron identification efficiency in 2011 (open markers) and 2012 (solid markers) as a function of the number of reconstructed primary vertices in the event. The blue circles show the efficiency for the Loose++ selection, the red triangles for the Medium++ and the green squares for the Tight++ [36].

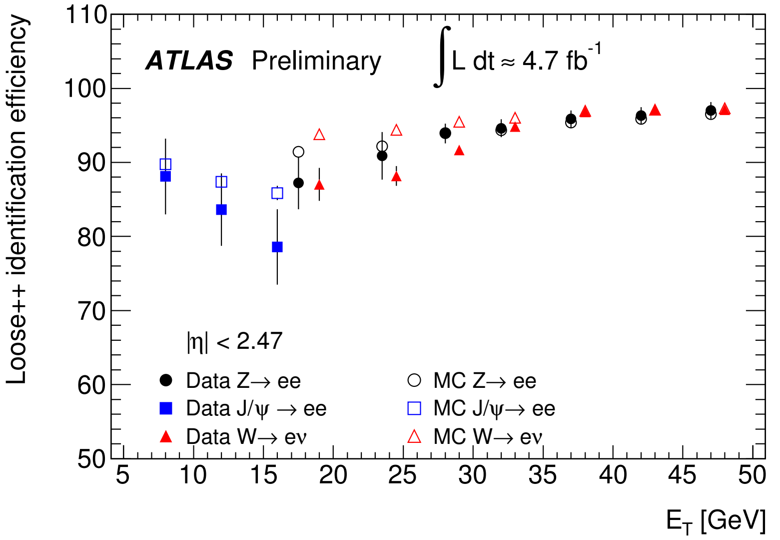

Figure 3.6: Efficiency of the Loose++ identification requirements as a function of the cluster transverse energy. The solid points indicate data based measurements whilst the open points indicate predictions from Monte Carlo. The different markers indicate the method used to measure the efficiency [37].

3.2.4 Muon Reconstruction and Identification

Muon reconstruction is based on combination of accurate measurements in the inner detector and the muon spectrometer [38, 39]. There are four categories of muons:

- **Combined**: combination of an MS track with an ID track. Combined muons have an acceptance limited by the ID at In general limited by the acceptance of the ID, $|\eta| < 2.5$.
- **Segment-Tagged**: combination of an ID track with an MS track segment. An MS track segment is a straight line track segment reconstructed in a single MS station where the segment did not form a full MS track. The track parameters of the reconstructed muon are taken solely from the ID track.
- **Stand-Alone**: a muon track reconstruction based only on MS measurements. Possible over the full acceptance of the MS, $|\eta| < 2.7$.
- **Calorimeter-Tagged**: ID tracks are tagged as originating from muons by matching them to calorimeter deposits consistent with a minimum ionising muon. No MS information is used.

Combined muons are the preferred muon type and will have the best track parameter resolution, since have a fully reconstructed track in both the ID and the MS. The ID provides the best momentum measurement at low to intermediate momenta, whereas the MS provides the better measurement at higher p_{T} (roughly for $p_{\mathrm{T}} > 100\,\mathrm{GeV}$). Combination with an ID track improves the momentum resolution over the range $4\,\mathrm{GeV} < p_{\mathrm{T}} < 100\,\mathrm{GeV}$. Segment-Tagged muons are useful to recover efficiency at low p_{T} where muons may only reach the inner layer of the muon chamber and in regions of limited detector acceptance. Stand-Alone muons extend coverage beyond the coverage of the ID. Calorimeter-Tagged muons can be used to recover acceptance at $|\eta| < 0.1$; nevertheless they suffer large fake rates from jets and electrons.

There are two parallel muon reconstruction chains in use in ATLAS, MUID and STACO [40]. Each uses slightly different track finding algorithms, and approach the combination of ID and MS tracks in different ways. MUID performs a global refit of hits in the MS and the ID, whereas STACO makes a statistical combination of the two track measurements, weighting the relative contributions according to their covariance matrices. The two chains are found to give similar performance. In this thesis all use muons are reconstructed with the STACO chain, so this chain is described in detail here.

The STACO algorithm uses the track parameters and covariance matrices of the ID and MS tracks to find a combined ID MS track with the smallest χ^2. For muons with $p_{\mathrm{T}} \lesssim 40\,\mathrm{GeV}$, the ID track is more precise because the solenoid field is strong enough to significantly bend the track, and because there is little material causing energy loss. In the high momentum $p_{\mathrm{T}} \gtrsim 100\,\mathrm{GeV}$ regime, the calorimeter energy loss is small in relation to the p_{T} of the muon, and the MS track has a higher resolution because of the long MS lever arm. Thus, the STACO CB track relies on the ID in the low p_{T} regime, on the MS in the high p_{T} regime, and on both ID and MS in the intermediate p_{T} regime.

The Muon Spectrometer tracks used by the STACO CB algorithm are reconstructed with the MUONBOY algorithm. The MUONBOY algorithm is based on combining track segments found in at least two of the three MS stations. The direction of a segment with respect to the interaction point (IP) is used to estimate its momentum, and to search for segments in nearby MS layers. At the end of the segment search, tracks are refit by using their individual hits. Finally, the MS track parameters are extrapolated to the IP, taking into account the magnetic field as well as the energy lost in the material.

Several additional selections are applied to the ID track used by the STACO CB algorithm in order to reduce fake rates and improve resolution.

Muon Reconstruction Efficiencies

In Figure 3.7 the observed reconstruction efficiency for muons reconstructed as either Combined or Segment-Tagged in the 2011 data is shown: it is measured using a tag and probe technique on Z boson decays [39], as well as the efficiency predicted by the Monte Carlo simulation. The efficiency is seen to drop significantly for $|\eta| < 0.1$. The efficiency for calorimeter tagged muons is also shown, and it is seen that they effectively suffer the loss in efficiency at $|\eta| < 0.1$. The muon reconstruction efficiency is seen to be almost constant as a function of p_{T}. In both p_{T} and η good agreement is seen between the Monte Carlo simulation and the data, but as with the electrons, scale-factors are applied to the Monte Carlo to reproduce the efficiency observed in data. The muon charge mis-identification rate is negligible.

Muon Momentum Resolution

In the Muon Spectrometrum the muon momentum resolution can be parameterised as:

$$\frac{\sigma_p}{p} = \frac{p_0^{\mathrm{MS}}}{p_{\mathrm{T}}} \oplus p_1^{\mathrm{MS}} \oplus p_2^{\mathrm{MS}} \cdot p_{\mathrm{T}} \tag{3.2}$$

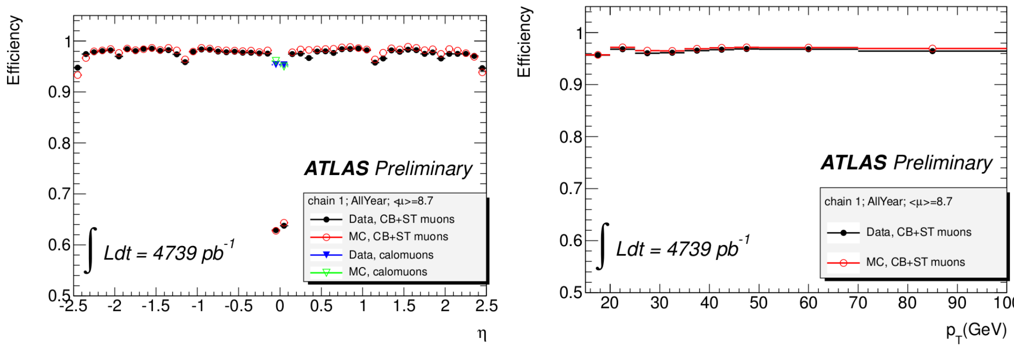

(a) (b)

Figure 3.7: Muon reconstruction efficiency in 2011 as a function of (a) the pseudorapidity and (b) the transverse momentum of the muon for muons reconstructed as either Combined or Segment-Tagged using the STACO algorithm. The solid black points show the efficiency observed in data, and the open red circles show the efficiency predicted by Monte Carlo simulation. In figure (a) the efficiencies for calorimeter tagged muons are also shown for $|\eta| < 0.1$ (solid blue triangles for data and open green triangles for Monte Carlo). Figures from [41].

where p_0^{MS}, p_1^{MS}, and p_2^{MS} are coefficients related to the energy loss in the calorimeters, multiple scattering and intrinsic resolution, respectively.
For the ID, the momentum resolution depends on the track length measured in the active elements: this resolution is reduced at the edges of the detector, where particles will not traverse all layers of the TRT. The ID muon momentum resolution can be parameterised as:

$$\frac{\sigma_p}{p} = \begin{cases} p_1^{\mathrm{ID}} \oplus p_2^{\mathrm{ID}} \cdot p_{\mathrm{T}}\,, & \text{for } \eta < 1.9\,, \\ p_1^{\mathrm{ID}} \oplus p_2^{\mathrm{ID}} \cdot p_{\mathrm{T}} \cdot \frac{1}{\tan^2\theta}\,, & \text{for } \eta > 1.9\,. \end{cases} \tag{3.3}$$

The muon momentum resolution is measured in data using $Z \to \mu\mu$ decays. The width of the reconstructed di-muon invariant mass peak at the Z pole is fitted to a convolution of a Breit-Wigner modelling the natural width of the Z boson, and a Gaussian modelling the muon momentum measurement resolution. The distributions measured in the ID and the MS are fitted independently to obtain separate measurements of the di-muon mass resolution in the two sub-detectors. An iterative fitting procedure is then carried out to obtain the parameters p_2^{ID}, p_1^{MS} and p_2^{MS}. For various momentum resolution values a series of simulated di-muon mass distributions are produced and matched to the one observed in data. The difference between the independent momentum measurements in the ID and MS is included in the fit.

3.2.5 Jet reconstruction and identification

Partons produced in particle interactions are not physically observable. They hadronise and produce a collimated shower of particles known as a jet. To reconstruct the jet, it is necessary to specify an algorithm to associate multiple energy deposits in the calorimeters to a single jet (clustering) and a recombination scheme to combine their four-momentum.

Jet algorithms need to be theoretically in agreement with respect to QCD divergences. Additionally, it must give the same physics results regardless of partons or particles from Monte Carlo simulation or calorimeter clusters.
There are two main classes of jet clustering algorithm: cone algorithms and successive combination algorithms. Cone algorithms start from seed objects and add in all other objects within a cone of a specified size in ΔR, where $\Delta R = \sqrt{\Delta\eta^2 + \Delta\phi^2}$. They are generally theoretically unsafe as soft or collinear emissions can affect the choice of seeds. Successive combination algorithms iteratively merge pairs of objects according to a definition of distance that generally involves the distance between the objects and their transverse momentum.

In ATLAS, the default jet clustering algorithm is a successive combination algorithm called anti-k_t (Figure 3.8) [42]. This combines objects according to the distance parameters $d_{i,j} = \min(p_{\mathrm{T},i}^{-2}, p_{\mathrm{T},j}^{-2}) \cdot \frac{\Delta R}{R}$ and $d_{i,\mathrm{beam}} = p_{\mathrm{T},i}^{-2}$ where $p_{\mathrm{T},i}$ is the transverse momentum of object i and ΔR is the distance between objects i, j in η, ϕ as defined above. The parameter R is analagous to the cone size in a cone based jet algorithm, and controls the size of the jet.

The four-momentum of the jet is obtained simply by summing the four-momentua of the constituent objects. This scheme conserves energy and momentum, and allows a meaningful definition for the jet mass.

The ATLAS hadronic calorimeters are non-compensating, so do not compensate for the different energy response of electromagnetically interacting particles and hadronically interacting particles, and do not account for energy lost from the hadronic shower (due to production of secondary particles or due to leakage of the shower out of the calorimeter). An important aspect of jet mesurements therefore is the calibration of the hadronic calorimeter response. First, the topological clusters are corrected to the EM scale, correcting their energy such that the response to purely electromagnetic showers would be correct.

The Jet Energy Scale (JES) correction is applied to jets constructed from the EM scale clusters in order to correct for the non compensating nature of the calorimeters, and also corrects for the leakage outside of the calorimeters, the effects of dead material and energy lost due to particles being deflected by the magnetic fields out of the jet.

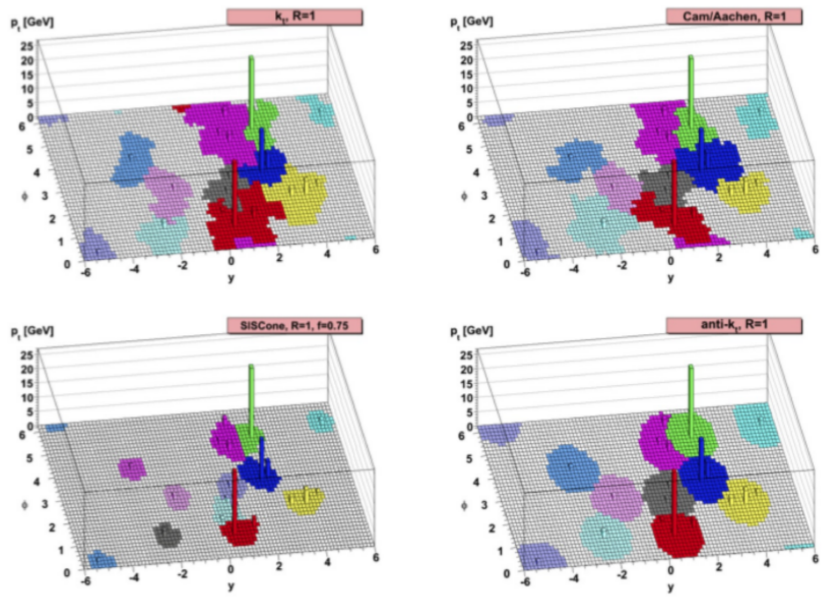

Figure 3.8: Jet reconstruction using four different algorithms. Anti-k_T algorithms is figured on bottom right.

b-tagging

To identify jets coming from b quarks, b-tagging is performed. b-jets can be identified through their characteristic features:

- the hadron with b quark has long lifetime ($\tau \approx 1.6\,\text{ps}$). It decays by weak interaction and is produced by b hadronization: accordingly, there will be a clear secondary vertex (with a separation $L = 1.8\,\text{mm}$ from the primary vertex at $p_\text{T} \approx 20\,\text{GeV}$);
- high molteplicity of charged tracks;
- decay particle at high p_T;

The b-jets can be identified using different algorythms. An important method makes use of the impact parameter (IP), and the secondary vertex reconstruction. The impact parameter of a track rapresents transverse distance to the primary vertex track. Thus primary vertex position is essential in b-tagging to measure the impact parameter. Another important point is the choice of the primary vertex, that is not trivial when there's pile-up. The current algorythms of b-tagging in ATLAS is called MV1(Muotivariate Tagger) based on a neural network.

3.2.6 Missing Transverse Energy

The missing transverse energy ($E_{\mathrm{T}}^{\mathrm{miss}}$) is the momentum which was not reconstructed in the transverse plane by detector elements. It'ss a very useful quantity, assuming that any imbalance observed in the transverse plane must be caused by an unobserved object, such as a miss more exotic particle or a simple neutrino. However, $E_{\mathrm{T}}^{\mathrm{miss}}$ can also be the result of mismeasured objects or "gaps" in the detector. Its reconstruction requires good knowledge of all objects considered for the vectorial sum.

The $E_{\mathrm{T}}^{\mathrm{miss}}$ algorithm [43] makes use of jets and electrons to take advantage of their precise calibration. Itcan thus be defined as:

$$E_{\mathrm{T}}^{\vec{\mathrm{miss}}} = -\sum_{electrons} E_{\mathrm{T}}^{\vec{e}} - \sum_{muons} p_{\mathrm{T}}^{\vec{\mu}} - \sum_{jets} p_{\mathrm{T}}^{\vec{jet}} - \sum_{clusters} E_{\mathrm{T}}^{\vec{cluster}} \tag{3.4}$$

3.3 ATLAS computing model

As seen in Section 3.1, the trigger output rate is $\sim 400\,\mathrm{Hz}$, as the output data dimension is $\sim 1.6\,\mathrm{MB}$ for event. Hence, in one year at the highest luminosity, the recorded data will be $10^{15}\,\mathrm{B}$ (1 PB). For this reason, sure computing system and more efficient software tools are been designed to handle a huge quantity of data: in the analysis and storage of data the LHC Grid plays an important role. ATLAS offline software provides a serious of tools for data analysis and store data in different formats, from raw data to "new data" (ready for analysis).

RAW Data [44] are events as output by the Event Filter (EF, the final stage of the HLT) for object reconstruction. Events arrive from the Event Filter in "byte-stream" format, reflecting the format in which data are delivered from the detector, rather than in any object-oriented representation. Each file will contain events belonging to a single run (corresponding to a prolonged period of data taking using the same trigger selections on the same fill in the accelerator), but the eve.

After the reconstraction process, event data are written as nor Event Summary Data (ESD). ESD is intermediate in size between RAW and Analysis Object Data. Its content is intended to make access to RAW data unnecessary for most physics applications other than for some calibration, reconstruction or identification. ESD has an object-oriented representation, and is stored in POOL [1] ROOT [2] files.

[1]POOL is the acronym of *Pool Of persistent Object for LHC*. It's a framework to store data and every member of ATLAS Collaboration have access to it via Grid.

[2]ROOT is an object-oriented framework aimed at solving the data analysis challenges of high-energy physics.

Item	Unit	Value
Raw Data Size	MB	1.6
ESD Size	MB	0.5
AOD Size	kB	100
TAG Size	kB	1
Simulated Data Size	MB	2.0
Simulated ESD Size	MB	0.5
Time for Reconstruction (1 ev)	kSI2k-sec	15
Time for Simulation (1 ev)	kSI2k-sec	100
Time for Analysis (1 ev)	kSI2k-sec	0.5
Event rate after EF	Hz	200
Operation time	seconds/day	50000
Operation time	days/year	200
Operation time (2007)	days/year	50
Event statistics	events/day	10^7
Eventi statistics (from 2008 onwards)	events/day	2×10^9

Table 3.2: The assumed event data sizes for various formats, the corresponding processing times and related operational parameters [44].

Analysis Object Data (AOD) is a reduced event representation, derived from ESD, suitable for analysis. It contains physics objects and other elements of analysis interest. It has an object-oriented representation, and is stored in POOL ROOT files.
For thumbnail information about events Tag Data (TAG) is used: it is an event-level metadata, stored in a relational database to facilitate queries for event selection,

An outline of the data flux is shown in Figure 3.9. As you can see in Table 3.2, format dimension decrease step by step. Nonetheless, the size of event data to be stored and the computational power to process them are huge too, on the order of TFlops [3]. For this reason, Atlas adopts a computational model distributed in all countries of the Collaboration, based on Grid.

Then AOD data is converted in DPD data. Derived Physics Data (DPD) is an n-tuple-style representation of event data for end-user analysis and histogramming. The inclusion of DPD in the Computing Model is an acknowledgment of the common practice by physicists of building subsamples

[3]The Flops (*Floating Point Operation Per Seconds*) is a measure of computer performance, especially in fields of scientific calculations that make heavy use of floating-point calculations. It's used to represent real number like digit or bit.

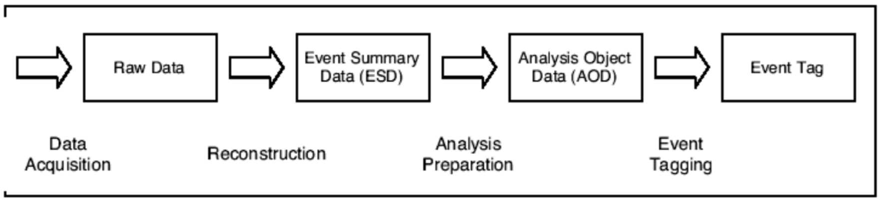

Figure 3.9: Data Flux diagram in ATLAS.

in a format suitable for direct analysis and display by means of standard analysis tools (PAW, ROOT, JAS etc.).

3.3.1 ATHENA framework: the ATLAS software

The requirement of a general software, simply modificable during twenty years (ATLAS expeiment lifetime), induced ATLAS Collaboration to adopt an object-oriented methodology, based on C++ language (also FORTRAN and Java). A framework like ATHENA allows to support different configuration file, reach an high level of programming abstraction.

The Athena framework [44] is an enhanced version of the Gaudi framework that was originally developed by the LHCb experiment, but is now a common ATLAS–LHCb project and is in use by several other experiments including GLAST and HARP. Athena and Gaudi are concrete realizations of a component-based architecture (also called Gaudi) which was designed for a wide range of physics data-processing applications. The fact that it is component-based has allowed flexibility in developing both a range of shared components and, where appropriate, components that are specific to the particular experiment and better meet its particular requirements.
Major design principles that influenced the development of Athena were:

- Abstract interfaces: these allow for the provision of different implementation providing similar functionality but optimized for particular environments (*e.g.* high-level trigger and offline, different persistency technologies). They also allow for easy manipulation of groups of components sharing a common interface.

- A clear separation between data and algorithms: this approach facilities, for example, the transparent change at run time of a specific algorythm without having to recompile or to reconfigure, making the framework very flexible.

- different lifetimes for many types of data [4].
- A clear separation between persistent and transient data: in general the algorithmic code operating on the data should be independent of the technology used to store it.

The ATHENA architecture is based on many "components", or else interacting softwares. The **Application Manager** is the overall driving intelligence that manages and coordinates the activity of all other components within the application. The major components that have been identified within the architecture are shown in Figure 3.10. Major components are:

- Algorithms, that share a common interface and provide the basic per-event processing capability of the framework. Each Algorithm performs a well-defined but configurable operation on some input data, in many cases producing some output data.
- Sequencer, that is a sequence of Algorithms, each of which might itself be another Sequencer, allowing for a tree structure of processing elements.
- Tools, that is similar to an Algorithm in that it operates on input data and can generate output data, but differs in that it can be executed multiple times per event.
- Transient Data Stores. The data objects accessed by Algorithms are organized in various transient data stores depending on their characteristics and lifetimes.
- Services, that provides services needed by the Algorithms.
- Converters. These are responsible for converting data from one representation to another.
- Properties. All components of the architecture can have adjustable properties that modify the operation of the component.

3.3.2 The ATLAS Virtual Organization and Grid

To analyse the huge volume of data produced at the LHC is a difficult task. It became immediatily clear that the required computing power to deal with the huge amount of data produced by the experiments was far over the

[4] For example, statistical data accumulated in histograms is long-lived compared to the data of an individual event.

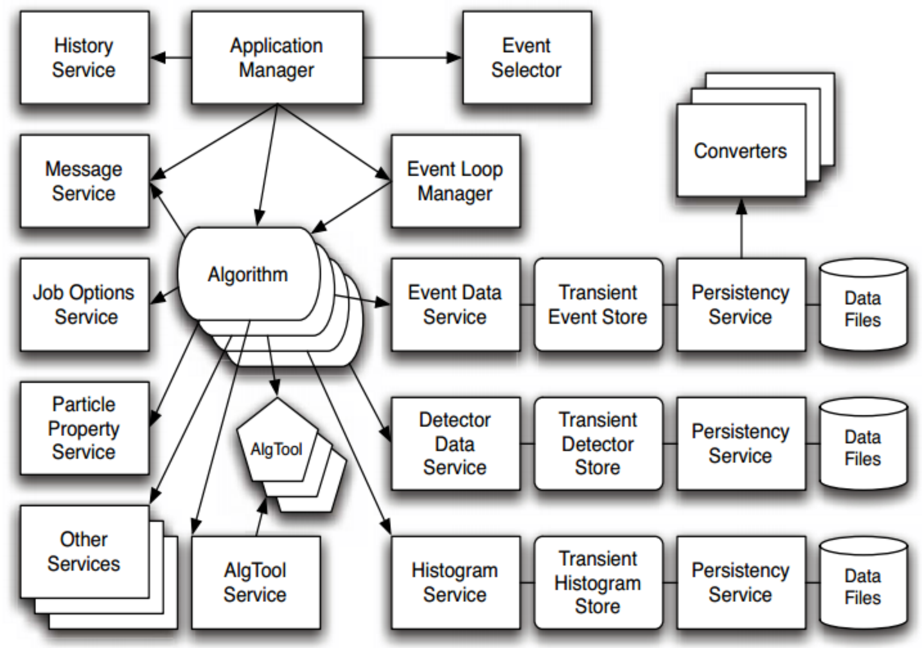

Figure 3.10: Athena Component Model: component instances and their relationships in terms of navigability and usage are shown.

capacity available at CERN. In 1999 the idea of a computing system extended worldwide to combine resources from all the participating institutes began to emerge: the "LHC Computing Grid" aim was to link Grid infrastructures and computer centers to distribute, store and analyze LHC data.

This approach rapidly evolved and today the *Worldwide LHC Computing Grid* (WLCG) combines massive multi-petabyte storage systems, and computing clusters with thousands of nodes connected by high-speed networks, from over 170 sites in 34 countries [45]. This distributed, Grid-based, infrastructure provides real-time access to LHC data and the power to process it, to more than 8000 physicists around the world, equally and regardless of their physical location.

All members of the ATLAS Collaboration are authorized to become members of the ATLAS Virtual Organization (VO), and therefore are allowed to submit jobs and gain access to Grid resources

The WLCG is spread worldwide (intentionally, for funding and sociological reasons) and is managed and operated by a collaboration between the experiments and the participating computer centers. It is now the world's largest computing Grid and provides all the production and analysis environments for the LHC experiments. Its layout is based on the two main global Grids currently in operation, the European Grid Infrastructure (EGI) in Europe and the Open Science Grid (OSG) in the United States. Other associated regional and national Grids are organized in four layers or Tiers across the world: Tier 0, Tier 1, Tier 2 and Tier 3, as shown in Figure 3.11.

Tier-0
It is the CERN Computer Centre. All data from the LHC passes through this meaning hub, but it provides less than 20% of the total computing capacity. CERN is responsible for the safe-keeping of the RAW data (first copy), first pass reconstruction, distribution of raw data and reconstruction output to the Tier-1s, and reprocessing of data during LHC down-times.

Tier-1
These are eleven large computer centres, responsible for the safe-keeping of a proportional share of RAW and reconstructed data, large-scale reprocessing and safe-keeping of corresponding output, distribution of data to Tier-2s and safe-keeping of simulated data.

Tier-2
The Tier-2s are typically scientific institutes or universities, which can provide adequate computing power for specific analysis tasks and store sufficient data. They handle analysis requirements and proportional share of simulated event production and reconstruction. There are currently around 140 Tier-2 sites covering most of the globe.

Tier-3
Though they are not officially part of the WLCG, Tier-3s are de-facto part of the computing model. They are widely used by physicists to run their own analyses and to access WLCG data. They consists in local computing resources, which are mainly small clusters in university departments research institutes. There is no formal bond between WLCG and Tier-3 resources.

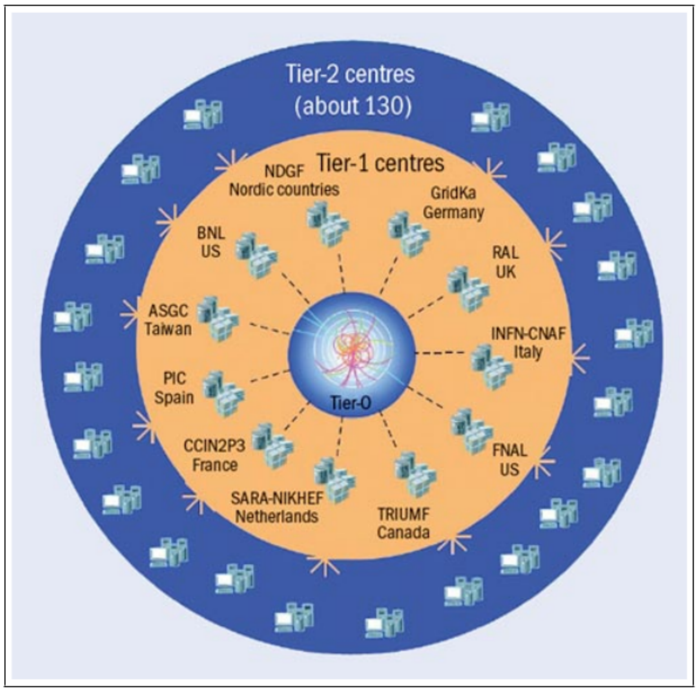

Figure 3.11: WLCG Tier structure.

Chapter 4

Higgs boson properties in $H \to ZZ^{(*)} \to 4\ell$ channel

On 4 July 2012, the ATLAS and CMS experiments announced the discovery of a new boson at $\sim 125\,\text{GeV}$, consistent with the Standard Model Higgs boson. A large number of measurements like mass, width, spin-parity (spin-CP), cross-section, couplings, branching ratios of the the new particle are now fundamental to reveal its nature and to answer the question if it is or not the Higgs boson predicted by the Standard Model.

The main subject of this thesis has been the study of the spin-parity properties of the new boson analyzing the $H \to ZZ^{(*)} \to 4\ell$ decay channel. The $H \to ZZ^{(*)} \to 4\ell$ channel, where $\ell = e$ or μ, is called "Golden channel" because of its clear signature giving an high potential of discovery. The complete reconstructed final state and its characteristics furnish a powerful tool in the measurement of all the Higgs parameters, in particular the spin-parity. The spin-parity properties influence the kinematics of the decay, therefore it's possible to extract these informations taking advantage of the reconstructed distributions of some sensible observables described in details in the next Sections.

In this thesis I used an approach based on a matrix element multivariate per-event likelihood to investigate on the spin-parity properties of the Higgs-like boson. This method, largely used in literature [47, 48], uses sensible variables to build a discriminant to discern between two different spin hypotheses. The hypotheses are tested in pair and the log-likelihood ratio is used as statistic test. After all a confidence level of exclusion is given.

A possible improvement to this study will be an estimation of the coupling parameters actually not achievable with a reasonable precision with the data recorded in ATLAS up to now ($\sim 25\,\text{fb}^{-1}$ with 43 events in the mass range used) because of the low statistics.

In this Chapter the properties of $H \to ZZ^{(*)} \to 4\ell$ are described. A theorical description of the decay amplitude in different spin-parity hypothesis is given, together with a description of the event selection and the mass measurement. Finally this Chapter provides a detailed description of my work, in particular using the MELA method. The latest update on the optimization of this analysis I developed is also presented.

4.1 The Golden channel and its Spin-parity properties

The search for the SM Higgs boson through the decay $H \to ZZ^{(*)} \to 4\ell$ provides good sensitivity over a wide mass range. At the LHC the main production mechanisms for this channel are the gluon-gluon fusion and the VBF production (see Section 4.2.2).

After the discovery of an Higgs-like boson this channel is exploited for the measure of its properties and in particular this thesis is dedicated to the spin-parity measurement. The four leptons final states permit a full reconstruction of leptons characteristics themselves and also of the two Z bosons in which the Higgs boson decays.

Four distinct final states, $\mu^+\mu^-\mu^+\mu^-$ (4μ), $\mu^+\mu^-e^+e^-$ ($2\mu 2e$), $e^+e^-\mu^+\mu^-$ ($2e2\mu$), and $e^+e^-e^+e^-$ ($4e$), are selected. The $2\mu 2e$ and $2e2\mu$ modes differ by the flavor of the lepton pair having a reconstructed invariant mass closest to the Z mass. The largest background in this search comes from continuum ($Z^{(*)}/\gamma^*$) production which includes the single resonance $Z \to 4\ell$. For four-lepton masses below 160 GeV, there are also important background contributions from $Z{+}jets$ and $t\bar{t}$ candidates arise either from decays of hadrons with b- or c-quark content, from photon conversions or from mis-identification of jets. The estimation of the background is always a delicate task but in particular for this kind of studies.

A SM Higgs boson is predicted to have spin zero and an even parity. However, the possibility of existence of Higgs look-alike with higher spins (e.g. 1 or 2) can't be excluded a priori.Furthermore some of the Beyond Standard Model (BSM) theories hypothesize also the CP mixing. Recent observation of the $\gamma\gamma$ decay disfavours the possibility of spin-1 (and odd C-parity) according to the Landau-Yang theorem.

In this thesis spins 0, 1 and 2 have been studied analyzing some suitable observables (*e.g.* decay and production angles).

4.2 Modelling spin and parity states

Taking into account all the different spin-parity hypotheses for the Higgs boson, in this analysis only spin 0, 1, and 2 have been considered and in particular J^{CP} equal to 0^+, 0^-, 1^+, 1^-, 2^+_m, 2^-. The spin-2 resonances are largely model-dependent, in this study the most popular ones have been used. in the next Sections details on these models will be given. For a spin-2 Higgs-like resonance, purely qq or gg produced states and some admixtures of the two are studied.

4.2.1 Scattering Amplitudes

To describe the decay process of a Higgs-like particle one of the first step is to write the most general scattering amplitude [49]. Because the aim of this thesis is the measurement of the spin-parity properties the scattering amplitude for the considered spin have been studied.

Spin-0

For a spin-0 Higgs-like resonance that decays in two bosons the most general theoretical scattering amplitude is:

$$A(X \to V_1V_2) = v^{-1}[g_1 M_V^2 \varepsilon_1^* \varepsilon_2^* + g_2 f^{*(1)}_{\mu\nu} f^{*(2)\mu\nu} + g_3 f^{*(1)\mu\nu} f^{*(2)}_{\mu\alpha} \frac{q_\nu q^\alpha}{\Lambda^2} + g_4 f^{*(1)}_{\mu\nu} \tilde{f}^{*(2)\mu\nu}]. \tag{4.1}$$

X represents the Higgs–like resonance, $V_{1,2}$ the two Z bosons, and the $g_{1,\ldots,4}$ are the effective coupling constants. The $f^{*(i)\mu\nu}$ denote the field strenght tensor of a gauge boson with momentum q_i. The scale at which physics beyond the Standard Model apperas is described by the constant Λ. A SM Higgs is expected to have $g_1 = 1$ and all other coupling constantes $g_{i\neq 1} = 0$. A pseudo–scalar Higgs would have $g_4 \neq 1$ (see Table 4.1).

Spin-1

For a spin-1 Higgs-like resonance the general amplitude can be written as:

$$A(X \to V_1V_2) = g_1[(\varepsilon_1^* q)(\varepsilon_2^* \varepsilon_X) + (\varepsilon_2^* q)(\varepsilon_1^* \varepsilon_X)] + g_2 \varepsilon_{\alpha\mu\nu\beta} \varepsilon_X^\alpha \varepsilon_1^{*\mu} \varepsilon_2^{*\nu} \tilde{q}^\beta. \tag{4.2}$$

where g_i are the coupling constants, $g_1 \neq 0$ corresponds to a vector resonance, $g_2 \neq 0$ to a pseudo-vector one, assuming parity conserving interactions, and ϵ_X is the polarization vector of the resonance X. Even if the presence of a Higgs-like renonance in the $\gamma\gamma$ decay channel rejects the spin-1 hypothesis, this model is still interesting in order to study the presence of different resonances with different helicities and couplings in this low mass region.

Spin-2

The most general amplitude of the decay of a spin-2 particle has 10 coupling constants $g_{1..10}$ and they can be in general complex numbers:

$$\begin{aligned}
&A(X \to V_1 V_2) = \Lambda^{-1} \Big[2g_1 X_{\mu\nu} f^{*(1)\mu\alpha} f^{*(2)\nu}_{\alpha} \\
&+2g_2 X_{\mu\nu} \frac{q_\alpha q_\beta}{\Lambda^2} f^{*(1)\mu\alpha} f^{*(2)\nu\beta} + g_3 \frac{\tilde{q}^\beta \tilde{q}^\alpha}{\Lambda^2} X_{\beta\nu} \left(f^{*(1)\mu\nu} f^{*(2)}_{\mu\alpha} + f^{*(2)\mu\nu} f^{*(1)}_{\mu\alpha} \right) \\
&+g_4 \frac{\tilde{q}^\mu \tilde{q}^\nu}{\Lambda^2} X_{\mu\nu} f^{*(1)\alpha\beta} f^{*(2)}_{\alpha\beta} \\
&+m_V^2 X_{\mu\nu} \left(2g_5 \epsilon_1^{*\mu} \epsilon_2^{*\nu} + 2g_6 \frac{\tilde{q}^\mu q_\alpha}{\Lambda^2} \left(\epsilon_1^{*\nu} \epsilon_2^{*\alpha} - \epsilon_1^{*\alpha} \epsilon_2^{*\nu} \right) + g_7 \frac{\tilde{q}^\mu \tilde{q}^\nu}{\Lambda^2} (\epsilon_1^* \epsilon_2^*) \right) \\
&+g_8 \frac{\tilde{q}^\mu \tilde{q}^\nu}{\Lambda^2} X_{\mu\nu} f^{*(1)\alpha\beta} \tilde{f}^{*(2)}_{\alpha\beta} \\
&+m_V^2 X_{\mu\alpha} \tilde{q}^\alpha \epsilon_{\mu\nu\rho\sigma} \left(g_9 \frac{q^\sigma}{\Lambda^2} \epsilon_1^{*\nu} \epsilon_2^{*\rho} + g_{10} \frac{q^\rho \tilde{q}^\sigma}{\Lambda^4} \left(\epsilon_1^{*\nu} (q\epsilon_2^*) + \epsilon_2^{*\nu} (q\epsilon_1^*) \right) \right) \Big] . \qquad (4.3)
\end{aligned}$$

q, q_1 and q_2 represent the 4-momenta of the X particle and of vector bosons and $\tilde{q} = q_1 - q_2$, m_V is the on-shell mass of gauge boson, v is the vacuum expectation value and ϵ_X is the polarization vector of X.

The coupling constants $g_{1..7}$ correspond to the decay of a 2^+ particle and $g_{8..10}$ to 2^- particle. Moreover both groups can contribute to the same amplitude and the CP-mixing is possible. The number of allowed spin-2 states is therefore very large, so it is not possible to study all of them. One can however try to exclude first the minimal models (for example 2^+_m), which corresponds to the lowest dimension operators.

The coupling parameters used in the analysis for each spin hypothesis tested are shown in Table 4.1. Both gg and $q\bar{q}$ production mechanisms have been studied, more details are provided in the next Section. This thesis shows also the most recent updates testing spin-2 models corresponding to the leading order of the higher dimension operators (usually noted as $2^\pm_h$); these models will be included in the next spin-parity official note.

4.2.2 Spin Admixtures: 2-states

The dominant production mechanism for a Higgs-like spin-0 particle in the studied mass range ($115 < m_{4\ell} < 130\,\mathrm{GeV}$) is the gluon-gluon (gg) fusion while the VBF and VH ($q\bar{q}$) have a much smaller production rate. In this spin-parity study only the gluon-gluon production mechanism have been considered. Moreover a spin-2 state can be produced both through gg fusion and through the s-channel $q\bar{q}$ fusion. The gg and $q\bar{q}$ production vertices have different tensor structure and in addition, the spectrum of the transverse momentum for the $q\bar{q}$ production is expected to be softer than for gg fusion.

J^P	Production configuration	Decay configuration	Comments
0^+	$gg \to X$:	$g_1 = 1$ $g_2 = g_3 = g_4 = 0$	Standard Model boson
0^-	$gg \to X$:	$g_4 = 1$ $g_1 = g_2 = g_3 = 0$	Pseudo-scalar boson
1^+	$q\bar{q} \to X$:	$g_1 = 0$ $g_2 = 1$	
1^-	$q\bar{q} \to X$:	$g_1 = 1$ $g_2 = 0$	
2^+_m	$gg \to X$: $g_1 = 1$	$g_1 = g_5 = 1$	Graviton-like tensor with minimal couplings
2^+_m	$q\bar{q} \to X$: $g_1 = 1$	$g_1 = g_5 = 1$	Graviton-like tensor with minimal couplings
2^+_h	$gg \to X$: $g_4 = 1$	$g_4 = 1$	Tensor with higher dimension operators
2^-	$gg \to X$: $g_1 = 1$	$g_8 = g_9 = 1$	"Pseudo-tensor"
2^-_h	$gg \to X$: $g_8 = 1$	$g_8 = 1$	"Pseudo-tensor"

Table 4.1: Coupling parameters for the spin-0, spin-1, spin-2 models considered in the analysis. For the $q\bar{q}$ channel the unique choice of coupling parameters was made across all the spin and parity states: $g_1 = 1$.

The relative fraction gg and $q\bar{q}$ production mechanisms for spin-2 bosons is currently unknown. To obtain a model-independent estimate, for further studies we will consider the following mixtures:

- 100% gg
- 75% gg 25% $q\bar{q}$
- 50% gg 50% $q\bar{q}$
- 25% gg 75% $q\bar{q}$
- 100% $q\bar{q}$

It is possible to create desired models by simply mixing events from the corresponding Monte Carlo datasets, because there's no interference in the production mechanism. The influence of the $q\bar{q}$ fraction on the separation with respect to the spin-0 hypothesis will be discussed.

4.3 Event selection and optimization

In this study the selection of the events mainly followed the one applied in the general $H \to ZZ^{(*)} \to 4\ell$ analysis (details can be found in [47]). In the next Subsections a description of the applied cuts and the MC samples used is given.

4.3.1 Signal and background simulation

A short description of the main event generators, used for simulating Monte Carlo (MC) samples in this analysis, is presented.

The MC signal samples for the spin and parity states discussed above were produced using the JHU generator [**?**]: JHU is a Leading Order (LO) generator used to simulate the decay of a SM Higgs boson with a mass of 125 GeV for the different spin-parity hypotheses in both the conditions of $\sqrt{s} = 7$ TeV and $\sqrt{s} = 8$ TeV. The Pythia MC generator is employed for the parton showers, using the parton density functions. Validation studies of the JHU Monte Carlo samples have been performed.

While the mis-modelling of the transverse momenta by the JHU generator does not directly affect the spin-dependent observables, it might have an impact on the event selection. In order to correct for this effect, a weight is applied to the JHU gg samples using as a reference the SM Higgs p_T distribution obtained with the POWHEG generator. Studies have shown that this procedure does not affect the expected separations between different spin-parity states [47].

No re-weighting procedure is applied to the $q\bar{q}$ p_T spectrum in this analysis. The systematic uncertainties are evaluated in the same way as for the gg spectrum.

Background simulation

The irreducible $ZZ^{(*)}$ background has been taken from POWHEG and is affected by a $\pm 5\%$ due to the QCD scale uncertainty. The production of a Z boson associated with jets is simulated using ALPGEN and it accounts for two different sources: Z+light jets and $Z+b\bar{b}$: in these samples the Drell-Yan contribution is included too. The production of $t\bar{t}$ pairs is modeled using MC@NLO. The simulation applied on the generated events is the ATLAS detector simulation, which is based on the GEANT4 framework.

4.3.2 Data samples

In this thesis all the results are obtained using data corresponding to integrated luminosities of 4.6 fb^{-1} at $\sqrt{s} = 7$ TeV and 20.7 fb^{-1} at $\sqrt{s} = 8$ TeV recorded with the ATLAS detector at the LHC, respectively during the full data taking periods in the 2011 and 2012.

4.3.3 Preselection: lepton identification and trigger selection

The events considered in this analysis are selected using single-lepton or di-lepton triggers. The single-muon trigger threshold is set to $p_{\mathrm{T}} = 24\,\mathrm{GeV}$ ($p_{\mathrm{T}} = 18\,\mathrm{GeV}$), while the single-electron trigger threshold is set to $E_{\mathrm{T}} = 25\,\mathrm{GeV}$ ($E_{\mathrm{T}} = 20 - 22\,\mathrm{GeV}$) for the 2012 (2011). For the di-muon triggers there are two thresholds: one symmetric requiring two muons firing $p_{\mathrm{T}} = 13\,\mathrm{GeV}$ and one asymmetric that require one muon firing $p_{\mathrm{T1}} = 18\,\mathrm{GeV}$ and one firing $p_{\mathrm{T2}} = 8\,\mathrm{GeV}$. For the di-electron triggers the thresholds are $E_{\mathrm{T}} = 12\,\mathrm{GeV}$ for both electrons. Finally, there are two electron-muon triggers with 12 or 24 GeV E_{T} electron thresholds, differing in their electron identification requirements, and an 8 GeV p_{T} muon threshold. The efficiency for events passing the offline selection to be selected by at least one of the above triggers is greater than 97% for events with muons and around 100% for four electron events. More detail could be found in the official note [47].

As said in the previous Chapter, electron candidates consist of clusters of energy deposited in the electromagnetic calorimeter associated with ID tracks [47].

Muon candidates are formed by matching reconstructed ID tracks with either complete or partial tracks reconstructed in the MS (combined muons and segment-tagged muons respectively, see Section 3.2.4). If a complete track is present, the two independent momentum measurements are combined; otherwise the momentum is measured using the ID. The muon reconstruction and identification coverage is extended by using tracks reconstructed in the forward region ($2.5 < |\eta| < 2.7$) of the MS, which is outside the ID coverage. In the centre of the barrel region ($|\eta| < 0.1$), which lacks MS geometrical coverage, ID tracks with $p_{\mathrm{T}} > 15\,\mathrm{GeV}$ are identified as muons if their calorimetric energy deposits are consistent with a minimum ionising particle. Only one muon per event is allowed which is reconstructed only in the MS or identified with the calorimeter.

4.3.4 Kinematic selection

This analysis searches for Higgs boson candidates by selecting two same-flavour, opposite-sign lepton pairs (a lepton quadruplet) in an event. The impact parameter of each lepton along the beam axis is required to be within 10 mm of the reconstructed primary vertex. To reject cosmic rays, muons with an ID track are required to have a transverse impact parameter, defined as the impact parameter in the bending plane with respect to the primary vertex, of less than 1 mm. The primary vertex is defined as the reconstructed vertex with the highest $\sum p_{\mathrm{T}}^2$ of associated tracks among the reconstructed vertices with at least three associated tracks. Each electron (muon) must satisfy $E_{\mathrm{T}} > 7\,\mathrm{GeV}$ ($p_{\mathrm{T}} > 6\,\mathrm{GeV}$) and be measured in the pseudo-rapidity range $|\eta| < 2.47$ ($|\eta| < 2.7$). The highest p_{T} lepton in the quadruplet must satisfy $p_{\mathrm{T}} > 20\,\mathrm{GeV}$, and the second (third) lepton in p_{T} order must satisfy $p_{\mathrm{T}} > 15\,\mathrm{GeV}$ ($p_{\mathrm{T}} > 10\,\mathrm{GeV}$). The leptons are required to be separated from each other by $\Delta R > 0.1$ if they are of the same flavour and $\Delta R > 0.2$ otherwise, with ΔR defined by $\Delta R = \sqrt{\Delta\eta^2 + \Delta\phi^2}$. Each event is required to have the triggering lepton(s) correctly matched to one or two of the selected leptons.

Multiple quadruplets within a single event are possible: for four muons or electrons there are two ways to pair the masses, and for five or more leptons there are multiple ways to choose the leptons. Only quadruplets with the same-flavour and opposite-sign lepton pair closest to the Z boson mass are kept. The pair with the mass closest to the Z boson mass is referred to as the leading di-lepton and its invariant mass, m_{12}, is required to be between 50 and 106 GeV. The remaining same-flavour, opposite-sign lepton pair is the sub-leading di-lepton and its invariant mass, m_{34}, is required to be in the range $m_{\mathrm{min}} < m_{34} < 115\,\mathrm{GeV}$, where m_{min} is 12 GeV for $m_{4\ell} < 140\,\mathrm{GeV}$ and rises linearly to 50 GeV at $m_{4\ell} = 190\,\mathrm{GeV}$ (see Table 4.2). For $m_{4\ell} > 190\,\mathrm{GeV}$ the m_{34} threshold is set to a constant values of 50 GeV. The Z boson corresponding to the leading (sub-leading) di-lepton pair is labelled Z_1 (Z_2). All possible same-flavour opposite-charge di-lepton combinations in the quadruplet must satisfy $m_{\ell\ell} > 5\,\mathrm{GeV}$ to remove events containing $J/\Psi \to \ell\ell$. The quadruplet with m_{12} closest to the Z PDG mass is selected. Then, the sub-leading di-lepton pair is formed using the remaining leptons. If two or more quadruplets satisfy the above selection, the one with the m_{34} value closest to the Z boson mass is selected. Four different analysis sub-channels: $4e$, $2e2\mu$, $2\mu2e$, 4μ, ordered by the flavour of the leading di-lepton are defined.

$m_{4\ell}$ (GeV)	≤ 140	160	165	180	≥ 190
threshold (GeV)	17.5	30	35	40	50

Table 4.2: Summary of thresholds applied to m_{34} for reference values of $m_{4\ell}$. For other $m_{4\ell}$ values, the selection requirement is obtained via linear interpolation.

4.3.5 Isolation and impact parameter significance cuts

The main backgrounds for the $H \to ZZ^{(*)} \to 4\ell$ channel are the reducible contributions from the Z+jets and $t\bar{t}$ and the irreducible contribution of the continuum ZZ. Cuts on the impact parameter and requirements on track and calorimeter isolation of the leptons lead to a reduction of the Z+jets and $t\bar{t}$ background.

The impact parameter significance, defined as the impact parameter divided by its uncertainty, $|d_0|/\sigma_{d_0}$, for all muons (electrons) is required to be lower than 3.5 (6.5). The normalised track isolation discriminant is defined as the sum of the transverse momenta of tracks, $\sum p_{\mathrm{T}}$, inside a cone of $\Delta R < 0.2$ around the lepton, excluding its track, divided by E_{T} for the electrons and p_{T} for the muons. Each lepton is required to have a normalised track isolation smaller than 0.15.

The normalised 2012 calorimetric isolation for electrons is computed as the sum of the positive-energy topological clusters in the electromagnetic and hadronic calorimeter with a reconstructed barycentre falling in a cone of $\Delta R < 0.2$ around the candidate electron cluster, divided by the electron E_{T} and the cut value is 0.2. In the case of muons, the normalised calorimetric isolation discriminant is defined as the sum of the calorimeter cells inside a cone of $\Delta R < 0.2$ around the muon direction, divided by the muon p_{T}. Muons are required to have a normalised calorimetric isolation less than 0.3 (0.15 in case of Stand-Alone muons).

4.3.6 Mass constraint

The final discriminating variable for this search is the four lepton invariant mass, $m_{4\ell}$. To improve the resolution on the mass measurement a correction on the momenta of the muons in the leading pair for the final state radiation (FSR) is applied. Adding the photon energies to the momenta of the Z boson candidates when needed narrows the peak in the invariant mass and it permit a reduction of the tails to lower mass values. An other way to improve the invariant mass resolution is applying a mass constraint to the leading di-lepton for $m_{4\ell} < 190\,\mathrm{GeV}$ and to both di-leptons for higher masses. The Z line-shape and the experimental uncertainty in the di-lepton mass are accounted for in the Z-mass constraint. The width of the reconstructed Higgs boson mass distribution is dominated by the experimental resolution for $m_H < 350\,\mathrm{GeV}$, while for higher m_H the reconstructed width is dominated by the natural width of the Higgs boson. The predicted natural width of the Higgs boson is approximately $4\,\mathrm{MeV}$ ($29\,\mathrm{GeV}$) at $m_H = 125(400)\mathrm{GeV}$.

Shown in Table 4.3 are the selection efficiencies for different spin and parity states generated at $\sqrt{s} = 8$ TeV after each selection, previously described.

Signal J^{PC}	Trigger selection	Kinematic cuts	m_{12} mass cut	m_{34} mass cut	all cuts
POWHEG 0^+	52.3%	11.53%	11.28%	10.21%	9.12%
JHU 0^+	53.0%	12.01%	11.72%	10.76%	9.29%
JHU 0^-	53.8%	11.03%	10.73%	10.33%	8.96%
JHU 1^+	45.2%	8.75%	8.61%	7.51%	6.81%
JHU 1^-	44.5%	8.24%	8.11%	6.56%	5.97%
JHU 2^+	52.2%	11.40%	11.16%	10.60%	9.16%
JHU 2^-	55.0%	12.48%	12.10%	10.67%	9.22%
JHU 2^+qq	46.5%	9.05%	8.86%	8.48%	7.46%
JHU 2^-qq	45.0%	7.90%	7.67%	6.87%	6.04%

Table 4.3: Selection efficiency for different spin and parity states generated at $\sqrt{s} = 8$ TeV with JHU MC generator compared to the POWHEG 0^+ in the 4μ channel.

4.3.7 Jet selection and event categorisation

To separately measure the cross sections for the ggF, VBF, and VH production mechanisms, each $H \to 4\ell$ candidate selected with the criteria described in the previous Chapter is assigned to one of three categories (VBF-like, VH-like, or ggF-like), depending on its characteristics. This selection is not used in this work of thesis: howover it is briefly described for the sake of completeness. The VBF-like category is defined by events with two high p_{T} jets widely separated in rapidity. Jets are reconstructed from topological clusters using an anti-kt algorithm. Events which do not satisfy the VBF-like criteria are considered for the VH-like category. Events are classified as VH-like if there is a lepton (e or μ), in addition to the four leptons forming the Higgs boson candidate, with $p_{\mathrm{T}} > 8$ GeV and more specific lepton requirements. Events which are not classified as VBF-like or VH-like are assigned to the ggF-like category.

4.4 Background estimation

One of the most delicate tasks in order to achieve Higgs discovery is a good estimation and control of the background contributions.

The level of the irreducible $ZZ^{(*)}$ background is estimated using MC simulation normalised to the theoretical cross section, while the rate and composition of the reducible Z+jets (or $\ell\ell$+jets because of $Z \to \ell\ell$) and $t\bar{t}$ background processes are evaluated with data-driven methods. The composition of the reducible backgrounds depends on the flavour of the sub-leading di-lepton pair and different approaches are taken for the $\ell\ell+\mu\mu$ and the $\ell\ell+ee$ final states.

$\ell\ell+\mu\mu$ reducible background

The $\ell\ell+\mu\mu$ reducible background arises from $t\bar{t}$ and Z+jets, where the Z+jets component has both a heavy quark $Zb\bar{b}$ part and another part from π/K in-flight decays. The number of background events from $t\bar{t}$ and Z+jets is estimated from two control regions: one with an enhanced $b\bar{b}$ contribution and π/K in-flight decays suppressed, and the other with the preference of both components.

$\ell\ell+ee$ reducible background

To estimate the $\ell\ell+ee$ background a cotrol region has been obtained by relaxing the electron selection criteria for the electrons of the sub-leading pair. In this case the events in the signal region are a subset of the events present in the $\ell\ell+ee$ control region. The $\ell\ell+ee$ background could be estimated using a control region with same-sign sub-leading di- electrons, and also by performing the full analysis but selecting same-sign pairs for the sub-leading di-electrons.

4.5 Systematic uncertainties

Detailed studies have been performed to estimate the systematic uncertainties. Here a short summary is reported.

The uncertainty on the muon identification and reconstruction efficiency results in an uncertainty on the yields for the signal and the dominant $ZZ^{(*)}$ background which is uniform over the mass range of interest, and amounts to $\pm 0.8\%$ and $\pm 0.4\%$ for the four muons and the mixed final states rispectively. The uncertainty on the electron identification and reconstruction efficiency results in an uncertainty on the yields for the signal of $\pm 9.4\%$, $\pm 8.7\%$ $\pm 2.4\%$ for the $4e$, $2\mu 2e$ and $2e2\mu$) final states rispectively at $m_{4\ell} = 125\,\mathrm{GeV}$.

The p_{T} re-weighting of the ggF process on the signal selection efficiency is added in the 2011 analysis only, but is not needed in the 2012 analysis because it is included in the event generation. This additional uncertainty is evaluated by varying the Higgs boson p_{T} spectrum in the gluon fusion process according to the PDF [1] and QCD scale uncertainties.

The background uncertainties on the data-driven methods depends on background contribution and channel decay. The overall uncertainty on the

[1]The PDF is the probability desity function, or density of a continuous random variable, is a function that describes the relative likelihood for this random variable to take on a given value.

integrated luminosity for the complete 2011 dataset is $\pm 1.8\%$ [50], while for the 2012 is $\pm 3.6\%$.

The impact of the electron energy scale uncertainty is determined from the $Z \to ee$ sample. This uncertainty is conservatively estimated to be less than $\pm 0.4\%(\pm 0.2\%)$ on the measured mass for the $4e(2e2\mu)$ channel, and is negligible for $2\mu 2e$ due to the low p_{T} of the electrons. Finally, mass-scale uncertainties related to final-state QED radiation modelling and to background contamination are also smaller than 0.1%. Similarly, the various components of the muon momentum measurement systematic uncertainty are determined using large samples of $J/\Psi \to \mu\mu$, $Y \to \mu\mu$, and $Z \to \mu\mu$ decays (more than 20 M J/Ψ decays have been collected in both 2011 and 2012). The uncertainty on the global mass scale coming from muons is estimated to be $\pm 0.2\%(\pm 0.1\%)$ for the $4\mu(2\mu 2e)$ channels.

4.6 Results of event selection

Results of the $H \to ZZ^{(*)} \to 4\ell$ channel played an important role in the discover of the Higgs in July 2012 and they have been obtained analysing the whole dataset of $4.6\,\mathrm{fb}^{-1}$ at $\sqrt{s} = 7\,\mathrm{TeV}$ for 2011 and $20.7\,\mathrm{fb}^{-1}$ at $\sqrt{s} = 8\,\mathrm{TeV}$ for 2012.

Table 4.4 exhibits the number of expected signal and background events for the irreducible and reducible background, as well as the signal-to-background ratio and the observed events inside a mass window of $125 \pm 5\,\mathrm{GeV}$.

32 events are observed, while around 27 events are expected both from background and signal at 125 GeV. In particular, from background alone, only 11 events are expected, which is significantly less than the observed 32. In Figure 4.1 the four-lepton invariant mass distribution of all channels is shown. A signal at approximately 125 GeV can clearly be seen.

4.6.1 Exclusion limits and p_0 value

Upper limits are set on the Higgs boson production cross section at 95% CL, using the $\mathrm{CL_S}$ modified frequentist formalism with the profile likelihood ratio test statistic [51]. The test statistic is evaluated using a maximum-likelihood fit of signal and background models to the observed $m_{4\ell}$ distribution. Figure 4.2 shows the observed and expected 95% CL cross section upper limits, as a function of m_H, for the combined $\sqrt{s} = 7\,\mathrm{TeV}$ and $\sqrt{s} = 8\,\mathrm{TeV}$ dataset.

The local p_0 value corresponding to the observed 32 events is shown in Figure 4.3 where the p_0 value is defined as the probability that fluctuations

	Signal	$ZZ^{(*)}$	$Z+\text{jets}$, $t\bar{t}$	S/B	Expected	Observed
			$\sqrt{s} = 7\,\text{TeV}$ and $\sqrt{s} = 8\,\text{TeV}$			
4μ	6.3±0.8	2.8±0.1	0.55±0.15	1.9	9.6±1.0	13
$2\mu 2e$	3.0±0.4	1.4±0.1	1.56±0.33	1.0	6.0±0.8	5
$2e2\mu$	4.0±0.5	2.1±0.1	0.55±0.17	1.5	6.6±0.8	8
$4e$	26±0.4	1.2±0.1	1.11±0.28	1.1	4.9±0.8	6
Total	15.9±2.1	7.6±0.4	3.74±0.93	1.4	27.1±3.4	32

Table 4.4: The numbers of expected signal events for the $m_H = 125\,\text{GeV}$ hypothesis and background events together with the numbers of observed events, in a window of $5\,\text{GeV}$ around $125\,\text{GeV}$ for $20.7\,\text{fb}^{-1}$ at $\sqrt{s} = 8\,\text{TeV}$ and $4.6\,\text{fb}^{-1}$ at $\sqrt{s} = 7\,\text{TeV}$ as well as for their combination.

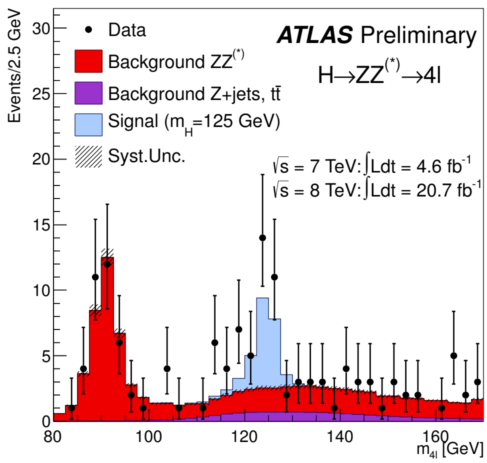

Figure 4.1: The distributions of the four-lepton invariant mass, $m_{4\ell}$, for the selected candidates compared to the background expectation for the combined $\sqrt{s} = 7\,\text{TeV}$ and $\sqrt{s} = 8\,\text{TeV}$ data sets in the low mass range.

of the background caused the observed excess. For the combined dataset the probability is 2.7×10^{-11} corresponding to a significance of 6.6σ. At a significance of 5σ it is valid to claim a discovery, so that with 6.6σ the $H \to ZZ^{(*)} \to 4\ell$ channel alone probe the existence of a new boson.

4.6.2 Mass measurement and couplings

The mass distributions are described using smooth, non-parametric, unbinned estimates [52] of the relevant probability density functions obtained from simulation. The value for the fitted mass from the profile likelihood

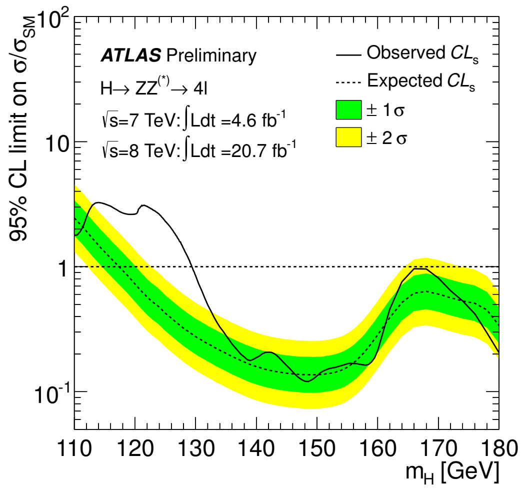

Figure 4.2: The expected (dashed) and observed (full line) 95% CL upper limit on the Standard Model Higgs boson production cross section as a function of m_H in the low mass region, divided by the expected SM Higgs boson cross section.

is $m_H = 124.3^{+0.6}_{-0.5}(\text{stat})^{+0.5}_{-0.3}(\text{sys})\text{GeV}$, where the systematic uncertainty is dominated by the energy and momentum scale uncertainties.

One of the useful measurement is the signal strength that is the ratio of the observed cross section to the expected cross section from Standard Model estimations. It is one if the Standard Model expectation is exactly fulfilled by the observed data. In $H \to ZZ^{(*)} \to 4\ell$ the measured cross section is larger than expected and leads to a signal strength of $\mu = 1.7^{+0.5}_{-0.4}$. A signal strength significantly grater then one could hint at physics beyond the Standard Model. For the $H \to ZZ^{(*)} \to 4\ell$ the signal strength is close to one within the error bars.

The measurement of a global signal strength factor can be extended to measure the signal strength factors for specific production modes. In this analysis, the production mechanisms are grouped into the "fermionic" and the "bosonic" ones. The first group consists of ggF and $t\bar{t}H$, while the latter one includes the VBF and VH modes. The measured values for $\mu_{\text{ggF}+t\bar{t}H} \times B/B_{\text{SM}}$ and $\mu_{\text{VBF+VH}} \times B/B_{\text{SM}}$ are $1.8^{+0.8}_{-0.5}$ and $1.2^{+3.8}_{-1.4}$, respectively.

Finally, the combination of all Higgs decay channel (signal strength and confidence level interval) are shown in Figure 4.4, where the markers indicate the maximum likelihood estimates ($\hat{\mu}$, $\hat{m}_H$) in the corresponding channels while the countours correspond to 68% and 95% confidence levels both including all systematic uncertainties. The measured mass, based on fits to the spectra of the high mass resolution channels $H \to \gamma\gamma$ and $H \to ZZ^{(*)} \to 4\ell$, is $m_H = 125.5 \pm 0.2(\text{stat})^{+0.5}_{-0.3}(\text{sys})\text{GeV}$ [53].

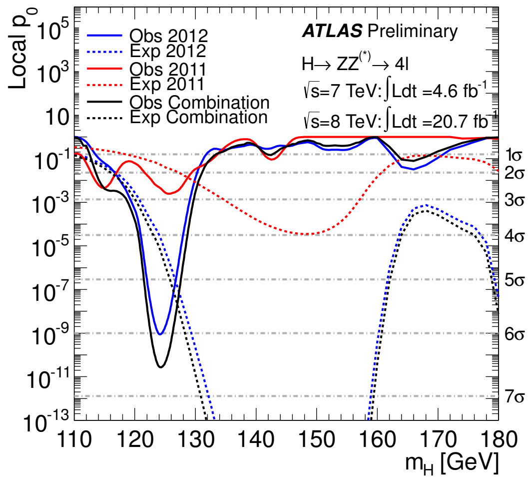

Figure 4.3: The observed local p_0 for the combination of the 2011 and 2012 data sets (solid black line); the $\sqrt{s} = 7\,\text{TeV}$ and $\sqrt{s} = 8\,\text{TeV}$ data results are shown in solid lines (blue and red, respectively). The dashed curves show the expected median local p_0 for the signal hypothesis when tested at the corresponding m_H.

4.7 Hypothesis Test: Exclusion limit and p-value

In this thesis I used the Hypothesis Test to discriminate between the different spin hypotheses. In the next Sections a brief introduction to the used method and its formalism is presented.

4.7.1 The profiled likelihood ratio for Hypothesis Test

The frequentist approach using the likelihood ratio as significance test is widely used in particle physics to estabilish discovery or exclusion. In addition to the parameter of interest, the signal and backgruond models will contain in general nuisance parameters. The nuisance parameters values are not known a priori but they can be fitted from the data.

To test a hypothesized value of μ the profile likelihood ratio is considered

$$\lambda(\mu) = \frac{L(\mu, \hat{\hat{\boldsymbol{\theta}}})}{L(\hat{\mu}, \hat{\boldsymbol{\theta}})} \tag{4.4}$$

where $\hat{\hat{\boldsymbol{\theta}}}$ in the numerator denotes the value of $\boldsymbol{\theta}$ that maximizes L for the specified μ, *i.e.*, it is the conditional maximum-likelihood (ML) estimator of $\boldsymbol{\theta}$ (and thus is a function of μ). The denominator is the maximized

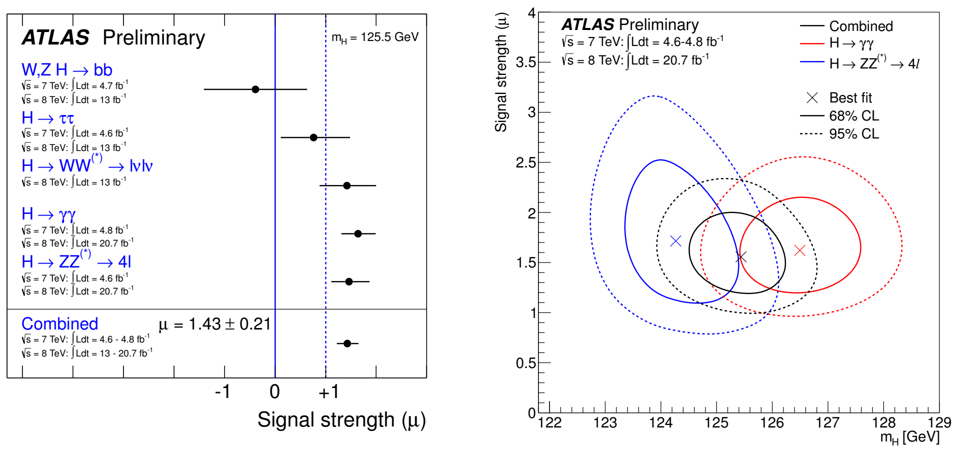

(a) (b)

Figure 4.4: (a) Measurements of the signal strength parameter for $m_H = 125.5\,\text{GeV}$ for the individual channels and for their combination. (b) Confidence level intervals in the (μ, m_H) for the $H \to ZZ^{(*)} \to 4\ell$ and $H \to \gamma\gamma$ channels and their combination, including all systematic uncertainties.

(unconditional) likelihood function, *i.e.*, $\hat{\mu}$ and $\hat{\boldsymbol{\theta}}$ are their ML estimators. The profile likelihood as funciton of μ is broadened because of the nuisance parameters and give a loss of informations about μ due to the systematic uncertainties.

$\lambda(\mu)$ vary between 0 and 1, with $\lambda(\mu)$ near 1 implying good agreement between the data and the hypothesized value of μ. Instead of using $\lambda(\mu)$, sometimes is convenient to use

$$q_\mu = -2 \ln \lambda(\mu) \tag{4.5}$$

as the basis of a statistical test. Higher values of q_μ thus correspond to increasing incompatibility between the data and μ.

We may define a test of a hypothesized value of μ by using the statistic q_μ directly as measure of discrepancy between the data and the hypothesis, with higher values of q_μ correspond to increasing disagreement. To quantify the level of disagreement the p-values is used. The definition of the p-values is given in Section 4.7.2 for a generic test statistic q.

Many analyses involving searches for a new signal process have been based on the statistic

$$q = -2 \ln \frac{L_{\text{s+b}}}{L_{\text{b}}} \tag{4.6}$$

where $L_{\text{s+b}}$ is the likelihood of the nominal signal model and L_{b} is that of the background only hypothesis. That is the logarithm of the ratio (commonly called the log-ratio) of the profiled likelihood ratio, where s+b corresponds to having the strength parameter $\mu = 1$ and b refers to $\mu = 0$. The statistic q can therefore be written as

$$q = -2 \ln \frac{L(\mu = 1, \hat{\hat{\boldsymbol{\theta}}}(1))}{L(\mu = 0, \hat{\hat{\boldsymbol{\theta}}}(0))} \tag{4.7}$$

In the same way, comparing two different hypothesis a more general log-ratio of the profiled likelihood ratio could be defined:

$$q = -2 \ln \frac{L(H_1)}{L(H_0)} \tag{4.8}$$

where H_0 and H_1 are the null and alternative hypothesis, respectively.

4.7.2 The CL_s method

The statistic test q is used to distinguish between the null hypothesis H_0 and the alternative one H_1 [51]. In order to determine which of the two hypotheses is favoured, H_0 or H_1, the p-value is defined as the probability which measures the compatibility of the data with the chosen hypothesis. If $f(q|H_0)$ denotes the PDF of q under the assumption of H_0 model, then the p-value can be expressed as (Figure 4.5)

$$p_{H_0} = P(q \geq q_{\mathrm{obs}}|H_0) = \int_{q_{\mathrm{obs}}}^{+\infty} f(q|H_0)\, dq \tag{4.9}$$

and the p-values of the H_1 hypothesis as

$$p_{H_1} = P(q \leq q_{\mathrm{obs}}|H_1) = \int_{-\infty}^{q_{\mathrm{obs}}} f(q|H_1)\, dq. \tag{4.10}$$

The smaller the p-value, the less data is compatible with the model. The conventional 95% confidence level of exclusion is defined as $1 - \alpha = 95\%$ if the p-value satisfies $p_{H_0} < \alpha$, where α equals to 0.05.

When the test statistics cannot discriminate between the different hypotheses this procedure is not appropriate. In the Higgs search for example the number of signal events is much less then the number of background events and the value of the p_{H_0} can easily reach the 5% excluding the presence of a signal. In this case the confidence estimator used is

$$CL_\mathrm{s} = \frac{p_{s+b}}{1 - p_b} \tag{4.11}$$

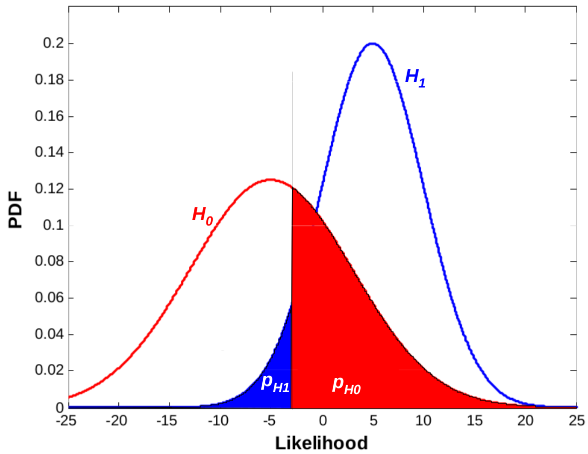

Figure 4.5: The distributions of the statistic test under the hypotheses H_0 and H_1, with the rispective p-value.

where p_{s+b} and p_b are the p-values for the signal+background and only background hypothesis, respectively.

Analogously for two generic hypothesis H_0 and H_1 the CL_s is defined:

$$CL_\mathrm{s} = \frac{p_{H_0}}{1 - p_{H_1}} < \alpha \ . \tag{4.12}$$

When the PDF's $f(q|H_1)$ and $f(q|H_0)$ values are widely apart, $1 - p_{H_1}$ is only slightly less than unity, not affecting the original exclusion ($CL_\mathrm{s} \to p_{H_0}$). On the contrary, if the two distributions are close to each other, $1 - p_{H_1}$ becomes small, and thus the p-value of H_0 hypothesis is increased to be protected from unreasonable exclusion.

Since CL_s is always larger than p_{H_0}, it is more conservative when the limit is excluded.

In particle physics, instead of using the p-value usually its conversion in significance is used. The equivalent significance Z is defined such that a Gaussian distributed variable found Z standard deviations above its mean has an upper-tail probability equal to p [2]. That is,

$$Z = \Phi^{-1}(1 - p) \tag{4.13}$$

where Φ^{-1} is the quantile (inverse of the cumulative distribution) of the standard Gaussian. For a signal process such as the Higgs boson, the particle

[2]This relation can be also defined by using a two-sided fluctuation of a Gaussian variable, with a $s\sigma$ significance corresponding to $p = 5.7 \times 10^{-7}$. We take the one-sided definition above as this gives $Z = 0$ for $p = 0.5$.

physics community has tended to regard rejection of the background hypothesis with a significance of at least $Z = 5$ as an appropriate level to constitute a discovery corrisponding to $p = 2.87 \times 10^{-7}$. For purposes of excluding a signal hypothesis, a threshold p-value of 0.05 (*i.e.*, 95% confidence level) is often used, which corresponds to $Z = 1.64$.

The sensitivity of an experiment is quantified by the expected significance in the assumption of the different hypotheses. For example, the sensitivity to discovery of a given signal process H_1 could be characterized by the expectation value, under the assumption of H_1, of the value of Z obtained from a test of H_0. This would not be the same as the Z obtained using Equation 4.13 with the expectation of the p-value, however, because the relation between Z and p is nonlinear. The median Z and p will, however, satisfy Equation 4.13 because this is a monotonic relation and therefore the commonly used espression "expected significance" is referred to the median.

4.8 Hypotesis test: the J^P-MELA analysis

In order to prove that the observed resonance correspond to a SM Higgs boson all the spin-parity hypotheses must be excluded in favour of the 0^+ state. For this thesis I developed and optimized a method to measure the spin-parity properties of a Higgs-like particle using the MELA approach. If an exclusion is not possible, a deeper look should be given to the other spin and parity states. If the 0^+ nature of the observed boson is confirmed, searches for possible CP-violating admixtures should be considered.

As said in the previous sections, the **M**atrix **E**lement **L**ikelihood **A**nalysis (MELA) [3] is based on the definition of the Matrix element starting from the most general definition of the tensorial structures of the $H \to ZZ^{(*)}$ decay.

In this analysis the MELA approach has been used to test pair-wise the different spin-parity hypotheses. In each test one spin-parity hypothesis is assumed and then the exclusion significance is evaluated with the respect to two second one. The goal is therefore to find a model for which the observed exclusion with respect to all other hypotheses will be comparable to the expected sensitivity given by the observed amount of data.

[3] The term MELA has been used to refer to a matrix element likelihood discriminant between the SM Higgs 0^+ state and the background. In the present case, the matrix element likelihood is used to discriminate between two different J^P states, and so is labelled J^P-MELA.

4.8.1 From Matrix Element to discriminating variables

The distributions of the useful observables are completely determined once the theoretical scattering amplitude fro each spin hypothesis is calculated.

The observables sensitive to the spin and parity of a generic higgs-like boson X are the masses of the two Z and the production and decay angles:

- m_{12}, the invariant mass of on-shell Z_1 boson;
- m_{34}, the invariant mass of off-shell Z_2 boson;
- θ^*, the production angle of the Z_1 defined in the four lepton rest frame;
- ϕ_1, the angle defined between the decay plane of the first lepton pair and a plane defined by the vector of the Z_1 in the four lepton rest frame and the positive direction of the collision axis;
- θ_1 and θ_2, the angles between negative final state leptons and the direction of flight of their respective Z bosons. The 4-vectors of leptons are calculated in the rest frame of the corresponding Z bosons;
- ϕ, the angle between the decay planes of four final state leptons expressed in the four leptons rest frame. [4]

In Figure 4.6 a sketch of the angular variables is shown.

The distributions of the masses and the angular variables for different spin hypotheses and for the ZZ background are shown in Figure 4.7 and Figure 4.8 respectively [49]. In spin zero hypothesis, the production cross-section does not depend on the production angle θ^* nor the decay angle ϕ_1 since X has no spin axis with which one can define these angles. Here, different parities can be distinguished by studying the decay angles ϕ, θ_1 and θ_2. However all the angles are important for discriminating between the cases of non-zero integer spin. Moreover, the shapes of the m_{12} and m_{34} distributions become sensitive to spin and parity for m_H below 180 GeV.

In this analysis, six hypotheses for spin-parity states are tested, namely J^P 0^+, 0^-, 1^+, 1^-, 2^+, 2^-. The spin-1 hypotheses are included for "completeness", because it is disfavoured under the assumption that the same particle is decaying to both $\gamma\gamma$ and four leptons. The spin-2 states correspond to a graviton-like tensor with minimal couplings (2^+_m) and a pseudo-tensor (2^-) . As said in Section 4.2.2, only ggF production is considered for the spin-0 and 1. Otherwise, for spin-2 states both ggF and $q\bar{q}$ annihilation are considered,

[4] A sixth angle, ϕ^*, is the azimuthal angle of Z_1 in the four lepton rest frame. This angle can be arbitrarily defined and does not carry any information about the process.

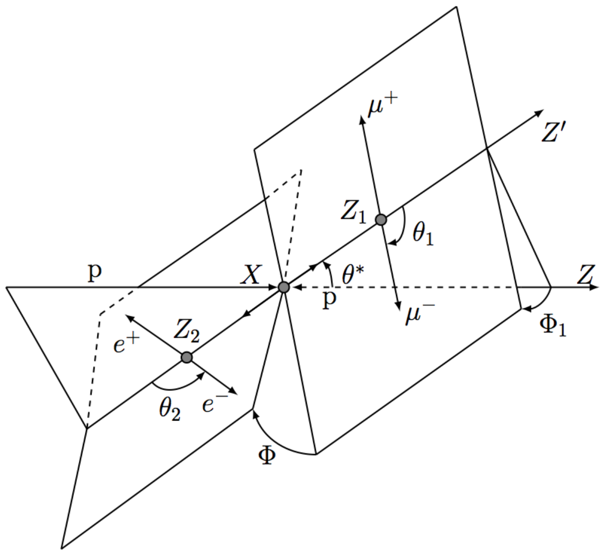

Figure 4.6: Production and decay angles in an $X \to ZZ^{(*)} \to 4\ell$ decay. The beam axis is in the laboratory frame, the Z_1 and Z_2 in the X rest frame and the leptons in their corresponding parent rest frames [49].

generating different final state angular distributions. Possible mixtures of gluon fusion and $q\bar{q}$ production, in steps of 25%, are also considered in this analysis.

Unlike the analysis for mass measurement, in the spin-parity analysis an amplied mass region is used to achieve more statistics: candidate events in the region $115\,\text{GeV} < m_{4\ell} < 130\,\text{GeV}$ are used. To improve the overall sensitivity, this mass region is split into two regions:

- low S/B, low signal over background region: 115-121 and 127-130 GeV;
- high S/B, high signal over background region: 121-127 GeV.

The sensitivity improvement resulting from the split into these two regions is estimated to be around 6% for all hypotheses tested.

4.8.2 The MELA statistical approach

The MELA approach uses the theoretical differential decay rate for the angles and m_{12} and m_{34} distributions, corrected for detector acceptance and analysis selection, to construct a matrix element based likelihood ratio as a discriminant between the different spin-parity hypotheses. In the calculation of the matrix elements both gluon–gluon fusion (gg), the primary production

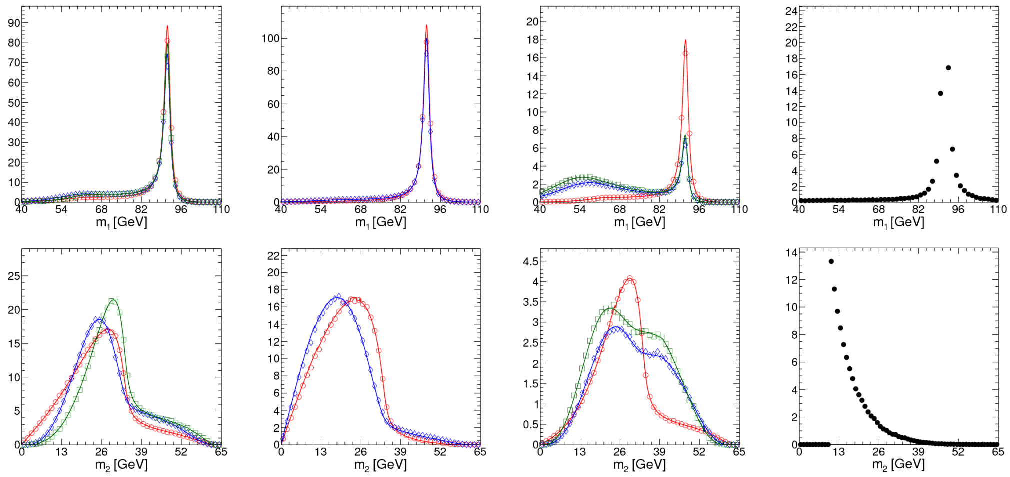

Figure 4.7: Distributions of the observables in the $X \to ZZ^{(*)}$ analysis, from left to right: spin-0, spin-1, and spin-2 signal,background. The signal hypotheses shown are J_m^+ (red circles), J_h^+ (green squares), J_m^- (blue diamonds). Background is shown with the requirements $m_2 > 10\,\text{GeV}$ and $120\,\text{GeV} < m_{4\ell} < 130\,\text{GeV}$. The observables shown from top to bottom: m_{12} and m_{34}. Points show simulated events and lines show projections of analytical distributions [49].

mode of the SM Higgs boson, and quark–antiquark annihilation ($q\bar{q}$) are taken into account.

In the adopted statistical approah pairs of signal hypotheses with different spin and parity are tested against each other.

The general probability model is:

$$\mathcal{P}^{ij} = \mu^{\text{signal}} \mathcal{L} f_i^{\text{signal}} N_{\text{signal}} \left[\varepsilon \cdot \text{PDF}^{ij}_{\text{signal 1}} + (1-\varepsilon) \cdot \text{PDF}^{ij}_{\text{signal 2}}) \right] \\ + \sum_{\text{backgrounds } (k)} f_i^{\text{background } k} N_{\text{background } k} \text{PDF}^{\text{ij}}_{\text{background k}}, \tag{4.14}$$

where μ^{signal} is signal strength, $\mathcal{L}$ is total luminosity, ε is the fraction of first signal hypothesis represented by the $\text{PDF}^{ij}_{\text{signal 1}}$. The first and the second signal hypotheses will be denoted hereafter as H_0 and H_1 respectively. The $N_{\text{background } k}$ and $\text{PDF}^{ij}_{\text{background } k}$ represent the number of events and the PDF of the k-th background respectively. The parameter of interest is ε. The parameters $\mathcal{L}$, $N_{\text{background } k}$, N_{signal} are nuisance parameters which are constrained by Gaussian terms, and their values and uncertainties are determined from the nominal analysis (as used for discovery) [47]. The parameter μ^{signal} is profiled. The indices i and j represent the S/B bins and the bins of the angular discriminant PDF respectively. The final likelihood

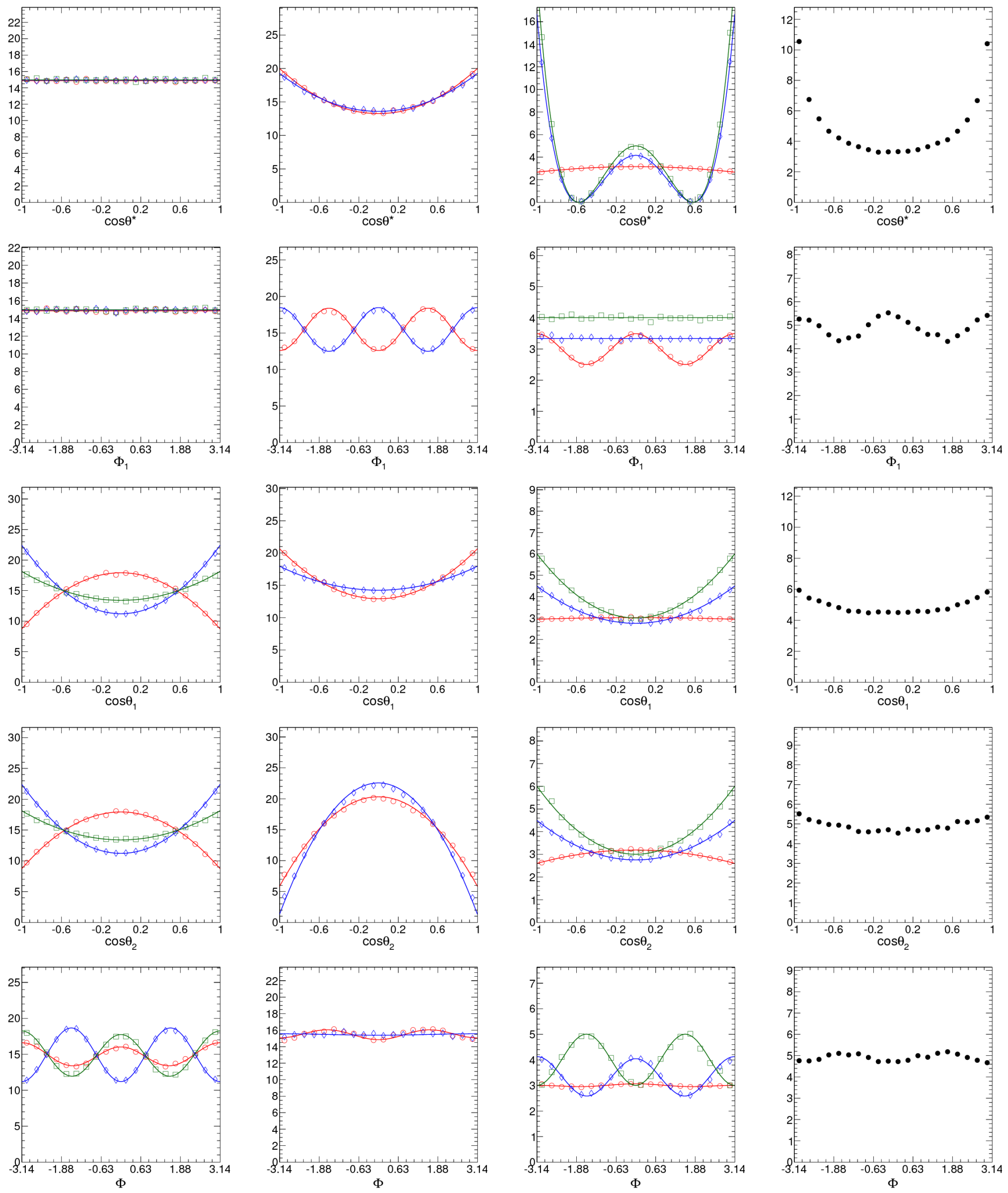

Figure 4.8: Distributions of the observables in the $X \to ZZ^{(*)}$ analysis, from left to right: spin-0, spin-1, and spin-2 signal,background. The signal hypotheses shown are J_m^+ (red circles), J_h^+ (green squares), J_m^- (blue diamonds). Background is shown with the requirements $m_2 > 10\,\text{GeV}$ and $120\,\text{GeV} < m_{4\ell} < 130\,\text{GeV}$. The observables shown from top to bottom: $\cos\theta^*$, ϕ_1, $\cos\theta_1$, $\cos\theta_2$ and ϕ. Points show simulated events and lines show projections of analytical distributions [49].

created then reads:

$$L = \prod_{ij} \text{Poiss}(N^{ij}_{\text{data}} | \mathcal{P}^{ij}) \tag{4.15}$$

where the systematic effects are not shown.

In the spin analysis, the signal and background likelihood shapes are obtained from their respective discriminant J^P-MELA (or pseudo-MELA, which takes into account all the systematic uncertainties), the test statistic used in the analysis is the log-ratio of profiled likelihood ratio $\log[L(H_1)/L(H_0)]$.

A series of pseudo-experiments are generated with the fixed N_{sig} to construct the distributions for the two hypothesis, which share the same backgrounds. The estimation of the background normalisation is obtained from the data and Monte Carlo. The total event yield in the signal region is taken from SM expectation.

The signal likelihood

The signal events are described by the extended likelihood function $\mathcal{L}$. The extended likelihood function is adopted when we record N independent multidimensional observations, $\{x_i\}$, $i = 1$, ..., N, of a distribution depending on a set of parameters θ: it may happen that these parameters also determine the rate, *i.e.* the expected rate $\lambda(\theta)$ is a function of θ. The extended likelihood function is defined as:

$$\begin{aligned} \mathcal{L}(m_{4\ell}, m_{Z_1}, m_{Z_2}, \vec{\Omega} | g_1, ..g_{10}, f_{z_0}, ..f_{z_2}) = \prod_{\text{categories}} \text{Pois}(N_S) \cdot \\ \prod_{\text{events}} \cdot PDF_s(m_{4\ell}, m_{Z_1}, m_{Z_2}, \vec{\Omega} | g_1, ..g_{10}, f_{z_0}, ..f_{z_2}) \end{aligned} \tag{4.16}$$

PDF_S is the probability density function for signal events; Pois(N_S) is a Poisson function of the number of signal events in a given category with expected value N_S; $m_{4\ell}$ is the invariant mass of the Higgs candidate; m_{Z_1} and m_{Z_2} are the masses of the two Z boson candidates; $\vec{\Omega}$ represents the five angular observables used to characterize the production ($cos\theta^\star$, ϕ_1), and decay ($cos\theta_1$, $cos\theta_2$, ϕ) of the Higgs candidate; the $g_i, i = 1\ldots$ and the $f_{z_0} \ldots f_{z_2}$ are the theory coupling parameters. The product of single event likelihood runs over all candidate events and all categories, as the different ZZ decay channels (4μ, $2e2\mu$, $2\mu 2e$, $4e$) or different measurements (for example the $\sqrt{s} = 7\,\text{TeV}$ and $\sqrt{s} = 8\,\text{TeV}$ ones).

The signal PDF describes the probability that a fully reconstructed and selected event corresponds to a given signal hypothesis. In order to take into account the detector acceptance and analysis selection additional corrections need to be applied on the PDFs. For events where reconstructed lepton pairs are correctly associated, *i.e.* where each lepton pair actually comes from the decay of the same Z boson (*good–paired candidates*), the theoretical PDF is corrected with an acceptance function, to fully take into account the effect of detector resolution and analysis cuts on the event–by–event observables $(m_{4\ell}, m_{Z_1}, m_{Z_2}, \vec{\Omega})$. In final states with four identical leptons ($4e$ and 4μ) can happend that the selection leads to a wrongly associate the leptons together to form a Z (wrong-paired candidates).

In previous analyses (see [47]) the wrong-paired candidates distrubutions were fitted and the empirical function found used to describe their behaviour. In this thesis a new approach has been used that permit a similar treatment for good- and wrong-paried events. In particular a wrong-pair PDF has been calculated starting from the theoretical good-pair one. As shown in Equation 4.17, the good-pair PDF is written as funtion of the masses and of the angular variables, a transformation that permit to have the PDF as a function of the leptons p_{T} have been developed. Once the dependence on the leptons p_{T} is clearly stated then the leptons are swapped to simulate the case of wrong paired events so the new PDF well represent the wrong paired cases. This method has been fully validated. The two dimentional correlations between observables (e.g. m_{12} and m_{34}) have been taken into account. The $m_{4\ell}$ PDF is the same as the one used for the right–paired candidates.

The signal PDF can therefore be written as follows:

$$\begin{aligned} PDF_S(m_{4\ell}, m_{Z_1}, m_{Z_2}, \vec{\Omega}|g_1, ..g_{10}, f_{z_0}, ..f_{z_2}) = \\ f_{RP} \cdot PDF_{RP}(m_{4\ell}, m_{Z_1}, m_{Z_2}, \vec{\Omega}|g_1, ..g_{10}, f_{z_0}, ..f_{z_2}) \cdot \mathrm{Acc}_{RP}(m_{Z_1}, m_{Z_2}, \vec{\Omega}) \\ +(1 - f_{RP}) PDF_{WP}(m_{4\ell}, m_{Z_1}, m_{Z_2}, \vec{\Omega}) \cdot \mathrm{Acc}_{WP}(m_{Z_1}, m_{Z_2}, \vec{\Omega}). \end{aligned} \tag{4.17}$$

Here f_{RP} represents the fraction of Right-Paired (RP) candidates, which are described by the PDF term $PDF_{RP}(m4l, m_{Z_1}, m_{Z_2}, \vec{\Omega}|g_1, ..g_{10}, f_{z0}, ..f_{z_2}) \cdot Acc_{RP}(\vec{\Omega})$, where PDF_{RP} is the underlying matrix element calculation and $Acc_{RP}(\vec{\Omega})$ is the correction term taking into account detector effects on the observables. The Wrong-Paired (WP) candidates, which only exist in the 4μ and $4e$ channels, are instead described by the analitical PDF term $PDF_{WP}(m4l, m_{Z_1}, m_{Z_2}, \vec{\Omega})$ and the wrong–pair acceptance term $Acc_{WP}(\vec{\Omega})$. The f_{RP} parameters are computed using MC simulation, and their values for each spin-parity hypothesis studied are provided in Table 4.5: RP fraction depends on spin and parity.

The fraction of wrong-paired candidates is always less then the 10% except in the 2^-_h case where f_{WP} is $\sim 45\%$. The present description of the total

Sample	fraction of mis-paired candidates	
channel	4μ	4e
Powheg ggH125	9.4 ± 0.4	11.0 ± 0.7
JHU ggH125 0^+	9.2 ± 0.5	10.9 ± 0.7
JHU ggH125 0^-	13.5 ± 0.6	13.9 ± 0.8
JHU qqH125 1^+	3.5 ± 0.3	4.1 ± 0.5
JHU qqH125 1^-	6.8 ± 0.3	6.9 ± 0.5
JHU ggH125 2^+	6.3 ± 0.4	6.5 ± 0.5
JHU qqH125 2^+	6.0 ± 0.4	6.5 ± 0.6
JHU ggH125 2^-	16.7 ± 0.6	15.9 ± 0.8
JHU qqH125 2^-	13.2 ± 0.7	16.8 ± 1.3
Powheg ZZ	17.8 ± 0.3	16.4 ± 0.4

Table 4.5: Fraction of mis–paired candidates within the mass window 115-130 GeV estimated on the JHU and PowHeg samples used.

PDF give similar risults then the previous analysis [47] in all the spin cases but give a great improvement in the case of the spin 2^-_h because of the great percentage of WP events.

Right-paired signal PDF

The RP signal PDF defined in Equation 4.17 is split in a term that describes the true behaviour of signal events as a function of the theory parameters and of the observables, and a term that accounts for the detector and analysis selection effects ($Acc_{RP}(\vec{\Omega})$). The acceptance term is parametrized empirically using fully simulated MC events, separately for each spin hypotheses, as described in more detail below. The dependence on the angular observables, the four-lepton mass and the Z bosons masses for the theoretical RP signal component of the PDF can be factorised as follows:

$$\begin{aligned} &PDF_{RP}(m4l, m_{Z_1}, m_{Z_2}, \vec{\Omega}|g_1, ..g_{10}, f_{z0}, ..f_{z_2}) = \\ &PDF(m4l) \cdot PDF_{RP}(m_{Z_1}, m_{Z_2}, \vec{\Omega}|g_1, ..g_{10}, f_{z0}, ..f_{z_2}). \end{aligned} \tag{4.18}$$

Detailed studies have been performed to estimate the correlations between the observables and as it is shown in Section 4.8.3 they are small enough to be neglected respect to statistical error that affect this analysis.

The description of the $PDF(m4l)$ is described by the sum of a Crystal-Ball function and a Gaussian: the parameters of this function have been fitted on fully simulated MC. The last term is given by the general angular distribution in the production and decay of a generic spin J ($J = 0$, 1, 2) particle. In the m_{Z_1} and m_{Z_2} terms a gaussian resolution is introduced to describe the resolution on the invariant masses of the Z bosons measurement and effects related to energy loss caused by initial or final state radiation emission. An additional acceptance correction is also applied on the Z masses term, which is extracted from fully simulated MC samples comparing the shape of reconstructed and truth events, in analogy with what was done for the angular observables in the old analysis.

Wrong-paired signal PDF

Similarly to what happens for the RP signal PDF, the WP signal PDF is described by two terms. The first term describes the behaviour of signal events, whereas the second one ($Acc_{WP}(\vec{\Omega})$) takes into account the detector and analysis selection effects. The wrong-paired component is written as follows:

$$PDF_{WP}(m4l, m_{Z_1}, m_{Z_2}, \vec{\Omega}) = PDF(m4l) \cdot PDF_{WP}(m_{Z_1}, m_{Z_2}) \cdot PDF_{WP}(\vec{\Omega}). \quad (4.19)$$

This term of the PDF is calculated from the theoretical good-pair one, separately for each spin hypotheses as described above.

4.8.3 Correletions between observables

For both the acceptance corrections on the right-paired and the wrong-paired candidates PDFs, the assumption that the angular observables are uncorrelated is made. Studies show that correlations between observables are indeed small, all the same this approximation can only reduce the power of separation of this method between the two hypotheses, but it cannot introduce any bias to the method.

Figure 4.9 shows the correlations between different observables, for the spin 0^+ and 2^+ hypotheses. These correlations are taken into account when estimating the systematic uncertainties.

4.8.4 Acceptance definition: right and wrong-pairing

The acceptance correction terms ACC_{RP} and ACC_{WP} in the signal PDF written in Equation 4.17 are extracted using half of the statistics of the fully simulated signal MC, while the other half being used for the closure tests and expected limits extraction (see Sections 4.8.6 and 5.2). In this way no

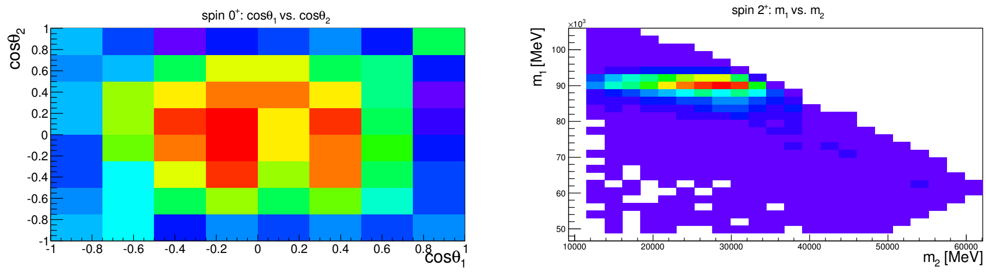

(a) (b)

Figure 4.9: These plots show the correlation (a) $(\cos\theta_1, \cos\theta_2)$ for the spin 0^+ hypothesis and (b) (m_2, m_1) for 2^+. Effects of correlation are taken into account for the estimation of systematic uncertainties.

effect that might bias the results are introduced. The acceptance for each of the angular observable x is defined as the ratio between the reconstructed angular distribution, x_{reco}, and the theoretical angular distribution, $\text{PDF}(x)$. The first one is obtained from the fully simulated signal MC, while the second one is obtained by projecting the theoretical 8-dimensional PDF over the interesting variable.

$$ACC(x) = \frac{x_{\text{reco}}}{\text{PDF}(x)} \tag{4.20}$$

Both RP and WP acceptances are fitted using functions of the general form:

$$f(x) = (a + bx + cx^2) \cdot \left(1 + \sum_{i=1}^{4} p_i \cdot cos(x \cdot i) + \sum_{j=1}^{4} q_j \cdot sin(x \cdot j)\right) \tag{4.21}$$

where a, b, c, p_i, q_j are free parameters of the fit on the signal MC distribution of the given observable x.

An important and also very delicate part of this thesis has been focused on the determination and optimization of the fit functions for all the angular variables for each final state and for each spin. The total number of fits performed is about 700 considering both RP and WP acceptances terms. To perform all these fits I developed a code using the RooFit library of ROOT [5].

The "truth" and "reconstructed" distributions of some observables are shown from Figures 4.10 to 4.13 for the spin-0^+ and 2^+ hypothesis. The "truth" distribution is the MC distribution (produced using the JHU generator)

[5] ROOT [54] is a data analysis framework largely used at CERN. It provides a set of object-oriented frameworks with all the functionality needed to handle and analyze large amounts of data in a very efficient way. The RooFit [55] library provides a toolkit for modeling the expected distribution of events in a physics analysis.

without detector and selection effects, otherwise the "reconstructed" one is obtained taking account of these effects.

In Figures 4.14 and 4.15 the RP and the WP angular acceptances distributions are shown for the spin 0^+ and 2^+ cases respectively. In the plots also the fit functions are shown. The distribution of the acceptances for all the spin hypotheses studied are reported in Appendix A.

4.8.5 Spin-2 $q\bar{q}$ and gg states admixtures

When studying the spin-2 hypotheses, in order to provide a more general statement on the nature of the Higgs-like particle the fraction of spin two bosons coming from $q\bar{q}$ (f_{qq}) production mechanisms is variated. As already said in Section 4.2.2, the relative fraction gg and $q\bar{q}$ production mechanisms for spin two bosons is currently unknown: therefore five values of f_{qq} are studied in the current analysis: $f_{qq} = 0\%, 25\%, 50\%, 75\%, 100\%$.

The PDF for a spin two Higgs-like boson corresponding to a generic f_{qq} production fraction, in the J^P-MELA approach, can be defined as the linear combination of purely produced qq and gg spin two states. No terms of interference are taken into account.

$$\begin{aligned} PDF_S(m_{4\ell}, m_{Z_1}, m_{Z_2}, \vec{\Omega}|g_1, ..g_{10}, f_{z_0}, f_{qq}, f_{z_2}) = \\ f_{qq}^{eff} \cdot PDF_S(m_{4\ell}, m_{Z_1}, m_{Z_2}, \vec{\Omega}|g_1, ..g_{10}, f_{z_0}, f_{qq} = 1, f_{z_2}) + \\ +(1 - f_{qq}^{eff}) \cdot PDF_S(m_{4\ell}, m_{Z_1}, m_{Z_2}, \vec{\Omega}|g_1, ..g_{10}, f_{z_0}, f_{qq} = 0, f_{z_2}). \end{aligned} \tag{4.22}$$

The two purely qq and gg spin two PDFs are already corrected for detector and selection effects, hence it is necessary to weight them using f_{qq}^{eff} and $(1 - f_{qq}^{eff})$ respectively, where f_{qq}^{eff} is the qq fraction weighted using the corresponding analysis selection efficiencies, which are in principle different depending on the production mechanism. In particular:

$$f_{qq}^{eff} = \frac{f_{qq} \cdot \epsilon_{qq}}{f_{qq} \cdot \epsilon_{qq} + (1 - f_{qq}) \cdot \epsilon_{gg}}.$$

In Table 4.6 the efficiencies ϵ_{qq} and ϵ_{gg} are shown. The efficiencies are computed using the signal MC samples.

The description provided by the weighted linear combination of the pure spin-2 states PDFs is proved by the closure tests, described in the next Section. In Figures 4.24 to 4.31 closure tests for the spin–2^+ with $f_{qq} = 50\%$ show a good agreement between the fully simulated MC events and the ones generated from the PDF defined in Equation 4.22. In Appendix B all other admixtures closure tests are shown.

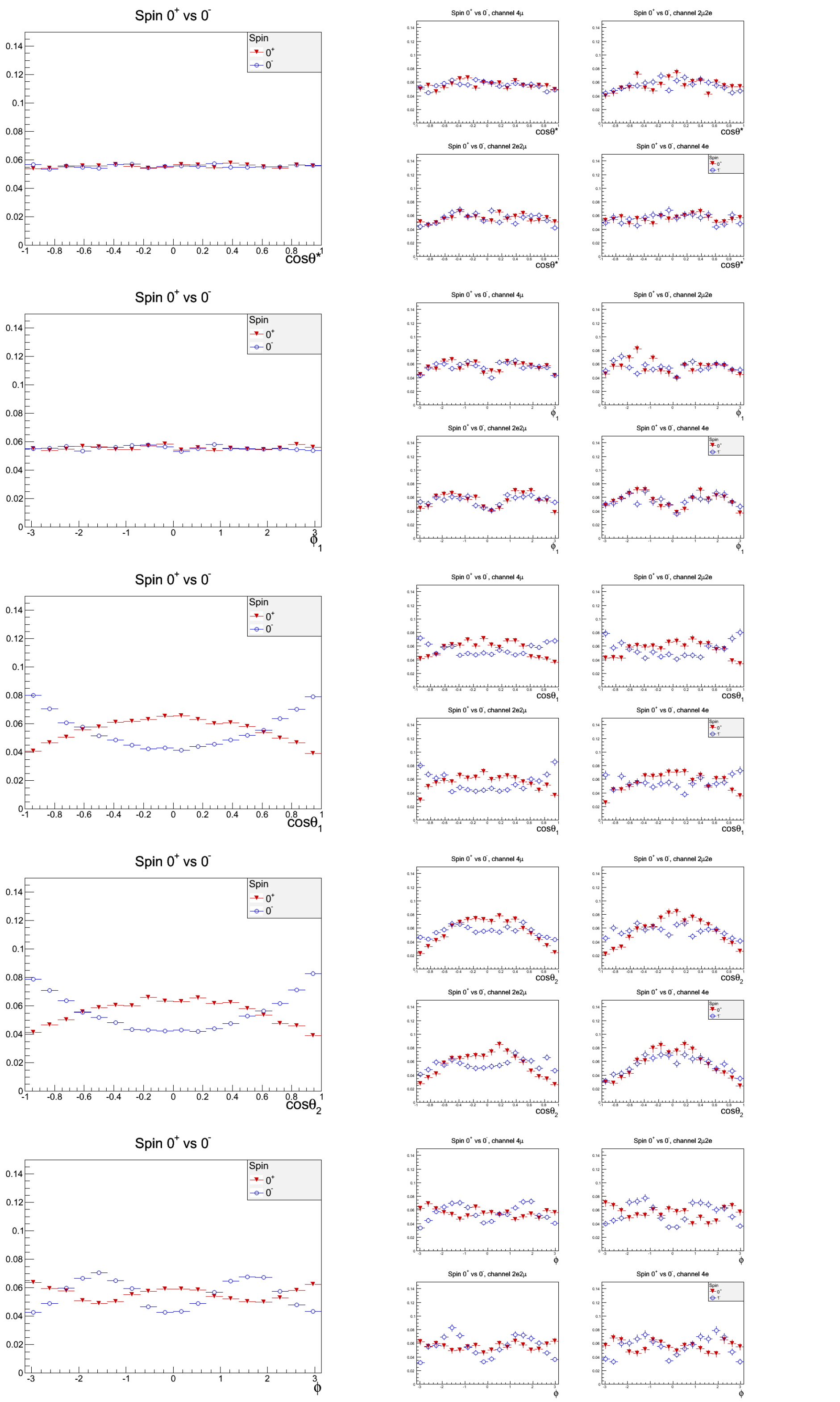

Figure 4.10: The distributions for the 0^+ (red triangles) and 0^- (blue circles) spin-parity hypotheses (MC data sample 2012) before ("truth", to the left) and after ("reconstructed", to the right) the detector and selection effects. The observables shown from top to bottom: $\cos\theta^*$, ϕ_1, $\cos\theta_1$, $\cos\theta_2$ and ϕ. In the reconstructed plot from left to right and top to bottom: 4μ, $2\mu 2e$, $4e$ and $2e2\mu$ channels.

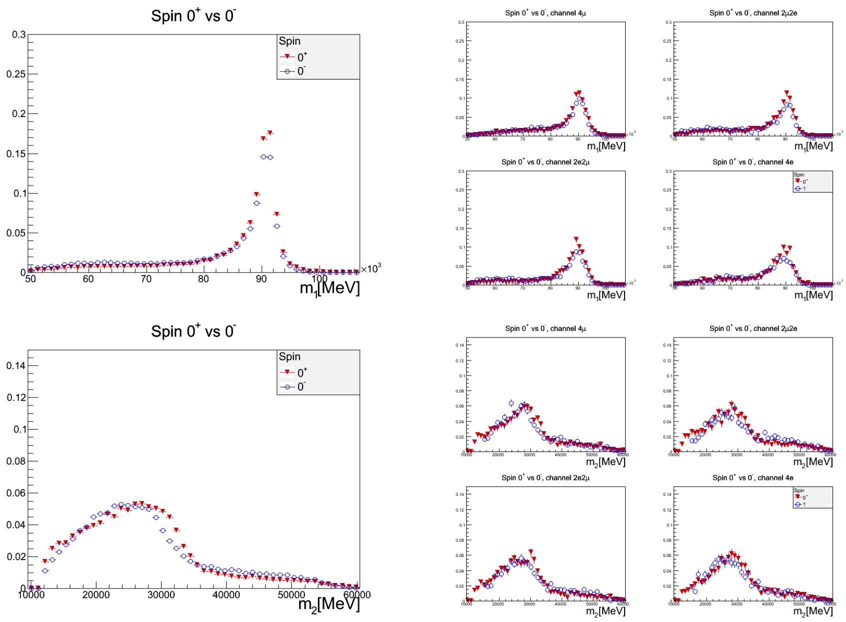

Figure 4.11: The distributions for the 0^+ (red triangles) and 0^- (blue circles) spin-parity hypotheses (MC data sample 2012) before ("truth", to the left) and after ("reconstructed", to the right) the detector and selection effects. The observables shown from top to bottom: m_1 and m_2. In the reconstructed plot from left to right and top to bottom: 4μ, $2\mu 2e$, $4e$ and $2e2\mu$ channels.

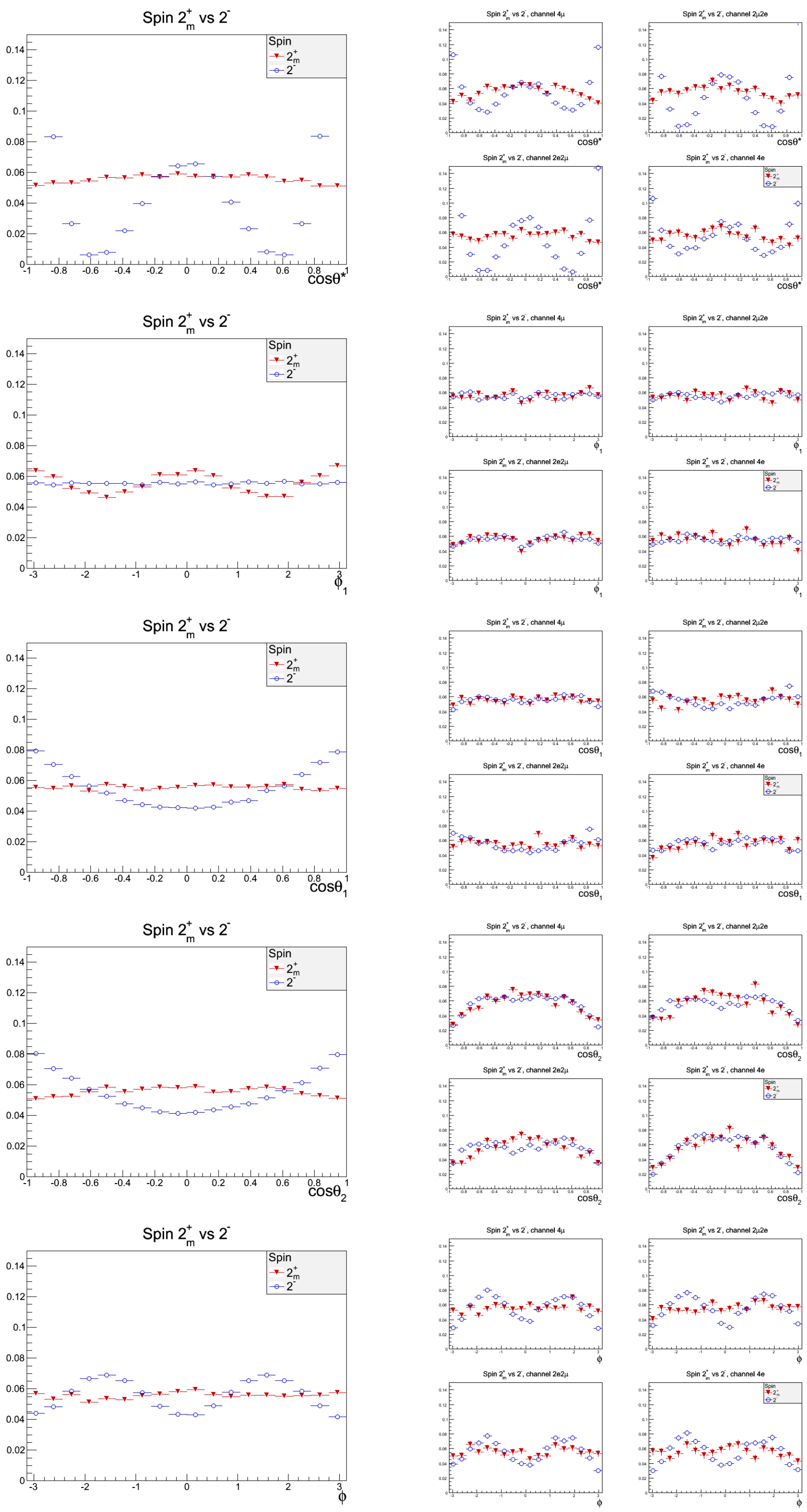

Figure 4.12: The distributions for the 2^+_m (red triangles) and 2^- (blue circles) spin-parity hypotheses (MC data sample 2012) before ("truth", to the left) and after ("reconstructed", to the right) the detector and selection effects. The observables shown from top to bottom: $\cos\theta^*$, ϕ_1, $\cos\theta_1$, $\cos\theta_2$ and ϕ. In the reconstructed plot from left to right and top to bottom: 4μ, $2\mu 2e$, $4e$ and $2e2\mu$ channels.

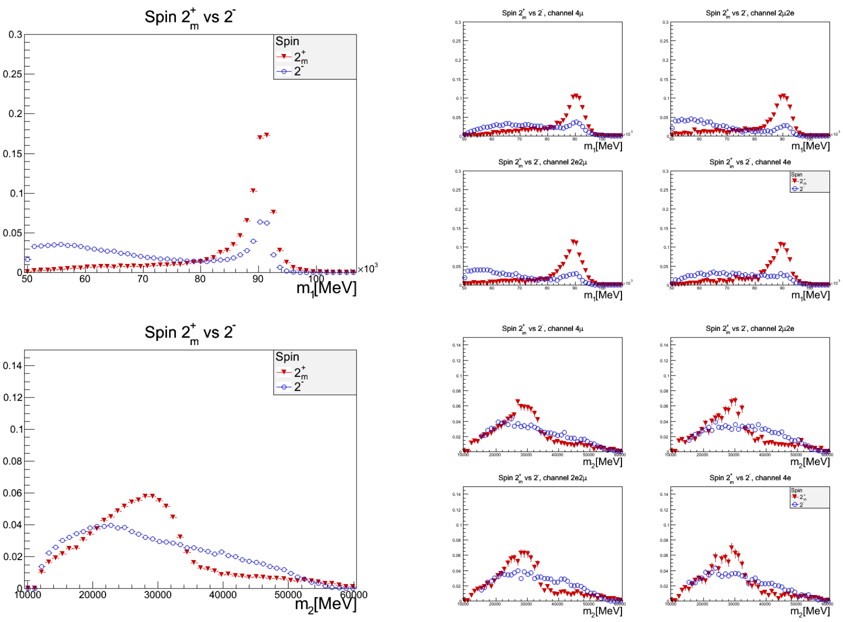

Figure 4.13: The distributions for the 2^+_m (red triangles) and 2^- (blue circles) spin-parity hypotheses (MC data sample 2012) before ("truth", to the left) and after ("reconstructed", to the right) the detector and selection effects. The observables shown from top to bottom: m_1 and m_2. In the reconstructed plot from left to right and top to bottom: 4μ, $2\mu 2e$, $4e$ and $2e2\mu$ channels.

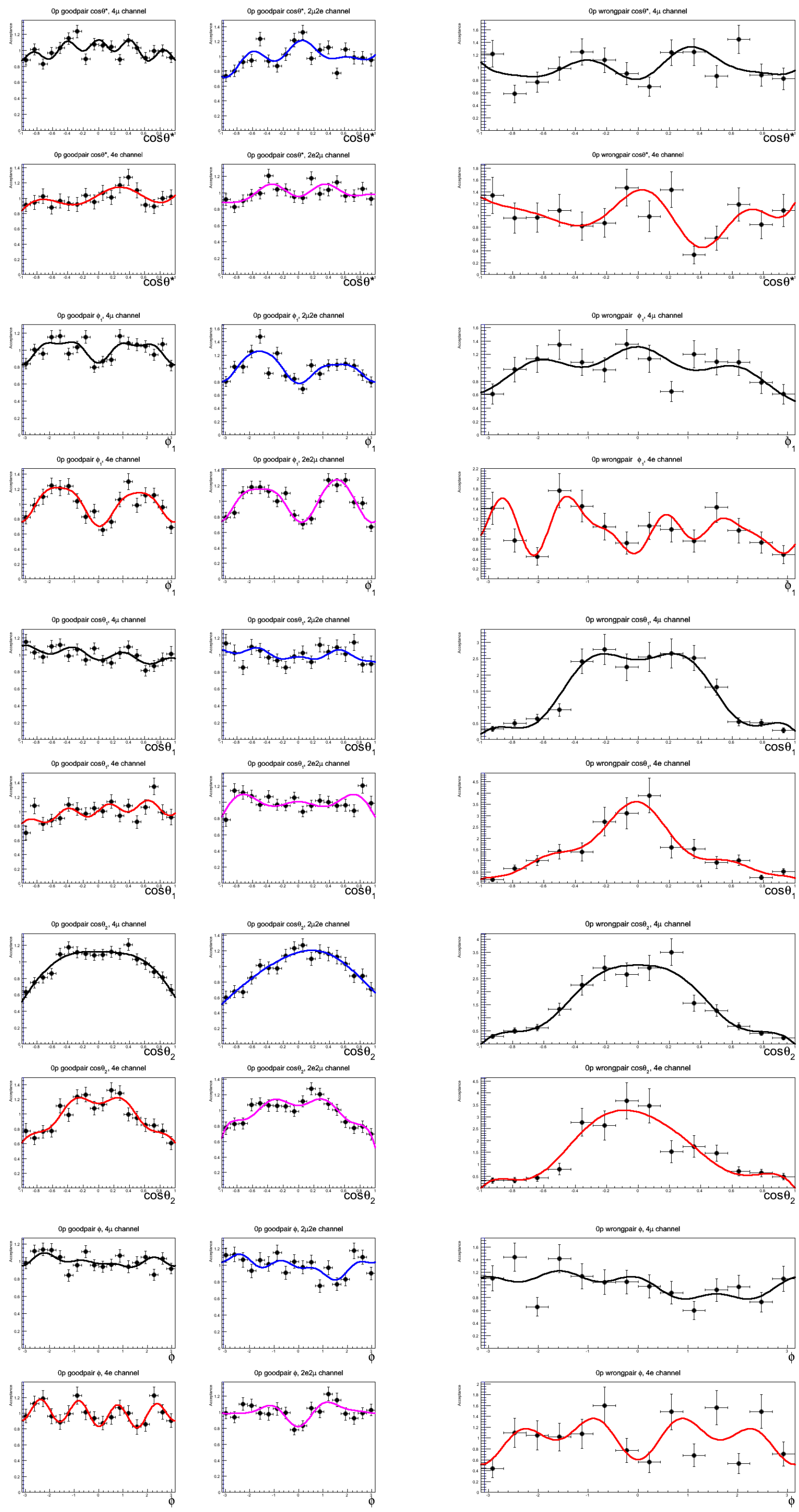

Figure 4.14: Acceptances fit (RP to the left and WP to the right) for the 0^+ spin-parity hypothesis (MC data sample 2012). The observables shown from top to bottom: $\cos\theta^*$, ϕ_1, $\cos\theta_1$, $\cos\theta_2$ and ϕ. In the RP plot from left to right and top to bottom: 4μ, $2\mu 2e$, $4e$ and $2e2\mu$ channels. In the WP plot from top to bottom: 4μ and $4e$ channels.

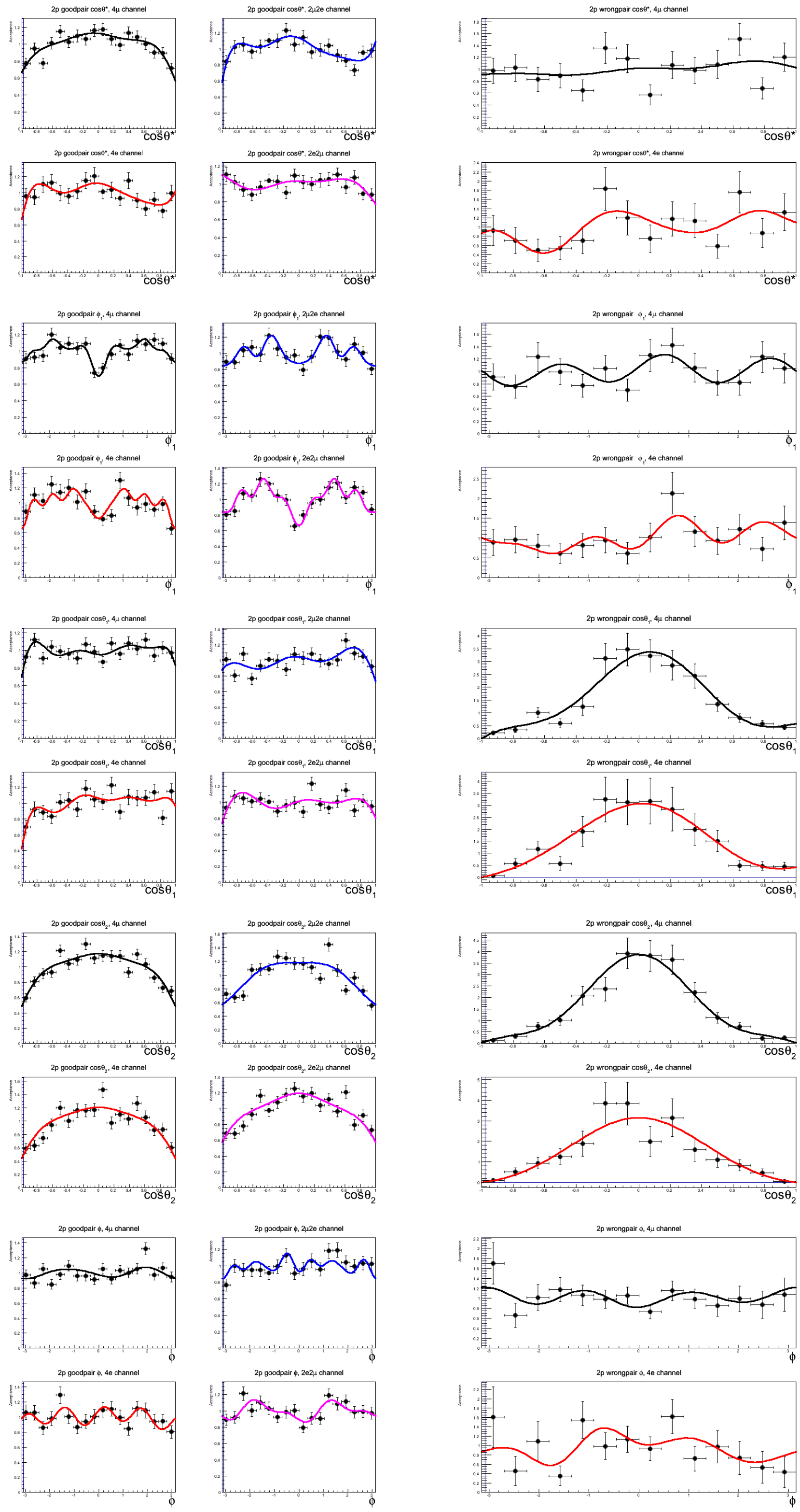

Figure 4.15: Acceptances fit (RP to the left and WP to the right) for the 2^+ spin-parity hypothesis (MC data sample 2012). The observables shown from top to bottom: $\cos\theta^*$, ϕ_1, $\cos\theta_1$, $\cos\theta_2$ and ϕ. In the RP plot from left to right and top to bottom: 4μ, $2\mu 2e$, $4e$ and $2e2\mu$ channels. In the WP plot from top to bottom: 4μ and $4e$ channels.

J^P	Production mechanism	Decay channel	Selection efficiency
2^+_m	$gg \to X$	$X \to 4\mu$	0.346 ± 0.003
2^+_m		$X \to 2\mu 2e$	0.216 ± 0.003
2^+_m		$X \to 2e2\mu$	0.279 ± 0.003
2^+_m		$X \to 4e$	0.181 ± 0.002
2^+_m	$q\bar{q} \to X$	$X \to 4\mu$	0.315 ± 0.002
2^+_m		$X \to 2\mu 2e$	0.193 ± 0.002
2^+_m		$X \to 2e2\mu$	0.254 ± 0.002
2^+_m		$X \to 4e$	0.165 ± 0.002
2^-	$gg \to X$	$X \to 4\mu$	0.356 ± 0.003
2^-		$X \to 2\mu 2e$	0.218 ± 0.003
2^-		$X \to 2e2\mu$	0.278 ± 0.003
2^-		$X \to 4e$	0.193 ± 0.002
2^-	$q\bar{q} \to X$	$X \to 4\mu$	0.233 ± 0.003
2^-		$X \to 2\mu 2e$	0.140 ± 0.002
2^-		$X \to 2e2\mu$	0.112 ± 0.002
2^-		$X \to 4e$	0.180 ± 0.002

Table 4.6: The Table shows the analysis selection efficiencies in each of the four decay channels for a spin-2 Higgs-like boson produced via $q\bar{q}$ annihilation or gg fusion.

4.8.6 Closure tests

The signal description in the likelihood 4.16 makes some simplifying assumptions (*i.e.* few factorizations and acceptance parametrizations with empirical models): the validity of these assumptions have to be verified. Moreover, in order to check the general methodology used to describe acceptance corrections for both RP and WP PDFs, a comparison ("closure test") can be made of the one-dimensional projections of the likelihood function over all the observables with respect to fully simulated samples of Higgs signals under several spin and parity hypotheses.

In order to avoid the introduction of any overtraining effect that might bias the test result, only half of the available signal JHU MC statistics is been used to obtain the closure tests, while the other half one is been used for the parametrization of the functions.

A good agreement between the projections of the signal likelihood and full MC simulation is reached: it indicates that the chosen parametrizations are adequate for a general description of the spin-parity states studied. The comparisons for all of the studied observables of a SM Higgs-like boson are shown in Figures 4.16 to 4.23. The distributions for all other spin hypotheses tested are shown in Appendix B.

As explained in the next Section, the residual discrepancies observed in the closure test will not be taken into account in the systematic uncertainties estimation because they are not expected to introduce any bias.

4.8.7 Systematic Uncertainties

Most of the systematic uncertainties for the spin-parity analysis are exactly the same to the one of the main analysis, described in Section 4.5. In particular theoretical uncertainties, background normalizations uncertainties and luminosity uncertainties are treated in the same way due to the fact that the event selection is the same. Other sources of uncertainties are related to the matrix element method only. These include effects induced by the uncertainties in the MC signal modeling and by the few approximations in the adopted likelihood functions.

Systematic uncertainties of normalization

The systematic effects that might affect the normalization consist in:

- the effect of the luminosity systematic uncertainty;
- the migration of events between the low and the high mass bins when shifting the Higgs mass value;

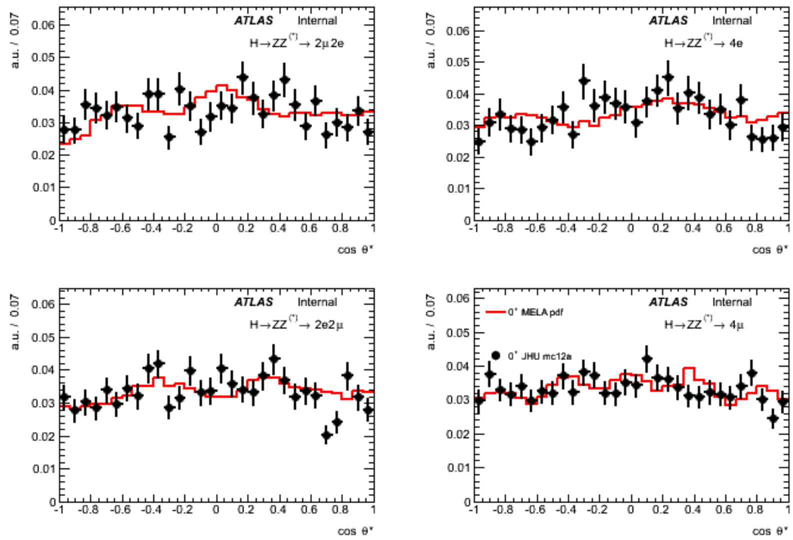

Figure 4.16: Comparison of the likelihood projection for a 0^+ Higgs-like resonance (red curve) and the corresponding JHU (black points) MC simulation for $\cos\theta^\star$. From left to right and top to bottom: 4μ,$2\mu 2e$,$4e$ and $2e2\mu$ channels.

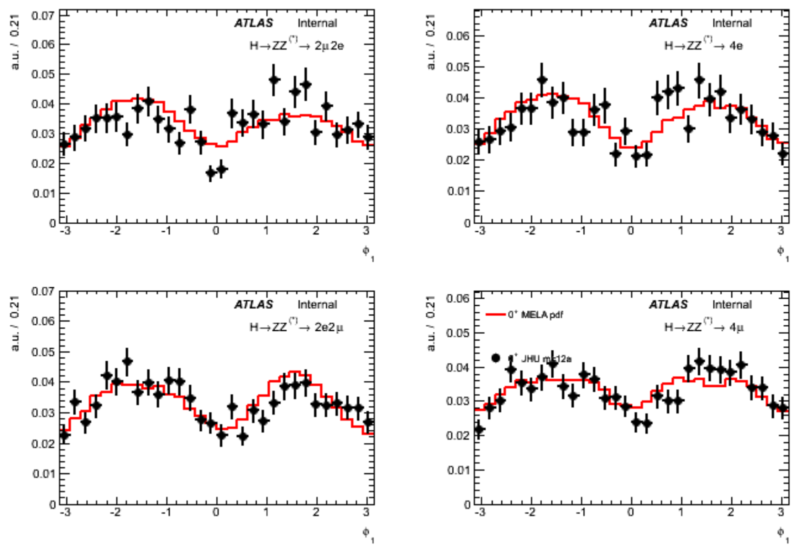

Figure 4.17: Comparison of the likelihood projection for a 0^+ Higgs-like resonance (red curve) and the corresponding JHU (black points) MC simulation for ϕ_1. From left to right and top to bottom: 4μ,$2\mu 2e$,$4e$ and $2e2\mu$ channels.

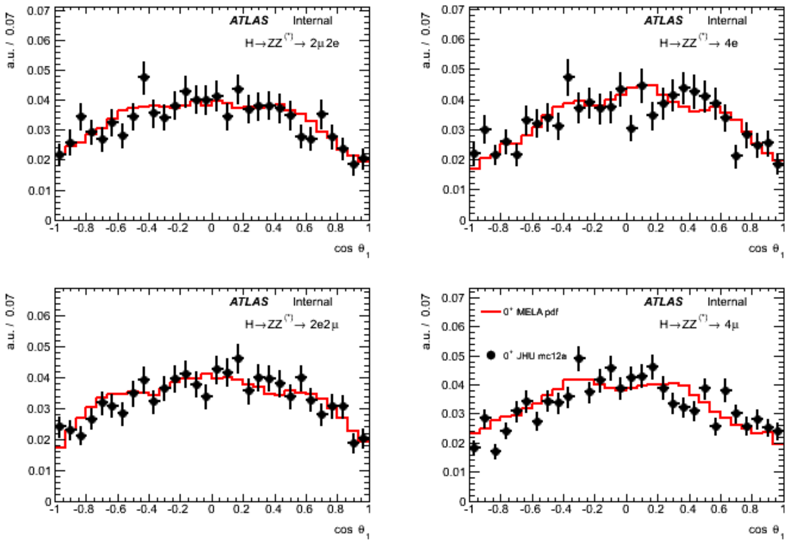

Figure 4.18: Comparison of the likelihood projection for a 0^+ Higgs-like resonance (red curve) and the corresponding JHU (black points) MC simulation for $\cos\theta_1$. From left to right and top to bottom: 4μ,$2\mu 2e$,$4e$ and $2e2\mu$ channels.

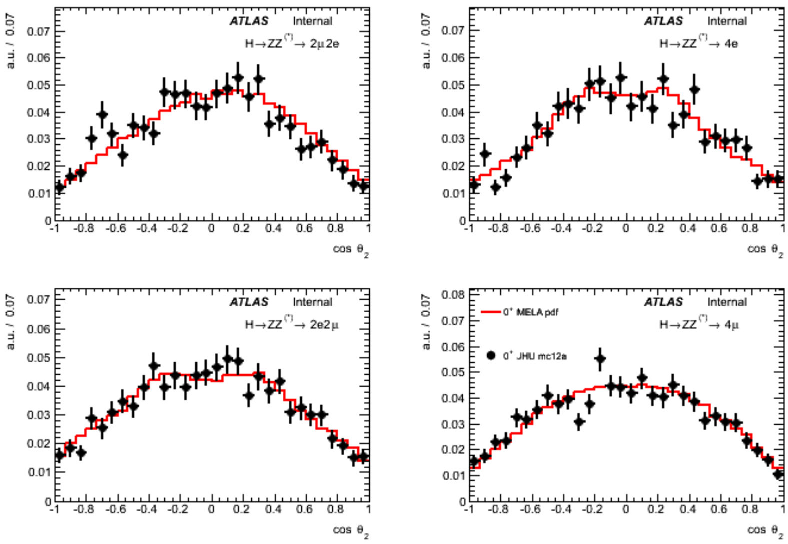

Figure 4.19: Comparison of the likelihood projection for a 0^+ Higgs-like resonance (red curve) and the corresponding JHU (black points) MC simulation for $\cos\theta_2$. From left to right and top to bottom: 4μ,$2\mu 2e$,$4e$ and $2e2\mu$ channels.

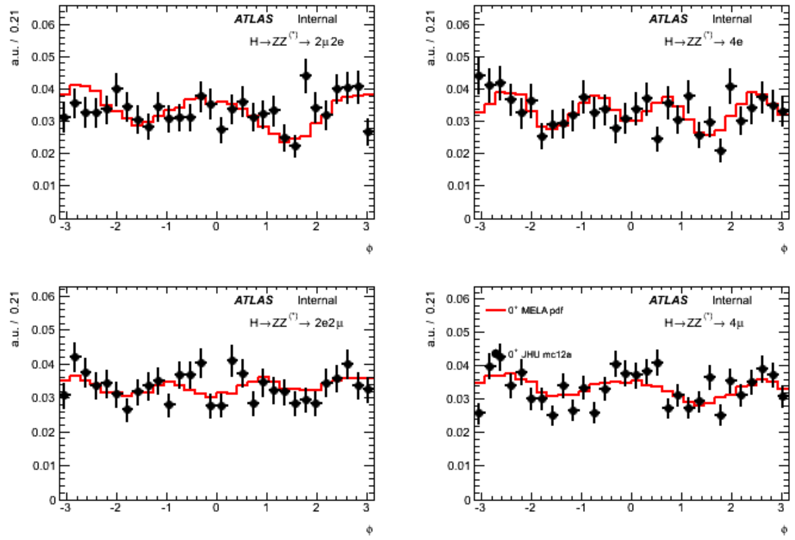

Figure 4.20: Comparison of the likelihood projection for a 0^+ Higgs-like resonance (red curve) and the corresponding JHU (black points) MC simulation for ϕ. From left to right and top to bottom: 4μ,$2\mu 2e$,$4e$ and $2e2\mu$ channels.

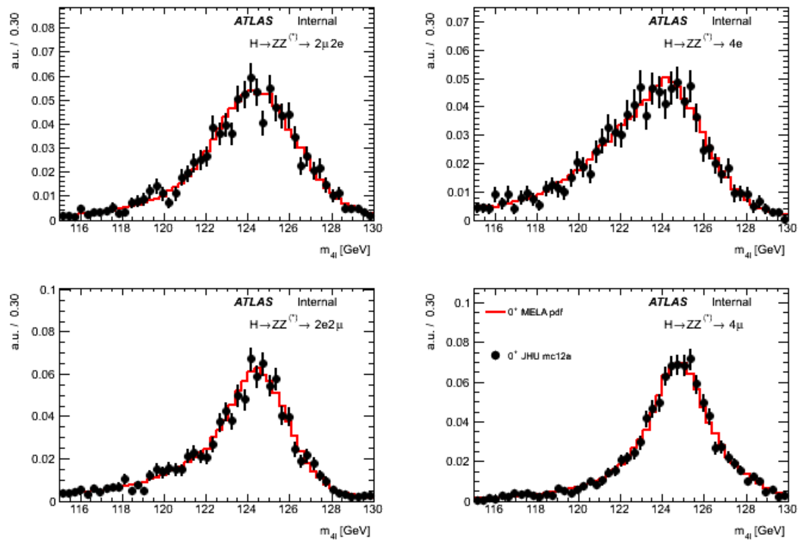

Figure 4.21: Comparison of the likelihood projection for a 0^+ Higgs-like resonance (red curve) and the corresponding JHU (black points) MC simulation for $m_{4\ell}$. From left to right and top to bottom: 4μ,$2\mu 2e$,$4e$ and $2e2\mu$ channels.

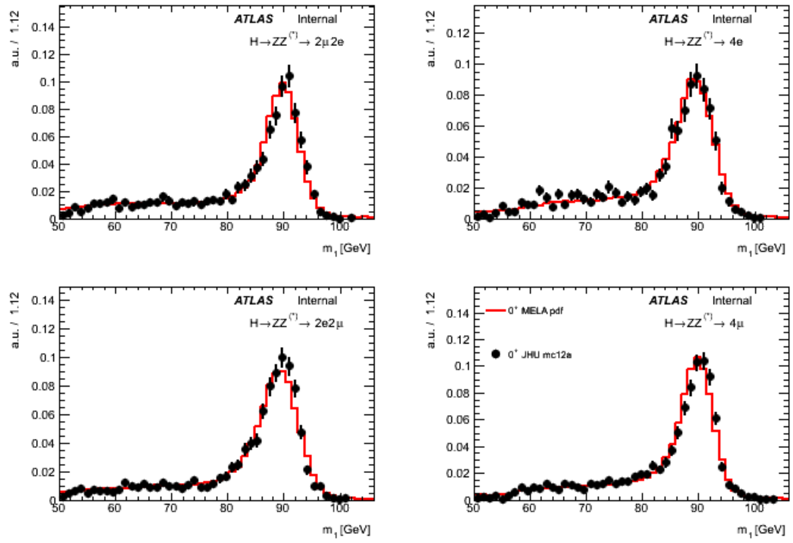

Figure 4.22: Comparison of the likelihood projection for a 0^+ Higgs-like resonance (red curve) and the corresponding JHU (black points) MC simulation for m_1. From left to right and top to bottom: 4μ,$2\mu2e$,$4e$ and $2e2\mu$ channels.

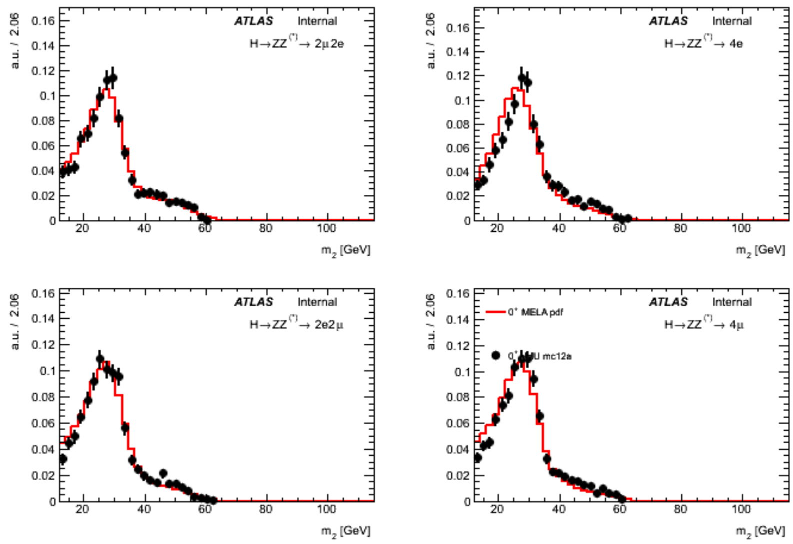

Figure 4.23: Comparison of the likelihood projection for a 0^+ Higgs-like resonance (red curve) and the corresponding JHU (black points) MC simulation for m_2. From left to right and top to bottom: 4μ,$2\mu2e$,$4e$ and $2e2\mu$ channels.

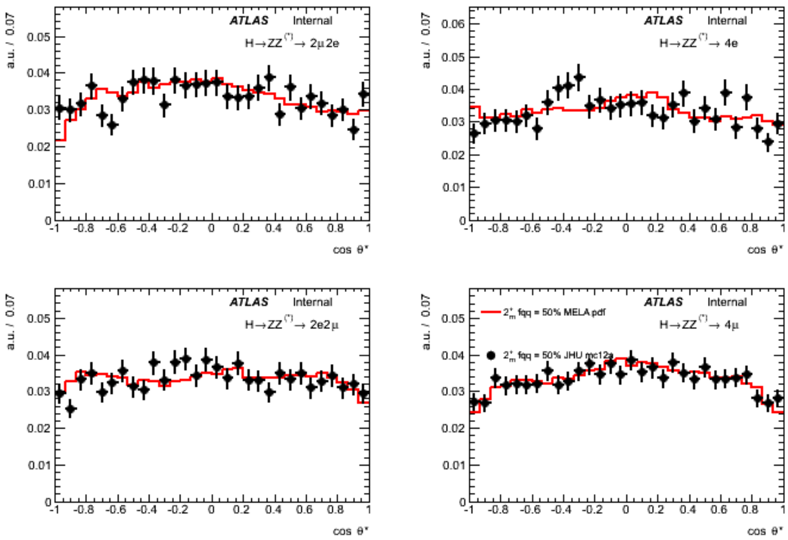

Figure 4.24: Comparison of the likelihood projection for a 2^{+} $f_{qq} = 50\%$ Higgs-like resonance (red curve) and the corresponding JHU (black points) MC simulation for $\cos\theta^{\star}$. From left to right and top to bottom: 4μ,$2\mu2e$,$4e$ and $2e2\mu$ channels.

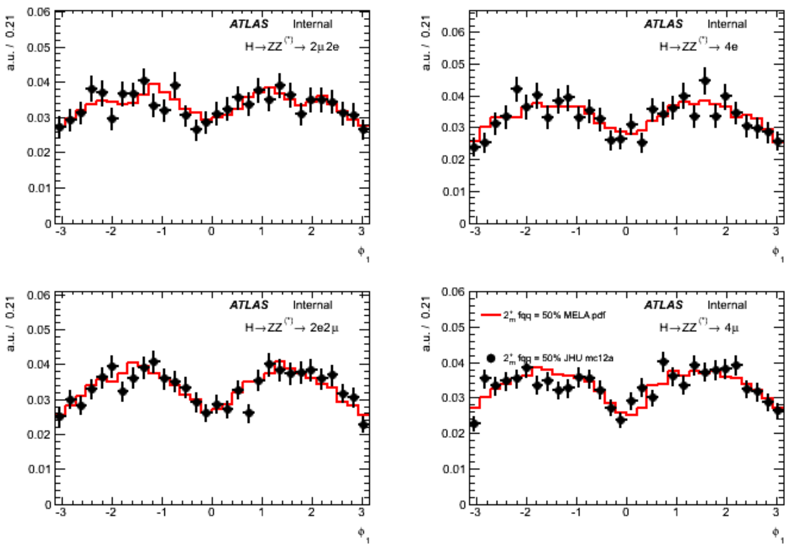

Figure 4.25: Comparison of the likelihood projection for a 2^{+} $f_{qq} = 50\%$ Higgs-like resonance (red curve) and the corresponding JHU (black points) MC simulation for ϕ_1. From left to right and top to bottom: 4μ,$2\mu2e$,$4e$ and $2e2\mu$ channels.

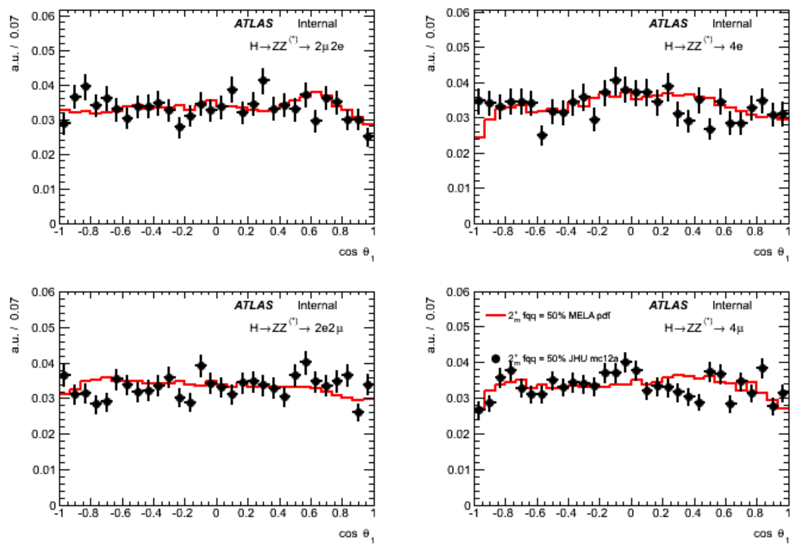

Figure 4.26: Comparison of the likelihood projection for a 2^+ $f_{qq} = 50\%$ Higgs-like resonance (red curve) and the corresponding JHU (black points) MC simulation for $\cos\theta_1$. From left to right and top to bottom: 4μ,$2\mu2e$,$4e$ and $2e2\mu$ channels.

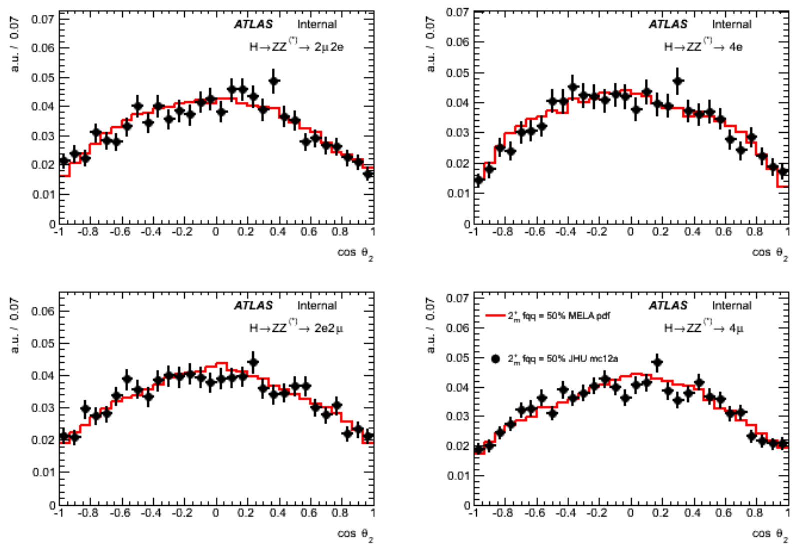

Figure 4.27: Comparison of the likelihood projection for a 2^+ $f_{qq} = 50\%$ Higgs-like resonance (red curve) and the corresponding JHU (black points) MC simulation for $\cos\theta_2$. From left to right and top to bottom: 4μ,$2\mu2e$,$4e$ and $2e2\mu$ channels.

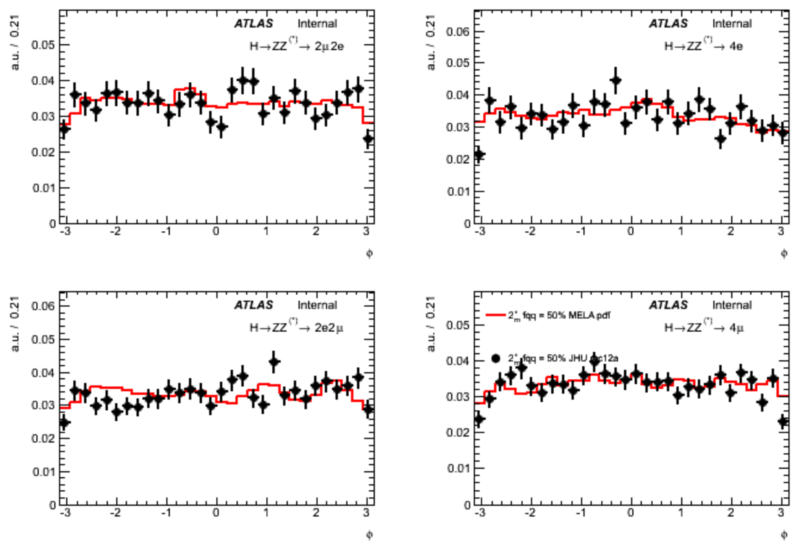

Figure 4.28: Comparison of the likelihood projection for a 2^{+} $f_{qq} = 50\%$ Higgs-like resonance (red curve) and the corresponding JHU (black points) MC simulation for ϕ. From left to right and top to bottom: 4μ,$2\mu 2e$,$4e$ and $2e2\mu$ channels.

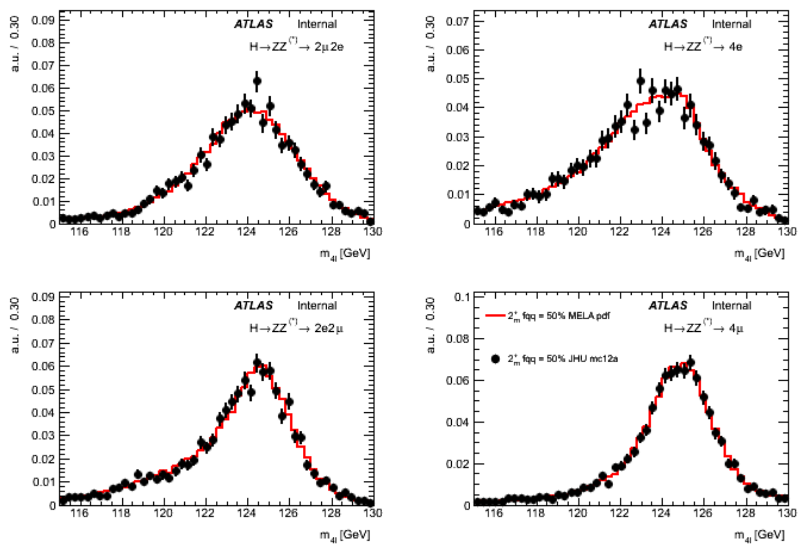

Figure 4.29: Comparison of the likelihood projection for a 2^{+} $f_{qq} = 50\%$ Higgs-like resonance (red curve) and the corresponding JHU (black points) MC simulation for $m_{4\ell}$. From left to right and top to bottom: 4μ,$2\mu 2e$,$4e$ and $2e2\mu$ channels.

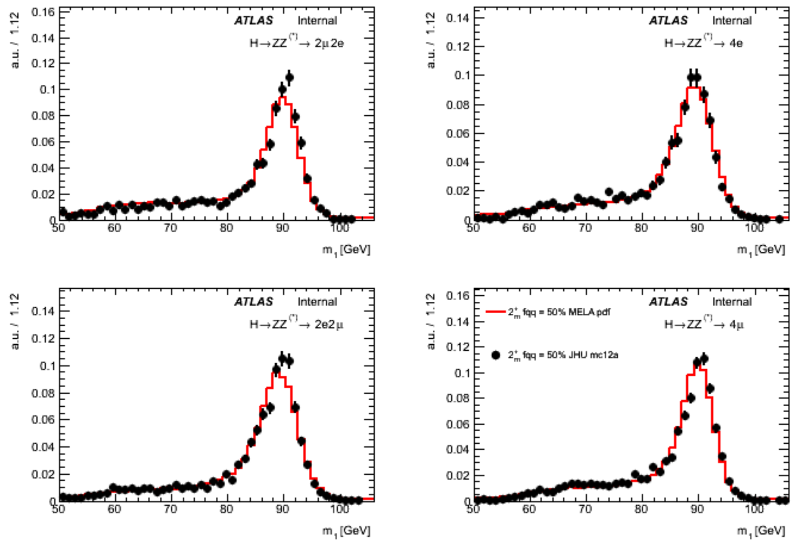

Figure 4.30: Comparison of the likelihood projection for a 2^+ $f_{qq} = 50\%$ Higgs-like resonance (red curve) and the corresponding JHU (black points) MC simulation for m_1. From left to right and top to bottom: 4μ,$2\mu2e$,$4e$ and $2e2\mu$ channels.

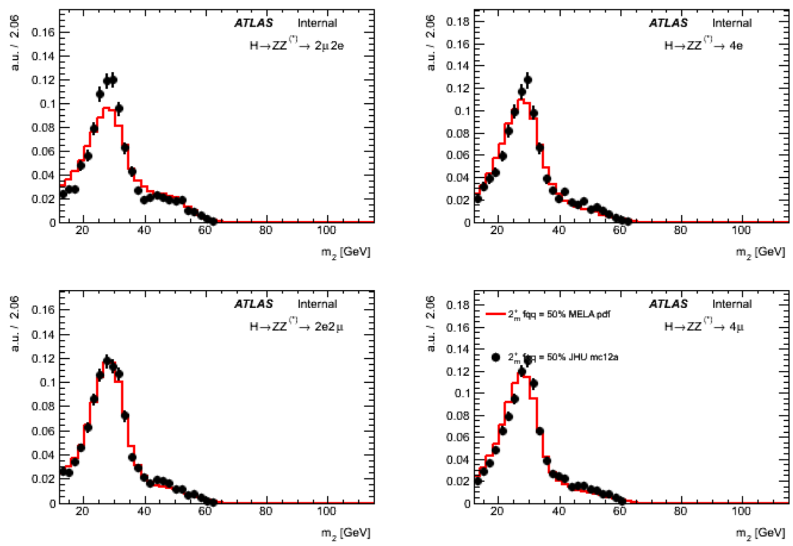

Figure 4.31: Comparison of the likelihood projection for a 2^+ $f_{qq} = 50\%$ Higgs-like resonance (red curve) and the corresponding JHU (black points) MC simulation for m_2. From left to right and top to bottom: 4μ,$2\mu2e$,$4e$ and $2e2\mu$ channels.

- the effects on the normalization of the reconstruction systematic uncertainties. The electron energy scale systematic in the channels containing electrons is the only one which not has a negligible effect;

- the ZZ and reducible background normalizations.

Systematic uncertainties of shape

The shape of the J^P-MELA discriminant is affected by additional systematic effects.

An uncertainty on the fraction of wrongly paired candidates has been derived by comparing the prediction for 0^+ provided by POWHEG and JHU MC generators (Table 4.5). The same relative uncertainty is assumed for all other spin parity hypotheses. This effect is treated as a shape systematic in the hypotheses testing procedure.

The limited statistics inside the control regions used to populate the reducible background templates introduce a statistical uncertainty.

Uncertainties on the Higgs p_{T} are expected to induce small variations on the acceptance as a function of the angular variables. The effect on the discriminating observables is very marginal. It is possible to re-derive all the acceptance fit and produce new J^P-MELA discriminants. The resulting change in shape is negligible and thus this effect has not been considered further.

The effect on the J^P-MELA discriminant of the systematic uncertainties described above is shown in Figure 4.32. Here the signal discriminants, for the illustration of the f_{RP} and electron energy scale systematic uncertainties, are shown for the 0^+ vs 0^- Hypothesis Test in the four electrons channel as an example. Moreover in Figure 4.33 a few examples of the reducible background discriminant are provided for the hypotheses test 0^+ vs 0^- and 0^+ vs 2^+ summing up the events in the four channels to reduce the statistical uncertainties.

4.8.8 The J^P-MELA discriminant

As previously mentioned, angular and mass shapes can also be exploited to measure the spin and parity of the new discovered resonance. The theoretical distributions in the $H \to ZZ^{(*)} \to 4\ell$ channel before acceptances alteration are shown in Figure 4.7 and Figure 4.8. Some angles (e.g., ϕ , $\cos\theta_1$) have large discrimination between odd and even parity. The case of spin-2 tends to lie in between the 0^+ and 0^- case.

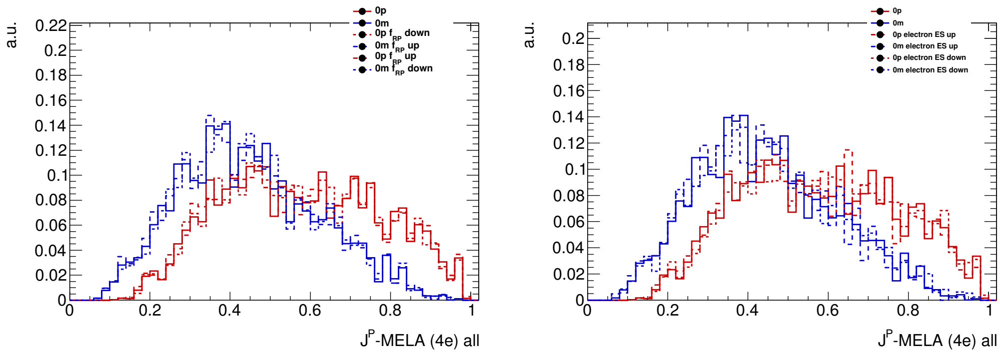

(a) (b)

Figure 4.32: J^P-MELA discriminant distributions obtained for the 0^+ vs 0^- Hypothesis Test obtained varying its shape within the (a) f_{RP} and (b) electron energy scale systematic uncertainties in the $4e$ channel using the MC simulated events.

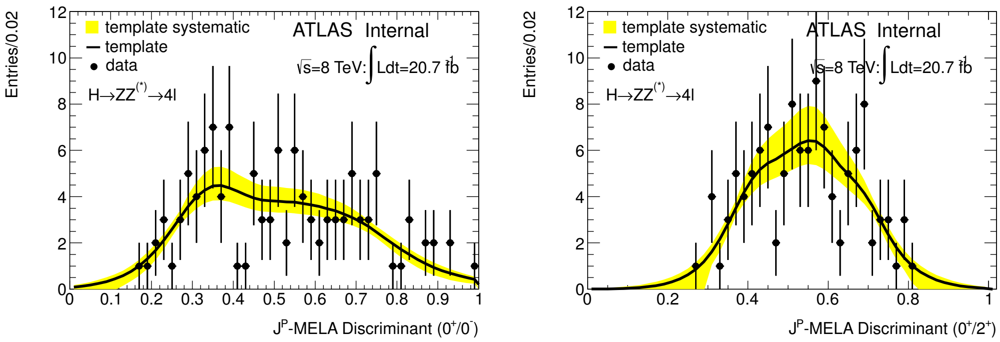

(a) (b)

Figure 4.33: J^P-MELA discriminant distributions obtained for the (a) 0^+ vs 0^- and (b) 0^+ vs 2^+ hypotheses test obtained for the reducible background. Here the black dots show the data distribution considering the four decay channels together, the continuous line is the smoothed distribution used as a discriminant for the reducible background in the given hypotheses test and the yellow band corresponds to the overall shape systematic uncertainty associated.

For Higgs boson discovery in $H \to ZZ^{(*)} \to 4\ell$ channel, the most optimal way to combine the discriminating variables in a single likelihood is by defining:

$$\mathrm{MELA}(\vec{x}) = \frac{P_{\mathrm{sig}}}{P_{\mathrm{sig}} + P_{\mathrm{bkg}}} = \left[1 + \frac{P_{\mathrm{bkg}}(m_1, m_2, \theta^*, \phi_1, \theta_1, \theta_2, \phi)}{P_{\mathrm{sig}}(m_1, m_2, \theta^*, \phi_1, \theta_1, \theta_2, \phi)}\right]^{-1} \tag{4.23}$$

where P_{sig} and P_{bkg} are the PDFs for signal and background.

Similarly to what happens for signal-background discrimination, the most optimal likelihood to discriminate between different spin-parity models can be built as

$$J^P\text{-MELA}(\vec{x}) = \frac{P(H_0|\vec{x})}{P(H_0|\vec{x}) + P(H_1|\vec{x})} = \left[1 + \frac{P(H_1|\vec{x})}{P(H_0|\vec{x})}\right]^{-1} \tag{4.24}$$

where $P(H_i|\vec{x})$ is the probability to have, in the hypothesis of type H_i, a vector of observables $\vec{x} = (m_{4\ell}, m_1, m_2, \vec{\Omega})$, which defines the full kinematic of the event itself. This discriminant is usually referred to as the *matrix element likelihood ratio*. In theory of probability it can be proven that it provides the highest possible discriminating power among the two hypotheses, in this case H_0 and H_1, provided that the probabilities $P(H_i, \vec{x})$ accurately describe the observed data.

Once the probability functions $P(H_i, \vec{x})$ are defined, the J^P-MELA discriminant is computed using fully simulated MC events. This way, if the probability density functions do not describe accurately the actual physics process, this will result in a sub-optimal discriminating power, *i.e.* in smaller separations between the two hypotheses tested, but no bias will be introduced in the procedure.

In Figures 4.34 to 4.37 the discriminants J^P-MELA for all the pairs of spin hypotheses are shown.

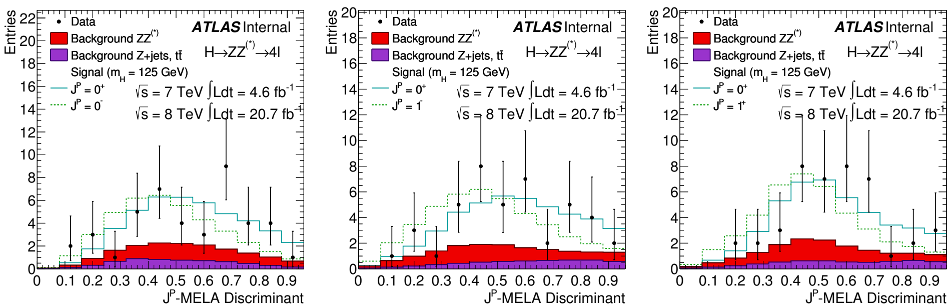

(a) (b) (c)

Figure 4.34: Distributions of the output of the MELA discriminants for data at $\sqrt{s} = 8\,\text{TeV}$ and Monte Carlo expectations. Each discriminant is shown for a pair of spin and parity hypotheses. (a) 0^+0^-; (b) 0^+1^-; (c) 0^+1^+.

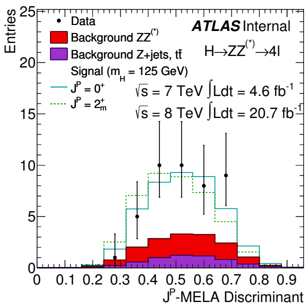

(a)

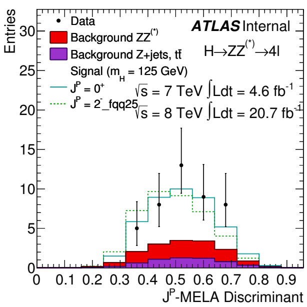

(b)

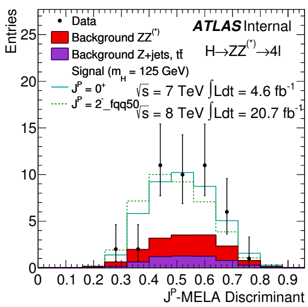

(c)

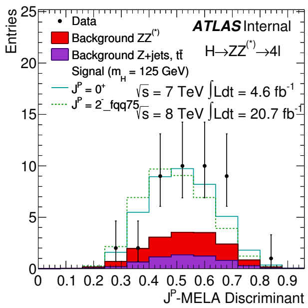

(d)

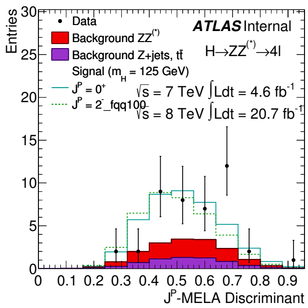

(e)

Figure 4.35: Distributions of the output of the MELA discriminants for data at $\sqrt{s} = 8\,\text{TeV}$ and Monte Carlo expectations. Each discriminant is shown for a pair of spin and parity hypotheses for the 0^+2^+ for different $gg/q\bar{q}$ admixtures: (a) $100\%gg$; (b) $75\%gg25\%q\bar{q}$; (c) $50\%gg50\%q\bar{q}$; $(d)25\%gg75\%q\bar{q}$; (e) $100\%q\bar{q}$.

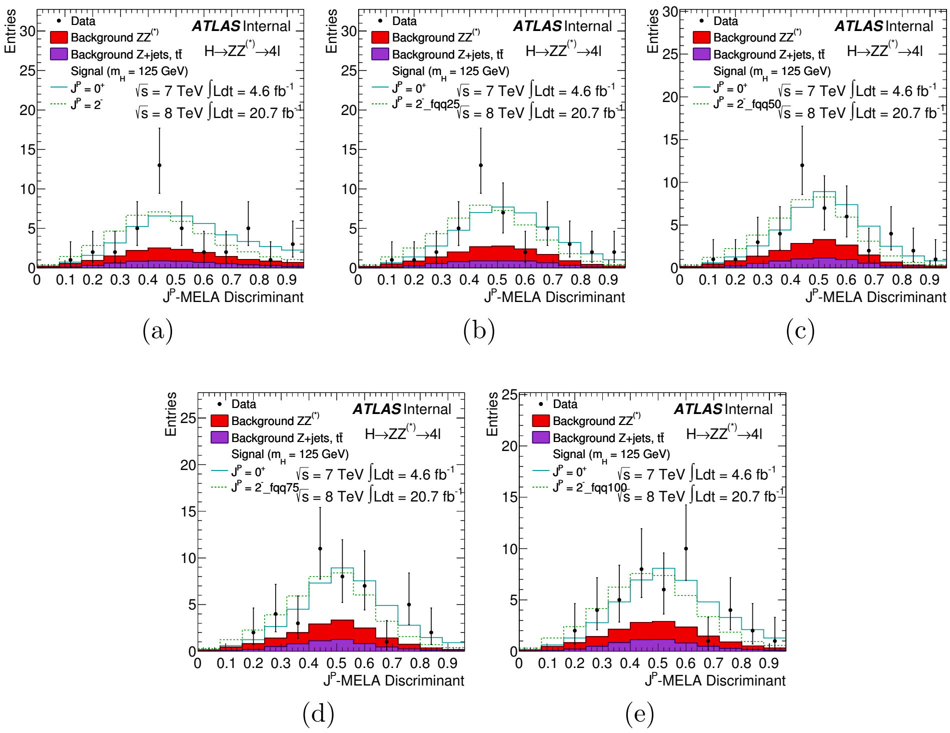

Figure 4.36: Distributions of the output of the MELA discriminants for data at $\sqrt{s} = 8\,\text{TeV}$ and Monte Carlo expectations. Each discriminant is shown for a pair of spin and parity hypotheses for the $0^{+}2^{-}$ for different $gg/q\bar{q}$ admixtures: (a) $100\%gg$; (b) $75\%gg25\%q\bar{q}$; (c) $50\%gg50\%q\bar{q}$; $(d)25\%gg75\%q\bar{q}$; (e) $100\%q\bar{q}$.

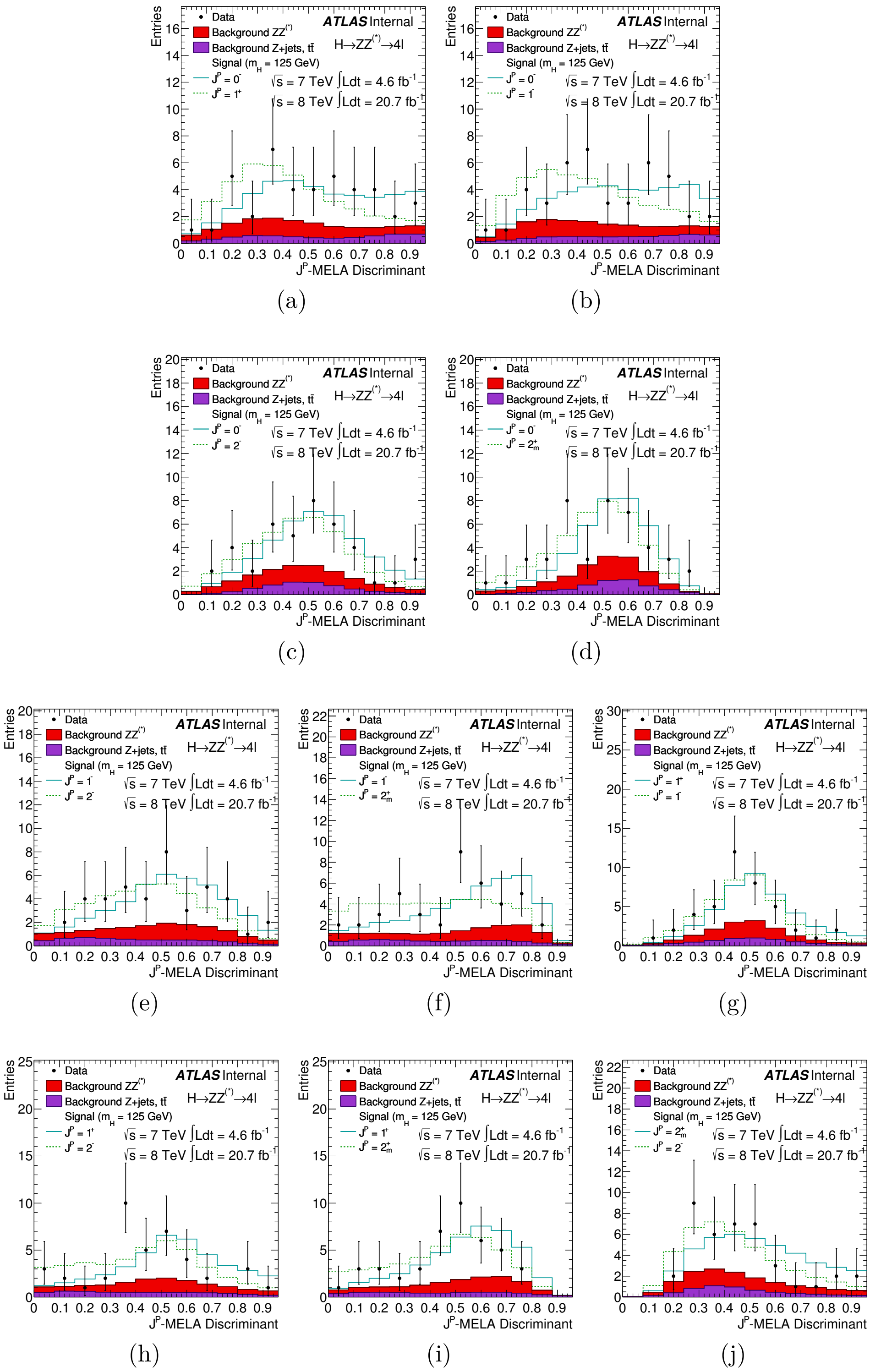

Figure 4.37: Distributions of the output of the MELA discriminants for data and Monte Carlo expectations at $\sqrt{s} = 8\,\text{TeV}$. Each discriminant is shown for a pair of spin and parity hypotheses. (a) 0^-1^+; (b) 0^-1^-. (c) 0^-2^-; (d) 0^-2^+;(e) 1^-2^-; (f) 1^-2^+; (g) 1^+1^-; (h) 1^+2^-; (i) 1^+2^+; (j) 2^+2^-.

Chapter 5

Analysis results

The construction of a good discriminant is essential to obtain the best power of separation between two different hypotheses. In this thesis work the J^P-MELA discriminant has been used. Studies to have realistic PDFs that give a good description of the spin-parity models have been performed and they have been shown in Chapter 4. In this Chapter the Hypothesis Test results are presented. The expected and the observed separation values for each spin pairs for 7 TeV, 8 TeV and for the combination of both the sets of measurements are reported in details.

5.1 Hypothesis Test results

The distributions for the test statistics described in Section 4.8.2 are shown. These distributions for each pair of alternative hypotheses are analysed and compared to data. About 500k pseudo-experiments for each hypothesis have been generated. In each experiment the expected number of signal and background events is fixed to the yield observed in the experiment. The estimates of the nuisance parameters are obtained from the fit of the likelihood model to the data. The signal strenght μ is profiled. In each pseudo-experiment, the expected number of signal and background events is fixed to the yield observed on data. All systematic uncertainties described in Section **??** are taken into account. The resulting distributions are shown from Figure 5.1 to Figure 5.4.

They provide an excellent reference on where the observed events are located comparing to the expected PDF of the discriminant. In Figure 5.1 it can be observed that in the case of the (0^+ vs 0^-) discriminant, the data are located approximately one σ to the left from the median of the 0^+ distribution. In this case this gives a strong preference towards 0^+. Similar observations can be made in all other cases including 0^+ as one of the hypotheses. It can also be noted that in no case data prefer 0^- and that in the case of (2^+_m vs 2^-) the data are located almost at the same distance from the medians of respective distributions. Figure 5.3 shows the median of the distributions of the log-ratio of the likelihoods, together with $\pm 1\sigma$ and $\pm 2\sigma$ bands around the tested hypothesis, for 0^+ vs 2^+_m with different values of the $q\bar{q}$ fraction, compared with the observation in data.

5.2 Expected Separations

Expected Separations on 2012 MC

The expected separation quantifies the separation between the two alternative spin-parity cases. Expected separations obtained comparing pair-wise the different spin-parity hypotheses are shown in terms of p–values and the corresponding number of Gaussian σ (between parentheses) in Table 5.1 for the 8 TeV dataset. In Table 5.2 the spin-2^+ and spin-2^- admixtures are tested against the SM Higgs-like resonace hypothesis for the 8 TeV dataset.

Expected Separations on 2011 MC

Table 5.3 shows the expected separations obtained for the 2011 analysis between the different signal hypotheses. The difference with respect to the results obtained for the 2012 analysis comes from the difference in yield and in signal to background ratio between the two analyses. In Tables 5.4 respectively various spin-2^+ and spin-2^- admixtures are tested against the SM Higgs-like resonance hypothesis.

Expected separations combining 2011 and 2012 MC

Table 5.5 shows the separations for 2011 and 2012 combined analysis. The systematic uncertainties are considered, conservatively, fully correlated between the two analyses. In Tables 5.6 various spin-2^+ and spin-2^- admixtures are tested against the SM Higgs-like resonance hypothesis.

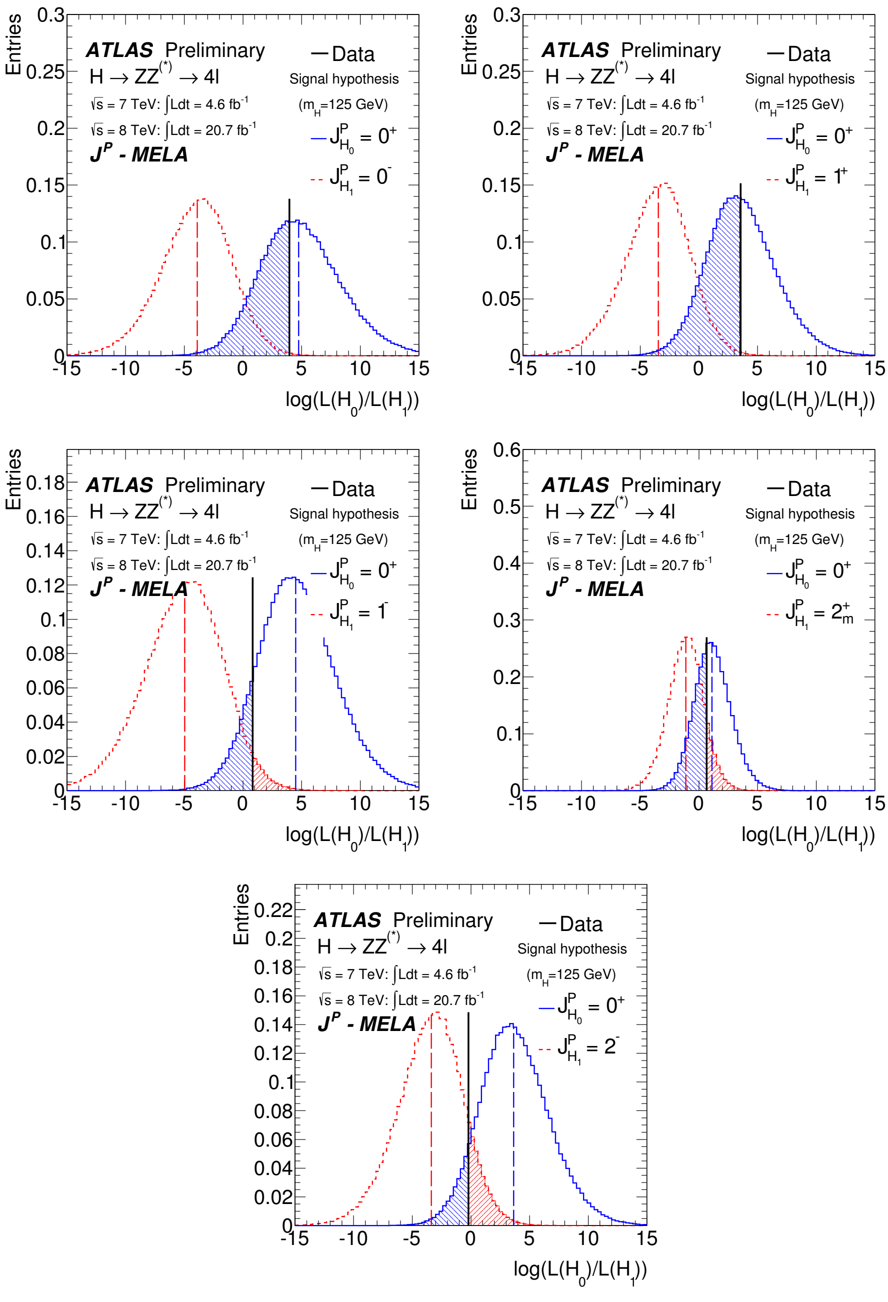

Figure 5.1: Distributions of the log-ratio of the likelihoods for each pair of spin and parity hypotheses and comparison to the observation in data.

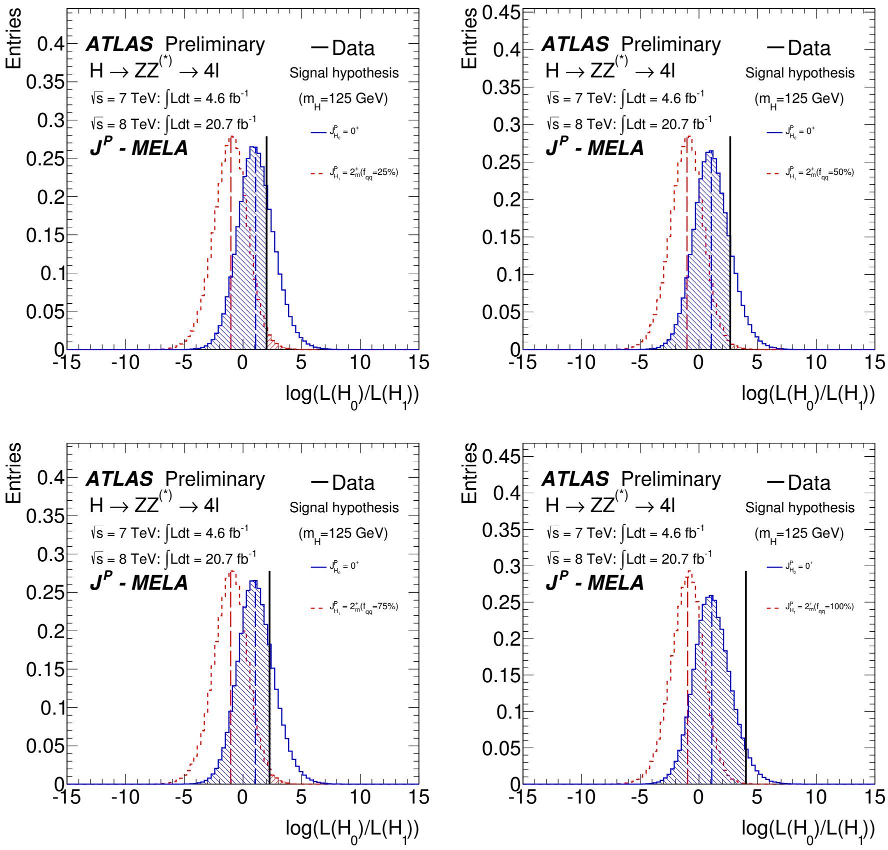

Figure 5.2: Distributions of the log-ratio of the likelihoods for each pair of spin and parity hypotheses and comparison to the observation in data.

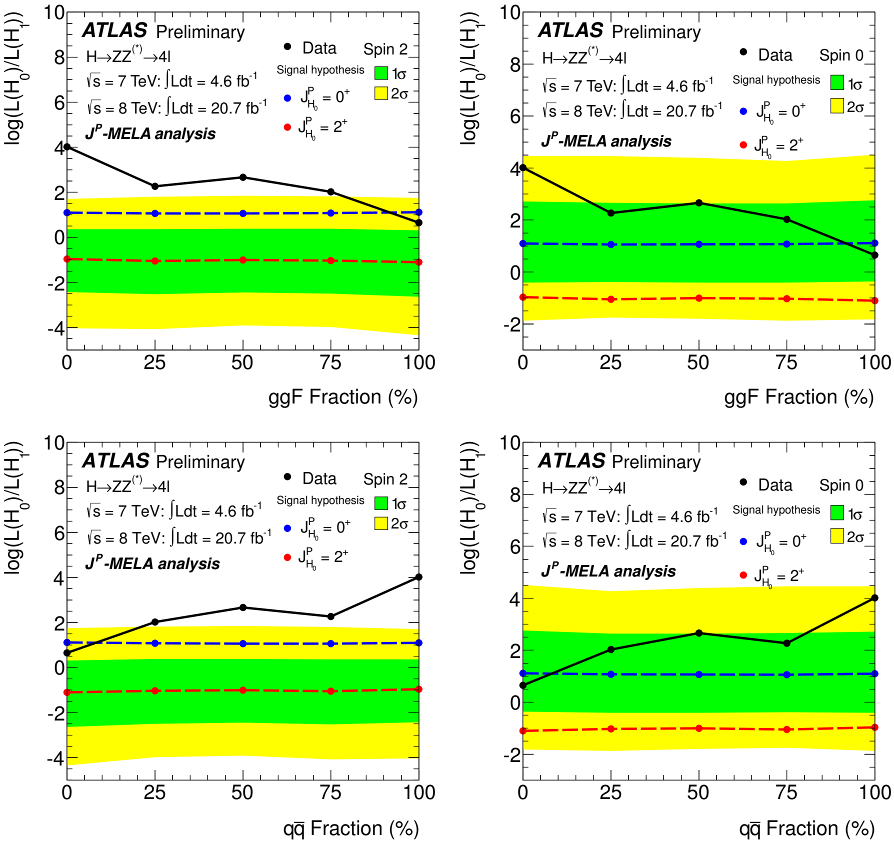

Figure 5.3: Median of the distributions of the log-ratio of the likelihoods for 0^+ vs 2^+_m with different values of the $q\bar{q}$ fraction, compared with the observation in data.

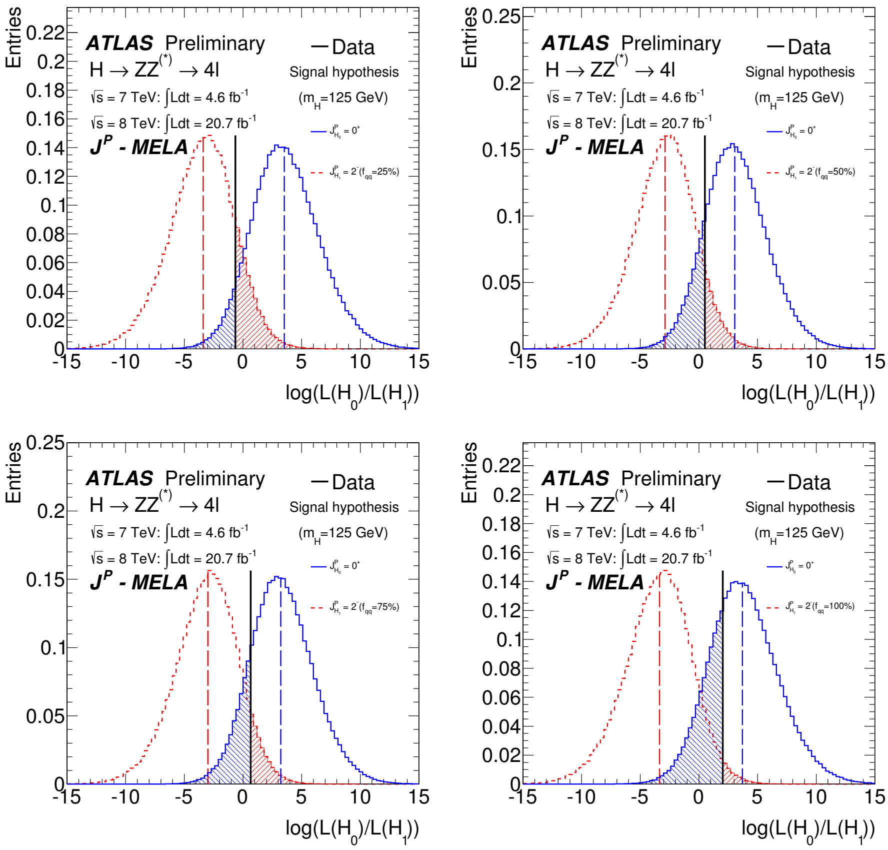

Figure 5.4: Distributions of the log-ratio of the likelihoods for each pair of spin and parity hypotheses and comparison to the observation in data.

tested\assumed	0^+	0^-	1^+	1^-	2^+_m	2^-
0^+	- -	0.0121 ± 0.0005 (2.2538 ± 0.0153)	0.0278 ± 0.0007 (1.9145 ± 0.0113)	0.0121 ± 0.0005 (2.2544 ± 0.0153)	0.1331 ± 0.0015 (1.1118 ± 0.0070)	0.0206 ± 0.0006 (2.0419 ± 0.0126)
0^-	0.0117 ± 0.0005 (2.2657 ± 0.0155)	- -	0.0050 ± 0.0003 (2.5728 ± 0.0214)	0.0055 ± 0.0003 (2.5446 ± 0.0207)	0.0249 ± 0.0007 (1.9612 ± 0.0118)	0.0347 ± 0.0008 (1.8160 ± 0.0105)
1^+	0.0206 ± 0.0006 (2.0407 ± 0.0126)	0.0029 ± 0.0002 (2.7578 ± 0.0267)	- -	0.0315 ± 0.0008 (1.8586 ± 0.0109)	0.0239 ± 0.0007 (1.9795 ± 0.0120)	0.0054 ± 0.0003 (2.5483 ± 0.0208)
1^-	0.0091 ± 0.0004 (2.3616 ± 0.0170)	0.0040 ± 0.0003 (2.6540 ± 0.0235)	0.0319 ± 0.0008 (1.8534 ± 0.0108)	- -	0.0044 ± 0.0003 (2.6210 ± 0.0226)	0.0155 ± 0.0005 (2.1571 ± 0.0140)
2^+_m	0.1261 ± 0.0015 (1.1451 ± 0.0071)	0.0250 ± 0.0007 (1.9605 ± 0.0118)	0.0321 ± 0.0008 (1.8502 ± 0.0108)	0.0052 ± 0.0003 (2.5610 ± 0.0211)	- -	0.0140 ± 0.0005 (2.1960 ± 0.0145)
2^-	0.0201 ± 0.0006 (2.0521 ± 0.0127)	0.0383 ± 0.0008 (1.7711 ± 0.0102)	0.0091 ± 0.0004 (2.3632 ± 0.0171)	0.0199 ± 0.0006 (2.0562 ± 0.0128)	0.0129 ± 0.0005 (2.2286 ± 0.0149)	- -

Table 5.1: Expected separations between different spin hypotheses using 8 TeV simulation.

tested\assumed	0^+	$2^+(25\%qq)$	$2^+(50\%qq)$	$2^+(75\%qq)$	$2^+(100\%qq)$
0^+	- -	0.1317 ± 0.0015 (1.1185 ± 0.0070)	0.1378 ± 0.0015 (1.0900 ± 0.0069)	0.1294 ± 0.0015 (1.1294 ± 0.0070)	0.1253 ± 0.0015 (1.1491 ± 0.0071)
$2^+(25\%qq)$	0.1328 ± 0.0015 (1.1133 ± 0.0070)				
$2^+(50\%qq)$	0.1317 ± 0.0015 (1.1185 ± 0.0070)				
$2^+(75\%qq)$	0.1244 ± 0.0015 (1.1532 ± 0.0071)				
$2^+(100\%qq)$	0.1225 ± 0.0014 (1.1625 ± 0.0071)				

tested\assumed	0^+	$2^-(25\%qq)$	$2^-(50\%qq)$	$2^-(75\%qq)$	$2^-(100\%qq)$
0^+	- -	0.0248 ± 0.0007 (1.9625 ± 0.0118)	0.0318 ± 0.0008 (1.8556 ± 0.0108)	0.0309 ± 0.0008 (1.8680 ± 0.0109)	0.0226 ± 0.0007 (2.0035 ± 0.0122)
$2^-(25\%qq)$	0.0241 ± 0.0007 (1.9750 ± 0.0119)				
$2^-(50\%qq)$	0.0303 ± 0.0008 (1.8761 ± 0.0110)				
$2^-(75\%qq)$	0.0313 ± 0.0008 (1.8619 ± 0.0109)				
$2^-(100\%qq)$	0.0218 ± 0.0006 (2.0178 ± 0.0123)				

Table 5.2: Expected separations between different spin hypotheses using 8 TeV simulation.

tested\assumed	0^+	0^-	1^+	1^-	2^+_m	2^-
0^+	- -	0.1521 ± 0.0015 (1.0274 ± 0.0066)	0.1922 ± 0.0017 (0.8697 ± 0.0062)	0.1483 ± 0.0015 (1.0438 ± 0.0066)	0.3031 ± 0.0020 (0.5156 ± 0.0057)	0.1698 ± 0.0016 (0.9549 ± 0.0064)
0^-	0.1489 ± 0.0015 (1.0413 ± 0.0066)	- -	0.1250 ± 0.0014 (1.1503 ± 0.0069)	0.1203 ± 0.0014 (1.1733 ± 0.0070)	0.1698 ± 0.0016 (0.9548 ± 0.0064)	0.2025 ± 0.0017 (0.8326 ± 0.0061)
1^+	0.1717 ± 0.0016 (0.9476 ± 0.0064)	0.0875 ± 0.0012 (1.3564 ± 0.0077)	- -	0.1985 ± 0.0017 (0.8470 ± 0.0062)	0.1814 ± 0.0017 (0.9100 ± 0.0063)	0.1094 ± 0.0013 (1.2298 ± 0.0072)
1^-	0.1333 ± 0.0015 (1.1110 ± 0.0068)	0.1067 ± 0.0013 (1.2444 ± 0.0072)	0.2002 ± 0.0017 (0.8408 ± 0.0062)	- -	0.1144 ± 0.0014 (1.2033 ± 0.0071)	0.1594 ± 0.0016 (0.9971 ± 0.0065)
2^+_m	0.2564 ± 0.0019 (0.6545 ± 0.0058)	0.1891 ± 0.0017 (0.8813 ± 0.0062)	0.1969 ± 0.0017 (0.8527 ± 0.0062)	0.1271 ± 0.0014 (1.1400 ± 0.0069)	- -	0.1590 ± 0.0016 (0.9987 ± 0.0065)
2^-	0.1652 ± 0.0016 (0.9732 ± 0.0064)	0.2028 ± 0.0017 (0.8317 ± 0.0061)	0.1369 ± 0.0015 (1.0944 ± 0.0068)	0.1777 ± 0.0016 (0.9243 ± 0.0063)	0.1579 ± 0.0016 (1.0033 ± 0.0065)	- -

Table 5.3: Expected separations between different spin hypotheses using 7 TeV simulation.

tested\assumed	0^+	$2^+(25\%qq)$	$2^+(50\%qq)$	$2^+(75\%qq)$	$2^+(100\%qq)$
0^+	- -	0.2939 ± 0.0020 (0.5420 ± 0.0057)	0.2907 ± 0.0020 (0.5514 ± 0.0057)	0.2878 ± 0.0020 (0.5598 ± 0.0057)	0.2929 ± 0.0020 (0.5450 ± 0.0057)
$2^+(25\%qq)$	0.2613 ± 0.0019 (0.6394 ± 0.0058)				
$2^+(50\%qq)$	0.2571 ± 0.0019 (0.6525 ± 0.0058)				
$2^+(75\%qq)$	0.2487 ± 0.0019 (0.6787 ± 0.0059)				
$2^+(100\%qq)$	0.2551 ± 0.0019 (0.6586 ± 0.0058)				

tested assumed	0^+	$2^-(25\%qq)$	$2^-(50\%qq)$	$2^-(75\%qq)$	$2^-(100\%qq)$
0^+	- -	0.1759 ± 0.0016 (0.9310 ± 0.0063)	0.1835 ± 0.0017 (0.9020 ± 0.0063)	0.1822 ± 0.0017 (0.9071 ± 0.0063)	0.1777 ± 0.0016 (0.9240 ± 0.0063)
$2^-(25\%qq)$	0.1687 ± 0.0016 (0.9593 ± 0.0064)				
$2^-(50\%qq)$	0.1882 ± 0.0017 (0.8847 ± 0.0062)				
$2^-(75\%qq)$	0.1892 ± 0.0017 (0.8808 ± 0.0062)				
$2^-(100\%qq)$	0.1780 ± 0.0016 (0.9230 ± 0.0063)				

Table 5.4: Expected separations between different spin hypotheses using 7 TeV simulation.

tested\assumed	0^+	0^-	1^+	1^-	2_m^+	2^-
0^+	- -	0.0025 (2.8116)	0.0046 (2.6015)	0.0009 (3.1167)	0.0676 (1.4936)	0.0043 (2.6291)
0^-	0.0011 (3.0647)	- -	0.0004 (3.3715)	0.0004 (3.3580)	0.0044 (2.6176)	0.0096 (2.3408)
1^+	0.0031 (2.7376)	0.0004 (3.3876)	- -	0.0074 (2.4391)	0.0031 (2.7328)	0.0005 (3.2664)
1^-	0.0010 (3.0883)	0.0005 (3.2777)	0.0067 (2.4727)	- -	0.0003 (3.4183)	0.0044 (2.6232)
2_m^+	0.0639 (1.5232)	0.0073 (2.4432)	0.0040 (2.6503)	0.0004 (3.3876)	- -	0.0023 (2.8291)
2^-	0.0032 (2.7247)	0.0082 (2.4015)	0.0011 (3.0490)	0.0028 (2.7730)	0.0013 (3.0015)	- -

Table 5.5: Expected separations between different spin hypotheses combining 7 and 8 TeV results.

tested\assumed	0^+	$2^+_m(f_{qq}=25\%)$	$2^+_m(f_{qq}=50\%)$	$2^+_m(f_{qq}=75\%)$	$2^+_m(f_{qq}=100\%)$
0^+	- -	0.0750 (1.4397)	0.0775 (1.4220)	0.0734 (1.4512)	0.0817 (1.3937)
$2^+_m(f_{qq}=25\%)$	0.0674 (1.4955)				
$2^+_m(f_{qq}=50\%)$	0.0678 (1.4922)				
$2^+_m(f_{qq}=75\%)$	0.0686 (1.4863)				
$2^+_m(f_{qq}=100\%)$	0.0652 (1.5122)				

tested assumed	0^+	$2^-(f_{qq}=25\%)$	$2^-(f_{qq}=50\%)$	$2^-(f_{qq}=75\%)$	$2^-(f_{qq}=100\%)$
0^+	- -	0.0043 (2.6239)	0.0078 (2.4196)	0.0065 (2.4828)	0.0045 (2.6133)
$2^-(f_{qq}=25\%)$	0.0039 (2.6637)				
$2^-(f_{qq}=50\%)$	0.0065 (2.4829)				
$2^-(f_{qq}=75\%)$	0.0057 (2.5300)				
$2^-(f_{qq}=100\%)$	0.0034 (2.7108)				

Table 5.6: Expected separations between different spin hypotheses combining 7 and 8 TeV results.

5.3 Observed Separations

Observed separations obtained comparing pair-wise the different spin-parity hypotheses are shown in terms of p-values and the corresponding number of Gaussian σ (between parentheses) in Tables:

- Table 5.7 and Tables 5.8 for 8 TeV;
- Table 5.9 and Tables 5.10 for 7 TeV;
- Table 5.11 and Tables 5.12 for 7 TeV and 8 TeV combined.

The integrated luminosity is $4.6\,\mathrm{fb}^{-1}$ at 7 TeV and $20.7\,\mathrm{fb}^{-1}$ at 8 TeV. The samples with different energies are supposed as independent measurements. Thus the correlations between the systematic uncertainties are taken into account for the combination of the results.

tested\assumed	0^+	0^-	1^+	1^-	2_m^+	2^-
0^+	- -	0.3540 ± 0.0021 (0.3746 ± 0.0057)	0.2460 ± 0.0019 (0.6872 ± 0.0060)	0.0266 ± 0.0007 (1.9336 ± 0.0115)	0.4817 ± 0.0022 (0.0458 ± 0.0055)	0.0572 ± 0.0010 (1.5789 ± 0.0089)
0^-	0.0051 ± 0.0003 (2.5702 ± 0.0213)	- -	0.0273 ± 0.0007 (1.9218 ± 0.0114)	0.0037 ± 0.0003 (2.6778 ± 0.0242)	0.0580 ± 0.0010 (1.5717 ± 0.0089)	0.1429 ± 0.0015 (1.0673 ± 0.0068)
1^+	0.0274 ± 0.0007 (1.9212 ± 0.0114)	0.0807 ± 0.0012 (1.4006 ± 0.0080)	- -	0.1347 ± 0.0015 (1.1045 ± 0.0069)	0.1776 ± 0.0017 (0.9247 ± 0.0065)	0.0111 ± 0.0005 (2.2883 ± 0.0158)
1^-	0.1415 ± 0.0015 (1.0735 ± 0.0068)	0.2645 ± 0.0019 (0.6295 ± 0.0059)	0.1013 ± 0.0013 (1.2741 ± 0.0075)	- -	0.1196 ± 0.0014 (1.1772 ± 0.0072)	0.4324 ± 0.0022 (0.1703 ± 0.0055)
2_m^+	0.0754 ± 0.0012 (1.4364 ± 0.0082)	0.1855 ± 0.0017 (0.8946 ± 0.0064)	0.0472 ± 0.0009 (1.6727 ± 0.0095)	0.0143 ± 0.0005 (2.1890 ± 0.0144)	- -	0.0396 ± 0.0009 (1.7553 ± 0.0101)
2^-	0.1653 ± 0.0016 (0.9730 ± 0.0066)	0.1163 ± 0.0014 (1.1938 ± 0.0072)	0.2074 ± 0.0018 (0.8153 ± 0.0062)	0.0055 ± 0.0003 (2.5421 ± 0.0207)	0.1473 ± 0.0016 (1.0479 ± 0.0068)	- -

Table 5.7: Observed separations between different spin hypotheses using 8 TeV data using the MELA approach.

tested\assumed	0^+	$2^+(25\%qq)$	$2^+(50\%qq)$	$2^+(75\%qq)$	$2^+(100\%qq)$
0^+	- -	0.7926 ± 0.0018 (-0.8156 ± 0.0062)	0.8373 ± 0.0016 (-0.9833 ± 0.0066)	0.7904 ± 0.0018 (-0.8079 ± 0.0062)	0.9423 ± 0.0010 (-1.5745 ± 0.0089)
$2^+(25\%qq)$	0.0117 ± 0.0005 (2.2663 ± 0.0155)				
$2^+(50\%qq)$	0.0064 ± 0.0004 (2.4871 ± 0.0195)				
$2^+(75\%qq)$	0.0120 ± 0.0005 (2.2575 ± 0.0154)				
$2^+(100\%qq)$	0.0010 ± 0.0001 (3.0820 ± 0.0409)				

tested\assumed	0^+	$2^-(25\%qq)$	$2^-(50\%qq)$	$2^-(75\%qq)$	$2^-(100\%qq)$
0^+	- -	0.0344 ± 0.0008 (1.8202 ± 0.0105)	0.0811 ± 0.0012 (1.3974 ± 0.0080)	0.0997 ± 0.0013 (1.2832 ± 0.0075)	0.2034 ± 0.0018 (0.8297 ± 0.0063)
$2^-(25\%qq)$	0.2507 ± 0.0019 (0.6723 ± 0.0060)				
$2^-(50\%qq)$	0.1671 ± 0.0016 (0.9656 ± 0.0066)				
$2^-(75\%qq)$	0.1311 ± 0.0015 (1.1213 ± 0.0070)				
$2^-(100\%qq)$	0.0384 ± 0.0008 (1.7695 ± 0.0102)				

Table 5.8: Observed separations between different spin hypotheses using 8 TeV data using the MELA approach.

tested\assumed	0^+	0^-	1^+	1^-	2^+_m	2^-
0^+	- -	0.5957 ± 0.0021 (-0.2423 ± 0.0055)	0.8986 ± 0.0013 (-1.2738 ± 0.0073)	0.8423 ± 0.0016 (-1.0039 ± 0.0065)	0.1376 ± 0.0015 (1.0912 ± 0.0067)	0.5470 ± 0.0021 (-0.1182 ± 0.0054)
0^-	0.0898 ± 0.0012 (1.3417 ± 0.0076)	- -	0.6916 ± 0.0020 (-0.5004 ± 0.0057)	0.6238 ± 0.0021 (-0.3154 ± 0.0055)	0.1704 ± 0.0016 (0.9527 ± 0.0064)	0.6410 ± 0.0021 (-0.3612 ± 0.0055)
1^+	0.0069 ± 0.0004 (2.4612 ± 0.0185)	0.0118 ± 0.0005 (2.2647 ± 0.0151)	- -	0.1741 ± 0.0016 (0.9383 ± 0.0064)	0.0015 ± 0.0002 (2.9671 ± 0.0341)	0.0095 ± 0.0004 (2.3447 ± 0.0164)
1^-	0.0074 ± 0.0004 (2.4352 ± 0.0180)	0.0335 ± 0.0008 (1.8319 ± 0.0104)	0.5306 ± 0.0022 (-0.0768 ± 0.0054)	- -	0.0132 ± 0.0005 (2.2209 ± 0.0145)	0.0073 ± 0.0004 (2.4406 ± 0.0181)
2^+_m	0.7083 ± 0.0020 (-0.5483 ± 0.0057)	0.5142 ± 0.0022 (-0.0356 ± 0.0054)	0.9467 ± 0.0010 (-1.6140 ± 0.0089)	0.7395 ± 0.0019 (-0.6417 ± 0.0058)	- -	0.4928 ± 0.0022 (0.0181 ± 0.0054)
2^-	0.1398 ± 0.0015 (1.0813 ± 0.0067)	0.0844 ± 0.0012 (1.3758 ± 0.0077)	0.7681 ± 0.0018 (-0.7325 ± 0.0060)	0.8873 ± 0.0014 (-1.2124 ± 0.0071)	0.1456 ± 0.0015 (1.0556 ± 0.0066)	- -

Table 5.9: Observed separations between different spin hypotheses using 7 TeV data using the MELA approach.

tested\assumed	0^+	$2^+(25\%qq)$	$2^+(50\%qq)$	$2^+(75\%qq)$	$2^+(100\%qq)$
0^+	- -	0.2316 ± 0.0018 (0.7337 ± 0.0060)	0.5888 ± 0.0021 (-0.2245 ± 0.0054)	0.5063 ± 0.0022 (-0.0158 ± 0.0054)	0.7425 ± 0.0019 (-0.6512 ± 0.0058)
$2^+(25\%qq)$	0.5763 ± 0.0021 (-0.1925 ± 0.0054)				
$2^+(50\%qq)$	0.2176 ± 0.0018 (0.7805 ± 0.0060)				
$2^+(75\%qq)$	0.2859 ± 0.0019 (0.5654 ± 0.0057)				
$2^+(100\%qq)$	0.0991 ± 0.0013 (1.2864 ± 0.0074)				

tested\assumed	0^+	$2^-(25\%qq)$	$2^-(50\%qq)$	$2^-(75\%qq)$	$2^-(100\%qq)$
0^+	- -	0.5756 ± 0.0021 (-0.1908 ± 0.0054)	0.7107 ± 0.0020 (-0.5555 ± 0.0057)	0.6305 ± 0.0021 (-0.3331 ± 0.0055)	0.6095 ± 0.0021 (-0.2780 ± 0.0055)
$2^-(25\%qq)$	0.1153 ± 0.0014 (1.1989 ± 0.0071)				
$2^-(50\%qq)$	0.0682 ± 0.0011 (1.4896 ± 0.0083)				
$2^-(75\%qq)$	0.1051 ± 0.0013 (1.2529 ± 0.0073)				
$2^-(100\%qq)$	0.0990 ± 0.0013 (1.2872 ± 0.0074)				

Table 5.10: Observed separations between different spin hypotheses using 7 TeV data using the MELA approach.

tested\assumed	0^+	0^-	1^+	1^-	2^+_m	2^-
0^+	- -	0.4046 (0.2416)	0.5075 (−0.0188)	0.1123 (1.2143)	0.3793 (0.3074)	0.0766 (1.4286)
0^-	0.0022 (2.8445)	- -	0.1019 (1.2707)	0.0105 (2.3093)	0.0378 (1.7766)	0.1681 (0.9616)
1^+	0.0028 (2.7690)	0.0134 (2.2153)	- -	0.0874 (1.3567)	0.0204 (2.0451)	0.0013 (3.0158)
1^-	0.0274 (1.9204)	0.1288 (1.1320)	0.1360 (1.0986)	- -	0.0300 (1.8810)	0.1680 (0.9621)
2^+_m	0.1127 (1.2122)	0.2126 (0.7976)	0.2499 (0.6747)	0.0498 (1.6470)	- -	0.0504 (1.6414)
2^-	0.1070 (1.2428)	0.0778 (1.4202)	0.3875 (0.2859)	0.0373 (1.7830)	0.0995 (1.2844)	- -

Table 5.11: Observed separations between different spin hypotheses combining 7 and 8 TeV MELA results.

tested\assumed	0^+	$2^+(25\%qq)$	$2^+(50\%qq)$	$2^+(75\%qq)$	$2^+(100\%qq)$
0^+	- -	0.7309 (-0.6154)	0.8411 (-0.9988)	0.7789 (-0.7685)	0.9550 (-1.6952)
$2^+(25\%qq)$	0.0166 (2.1297)				
$2^+(50\%qq)$	0.0056 (2.5346)				
$2^+(75\%qq)$	0.0115 (2.2748)				
$2^+(100\%qq)$	0.0005 (3.3048)				

tested\assumed	0^+	$2^-(25\%qq)$	$2^-(50\%qq)$	$2^-(75\%qq)$	$2^-(100\%qq)$
0^+	- -	0.0568 (1.5823)	0.1521 (1.0275)	0.1539 (1.0200)	0.2729 (0.6042)
$2^-(25\%qq)$	0.1446 (1.0600)				
$2^-(50\%qq)$	0.0765 (1.4290)				
$2^-(75\%qq)$	0.0680 (1.4912)				
$2^-(100\%qq)$	0.0180 (2.0980)				

Table 5.12: Observed separations between different spin hypotheses combining 7 and 8 TeV MELA results.

5.4 Summary results

It can be observed, that for all the pairs where the Standard Model 0^+ hypothesis is present, it is preferred over all the alternatives. It can be further noted that the in all cases the CP- odd hypothesis 0^- is disfavoured comparing to any alternative. In the case of spin-2 hypotheses, the data show no strong preferences. A small shift towards 2^+_m is however observed, also for all the 2^+_m admixtures. This can be attributed to the fact that the distributions of observables for the 2^+_m are very close to those of the 0^+ state. Similarly the data show no strong preferences for the 2^- hypothesis too.

The SM expectation of $J^{PC} = 0^+$ is currently the favorite model. The alternative spin and parity hypotheses are excluded in favour of 0^+ with the $1 - CL_\mathrm{s}$ confidence levels shown in Table 5.13.

Exclusion in favour of 0^+			
	expected p-value	observed p-value (σ)	$1 - CL_\mathrm{s}(\%)$
0^-	0.0011 (3.06)	0.0022 (2.84)	99.6
1^+	0.0031 (2.74)	0.0028 (2.77)	99.4
1^-	0.0010 (3.09)	0.0027 (1.92)	96.9
2^+_m	0.064 (1.52)	0.11 (1.21)	81.8
2^-	0.0032 (2.72)	0.11 (1.24)	88.4

Table 5.13: Expected and observed separations and the corresponding number of Gaussian σ (between parentheses) between different spin hypotheses combining 7 and 8 TeV MELA results.

Conclusions

This thesis work has been dedicated to the study of the spin-parity properties of a Higgs-like boson and in particular of the new discovered boson in the $H \to ZZ^{(*)} \to 4\ell$ decay channel. This analysis refers to the whole dataset colleted in proton-proton collisions by the ATLAS experiment at LHC during the 2011 with a luminosity of $4.6\,\mathrm{fb}^{-1}$ and $\sqrt{s} = 7\,\mathrm{TeV}$ and during the 2012 with a luminosity of $20.7\,\mathrm{fb}^{-1}$ and $\sqrt{s} = 8\,\mathrm{TeV}$. The event selection criteria and the estimation of the background have been discussed in Section 4.3.

Presently the number of observed events is 32 inside a mass window of $125 \pm 5\,\mathrm{GeV}$, with 27 events expected considering both the background and the signal at 125 GeV. The only-background hypothesis is excluded with a p-value of 2.7×10^{-11}, corresponding to a significance of 6.6σ. In $H \to ZZ^{(*)} \to 4\ell$ the value of the measured mass is $m_H = 124.3^{+0.6}_{-0.5}(\mathrm{stat})^{+0.5}_{-0.3}(\mathrm{sys})\mathrm{GeV}$, with a signal strength (the ratio of the observed cross section to the expected one) of $\mu = 1.7^{+0.5}_{-0.4}$.

The measured mass, combining the high mass resolution channels $H \to \gamma\gamma$ and $H \to ZZ^{(*)} \to 4\ell$, is $m_H = 125.5 \pm 0.2(\mathrm{stat})^{+0.5}_{-0.3}(\mathrm{sys})\mathrm{GeV}$ while the combined value of the signal strenght is $\mu = 1.43 \pm 0.21$ (see Section 4.6).

In order to test the compatibility of the new observed narrow resonance at 125 GeV with the SM Higgs boson all the spin-parity hypotheses must be excluded in favour of the 0^+ state. For this thesis I developed and optimized a method to test the spin-parity properties of a Higgs-like particle using a multivariate approach based on a matrix element per-event likelihood (MELA).

This method, largely used in literature [47, 48], uses sensible variables to build a discriminant to separate between two different spin hypotheses. The hypotheses are tested in pair and the log-likelihood ratio is used as test statistic. This analysis has lead to an improvement on the description of the signal PDF permitting a more realistic description of the different spin-parity states.

To properly evaluate the test statistic the MELA theoretical PDF must be modified with corrections terms coming from detector acceptance and $H \to ZZ^{(*)} \to 4\ell$ selection procedure. The acceptance terms for angular variables required the determination and optimization of the fit functions for each spin and for each final state (about 700 functions). The closure tests performed on MC JHU signal sample show a very good agreement between MELA PDF and MC JHU description, this way confirming the improvements of the MELA method proposed in this thesis.

Finally the Hypothesis Tests between different spin-parity cases have been performed. The Standard Model 0^+ hypothesis has been tested with 0^-, 1^+, 1^-, assuming purely ggF production. Also 0^+ hypothesis has been compared to the 2^+_m and 2^- hypotheses for varying fractions of ggF and $q\bar{q}$ production: the investigation of various fractions of production shows that the expected separation is independent of the production fractions.

The Higgs-like boson is found to be compatible with the SM 0^+ hypothesis when compared with other J^P hypotheses. The alternative hypotheses are excluded with the $1 - CL_\mathrm{s}$ confidence levels shown in Table:

Exclusion in favour of 0^+	
tested hypothesis	$1 - CL_\mathrm{s}(\%)$
0^-	99.6
1^+	99.4
1^-	96.9
2^+_m	81.8
2^-	88.4

Bibliography

[1] S. L. Glashow, *Nucl. Phys.* **22**:579 (1961).

[2] S. Weinberg, *Phys. Rev. Lett.* **19**:1264 (1967).

[3] A. Salam, *Elementary Particle Theory: Groups and Analycity*, pag.367 (ed. Svartholm); Almquist and Wiksell(Stocholm) (1968).

[4] P.W. Higgs, *Phys. Rev. Lett.* 13 (1964) 508; *Phys. Rev.* 145 (1966) 1156; F. Englert and R. Brout, *Phys. Rev. Lett.* 13 (1964) 321.

[5] J. B. et al. (Particle Data Group) *The Review of Particle Physics.*

[6] S. Choudhury, G. C. Joshi, S. Mahajan, and B. H. McKellar, *Probing large distance higher dimensional gravity from lensing data*, Astropart.Phys. **21** (2004) 559-563.

[7] J. Wess, B. Zumino, *Supergauge Transformations in Four-Dimensions, Nucl. Phys.* B70 (1974) 39-50.

[8] J. R. Ellis and G. L. Fogli, *New bounds on m(t) and first bounds on M(H) from precision electroweak data*, Phys. Lett. B **249** (1990) 543; J. R. Ellis, G. L. Fogli and E. Lisi, *Bounds on M(H) from electroweak radiative corrections*, Phys. Lett. B **274** (1992) 456 and *Indirect bounds on the Higgs boson mass from precision electroweak data*, Phys. Lett. B **318** (1993) 148.

[9] T. Hambye and K. Riesselmann, *Matching conditions and Higgs boson mass upper bounds reexamined*, Phys. Rev. D **55** (Jun, 1997) 7255-7262.

[10] *Search for the Standard Model Higgs boson at LEP*, Physics Letters B **565** (2003) no.0, 61-75.

[11] Tevatron New Physics Higgs Working Group, CDF Collaboration, D0 Collaboration Collaboration, C. Group, D. Collaborations, the Tevatron New Physics, and H. Working, *Updated Combination of CDF and D0*

Searches for Standard Model Higgs Boson Production with up to $10.0\,\mathrm{fb}^{-1}$ *of Data.*

[12] LHC Higgs Cross Section Working Group, S. Dittmaier, C. Mariotti, G. Passarino, and R. Tanaka (Eds.), *Handbook of LHC Higgs Cross Sections: 2. Differential Distributions*, CERN-2012-002 (CERN, Geneva, 2012).

[13] A. Bredenstein, A. Denner, S. Dittmaier, and M. Weber, *Radiative corrections to the semileptonic and hadronic Higgs-boson decays* $H \to WW/ZZ \to 4 fermions$, JHEP **0702** (2007) 080.

[14] ATLAS Collaboration, *The ATLAS Technical Design Report*, `http://atlas.web.cern.ch/Atlas/GROUPS/PHYSICS/TDR/access.html`.

[15] ATLAS Collaboration, *The ATLAS Experiment at the CERN Large Hadron Collider*, Journal of Instrumentation 3 (2008) S08003..

[16] L. Evans and P. Bryant, *LHC Machine*, JINST, 3:S08001, 2008.

[17] L. Maiani, *A caccia del bosone di Higgs. Magneti, governi, scienziati e particelle nell'impresa scientifica del secolo*, Mondadori, 2013.

[18] ATLAS Experiment @2011 CERN. ATLAS Photos, `http://www.atlas.ch/photos/index.html`.

[19] The TOTEM Collaboration, G. Antchev, P. Aspell, I. Atanassov, et al., *First measurement of the total proton-proton cross-section at the LHC energy of* $7\,\mathrm{TeV}$, EPL (Europhysics Letters) **96** (2011) no.2, 21002.

[20] The TOTEM collaboration *A luminosity-independent measurement of the proton-proton total cross-section at* $\sqrt{s} = 8\,\mathrm{TeV}$, Phys. Rev. Lett. 111, 012001 (2013)

[21] ATLAS, *Luminosity Public Results*, `https://twiki.cern.ch/twiki/bin/view/AtlasPublic/LuminosityPublicResults`.

[22] S. Chatrchyan, G. Hmayakyan, V. Khachatryan, A. Sirunyan, W. Adam, T. Bauer, T. Bergauer, H. Bergauer, M. Dragicevic, J. Ero, et al., *The CMS experiment at the CERN LHC*, Journal of Instrumentation 3 (2008) S08004.

[23] K. Aamodt, A. Quintana, R. Achenbach, S. Acounis, D. Adamova, C. Adler, M. Aggarwal, F. Agnese, G. Rinella, Z. Ahammed, et al., *The ALICE experiment at the CERN LHC*, Journal of Instrumentation 3 (2008) S08002.

[24] R. LHCb, *Technical Design Report*, CERN/LHCC 37 (2000) 2000.

[25] M. Bozzo, *Total cross section, elastic scattering and diffraction dissociation at LHC.*

[26] ATLAS Collaboration, *Technnical Proposal for the CERN LHCf Experiment: Measurement of Photons and Neutral Pions in the Very Forward Region of LHC*, (2005).

[27] J.L. Caron, *ATLAS detector in A4 format with English captions*, Mar, 1998.

[28] ATLAS Collaboration, *ATLAS Muon Spectrometer Technical Design Report*, CERN, Geneva, 1997.

[29] ATLAS Collaboration, *Expected Performance of the ATLAS Experiment - Detector, Trigger and Physics.*

[30] T. Cornelissen, M. Elsing, I. Gavrilenko, et al., *The new ATLAS track reconstruction (NEWT)*, Journal of Physics: Conference Series **119** (2008) no.3, 032014.

[31] R. Fruhwirth, *Application of Kalman filtering to track and vertex fitting*, Nucl.Instrum.Meth. **A262** (1987) 444–450.

[32] T. G. Cornelissen, M. Elsing, I. Gavrilenko, et al., *The global χ^2 track fitter in ATLAS.* Journal of Physics: Conference Series **119** (2008) no.3, 032013.

[33] G. Piacquadio, K. Prokofiev, and A. Wildauer, *Primary vertex reconstruction in the ATLAS experiment at LHC*, Journal of Physics: Conference Series **119** (2008) no.3, 032033.

[34] W. Waltenberger, R. Frhwirth and P. Vanlaer, *Adaptive vertex fitting*, Journal of Physics G: Nuclear and Particle Physics **34** (2007) no. 12, N343.

[35] ATLAS Collaboration, *Expected electron performance in the ATLAS experiment*, ATL-PHYS-PUB-2011-006, Apr, 2011.

[36] ATLAS Collaboration, *Electron identification efficiency dependence on pileup.*

[37] ATLAS Collaboration, *Identification efficiency measurement for electrons with transverse energy between 7 and 50 GeV.*

[38] ATLAS Collaboration, *Muon Reconstruction Performance*, ATLAS-CONF-2010-064, Jul, 2010.

[39] ATLAS Collaboration, *Muon reconstruction efficiency in reprocessed 2010 LHC proton-proton collision data recorded with the ATLAS detector*. ATLAS-CONF-2011-063, Apr, 2011.

[40] R. Nicolaidou, L. Chevalier, S. Hassani, et al., *Muon identification procedure for the ATLAS detector at the LHC using Muonboy reconstruction package and tests of its performance using cosmic rays and single beam data*, Journal of Physics: Conference Series **219** (2010) no. 3, 03205.

[41] ATLAS Collaboration, *Pile-up Depedence of the ATLAS Muon Performance*.

[42] M. Cacciari, G. P. Salam, and G. Soyez, *The anti-k_t jet clustering algorithm*, Journal of High Energy Physics **2008** (2008) no.4, 063.

[43] ATLAS Collaboration, *Reconstruction and Calibration of Missing Transverse Energy and Performance in Z and W events in ATLAS Proton-Proton Collisions at $\sqrt{s} = 7\,\mathrm{TeV}$*, ATLAS-CONF-2011-080.

[44] ATLAS Collaboration, *Computing Technical Design Report*, Vol.3, CERN/LHCC 2005-022 (2005).

[45] The WLCG website, `http://lcg.web.cern.ch/lcg/public`.

[46] ATLAS Collaboration, *Observation of a new particle in the search for the Standard Model Higgs boson with the ATLAS detector at the LHC*, Phys.Lett. B716 (2012) 1-29, arXiv:1207.7214 .

[47] ATLAS Collaboration, *Measurements of the properties of the Higgs-like boson in the four lepton decay channel with the ATLAS detector using $SI25fb^{-1}$ of proton-proton collision data*, ATLAS-CONF-2013-013.

[48] CMS Collaboration, *Study of the Mass and Spin-Parity of the Higgs Boson Candidate via Its Decays to Z Boson Pairs*, Phys. Rev. Lett. 110 (2013) 081803.

[49] S. Bolognesi, Y. Gao, A. V. Gritsan, K.l Melnikov, M. Schulze, N. V. Tran, A. Whitbeck, *On the spin and parity of a single-produced resonance at the LHC*. Phys. Rev. D86:095031, 2012, arXiv:1208.4018 .

[50] ATLAS Collaboration, *Improved luminosity determination in pp collisions at $\sqrt{s} = 8\,\text{TeV}$ using the ATLAS detector at the LHC*, CERN-PH-EP-2013-026, arXiv:1302.4393 .

[51] G. Cowan, K. Cranmer, E. Gross, O. Vitells, *Asymptotic formulae for likelihood-based tests of new physics*, Eur.Phys.J.C71:1554,2011 , arXiv:1007.1727 .

[52] K. Cranmer, *Kernel estimation in high-energy physics*, Comput.Phys.Commun. 136 (2001) 198-207, arXiv:hep-ex/0011057 .

[53] ATLAS Collaboration, *An update of combined measurements of the new Higgs-like boson with high mass resolution channels*, ATLAS-CONF-2012-170.

[54] ROOT - A Data Analysis Framework, `http://root.cern.ch/drupal/`.

[55] RooFit - Toolkit for Data Modelling, `http://roofit.sourceforge.net/`.

Appendix A

Acceptance plots for all spin-parity hypothesis

In the following Appendix the acceptance distributions of all the angular observables for all the spin hypothesis (MC samples 2011 and 2012) are shown. Figure illustrates RP and WP acceptance distributions and the respective fitting function: each function is been optimized in this work of thesis. The acceptance distributions of the ZZ background are also shown.

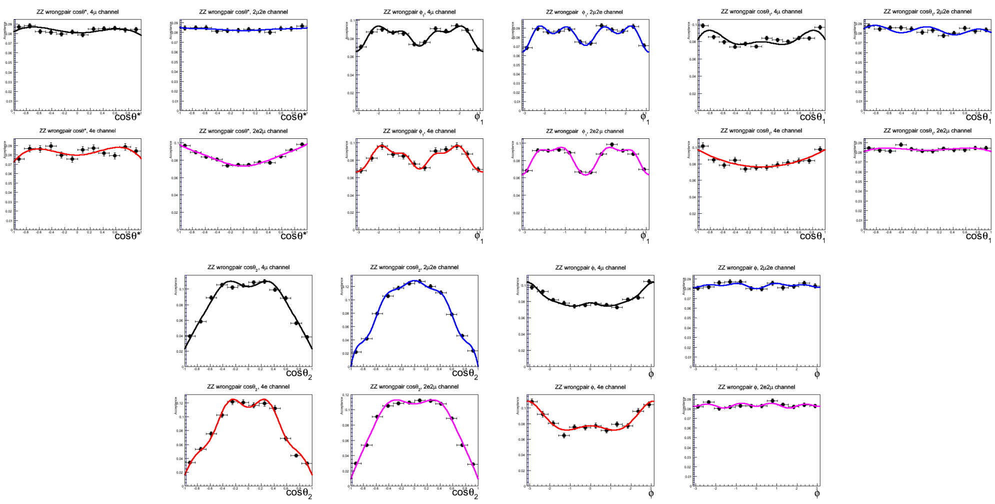

Figure 5.5: Acceptances fit (defined WP in the code) for the ZZ background (MC data sample 2012). For 2011 analysis ZZ MC 2012 background is used too, due the high statistics in the 2012 dataset. The observables shown from left to right and top to bottom: $\cos\theta^*$, ϕ_1, $\cos\theta_1$, $\cos\theta_2$ and ϕ. In each plot from top to bottom: 4μ and $4e$ channels.

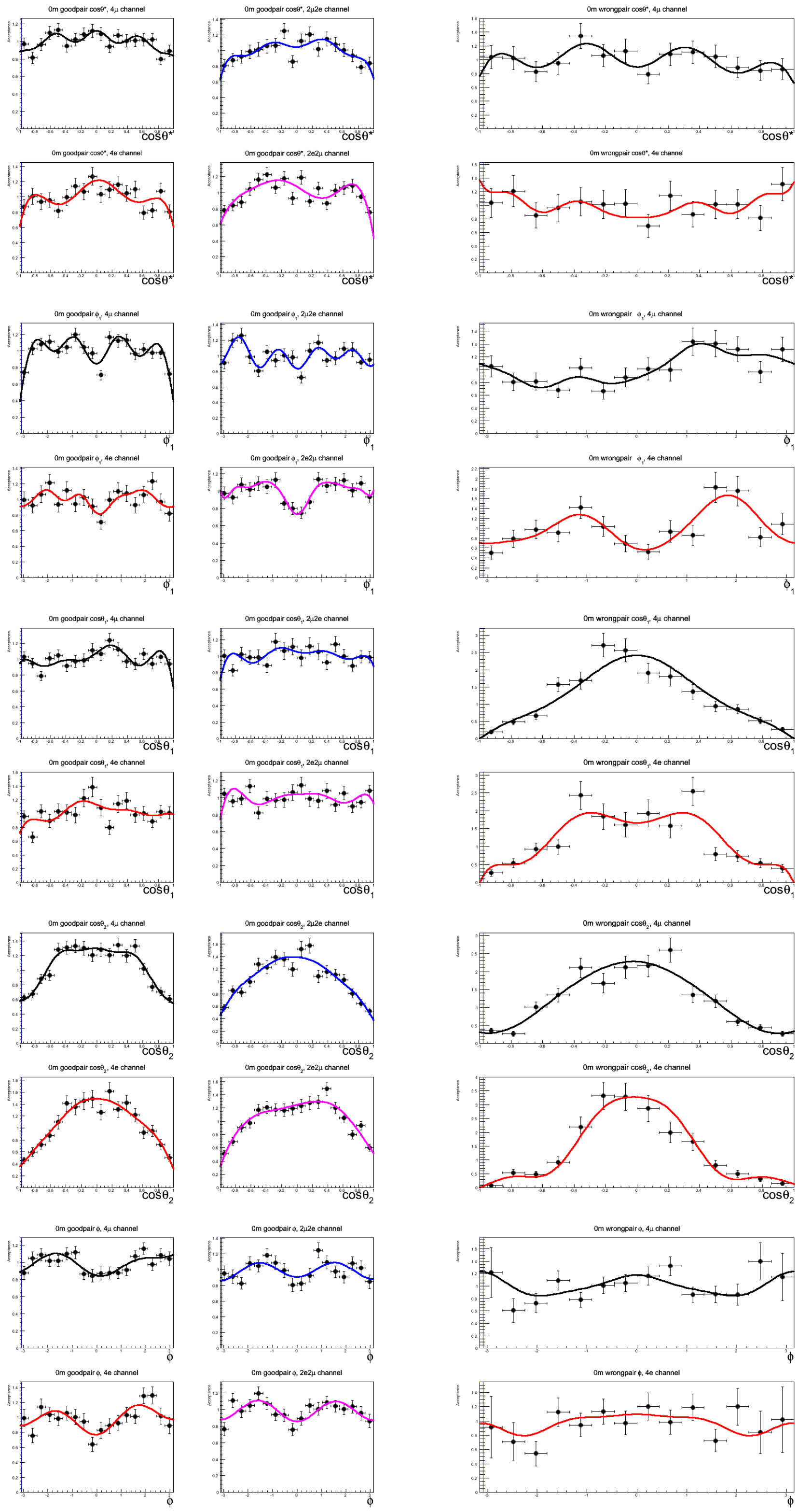

Figure 5.6: Acceptances fit (RP to the left and WP to the right) for the spin 0^- hypothesis (MC data sample 2012). The observables shown from top to bottom: $\cos\theta^*$, ϕ_1, $\cos\theta_1$, $\cos\theta_2$ and ϕ. In the RP plot from left to right and top to bottom: 4μ, $2\mu 2e$, $4e$ and $2e2\mu$ channels. In the WP plot from top to bottom: 4μ and $4e$ channels.

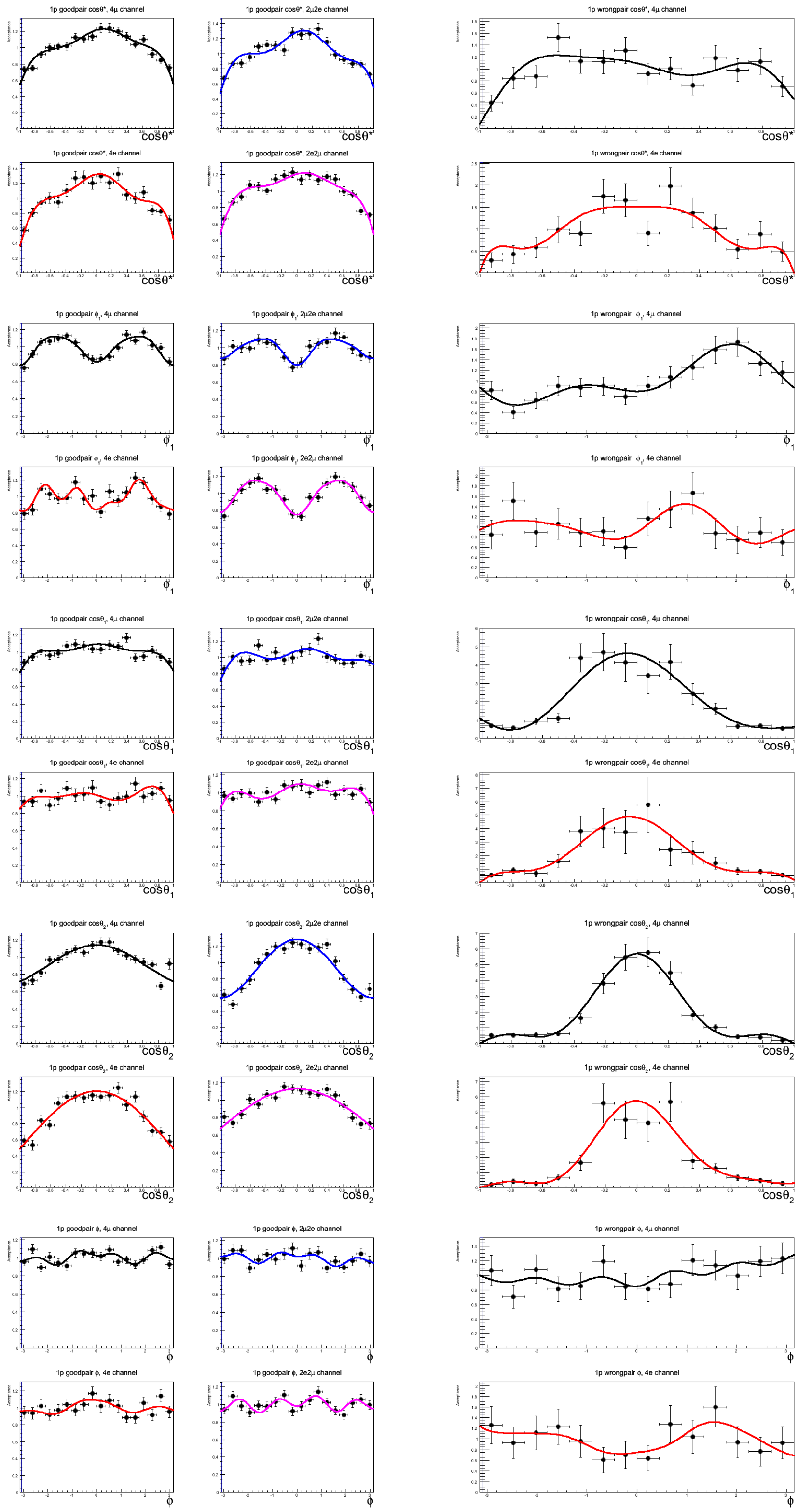

Figure 5.7: Acceptances fit (RP to the left and WP to the right) for the spin 1^+ hypothesis (MC data sample 2012). The observables shown from top to bottom: $\cos\theta^*$, ϕ_1, $\cos\theta_1$, $\cos\theta_2$ and ϕ. In the RP plot from left to right and top to bottom: 4μ, $2\mu 2e$, $4e$ and $2e2\mu$ channels. In the WP plot from top to bottom: 4μ and $4e$ channels.

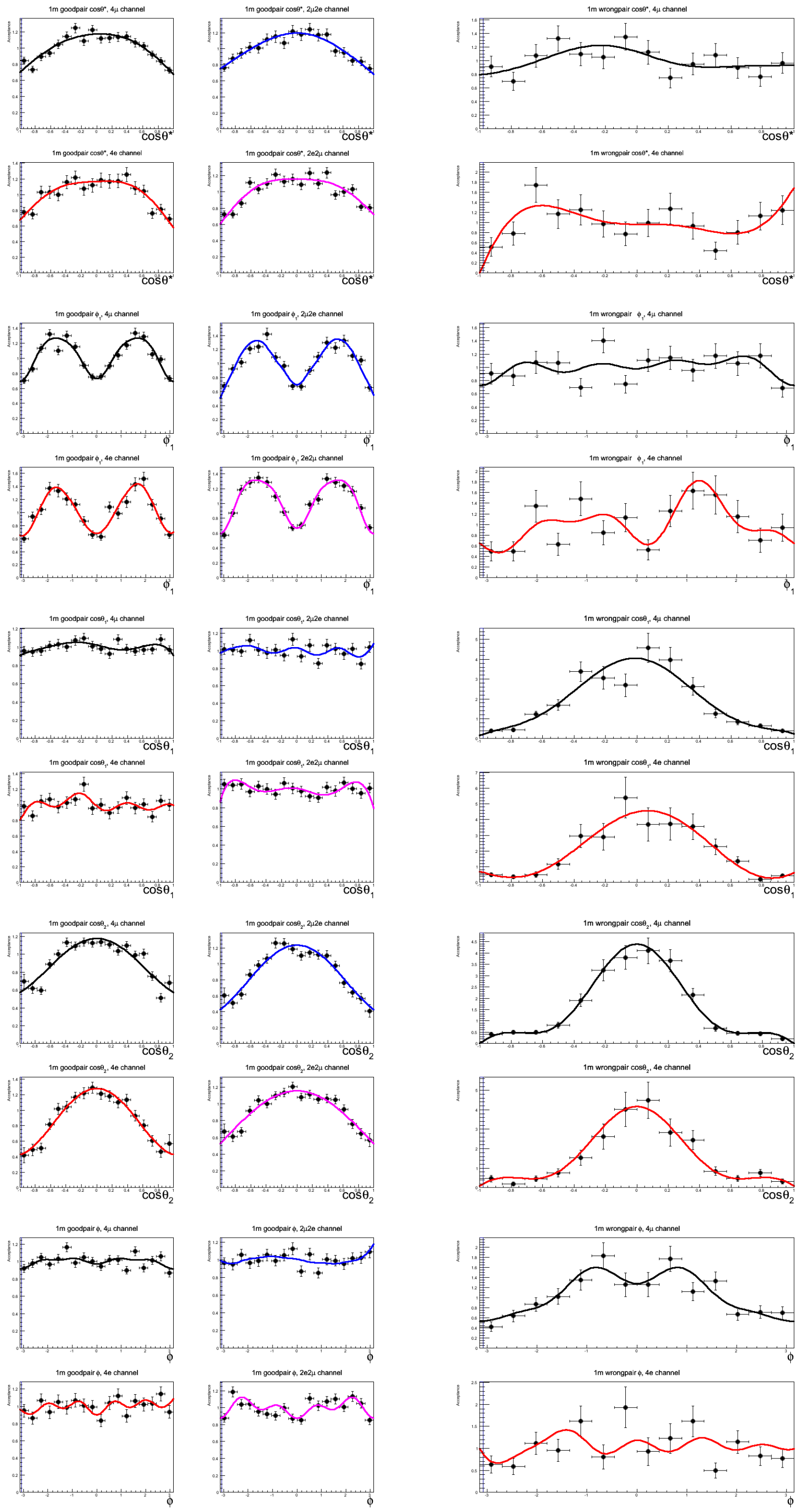

Figure 5.8: Acceptances fit (RP to the left and WP to the right) for the spin 1^- hypothesis (MC data sample 2012). The observables shown from top to bottom: $\cos\theta^*$, ϕ_1, $\cos\theta_1$, $\cos\theta_2$ and ϕ. In the RP plot from left to right and top to bottom: 4μ, $2\mu 2e$, $4e$ and $2e2\mu$ channels. In the WP plot from top to bottom: 4μ and $4e$ channels.

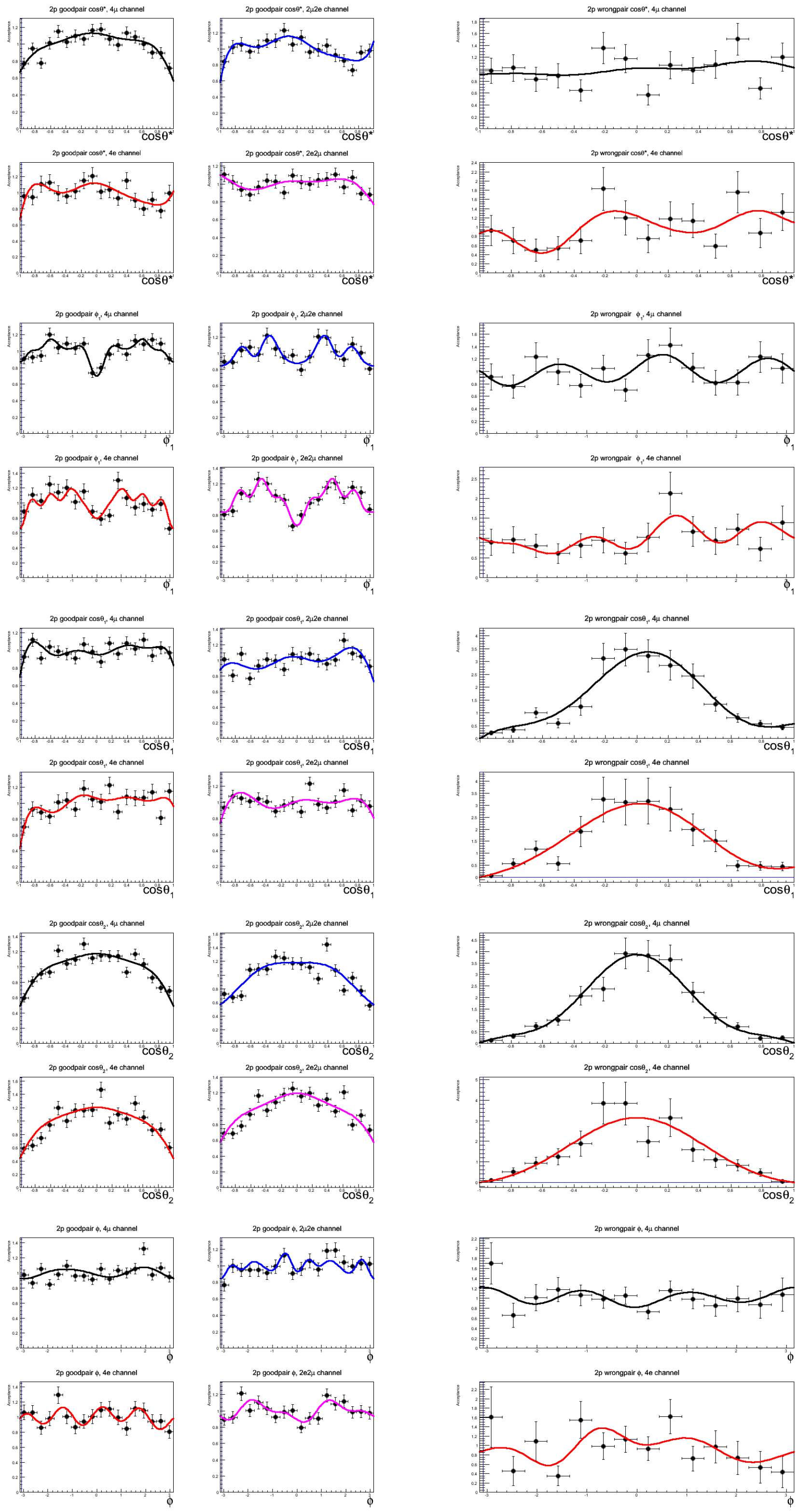

Figure 5.9: Acceptances fit (RP to the left and WP to the right) for the spin 2^+ 100% ggF hypothesis (MC data sample 2012). The observables shown from top to bottom: $\cos\theta^*$, ϕ_1, $\cos\theta_1$, $\cos\theta_2$ and ϕ. In the RP plot from left to right and top to bottom: 4μ, $2\mu2e$, $4e$ and $2e2\mu$ channels. In the WP plot from top to bottom: 4μ and $4e$ channels.

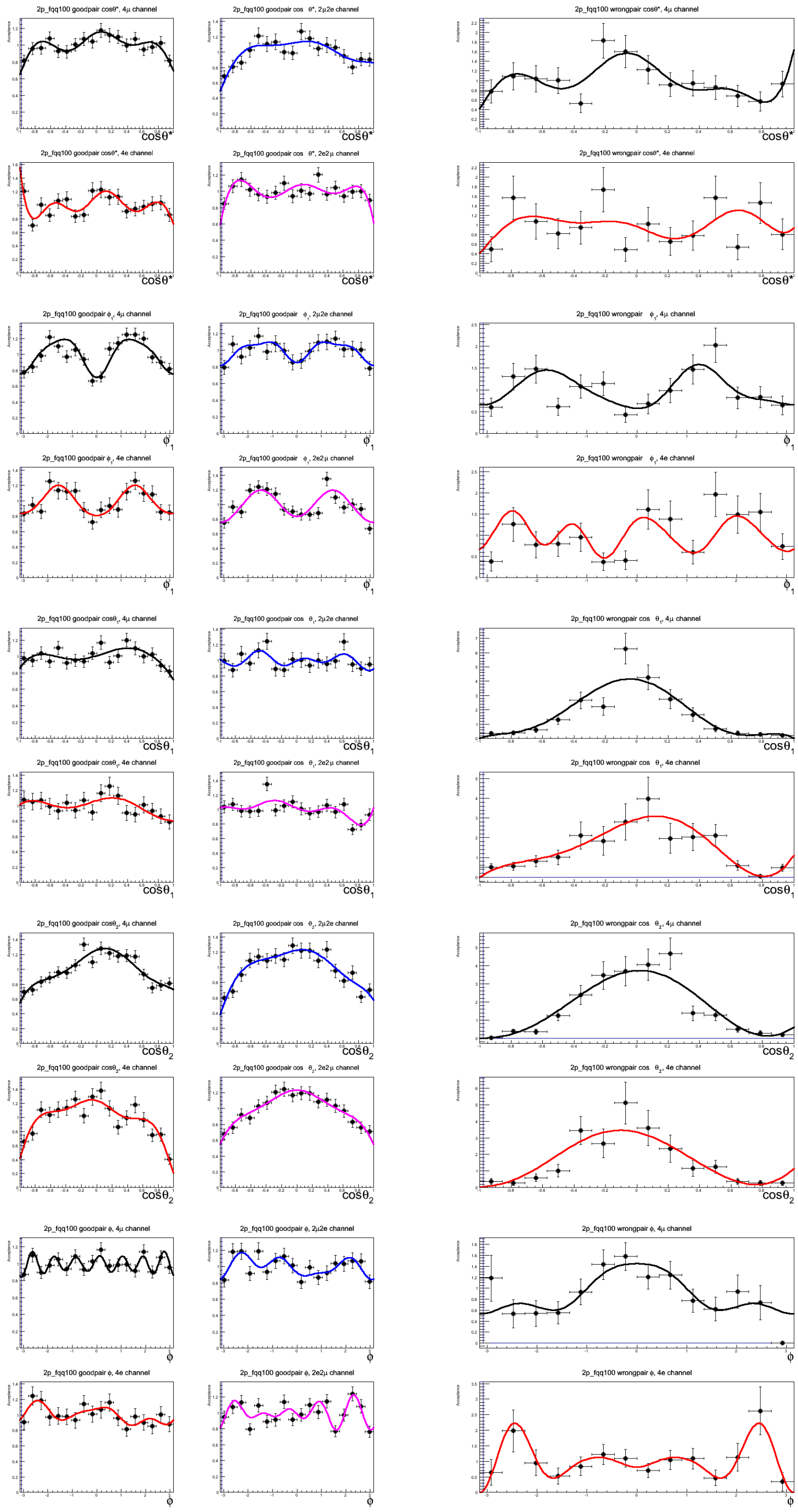

Figure 5.10: Acceptances fit (*RP* to the left and *WP* to the right) for the spin 2^+ ($f_{qq} = 100\%$) hypothesis (MC data sample 2012). The observables shown from top to bottom: $\cos\theta^*$, ϕ_1, $\cos\theta_1$, $\cos\theta_2$ and ϕ. In the *RP* plot from left to right and top to bottom: 4μ, $2\mu 2e$, $4e$ and $2e2\mu$ channels. In the *WP* plot from top to bottom: 4μ and $4e$ channels.

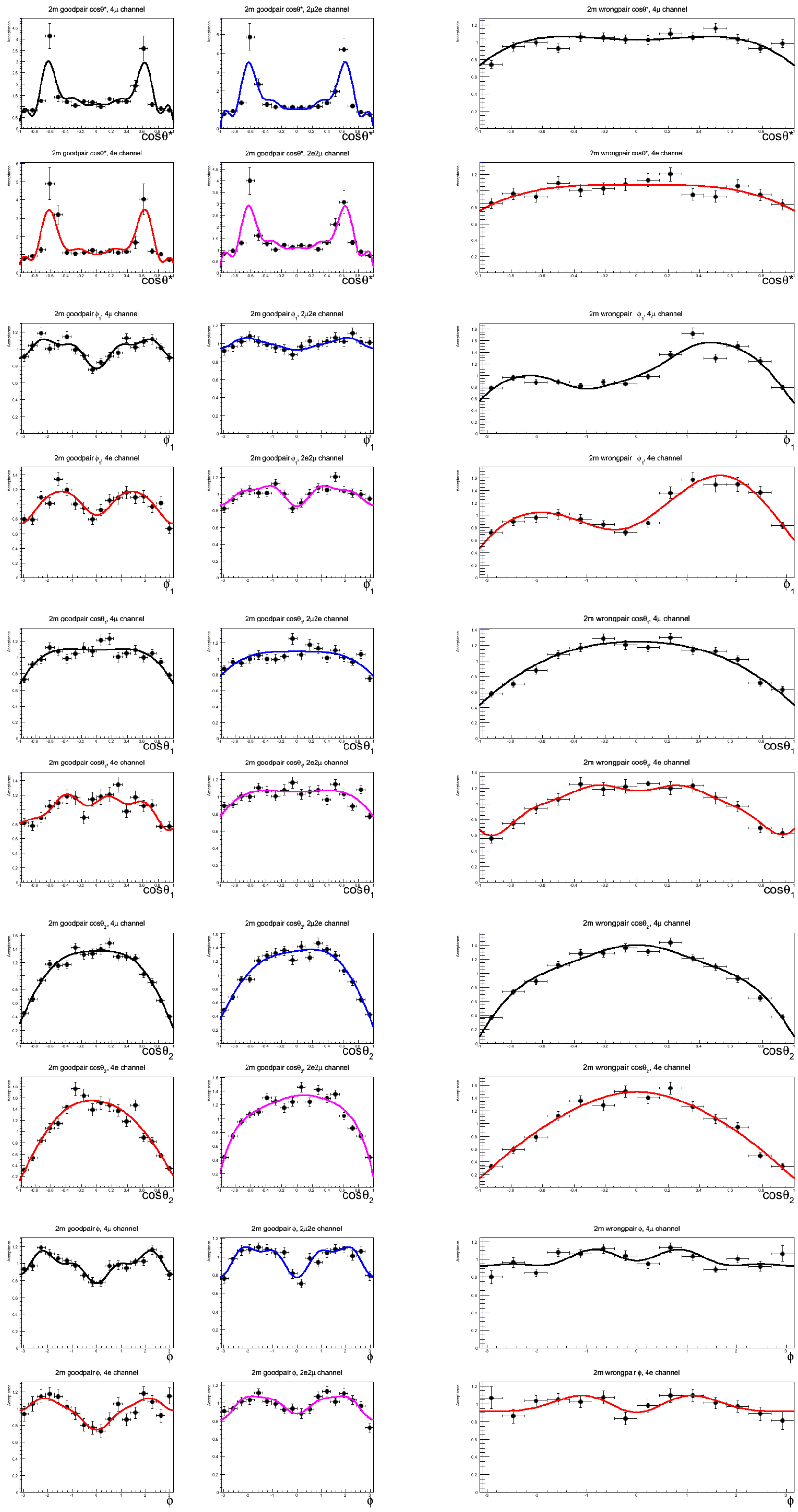

Figure 5.11: Acceptances fit (RP to the left and WP to the right) for the spin 2^{-} 100% ggF hypothesis (MC data sample 2012). The observables shown from top to bottom: $\cos\theta^{*}$, ϕ_1, $\cos\theta_1$, $\cos\theta_2$ and ϕ. In the RP plot from left to right and top to bottom: 4μ, $2\mu 2e$, $4e$ and $2e2\mu$ channels. In the WP plot from top to bottom: 4μ and $4e$ channels.

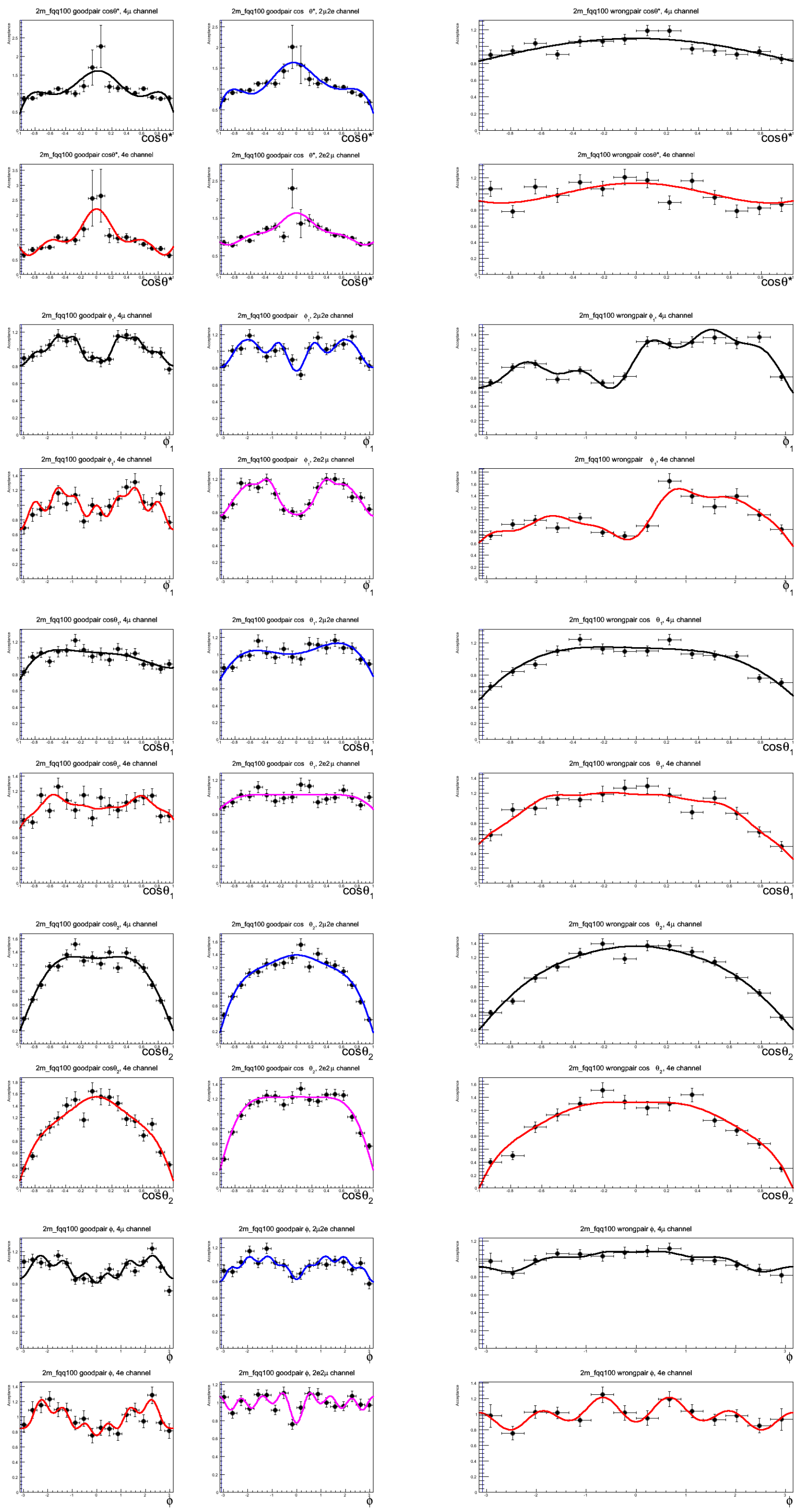

Figure 5.12: Acceptances fit (RP to the left and WP to the right) for the spin 2^- ($f_{qq} = 100\%$) hypothesis (MC data sample 2012). The observables shown from top to bottom: $\cos\theta^*$, ϕ_1, $\cos\theta_1$, $\cos\theta_2$ and ϕ. In the RP plot from left to right and top to bottom: 4μ, $2\mu2e$, $4e$ and $2e2\mu$ channels. In the WP plot from top to bottom: 4μ and $4e$ channels.

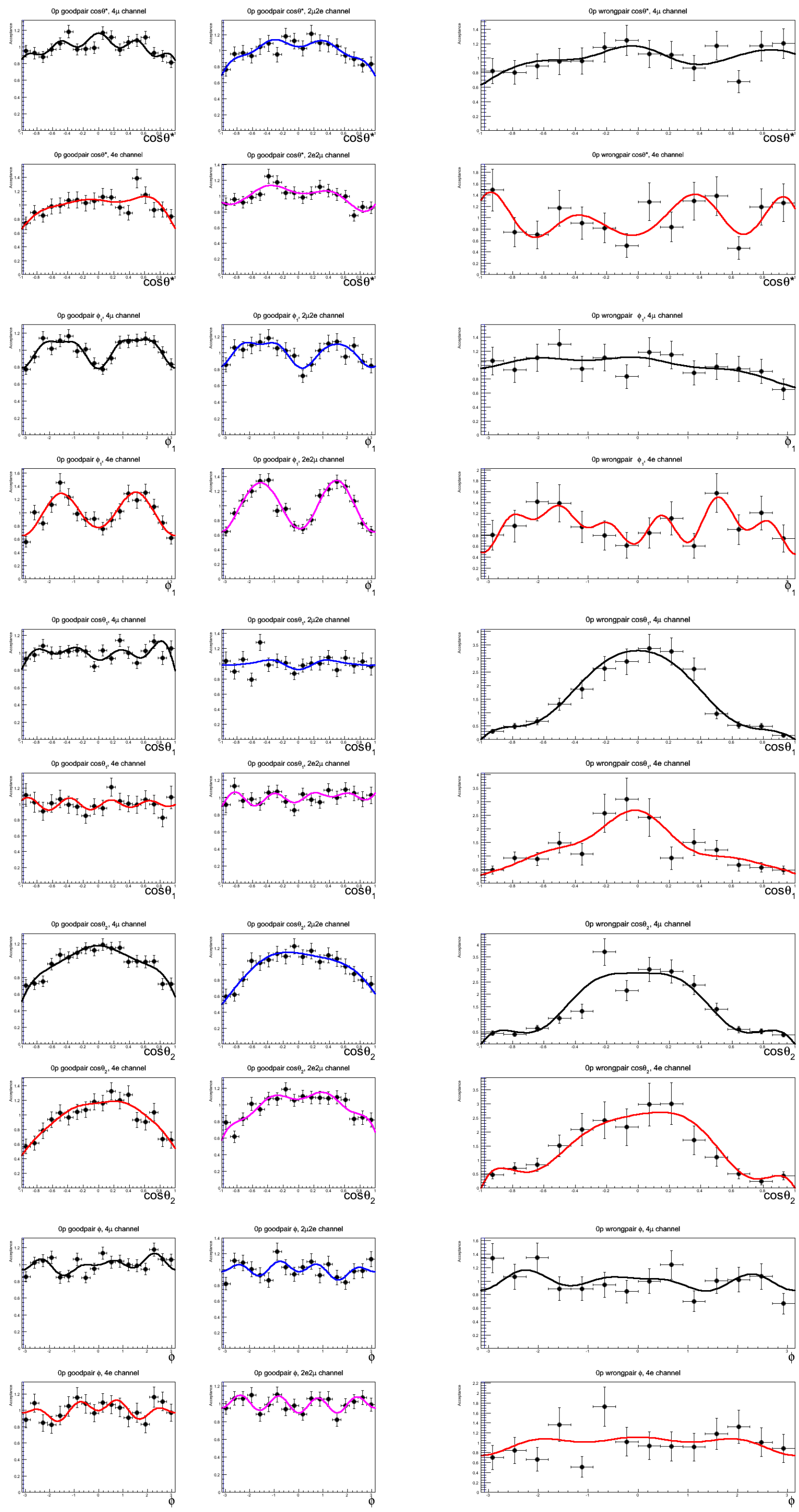

Figure 5.13: Acceptances fit (RP to the left and WP to the right) for the spin 0^+ hypothesis (MC data sample 2011). The observables shown from top to bottom: $\cos\theta^*$, ϕ_1, $\cos\theta_1$, $\cos\theta_2$ and ϕ. In the RP plot from left to right and top to bottom: 4μ, $2\mu 2e$, $4e$ and $2e2\mu$ channels. In the WP plot from top to bottom: 4μ and $4e$ channels.

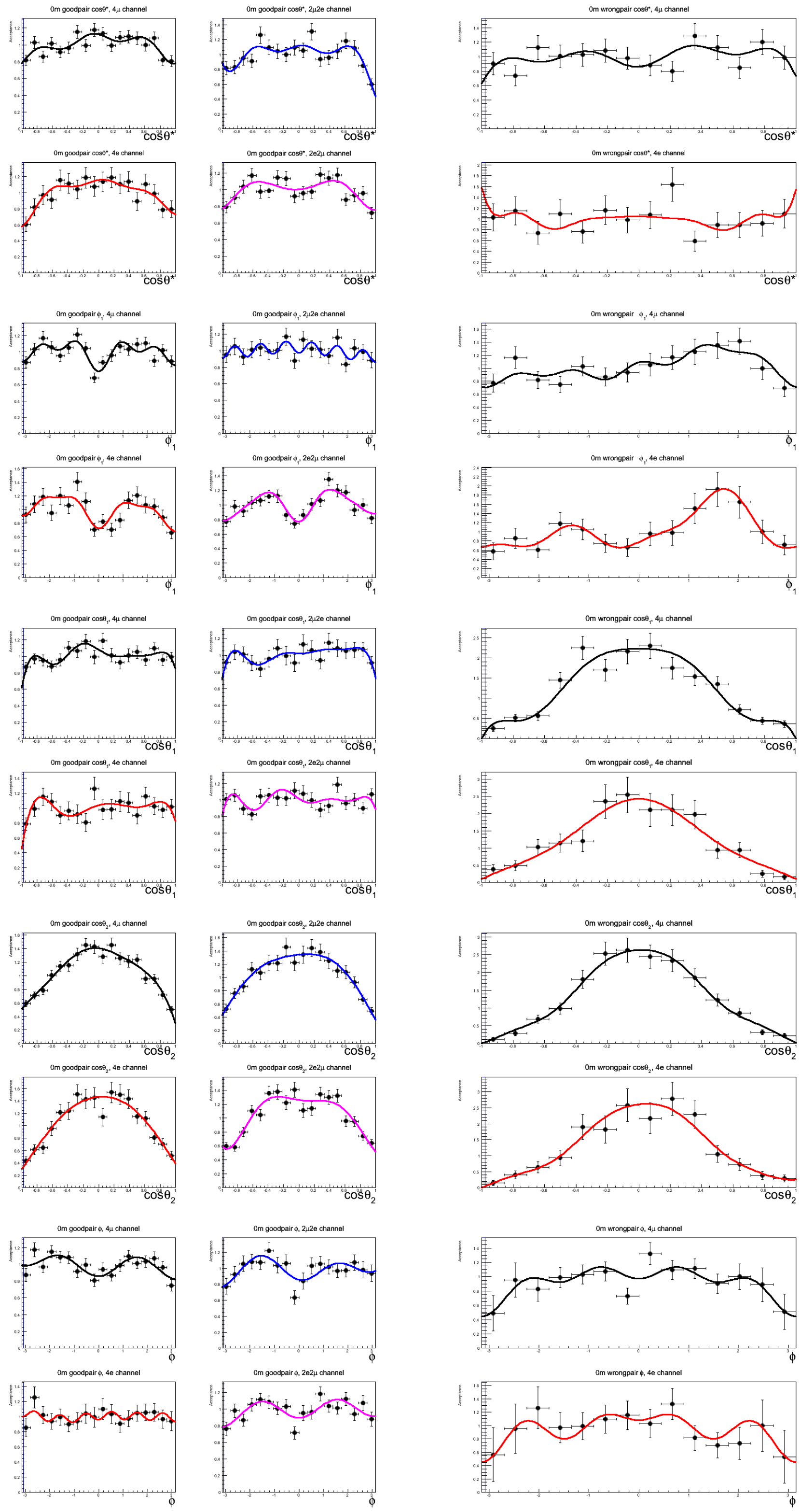

Figure 5.14: Acceptances fit (RP to the left and WP to the right) for the spin 0^- hypothesis (MC data sample 2011). The observables shown from top to bottom: $\cos\theta^*$, ϕ_1, $\cos\theta_1$, $\cos\theta_2$ and ϕ. In the RP plot from left to right and top to bottom: 4μ, $2\mu 2e$, $4e$ and $2e2\mu$ channels. In the WP plot from top to bottom: 4μ and $4e$ channels.

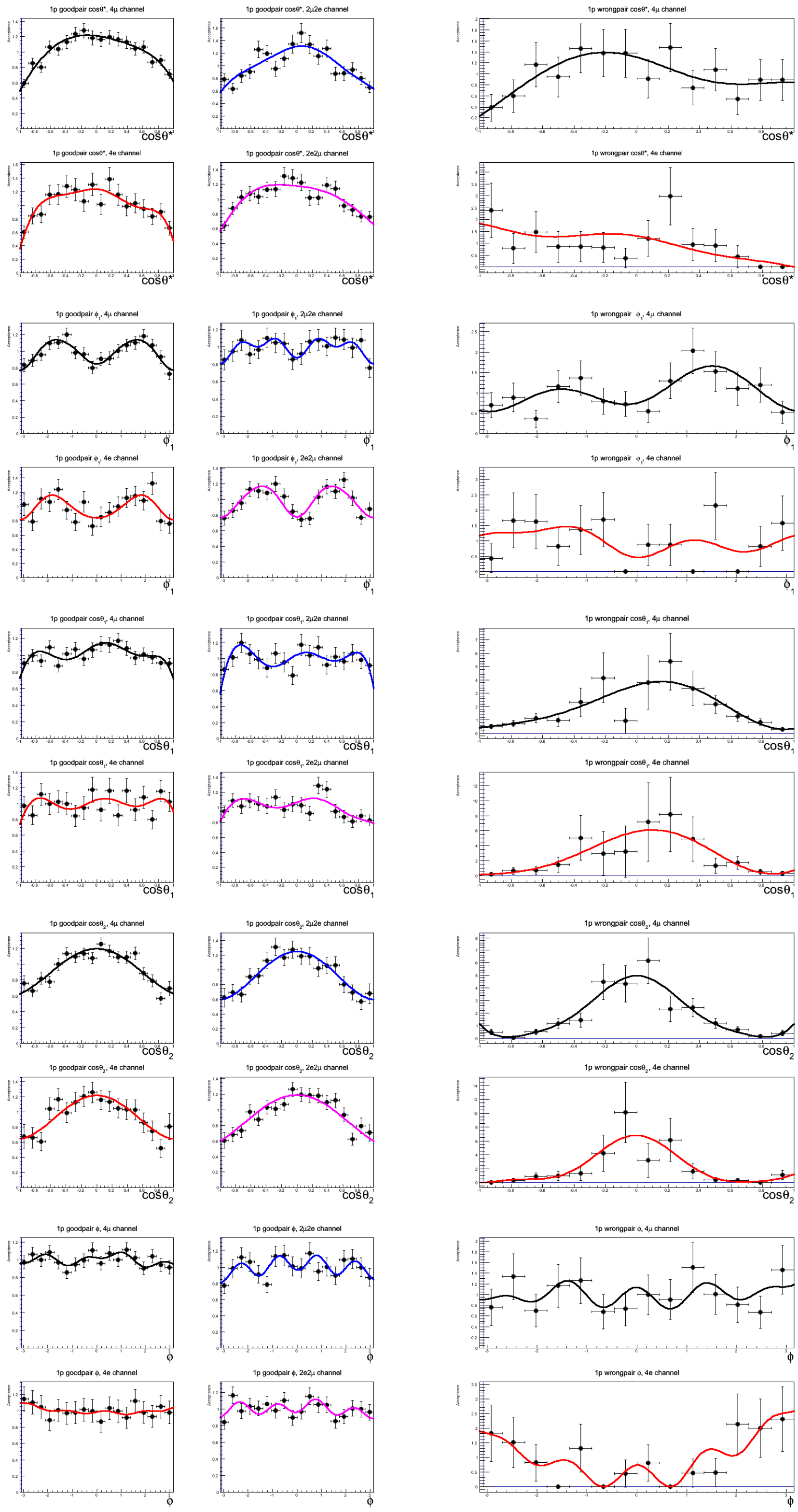

Figure 5.15: Acceptances fit (RP to the left and WP to the right) for the spin 1^+ hypothesis (MC data sample 2011). The observables shown from top to bottom: $\cos\theta^*$, ϕ_1, $\cos\theta_1$, $\cos\theta_2$ and ϕ. In the RP plot from left to right and top to bottom: 4μ, $2\mu 2e$, $4e$ and $2e2\mu$ channels. In the WP plot from top to bottom: 4μ and $4e$ channels.

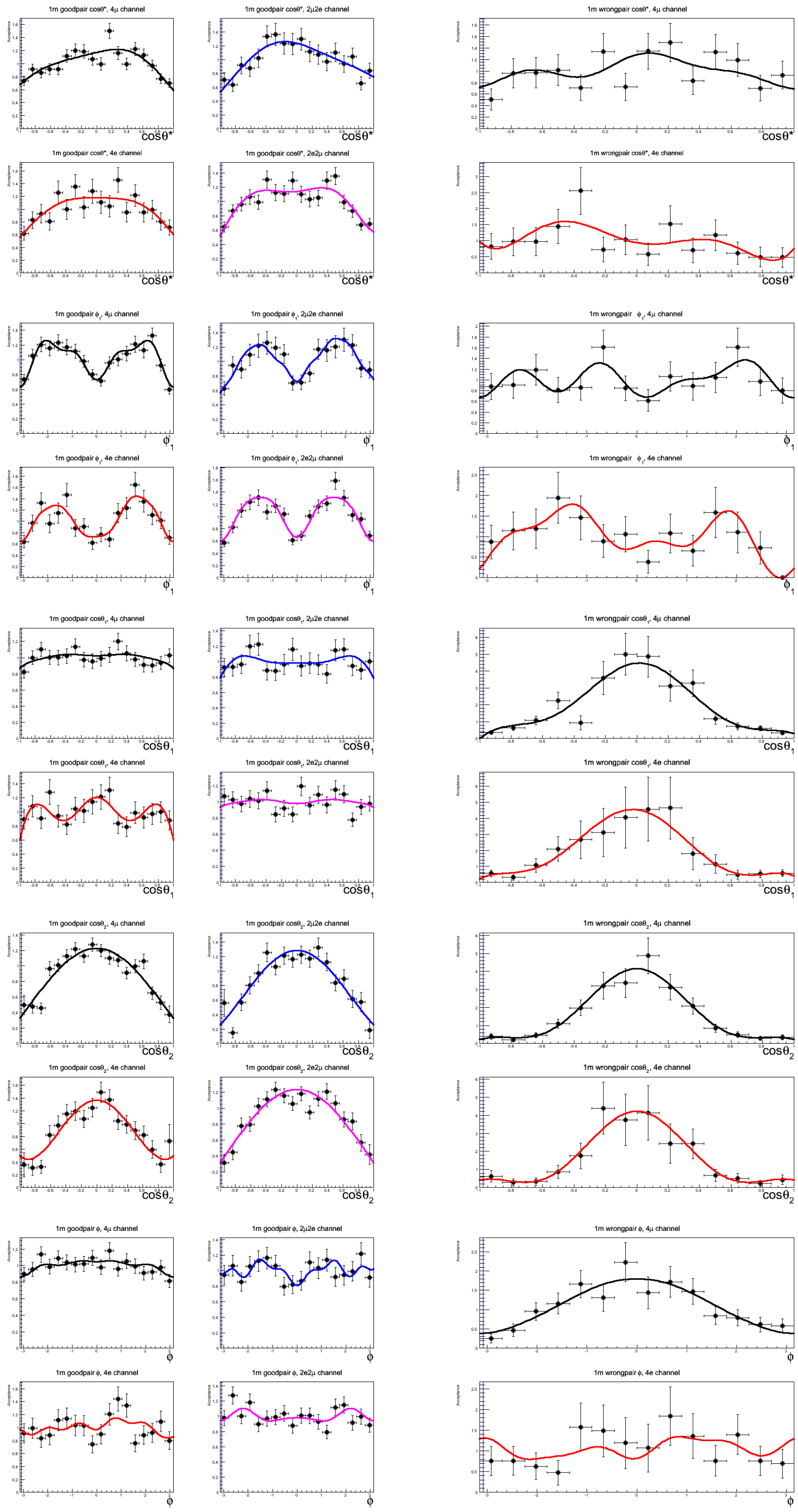

Figure 5.16: Acceptances fit (RP to the left and WP to the right) for the spin 1^- hypothesis (MC data sample 2011). The observables shown from top to bottom: $\cos\theta^*$, ϕ_1, $\cos\theta_1$, $\cos\theta_2$ and ϕ. In the RP plot from left to right and top to bottom: 4μ, $2\mu 2e$, $4e$ and $2e2\mu$ channels. In the WP plot from top to bottom: 4μ and $4e$ channels.

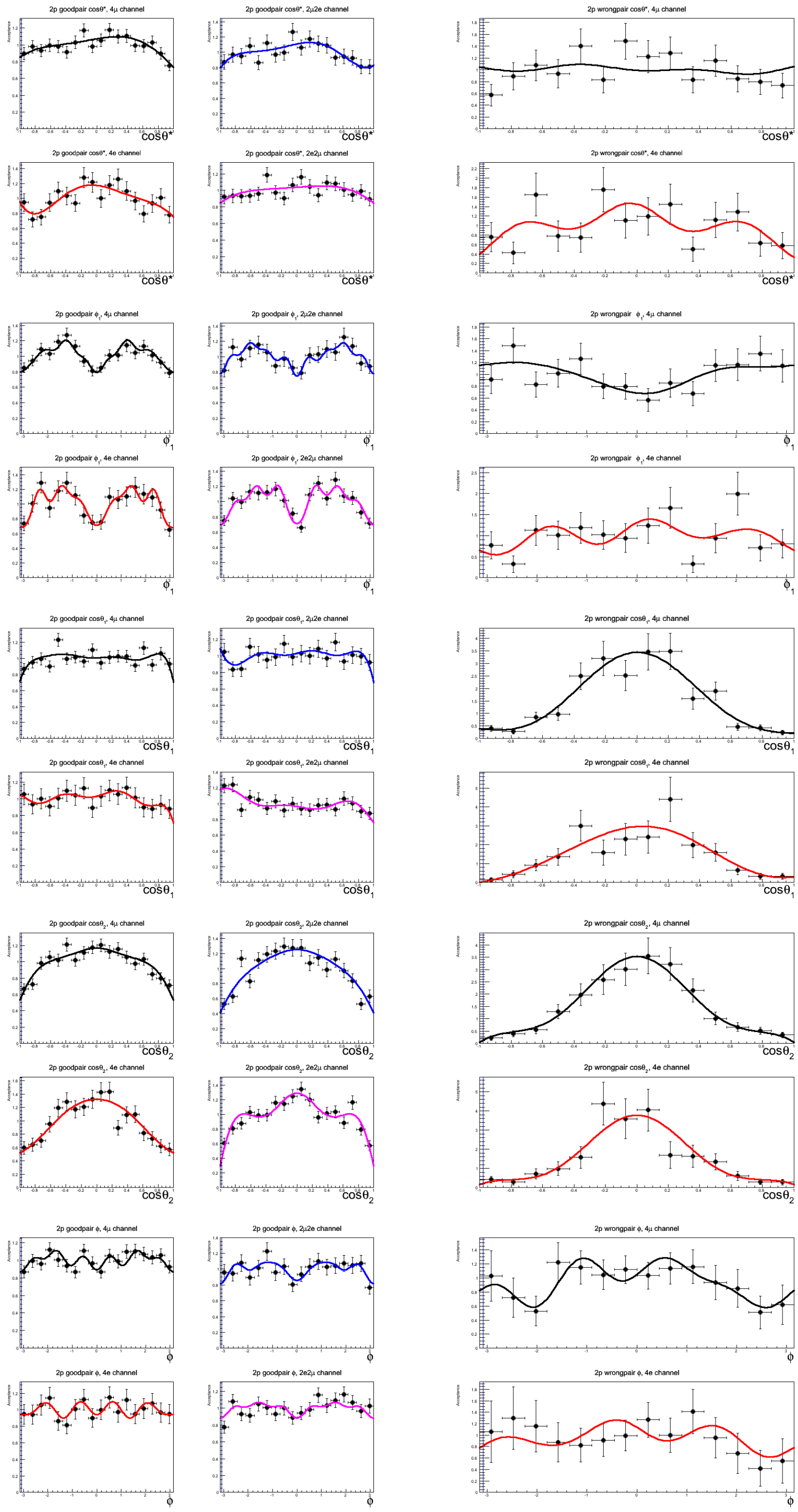

Figure 5.17: Acceptances fit (RP to the left and WP to the right) for the spin 2^+ 100% ggF hypothesis (MC data sample 2011). The observables shown from top to bottom: $\cos\theta^*$, ϕ_1, $\cos\theta_1$, $\cos\theta_2$ and ϕ. In the RP plot from left to right and top to bottom: 4μ, $2\mu 2e$, $4e$ and $2e2\mu$ channels. In the WP plot from top to bottom: 4μ and $4e$ channels.

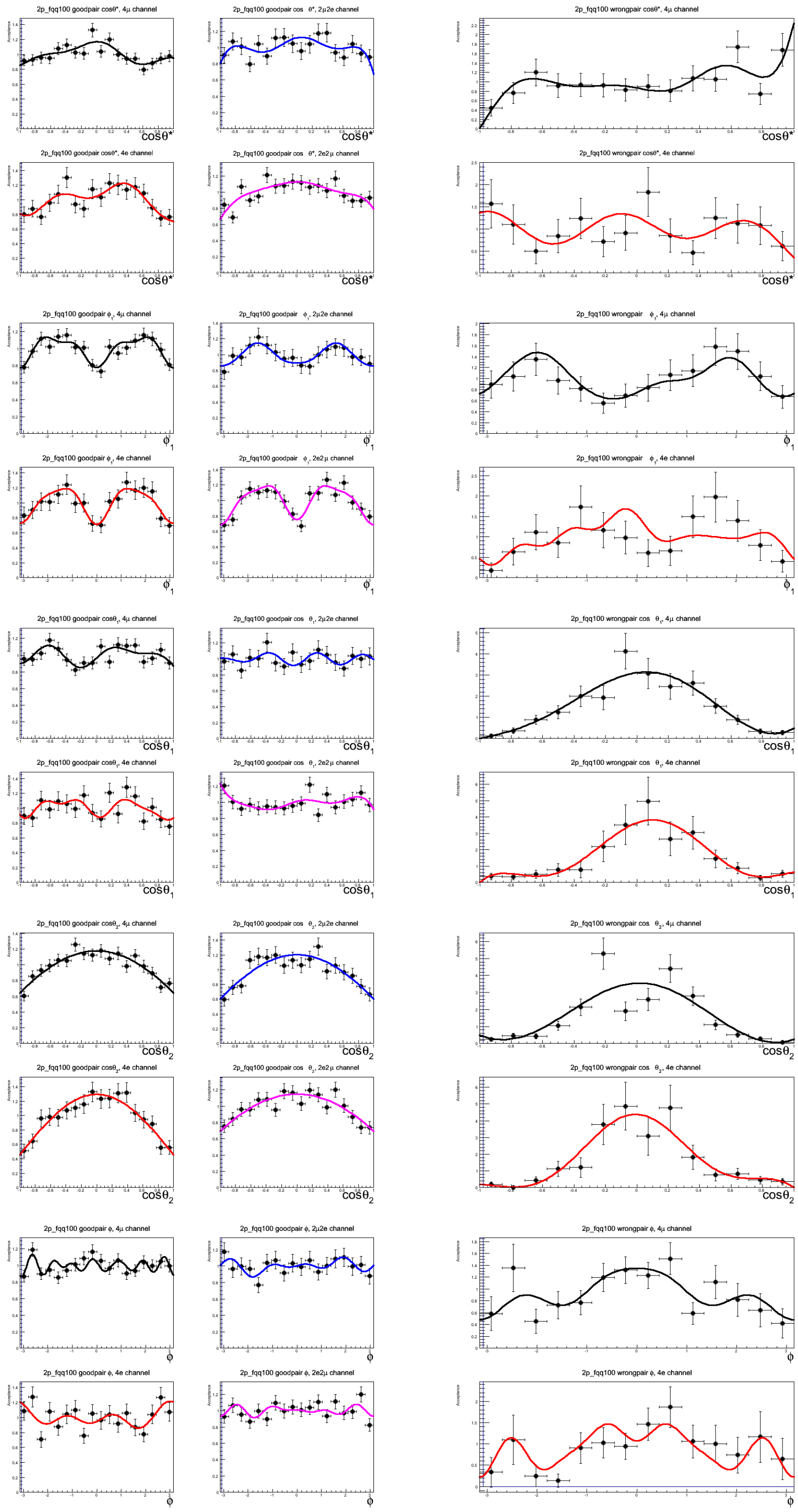

Figure 5.18: Acceptances fit (RP to the left and WP to the right) for the spin 2^+ ($f_{qq} = 100\%$) hypothesis (MC data sample 2011). The observables shown from top to bottom: $\cos\theta^*$, ϕ_1, $\cos\theta_1$, $\cos\theta_2$ and ϕ. In the RP plot from left to right and top to bottom: 4μ, $2\mu 2e$, $4e$ and $2e2\mu$ channels. In the WP plot from top to bottom: 4μ and $4e$ channels.

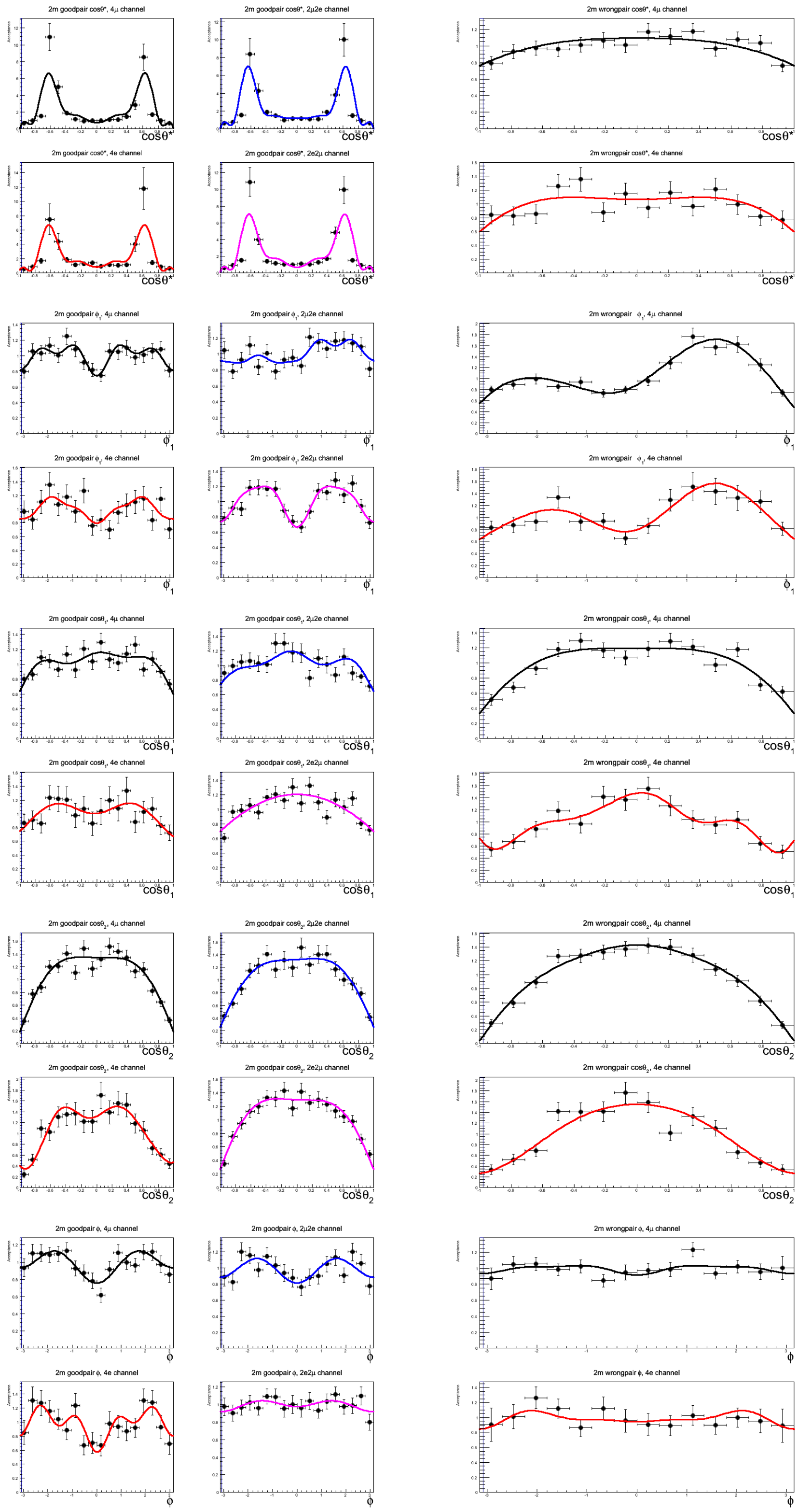

Figure 5.19: Acceptances fit (RP to the left and WP to the right) for the spin 2^- 100% ggF hypothesis (MC data sample 2011). The observables shown from top to bottom: $\cos\theta^*$, ϕ_1, $\cos\theta_1$, $\cos\theta_2$ and ϕ. In the RP plot from left to right and top to bottom: 4μ, $2\mu 2e$, $4e$ and $2e2\mu$ channels. In the WP plot from top to bottom: 4μ and $4e$ channels.

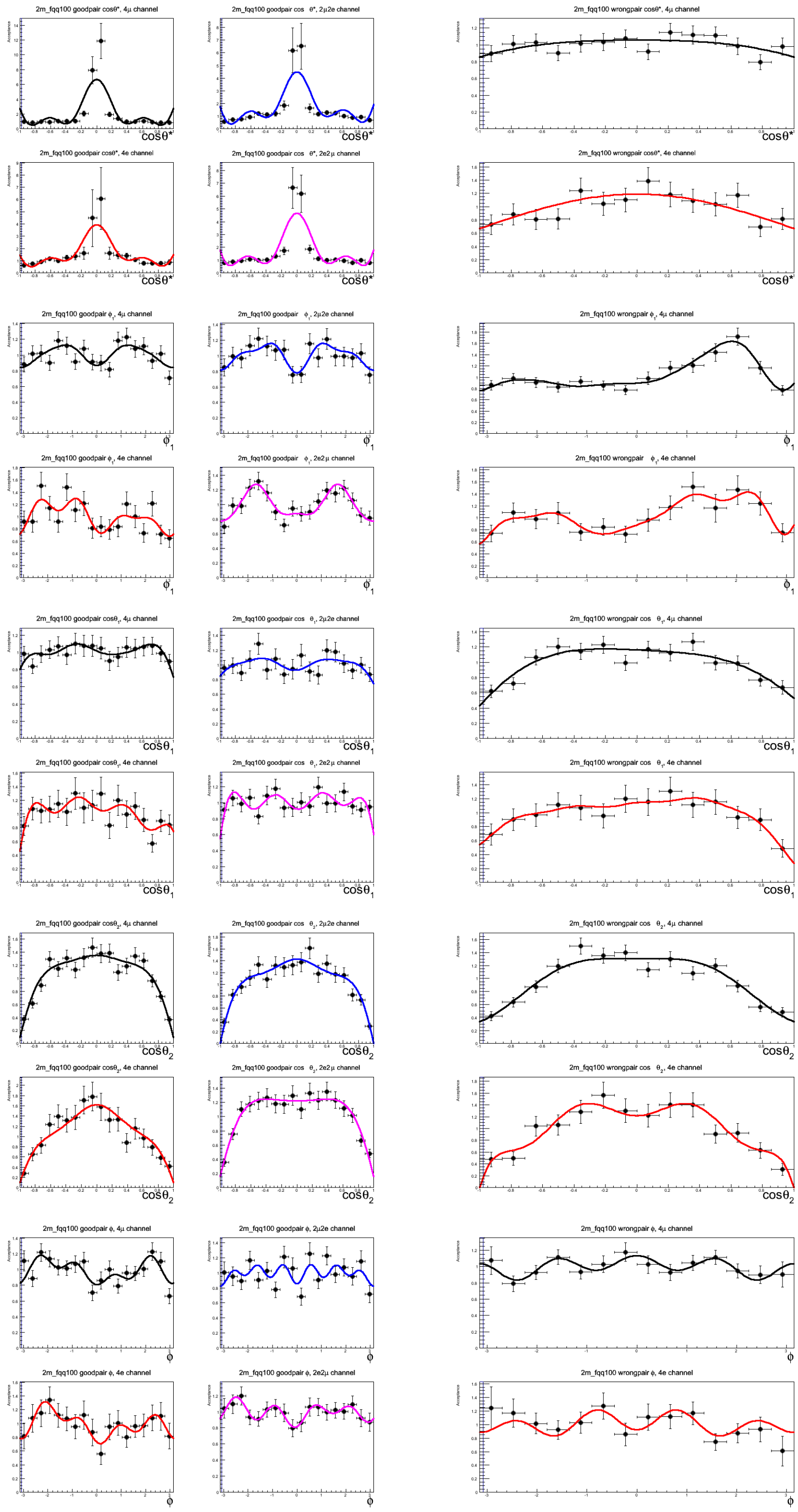

Figure 5.20: Acceptances fit (RP to the left and WP to the right) for the spin 2^- ($f_{qq} = 100\%$) hypothesis (MC data sample 2011). The observables shown from top to bottom: $\cos\theta^*$, ϕ_1, $\cos\theta_1$, $\cos\theta_2$ and ϕ. In the RP plot from left to right and top to bottom: 4μ, $2\mu 2e$, $4e$ and $2e2\mu$ channels. In the WP plot from top to bottom: 4μ and $4e$ channels.

Appendix B

Closure test for all spin-parity hypothesis

In the following Figures the comparisons for all of the observables taken into account in the analysis and for all spin hypotheses tested are shown (only MC 2012 for the sake of brevity). An overall good agreement is observed, confirming that the PDF accurately describes the processes studied for all the spin hypotheses considered. As already stated, the residual discrepancies observed are not expected to introduce any bias in the hypothesis testing procedure.

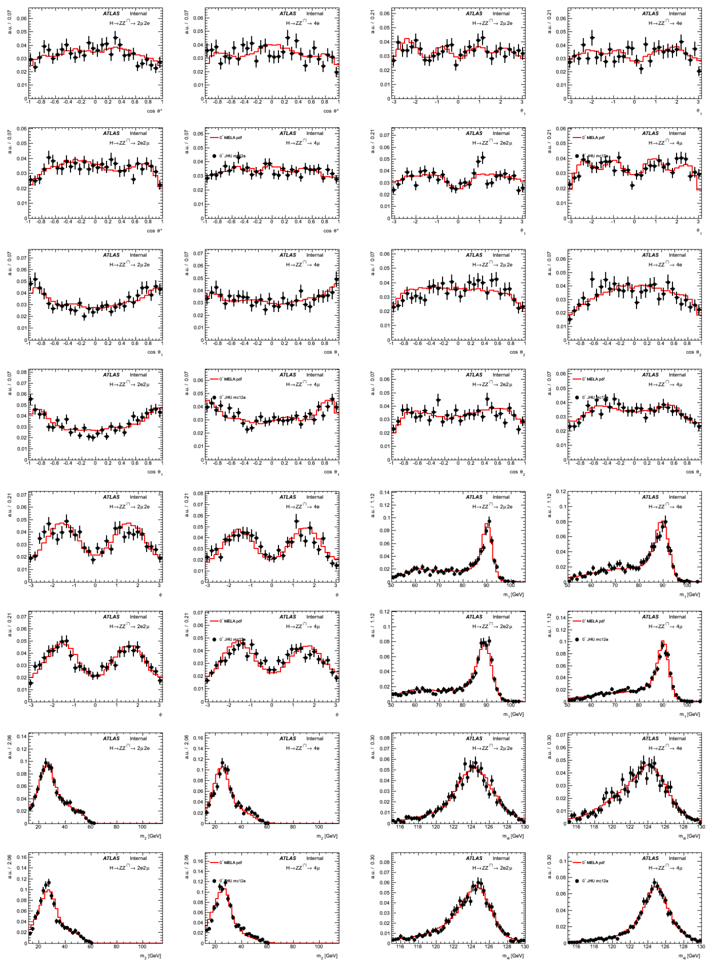

Figure 5.21: Comparison of the likelihood projection for a 0^- Higgs–like resonance (red curve) and the corresponding JHU (black points) MC simulation for the eight observable, from left to right and top to bottom: $\cos\theta^*$, ϕ_1, $\cos\theta_1$, $\cos\theta_2$, ϕ, m_1, m_2 and $m_{4\ell}$. In each plot from left to right and top to bottom for each observable: 4μ,$2\mu 2e$,$4e$ and $2e2\mu$ channels.

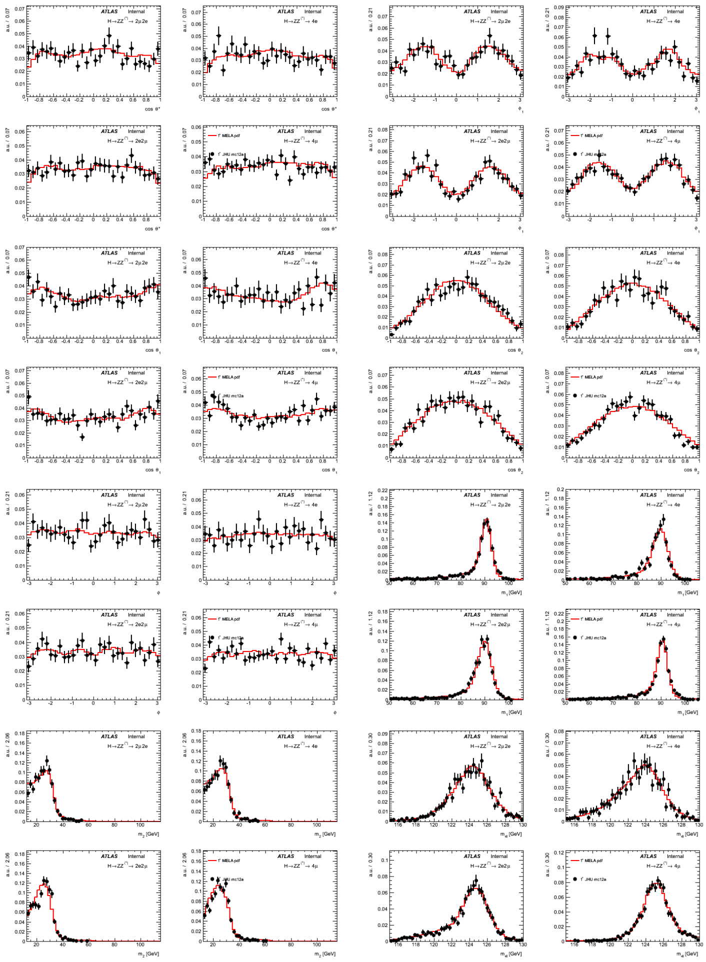

Figure 5.22: Comparison of the likelihood projection for a 1^+ Higgs–like resonance (red curve) and the corresponding JHU (black points) MC simulation for the eight observable, from left to right and top to bottom: $\cos\theta^*$, ϕ_1, $\cos\theta_1$, $\cos\theta_2$, ϕ, m_1, m_2 and $m_{4\ell}$. In each plot from left to right and top to bottom for each observable: 4μ,$2\mu2e$,$4e$ and $2e2\mu$ channels.

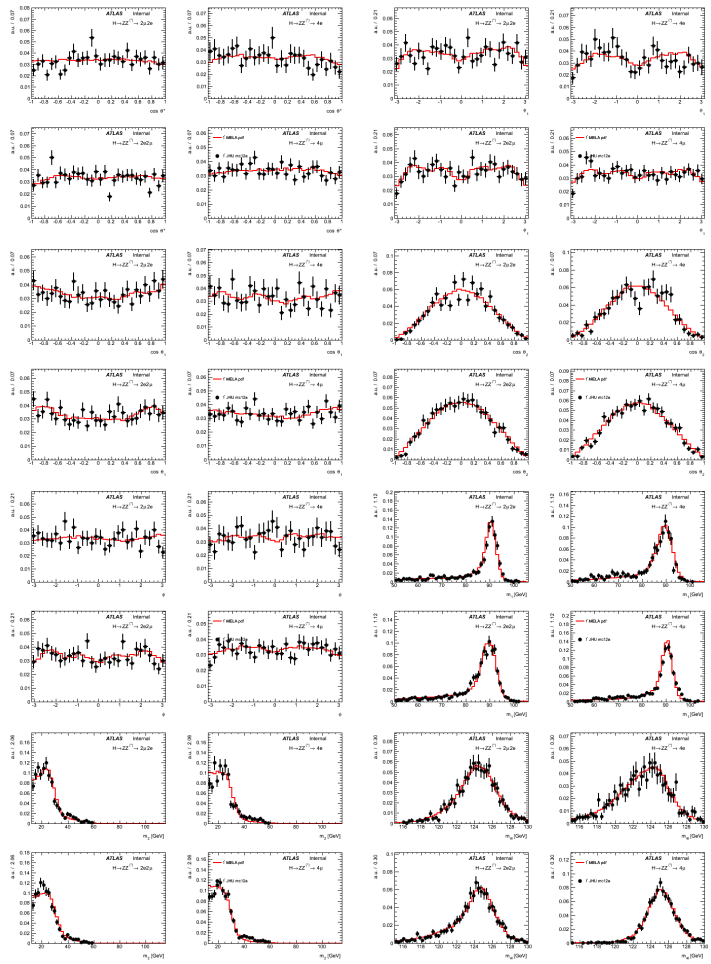

Figure 5.23: Comparison of the likelihood projection for a 1^- Higgs–like resonance (red curve) and the corresponding JHU (black points) MC simulation for the eight observable, from left to right and top to bottom: $\cos\theta^*$, ϕ_1, $\cos\theta_1$, $\cos\theta_2$, ϕ, m_1, m_2 and $m_{4\ell}$. In each plot from left to right and top to bottom for each observable: 4μ,$2\mu2e$,$4e$ and $2e2\mu$ channels.

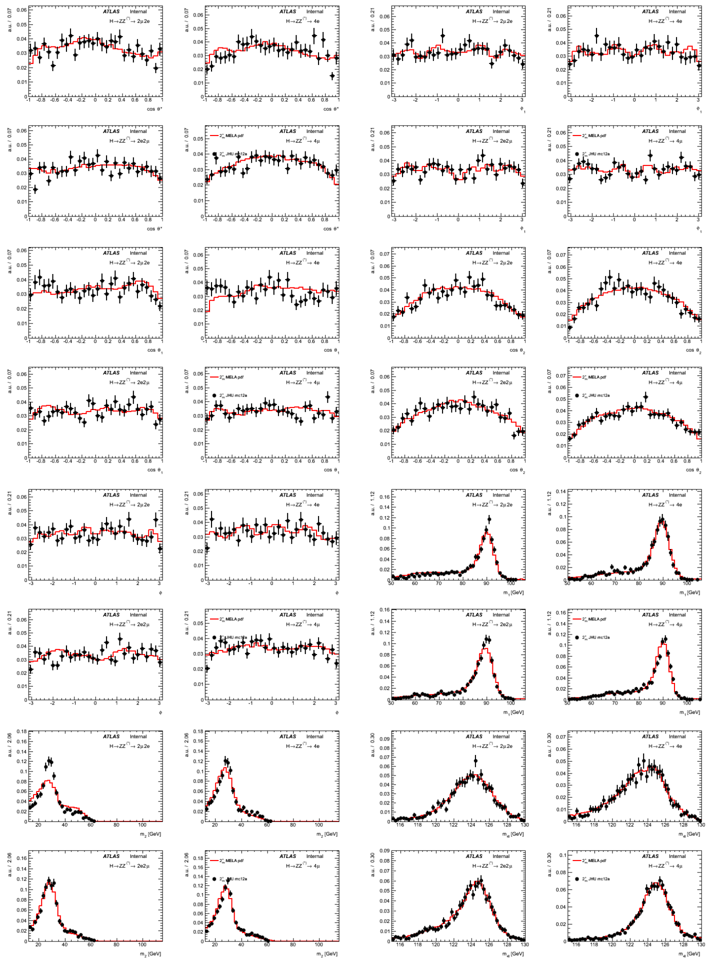

Figure 5.24: Comparison of the likelihood projection for a 2^+ Higgs–like resonance (red curve) and the corresponding JHU (black points) MC simulation for the eight observable, from left to right and top to bottom: $\cos\theta^*$, ϕ_1, $\cos\theta_1$, $\cos\theta_2$, ϕ, m_1, m_2 and $m_{4\ell}$. In each plot from left to right and top to bottom for each observable: 4μ,$2\mu2e$,$4e$ and $2e2\mu$ channels.

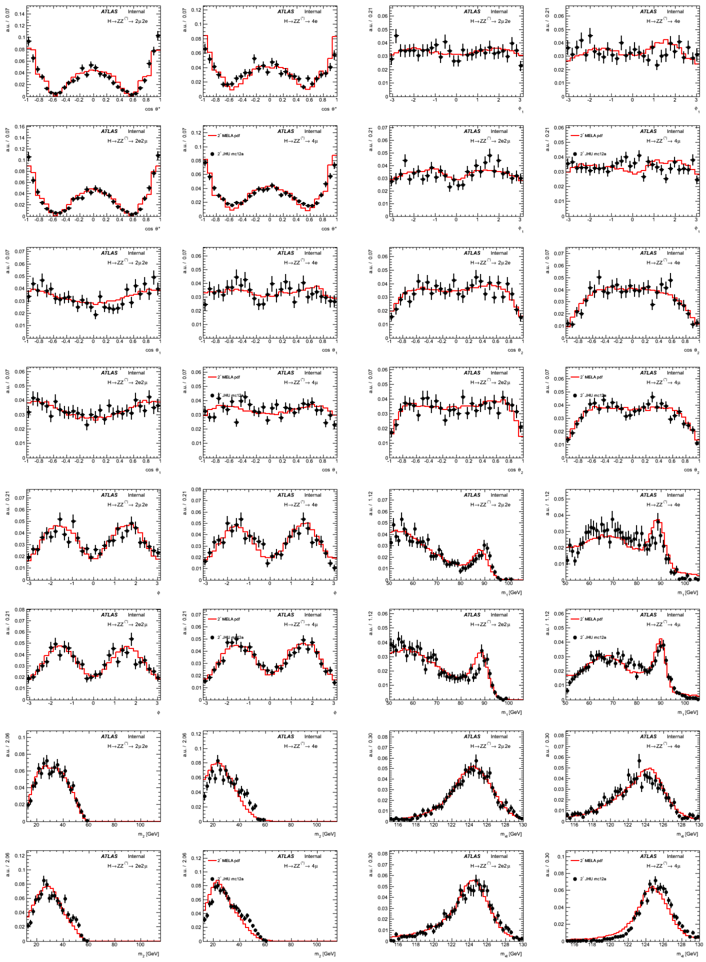

Figure 5.25: Comparison of the likelihood projection for a 2^- Higgs–like resonance (red curve) and the corresponding JHU (black points) MC simulation for the eight observable, from left to right and top to bottom: $\cos\theta^*$, ϕ_1, $\cos\theta_1$, $\cos\theta_2$, ϕ, m_1, m_2 and $m_{4\ell}$. In each plot from left to right and top to bottom for each observable: 4μ,$2\mu2e$,$4e$ and $2e2\mu$ channels.

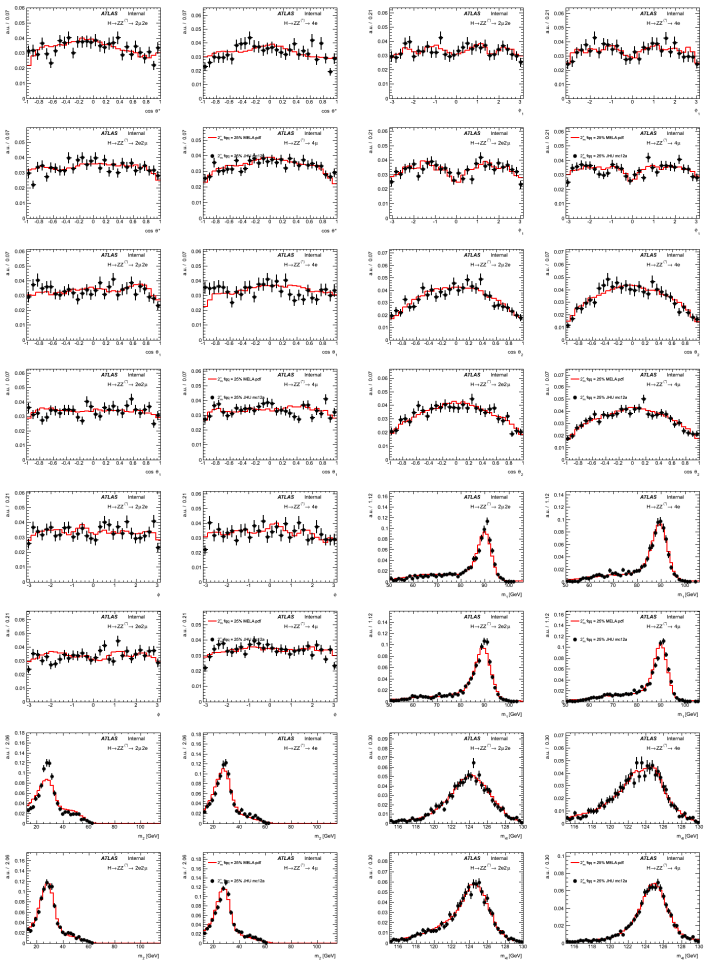

Figure 5.26: Comparison of the likelihood projection for a 2^+ $f_{qq} = 25\%$ Higgs–like resonance (red curve) and the corresponding JHU (black points) MC simulation for the eight observable, from left to right and top to bottom: $\cos\theta^*$, ϕ_1, $\cos\theta_1$, $\cos\theta_2$, ϕ, m_1, m_2 and $m_{4\ell}$. In each plot from left to right and top to bottom for each observable: 4μ,$2\mu 2e$,$4e$ and $2e2\mu$ channels.

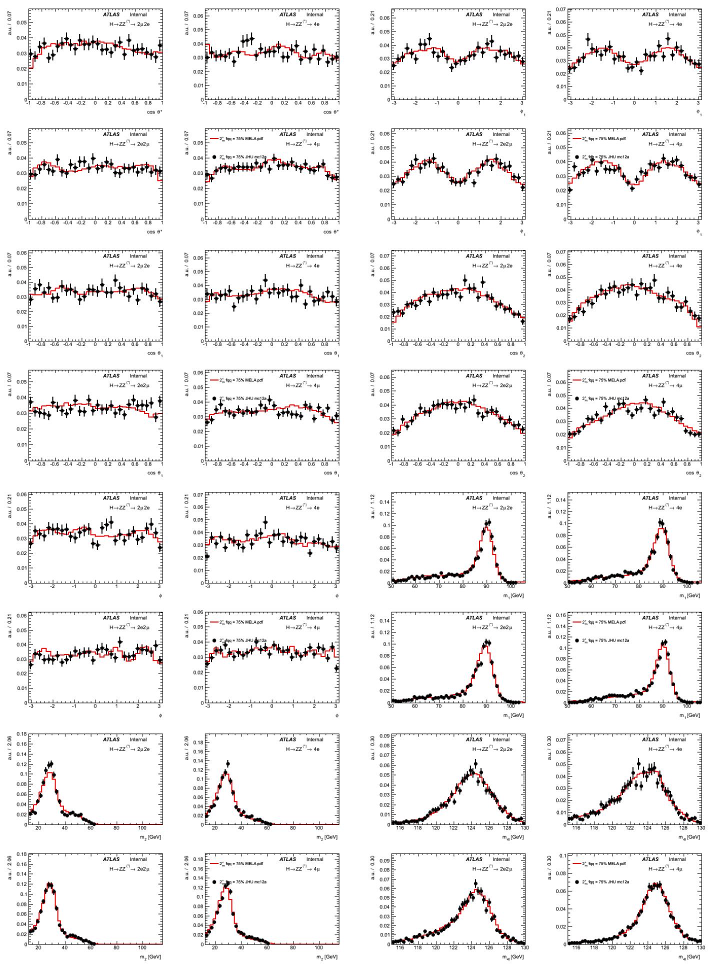

Figure 5.27: Comparison of the likelihood projection for a 2^+ $f_{qq} = 75\%$ Higgs–like resonance (red curve) and the corresponding JHU (black points) MC simulation for the eight observable, from left to right and top to bottom: $\cos\theta^*$, ϕ_1, $\cos\theta_1$, $\cos\theta_2$, ϕ, m_1, m_2 and $m_{4\ell}$. In each plot from left to right and top to bottom for each observable: 4μ,$2\mu2e$,$4e$ and $2e2\mu$ channels.

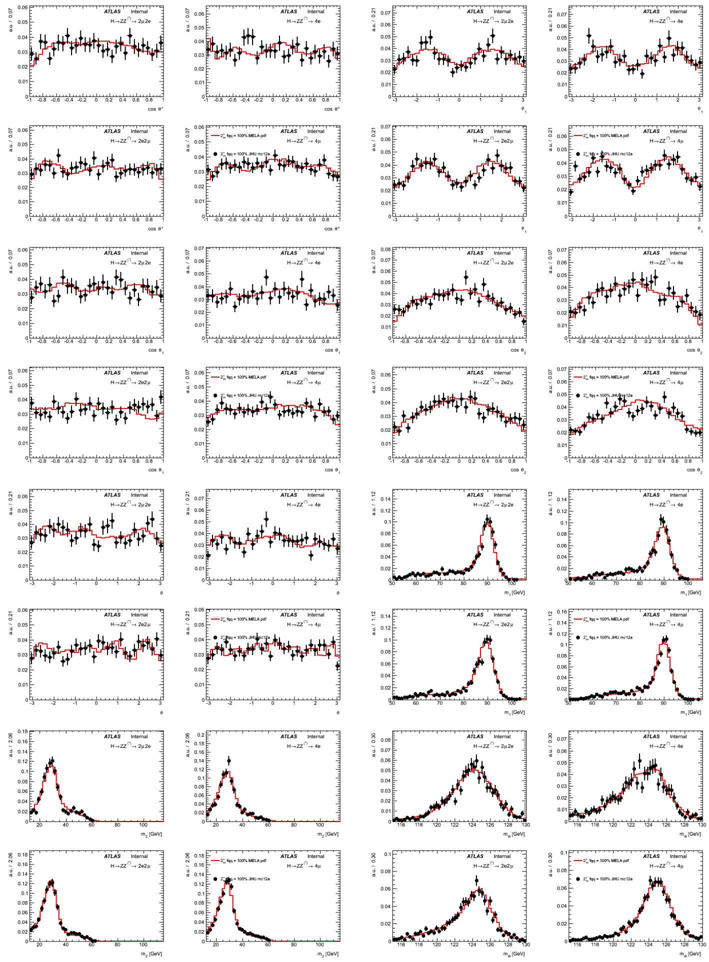

Figure 5.28: Comparison of the likelihood projection for a 2^+ $f_{qq} = 100\%$ Higgs–like resonance (red curve) and the corresponding JHU (black points) MC simulation for the eight observable, from left to right and top to bottom: $\cos\theta^*$, ϕ_1, $\cos\theta_1$, $\cos\theta_2$, ϕ, m_1, m_2 and $m_{4\ell}$. In each plot from left to right and top to bottom for each observable: 4μ,$2\mu2e$,$4e$ and $2e2\mu$ channels.

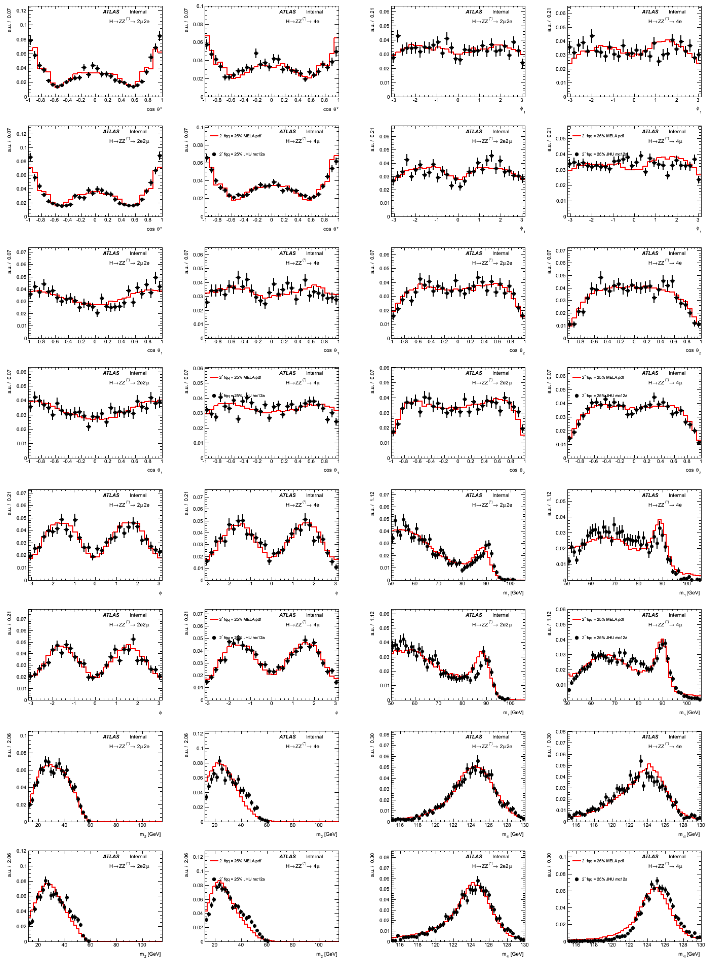

Figure 5.29: Comparison of the likelihood projection for a 2^- $f_{qq} = 25\%$ Higgs–like resonance (red curve) and the corresponding JHU (black points) MC simulation for the eight observable, from left to right and top to bottom: $\cos\theta^*$, ϕ_1, $\cos\theta_1$, $\cos\theta_2$, ϕ, m_1, m_2 and $m_{4\ell}$. In each plot from left to right and top to bottom for each observable: 4μ,$2\mu2e$,$4e$ and $2e2\mu$ channels.

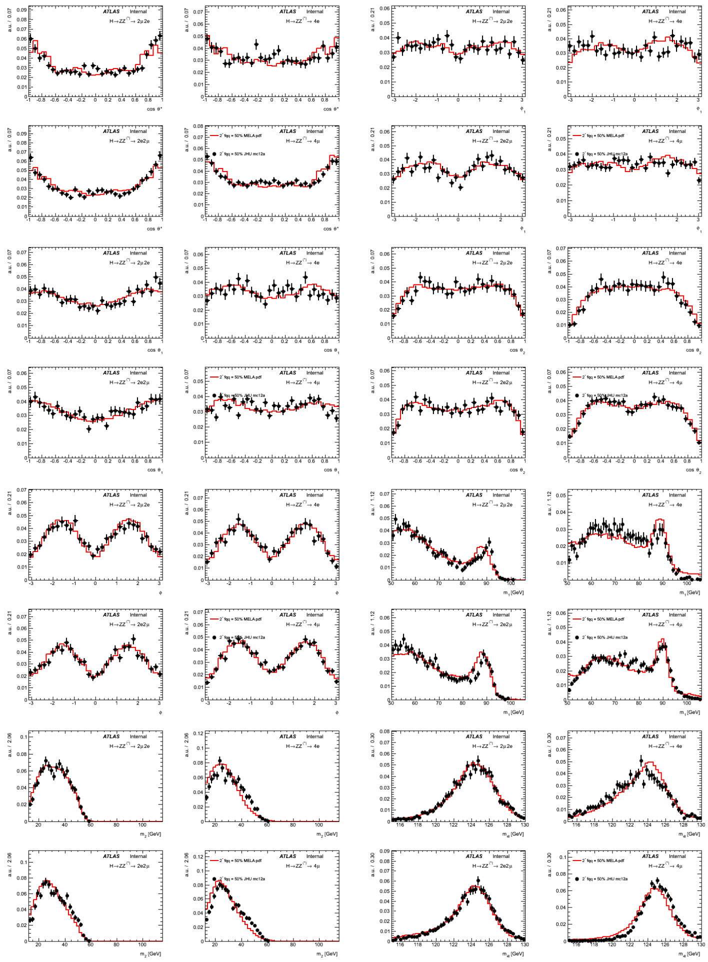

Figure 5.30: Comparison of the likelihood projection for a 2^- $f_{qq} = 50\%$ Higgs–like resonance (red curve) and the corresponding JHU (black points) MC simulation for the eight observable, from left to right and top to bottom: $\cos\theta^*$, ϕ_1, $\cos\theta_1$, $\cos\theta_2$, ϕ, m_1, m_2 and $m_{4\ell}$. In each plot from left to right and top to bottom for each observable: 4μ,$2\mu2e$,$4e$ and $2e2\mu$ channels.

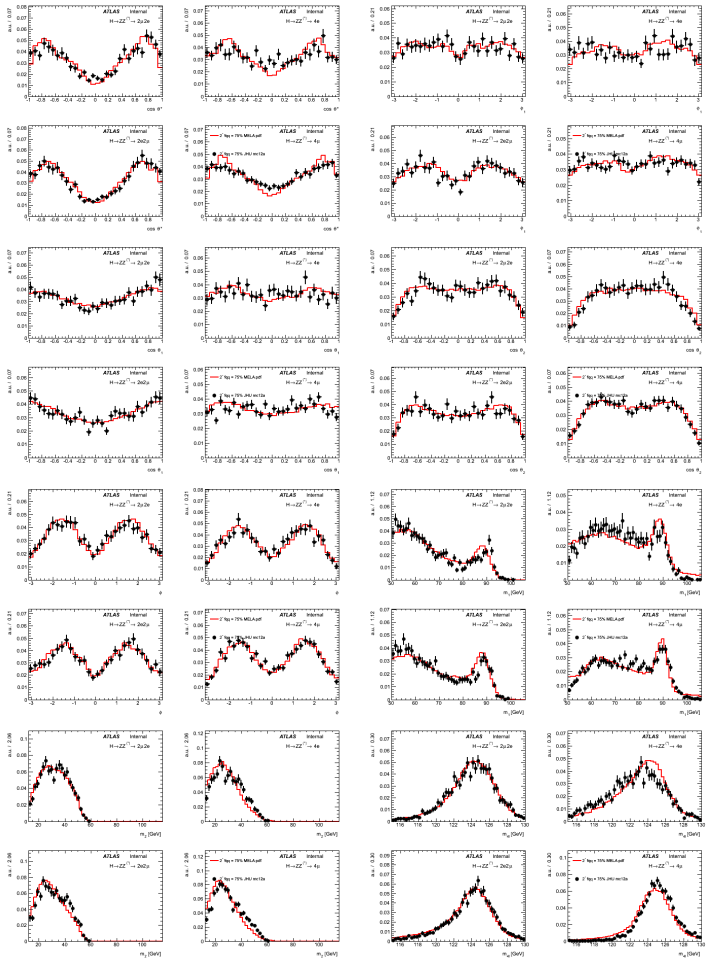

Figure 5.31: Comparison of the likelihood projection for a 2^- $f_{qq} = 75\%$ Higgs–like resonance (red curve) and the corresponding JHU (black points) MC simulation for the eight observable, from left to right and top to bottom: $\cos\theta^*$, ϕ_1, $\cos\theta_1$, $\cos\theta_2$, ϕ, m_1, m_2 and $m_{4\ell}$. In each plot from left to right and top to bottom for each observable: 4μ,$2\mu 2e$,$4e$ and $2e2\mu$ channels.

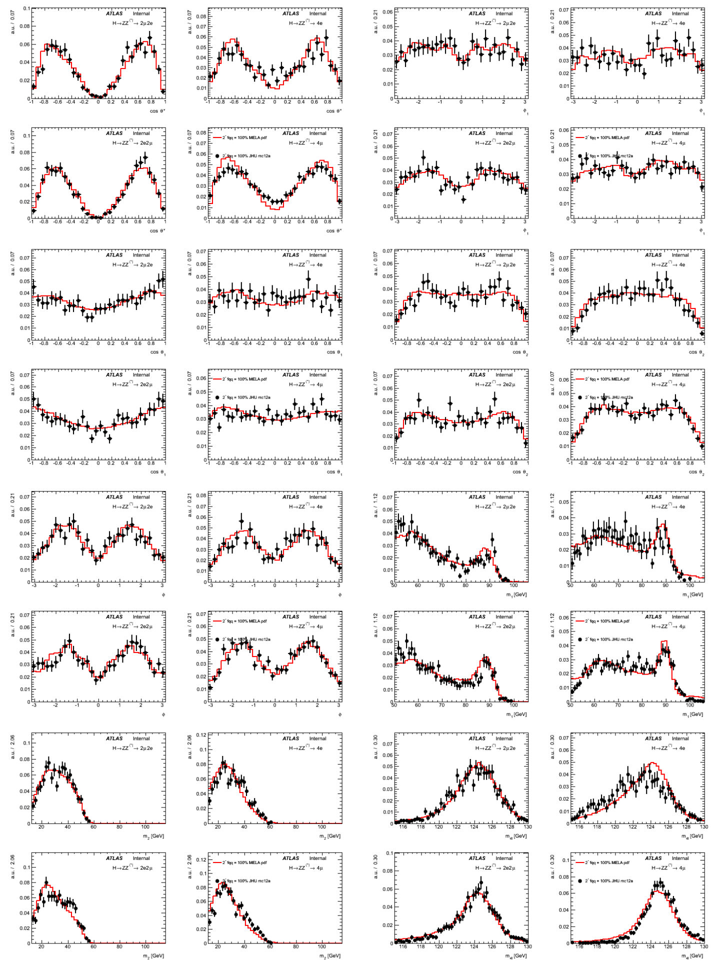

Figure 5.32: Comparison of the likelihood projection for a 2^- $f_{qq} = 100\%$ Higgs–like resonance (red curve) and the corresponding JHU (black points) MC simulation for the eight observable, from left to right and top to bottom: $\cos\theta^*$, ϕ_1, $\cos\theta_1$, $\cos\theta_2$, ϕ, m_1, m_2 and $m_{4\ell}$. In each plot from left to right and top to bottom for each observable: 4μ,$2\mu 2e$,$4e$ and $2e2\mu$ channels.

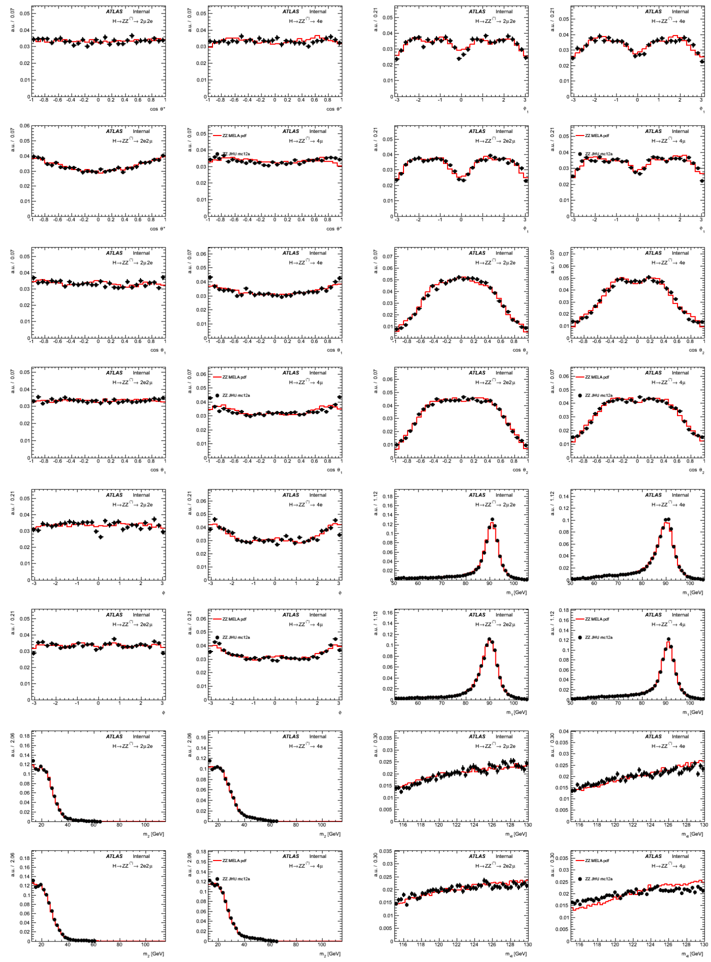

Figure 5.33: Comparison of the likelihood projection for the ZZ background (red curve) and the corresponding JHU (black points) MC simulation for the eight observable, from left to right and top to bottom: $\cos\theta^*$, ϕ_1, $\cos\theta_1$, $\cos\theta_2$, ϕ, m_1, m_2 and $m_{4\ell}$. In each plot from left to right and top to bottom for each observable: 4μ,$2\mu2e$,$4e$ and $2e2\mu$ channels.